Differential aerodynamic forces as a means to control satellite formation flight

A thesis accepted by the Faculty of Aerospace Engineering and Geodesy
of the University of Stuttgart in fulfillment of the requirements
for the degree of Doctor of Engineering Sciences (Dr.-Ing.)

by

Constantin Roland Traub
born in
Friedrichshafen

Main referee:	Prof. Dr.-Ing. Stefanos Fasoulas
Co-referee:	Prof. Dr.-Ing. Enrico Stoll
Co-referee:	Dr. Jan Thoemel
Day of the exam:	02.06.2023

Institute of Space Systems
University of Stuttgart
2023

To my family.

Preface

This dissertation falls into the realm of guidance (*"Where am I going?"*), navigation (*"Where am I?"*), and control (*"How do I get there?"*). Funny enough, I essentially asked myself the exact same questions after I returned home from my stay as a visiting scientist at NASA's Johnson Space Center in Houston in 2017. The first two questions were easy to answer. I had just successfully completed my master's degree in aerospace engineering at the Technical University of Munich and had known for some time that I wanted to pursue an academic career. So the last question to answer was how I could achieve this goal. Although this question is easy to answer in theory, putting it into practice requires much more than intrinsic motivation, as a large part is a confluence of luck and opportunity. It takes a professor who believes in your abilities, strong family support, colleagues who offer advice, friends who build you back up in bad times and role models to look up to. I consider myself very lucky to have been able to experience all of this and would like to take this opportunity to express my gratitude.

The opportunity was given to me by Prof. Stefanos Fasoulas, who offered me a long-term position after a single personal interview. Due to your selfless nature and your motivation for the cause, you have always been a role model for me, both professionally and personally. I still have a lot of growing and learning to do and I am grateful to be able to continue on that journey. This dissertation is dedicated my loving parents and my dear sister, without whom nothing would be possible. My parents, Jutta and Roland, allowed me a childhood free of worries, to develop freely and finally to find the role in life that suits me best. Thank you for giving me everything without ever asking for anything in return. With my sister, Alexandra, I can share all of my doubts, fears and insecurities and she regularly reminds me that it is perfectly okay to have them - thank you! I would like to thank my colleagues and the stuff at the Institute of Space Systems, who have supported me along the way and with whom I have shared many moments of joy but also sacrifice. What pleases me most is that many of them have become friends over time. And I most certainly don't take for granted that my best friends are still by my side, as I am well aware that, at times, their lives have been impacted by this work, too, be it due to fluctuating moods on my part or a lack of time for join holidays. *All of you were an indispensable part of the control that led me to my goal. For that, I will be eternally grateful.*

The content of this dissertation results from my time as a research associate at the Institute of Space Systems (IRS) at the University of Stuttgart (Jan. 2018 - Dec. 2022), during which, in parallel to my research activities, I participated in the Horizon 2020 project *'DISCOVERER'*[1],

[1] Disruptive Technologies for Very Low Earth Orbit Platforms.

made a major contribution to the development of a new lecture series *'Orbital Mechanics in LEO'*, and contributed intensively to the outline proposal of the Collaborative Research Center (CRC) *'Advancing Technology of Very Low-Altitude Satellites'* (ATLAS), for which the full proposal is currently being finalized. Insights, ideas, and findings have emerged from all of these activities, which have been incorporated into this work and without which it would not have been possible.

Finally, I would like to thank all the aspiring students I have supervised. The success of my dissertation was largely possible because of your motivation and dedication.

Constantin Roland Traub, Stuttgart, Germany, June 2023

Contents

Abstract

In the case of satellite formations, for which perturbing effects must be routinely compensated, the limitations of dedicated propulsion systems can be overcome by exploiting natural resources. In the best case, it is the major perturbing effect that is benefited from. In the Very-Low Earth Orbit regime, an emerging area associated with far-reaching potential but also enormous challenges, this is the aerodynamic drag acting on a satellite.

This dissertation aims to contribute to this promising field by addressing the governing research question *"How can optimal simultaneous three-dimensional relative motion control of satellite formations in the Very-Low Earth Orbit regime be realized via differential lift and drag?"*. The goal is to provide a comprehensive and holistic overall system view of the methodology. Particular emphasis is placed on the further development and characterization of the differential lift methodology, which has received little attention in the literature but is essential for three-dimensional formation flight control. The common thread running through this dissertation is the consideration of orbital decay, which is the major challenge that must be overcome to enable a sustained operation in this regime. Whenever possible, efforts were made to minimize it. This ranges from the development of a planning tool for trajectories which are optimal in a sense that the resulting decay during the maneuver is minimized to the design of optimal satellite geometries for Very-Low Earth Orbit applications. In combination, this provides a holistic view of the problem which is not yet available in the literature and insights that could hardly be obtained by other means. In addition, analytic algorithms have been (further) developed and combined to form a flexible analysis tool which allows computationally efficient preliminary assessments.

As the nature of the in- and out-of-plane relative motion fundamentally differs, so does its control. The unstable nature of the in-plane motion can be exploited for efficient maneuvers via passive drifting periods during which no control inputs are required. In contrast, the out-of-plane motion is quasi-stable and its sinusoidal nature necessitates that both satellites actively rotate in an oscillating and opposing manner to steadily produce differential lift in the desired direction. The challenge is thus to combine the different requirements in the best possible way, which represents a task which is predestined to be tackled via optimal control theory. In this work, simultaneous in- and out-of-plane control is achieved by applying yaw angle deviations. This is the most suitable approach for the given task, as it enables to exert both control forces simultaneously and in the optimal direction, i.e., differential lift perpendicular to the orbital plane. After demonstrating that the proposed approach can be used to schedule arbitrary three-dimensional formation flight maneuvers with minimal orbital decay, parameter studies targeting to explore the design space of possible maneuver variants have been conducted. The results demonstrate that the resulting

maneuver characteristics is primarily determined by (a) the balance between the difficulties of the two control tasks with respect to the available maneuver time, (b) the dynamic pressure and (c) the satellite design. These insights enabled to sub-divide the overall resulting decay into three different types and to develop targeted strategies for their respective reduction. Moreover, it allowed to identify the necessary condition which ensures a most efficient maneuver realization. Accordingly, the control tasks have to be balanced in a way that the decay which is inevitably induced during the out-of-plane control can effectively be exploited for the in-plane control.

With respect to a real mission application, however, it must be concluded from the results of the analysis that for state-of-the-art satellites the possibilities for out-of-plane adjustments via differential lift are limited and that its application is associated with severe levels of orbital decay. An essential cause is that the deposition of atomic oxygen, the major atmospheric constituent in this orbital regime, on the traditional satellite surface materials causes diffuse re-emission and ultimately the low lift coefficients experienced in-orbit to date. Consequently, it is anticipated that this methodology will find seldom application in the immediate future. As soon as materials with long-term specular or quasi-specular reflective properties become available, this evaluation will turn out differently as they have a far-reaching potential for the methodology. While improvements in the most critical parameter, the achievable lift-to-drag ratio, could be achieved for diffusely emitting materials through targeted design optimization (around 8 %), the potential for reflective materials exceeds this by orders of magnitude (around 1520 %).

The tools and methods developed within this work, however, can not only equally be employed for state-of-the-art and improved satellites designs, but in addition help to identify ideal designs in the first place. Consequently, they represent a lasting contribution to the research field. Furthermore, they serve as a valuable basis for a variety of other promising research tasks, which are briefly outlined at the end of this dissertation.

Kurzfassung

Im Falle von Satellitenformationen, bei denen Störeinflüsse routinemäßig kompensiert werden müssen, können die Nachteile dedizierter Antriebssysteme durch die Nutzung natürlicher Ressourcen überwunden werden. Im besten Fall sollte dafür der größte Störeinfluss genutzt werden. Im Bereich der sehr niedrigen Erdumlaufbahnen (engl. Very-Low Earth Orbit regime), einem aufstrebenden Bereich der mit weitreichendem Potenzial aber auch enormen Herausforderungen assoziiert wird, ist dies der aerodynamische Widerstand, der auf den Satelliten wirkt.

Diese Dissertation soll einen Beitrag zu diesem vielversprechenden Feld leisten, indem sie sich der leitende Forschungsfrage *"Wie kann eine optimale simultane dreidimensionale Regelung von Satellitenformationen im Very-Low Earth Orbit Regime durch differentiellen Auftrieb und Widerstand realisiert werden?"* widmet. Ziel ist es, eine umfassende und ganzheitliche Gesamtsystemsicht der Methodik zu erarbeiten. Besonderes Augenmerk wird dabei auf die Weiterentwicklung und Charakterisierung der Methode des differentiellen Auftriebs gelegt, die in der Literatur bislang wenig Beachtung fand, aber für eine dreidimensionale Regelung unerlässlich ist. Der rote Faden, der sich durch diese Dissertation zieht, ist die Berücksichtigung des orbitalen Höhenverlusts, der die größte Herausforderung darstellt, die überwunden werden muss, um einen dauerhaften Betrieb in diesem Regime zu ermöglichen. Wann immer es möglich war, wurden Anstrengungen unternommen, diesen zu minimieren. Dies reicht von der Entwicklung eines detaillierten Planungstools für Trajektorien, die in dem Sinne optimal sind, dass der resultierende Höhenverlust während des Manövers minimiert wird, bis hin zum Entwurf optimaler Satellitengeometrien für Anwendungen im Bereich der sehr niedrigen Erdorbits. In Kombination ermöglicht dies eine ganzheitliche Sicht auf die zu untersuchende Problemstellung, die in der Literatur bislang noch nicht verfügbar ist, und Erkenntnisse, die mit anderen Mitteln kaum zu erlangen sind. Darüber hinaus wurden analytische Algorithmen (weiter)entwickelt und zu einem flexiblen Analysetool kombiniert, das effiziente Voruntersuchungen ermöglicht.

Da sich das Wesen der Relativbewegung innerhalb und außerhalb der Ebene grundlegend unterscheidet, gilt dies auch für ihre Regelung. Die Bewegung innerhalb der Bahnebene ist instabil, was für effiziente Manöver durch passive Driftperioden ausgenutzt werden kann, während derer keine Steuereingaben erforderlich sind. Im Gegensatz dazu ist die Bewegung außerhalb der Bahnebene quasistabil und periodisch, was oszillierende und gegenläufige Rotationen beider Satelliten erfordert, um kontinuierlich differentiellen Auftrieb in der gewünschten Richtung zu erzeugen. Die Herausforderung besteht demnach darin, die verschiedenen Anforderungen bestmöglich zu kombinieren, was eine Aufgabe darstellt, die prädestiniert ist, mit Hilfe der Theorie der optimalen Regelung gelöst zu werden. In dieser Arbeit wird eine gleichzeitige Regelung

der Bewegung in- und außerhalb der Bahnebene durch die Anwendung von Gierwinkelabweichungen erzielt. Dies ist der am besten geeignete Ansatz für die gestellte Aufgabe, da er es ermöglicht, beide Steuerkräfte gleichzeitig und in der optimalen Richtung auszuüben, d.h. differentieller Auftrieb senkrecht zur Bahnebene. Nachdem gezeigt wurde, dass der vorgeschlagene Ansatz zur Planung beliebiger dreidimensionaler Formationsflugmanöver mit minimalem Höhenverlust verwendet werden kann, wurden Parameterstudien durchgeführt, um den Designraum möglicher Manövervarianten zu erkunden. Die Ergebnisse zeigen, dass die resultierende Manövercharakteristik in erster Linie durch (a) die Balance zwischen den Anforderungen der beiden Steuerungsaufgaben in Bezug auf die verfügbare Manöverzeit, (b) den dynamischen Druck und (c) das Satellitendesign bestimmt wird. Diese Erkenntnisse ermöglichten es, den resultierenden Höhenverlust in drei verschiedene Arten zu unterteilen und gezielte Strategien zu dessen Verringerung zu entwickeln. Darüber hinaus konnte die notwendige Bedingung identifiziert werden um eine möglichst effiziente Durchführung des Manövers zu gewährleisten. Demnach müssen die Regelungsaufgaben so ausbalanciert sein, dass der bei der Regelung der Bewegung außerhalb der Bahnebene zwangsläufig entstehende Höhenverlust effektiv für eine Regelung der Bewegung innerhalb der Bahnebene ausgenutzt werden kann.

Im Hinblick auf eine reale Missionsanwendung muss jedoch auf Grundlage der Ergebnissen der Analyse gefolgert werden, dass für traditionelle Satelliten die Möglichkeiten einer Einflussnahme auf die Bewegung außerhalb der Bahnebene durch differentiellen Auftrieb begrenzt und Regeleingriffe mit einem enormen orbitalen Höhenverlust verbunden sind. Eine wesentliche Ursache dafür ist, dass die Ablagerung von atomarem Sauerstoff, dem Hauptbestandteil der Atmosphäre in diesem Regime, auf den herkömmlichen Satellitenoberflächenmaterialien zu einer diffusen Re-emission und letztlich zu den bisher geringen Auftriebskoeffizienten im Orbit führt. Es ist daher zu erwarten, dass diese Methode in absehbarer Zeit nur bedingt Anwendung finden wird. Sobald Materialien mit langfristig spiegelnden oder quasispiegelnden Reflexionseigenschaften zur Verfügung stehen, wird diese Bewertung jedoch anders ausfallen, da diese weitreichendes Potenzial für die Methodik bergen. Während bei diffus re-emittierenden Materialien durch gezielte Designoptimierung Verbesserungen im relevantesten Parameter, dem erzielbaren Auftriebs-zu-Widerstand-Verhältnis, erreicht werden konnten (ca. 8 %), übersteigt das Potenzial bei reflektierenden Materialien dies um Größenordnungen (ca. 1520 %).

Die in dieser Arbeit entwickelten Tools und Methoden können aber nicht nur gleichermaßen für traditionelle sowie verbesserte Satellitendesigns eingesetzt werden, sondern helfen darüber hinaus, ideale Designs überhaupt erst zu identifizieren. Somit stellen diese einen anhaltenden Beitrag zum Forschungsfeld dar. Darüber hinaus dienen sie als wertvolle Grundlage für eine Vielzahl weiterer vielversprechender Forschungsaufgaben, die am Ende dieser Arbeit kurz skizziert werden.

Nomenclature

Latin symbols

A_s, B_s, D_s	Auxiliary parameter for the SS equations
a	Semi-major axis
Δa	Difference in semi-major axis
A_p	Average of all eight a_p values in a UTC day
a_p	Planetary equivalent amplitude
$A_{plan,k}, A_{proj,k}$	Geometric and projected area of the k'th panel
A_{ref}	Total satellite surface area projected in the free stream
$A_{ref,S}$	Arbitrary reference area for the Sentman and Schamberg model
$A_\rho, B_\rho, C_\rho, D_\rho$	Fitting parameter of the analytic density model
$\Delta a_t, \Delta a_n, \Delta a_i, \Delta a_e$	Total, natural, induced and exploited decay
δa	First entry of $\delta\bar{\boldsymbol{\varepsilon}}_{ns}$
c	The Schweighardt-Sedwick coefficient
C_D, C_L	Drag and lift coefficient
$C_{D,k}, C_{L,k}$	Drag and lift coefficient of the k'th panel
$C_{D,max}, C_{D,min}$	Maximum and minimum drag coefficient
$C_{L,max}, C_{L,min}$	Maximum and minimum lift coefficient
d	Second entry of $\bar{\boldsymbol{\alpha}}$
Δd	In-plane control distance
E	Energy of a particle
e	Eccentricity
E_i, E_r	Kinetic energy carried by the incident and reflected particles
e_{ip}, e_{op}	In- and out-of-plane eccentricity
$\Delta e_{ip,max}$	Feasibility range
e_{MSE}	Mean squared error
E_w	Kinetic energy that would be carried away in complete equilibrium
$f_{D,max}, f_{D,min}$	Specific drag force in the maximal and minimal drag configuration
$f_{D,@L_{max}}$	Specific drag force in the maximum lift configuration
$f_{L,max}$	Specific lift force in the maximum lift configuration
f_M	Maxwell coefficient
$F_{10.7}, \bar{F}_{10.7}$	Daily and 81-day average 10.7 cm radio flux
$+\Delta\delta f_L, +\Delta\delta f_D$	Increase in the specific differential lift and drag force
G, P, Q, Z	Auxiliary parameter for the Sentman model
g	Gravitational attraction
$H^\star$	Density scale height
h	Altitude
h_b	Extrusion height
I	Momentum of a particle
i	Inclination

I_x, I_y, I_z	Moment of inertia around the ${}^{\mathcal{B}}\hat{\boldsymbol{x}}$ -, ${}^{\mathcal{B}}\hat{\boldsymbol{y}}$ -, and ${}^{\mathcal{B}}\hat{\boldsymbol{z}}$ - axes
δi	Third entry of $\delta\bar{\boldsymbol{\mathcal{E}}}_{ns}$
J_n	n-th order zonal harmonics of the Earth's gravity field
k_α, k_β, k_z	Shift of the center of the circular motion due to $\delta f_{L,x}$, δf_D and $\delta f_{L,z}$
K_p	Planetary index
Kn	Knudsen number
k_S, l_S, t_S	Cosines between the force direction and the local x -, y -, and z - axes
L	Characteristic reference length
M_k	Mean anomaly
$M, \bar{M}$	Molar and mean molar mass
m	Mass of the satellite
m_m	Molecular mass
n	Mean motion
n_i	Particle number density of i'th species
n_{MC}	Number of Monte Carlo runs
n_s	Number of switches
P	Orbital period
p	Normal momentum
p_i, p_r	Normal momentum of the incident and the reflected particles
p_k	Semi-parameter
p_w	Normal momentum carried away in full equilibrium
p_∞	Atmospheric pressure
q	Dynamic pressure
q_1, q_2	Fourth and fifth entry of $\bar{\boldsymbol{\mathcal{E}}}$
$\delta q_1, \delta q_2$	Fourth and fifth entry of $\delta\bar{\boldsymbol{\mathcal{E}}}_{ns}$
r_{mp}, r_{rms}	Ratio of velocities (most probable and root mean squared)
r_n	Nose radius
s	Molecular speed ratio
T	Temperature
t	Time
$t_{comp.}$	Computational time to schedule the control pattern
T_e	Exospheric temperature
t_f	Final maneuver time
$t_{f,g}$	Initial guess for the maneuver time
$t_{f,max}, t_{f,min}$	Maximum and minimum final maneuver time
T_{ip}, T_{op}	Period of the in- and out-of-plane motion
$T_{k,i}, T_{k,r}$	Kinetic temperature of the incident and reflected particles
t_L	Satellite lifetime
T_∞	Atmospheric temperature
$+\Delta t_L$	Increase in satellite lifetime
t_{P1}, t_{P2}, t_{P3}	Time required for phase #1, #2 and #3
T_r	Kinetic temperature of the reflected particles
T_w	Temperature of the surface
$T_{W,max}$	Maximum torque commanded to the reaction wheels
u	True argument of latitude
V_b	Volume of the main satellite body
v_{circ}	Circular orbit velocity
v_d	Fourth entry of $\bar{\boldsymbol{\alpha}}$
v_{ra}, v_{tr}	Satellite velocity in the radial and transversal direction
$v_{r,mp}, v_{r,rms}$	Most probable and root mean squared re-emission velocity

v_t	Gas thermal velocity
w_n	Nose width
$\bar{x}, \bar{y}$	Average in-plane states for the SS equations
x_r	Step size for the midpoint circle algorithm
$\bar{x}_{sc}$	$\bar{x}$ coordinate of the switch curve
X_S, Y_S, Z_S	Axes of the body frame for the Sentman model
x_S, y_S, z_S	Axes of the local frame of a surface area for the Sentman model
$\boldsymbol{F}_A$	Aerodynamic force vector
$\boldsymbol{F}_D, \boldsymbol{F}_L$	Aerodynamic drag and lift vector
$\boldsymbol{f}_A$	Specific aerodynamic force vector
$\boldsymbol{f}_D, \boldsymbol{f}_L$	Specific aerodynamic drag and lift vector
$\boldsymbol{f}_p$	Specific perturbing force vector
$\delta \boldsymbol{f}_A$	Specific differential aerodynamic force vector
$\delta \boldsymbol{f}_D, \delta \boldsymbol{f}_L$	Specific differential aerodynamic drag and lift vector
$\boldsymbol{h}$	Specific angular momentum vector
$\hat{\boldsymbol{n}}$	Local normal vector of a surface element
$\hat{\boldsymbol{n}}_k$	Local normal vector of the k'th panel
$\boldsymbol{q}$	Accelerations caused by non-conservative perturbing forces
$\hat{\boldsymbol{u}}_L$	Effective lift direction unit vector
$\hat{\boldsymbol{u}}_{L,k}$	Effective lift direction unit vector of the k'th panel
$\boldsymbol{r}, \boldsymbol{v}$	Inertial satellite position and velocity vector
$\boldsymbol{r}_{rel}, \dot{\boldsymbol{r}}_{rel}, \ddot{\boldsymbol{r}}_{rel}$	Relative position, velocity and acceleration vector
$\boldsymbol{u}$	Control vector
$\boldsymbol{v}_i$	Velocity vector of the incident particles
$\boldsymbol{v}_m$	Gas macroscopic velocity vector
$\boldsymbol{v}_r$	Velocity vector of the reflected particles
$\boldsymbol{v}_{rel}$	Velocity relative to the local atmosphere
$\boldsymbol{v}_{rot}$	Co-rotation velocity vector of the atmosphere with the Earth
$\boldsymbol{v}_w$	Thermospheric wind velocity vector
$\boldsymbol{x}$	State vector

Greek symbols

α, β	Oscillating in-plane states for the SS equations
α_A	Angle of attack
α_S	Inclination angle of a surface element for the Sentman model
α_T	Energy accommodation coefficient
$\alpha_{T,p}$	Partial energy accommodation coefficient
α_n, α_t	Normal and tangential energy accommodation coefficient
$\bar{\alpha}_0, \tilde{\alpha}_0$	Fifth entry of $\bar{\boldsymbol{\alpha}}$ and $\tilde{\boldsymbol{\alpha}}$
β_A	Angle of sideslip
β_D, β_L	Ballistic drag and lift coefficient
$\beta_{D,min}$	Minimum ballistic (drag) coefficient
$\beta_{D,max}$	Maximum ballistic (drag) coefficient
$\beta_{D,@L_{max}}$	Ballistic (drag) coefficient in the maximum lift configuration
$\bar{\beta}_0, \tilde{\beta}_0$	Sixth entry of $\bar{\boldsymbol{\alpha}}$ and $\tilde{\boldsymbol{\alpha}}$
ϵ	Auxiliary parameter to account for J_2
ζ	Transformation function
η	Auxiliary variable for $\boldsymbol{\mathcal{E}}_{ns}$

$\theta, \dot{\theta}$	Pitch angle and its time derivative
θ_k	True anomaly
θ_i, θ_r	Incident and reflection angle
θ_{ip}, θ_{op}	Phase angle of the in- and the out-of-plane motion
ϑ, φ, χ	Cosines between the local axes and $\boldsymbol{v}_m$
λ	Mean free path length
λ_{ns}	Mean argument of latitude
$\delta\lambda$	Second entry of $\delta\bar{\boldsymbol{\mathcal{E}}}_{ns}$
Π	Potential energy of the satellite
ρ	Density
$\rho_{i,AM}, \rho_{i,ref}$	Density predicted by the analytic model and reference density
ρ_x, ρ_z	First and third entry of $\bar{\boldsymbol{\alpha}}$
ρ_1, ρ_2, ρ_3	First, second and third entry of $\tilde{\boldsymbol{\alpha}}$
$\Delta\rho_z$	Out-of-plane control distance
σ_t, σ_n	Tangential and normal momentum accommodation coefficient
τ	Tangential momentum
τ_i, τ_r	Tangential momentum of the incident and the reflected particles
$\phi, \dot{\phi}$	Roll angle and its time derivative
$\psi, \dot{\psi}$	Yaw angle and its time derivative
ψ_i, ψ_r	Angle of incident and reflection (complementary to θ_i, θ_r)
ψ_{max}, ψ_{min}	Maximum and minimum yaw angle
$\dot{\psi}_{max}, \dot{\psi}_{min}$	Maximum and minimum time derivative of the yaw angle
Ω	Right ascension of the ascending node
$\delta\Omega$	Sixth entry of $\delta\bar{\boldsymbol{\mathcal{E}}}_{ns}$
ω	Argument of perigee
$\bar{\boldsymbol{\alpha}}, \tilde{\boldsymbol{\alpha}}$	Set of parameter to define the solutions to the CW and the TH equation
$\boldsymbol{\rho}, \dot{\boldsymbol{\rho}}, \ddot{\boldsymbol{\rho}}$	Relative position, velocity and acceleration vector in the $\mathcal{L}$ - frame
$\boldsymbol{\omega}$	Angular velocity vector

Others

$\boldsymbol{\mathcal{E}}$	Oscillating Keplerian elements	$\bar{\boldsymbol{\mathcal{E}}}$	Mean Keplerian elements
$\boldsymbol{\mathcal{E}}_{ns}$	Oscillating non-singular elements	$\bar{\boldsymbol{\mathcal{E}}}_{ns}$	Mean non-singular elements
$\delta\bar{\boldsymbol{\mathcal{E}}}_{ns}$	Mean differential non-singular elements	$\delta\bar{\boldsymbol{\mathcal{E}}}$	Mean differential Keplerian elements
$\mathcal{R}$	Disturbing function	$\mathcal{J}$	Cost functional

Subscripts

A	Aerodynamic	c	Chief	D	Drag	d	Deputy	f	Final
i	Incident	L	Lift	ns	Nearly-nonsingular	r	Reflected	0	Initial

Chemical elements

Ar	Argon	H	Hydrogen	He	Helium
N	Atomic nitrogen	N_2	Molecular nitrogen		
O	Atomic oxygen	O_2	Molecular oxygen		

Reference frames

$\mathcal{B}$	Body fixed frame	$\left\{{}^{\mathcal{B}}\hat{\boldsymbol{x}},\ {}^{\mathcal{B}}\hat{\boldsymbol{y}},\ {}^{\mathcal{B}}\hat{\boldsymbol{z}}\right\}$
$\mathcal{F}$	Frenet frame	$\left\{\hat{\boldsymbol{n}},\ \hat{\boldsymbol{t}},\ \hat{\boldsymbol{w}}\right\}$
$\mathcal{J}$	Earth-centered inertial frame	$\left\{\hat{\boldsymbol{I}},\ \hat{\boldsymbol{J}},\ \hat{\boldsymbol{K}}\right\}$
$\mathcal{L}$	Local-vertical-local-horizontal frame	$\left\{\hat{\boldsymbol{x}},\ \hat{\boldsymbol{y}},\ \hat{\boldsymbol{z}}\right\}$
$\mathcal{T}$	True of date frame	$\left\{{}^{\mathcal{T}}\hat{\boldsymbol{I}},\ {}^{\mathcal{T}}\hat{\boldsymbol{J}},\ {}^{\mathcal{T}}\hat{\boldsymbol{K}}\right\}$

Constants

$\mathcal{R}$	8.31446261815324	$\mathrm{J\,mol^{-1}\,K^{-1}}$	Universal gas constant
G	6.673×10^{-11}	$\mathrm{m^3\,kg^{-1}\,s^{-2}}$	Gravitational constant
k_b	$1.380\,649 \times 10^{-23}$	$\mathrm{J\,K^{-1}}$	Boltzmann constant
J_2	$1.082\,626\,7 \times 10^{-3}$	$-$	Zonal potential coefficient of degree two
R_e	$6.378\,136\,3 \times 10^{6}$	m	Average equatorial radius of the Earth
m_e	$5.973\,332 \times 10^{24}$	kg	Mass of the Earth
μ_e	$398\,600.4415 \times 10^{9}$	$\mathrm{m^3\,s^{-2}}$	Gravitational parameter of the Earth
ω_e	$0.729\,211\,585\,530 \times 10^{-4}$	$\mathrm{rad\,s^{-1}}$	Angular velocity of the Earth
e_e	0.081 819 221 456	$-$	Eccentricity of the Earth

Abbreviations and acronyms

ABEP	Atmosphere-breathing electric propulsion
ATLAS	Advancing Technology of Very Low-Altitude Satellites
CF	Circular formation
CLL	Cercignani-Lampis-Lord
COTS	Commercial off-the-shelf
CRC	Collaborative Research Centers
DISCOVERER	Disruptive Technologies for Very Low Earth Orbit Platforms
DSMC	Direct Simulation Monte Carlo
DSS	Distributed space systems
DTM	Drag-temperature model
ECI	Earth-centered inertial
EUV	Extreme ultraviolet
FLP	Flying Laptop
FMF	Free molecular flow
GOCE	Gravity Field and Steady-State Ocean Circulation Explorer
GPS	Global Positioning System
GRACE	Gravity Recovery and Climate Experiment
GSI	Gas-surface interactions
GVP	Gauss' form of the variational equations
HCW	Hill or Clohessy–Wiltshire equations
HWM	Horizontal wind model
IPF	In-plane formation
IR	Infrared
ISS	International Space Station
JB	Jacchia-Bowman

LEO	Low Earth Orbit
LPE	Lagrange's planetary equations
LQR	Linear-quadratic regulator
LVLH	Local-vertical/local-horizontal
MC	Monte Carlo
mp	Most probable
MPC	Model predictive controller
MSIS	Mass Spectrometer and Incoherent Scatter Radar
NRLMSISE	Naval Research Laboratory MSIS Radar Exosphere
PCF	Projected circular formation
RAAN	Right ascension of the ascending node
rms	Root mean square
SC	Switch curve
SESAM	Semiempirical model for satellite energy accommodation coefficients
SFF	Satellite formation flight
SRP	Solar radiation pressure
SS	Schweighardt-Sedwick
TH	Tschauner-Hempel
ToD	True of date
UTC	Universal Time Coordinated
VLEO	Very-Low Earth Orbit
VOP	Variation-of-parameters

Part I

Fundamentals

Chapter 1

Introduction

"I would rather have questions that can't be answered
than answers that can't be questioned."
— Richard P. Feynman

It may be permitted to begin this dissertation with a biological inspiration[2]: in the presence of a predator like a hawk or peregrine falcon, starlings form huge groups, so called murmurations, and the flock's movement is based on evasive maneuvers. As there is safety in numbers, the coordinated effort allows the flock to achieve a common goal which would otherwise be impossible to achieve by an individual starling. [7, 54] Such a well-coordinated movement of two or more animals of the same species is commonly referred to as a *formation* [51], and is impressively depicted in Fig. 1.1, which shows a murmuration of starlings taking the shape of a large flying bird, captured over the Costa Brava, Spain, in December 2016 [12]. It can easily be interfered that the deterrent effect of the murmuration supersedes the effect of an individual starling. This unique approach of working together in the kingdom of animals serves as an biological inspiration for the space industry today, in which single operating satellites are often replaced by a multitude of small, unconnected satellites operating in a coordinated fashion [51]. The latter is commonly referred to as a *distributed space system* (DSS) which, according to Cappelletti, Battistini, and Malphrus [25], is formally defined as: *"*[...] *a system consisting of multiple space elements that can communicate, coordinate and interact in order to achieve a common goal"* or scientific objective. A distribution of spacecraft may increase the scientific return of space missions and offers advantages such as cost reductions, improvement of robustness, and increase of flexibility. In addition, several types of missions would be hardly feasible without a payload distribution. [25]

DSS may be classified by different metrics. Among others, the degree of autonomy, the nature of communication, the inter-satellite distance, the type of control and its accuracy, the number of satellites or the types of relative trajectories are consulted [76]. This dissertation limits itself to a discussion of satellite formations which, according to Scharf, Hadaegh, and Ploen [138], are defined as: *"A set of more than one spacecraft whose dynamic states are coupled through a common control law."* [138]. Furthermore, the authors extend that at least one member of the

[2] Inspired by the brilliant inaugural talk given by Prof. Eberhard Gill [51] at TU Delft in 2008.

Figure 1.1: Picture of a murmuration of starlings taking the shape of a large flying bird, captured near Sant Pere Pescador in Catalonia, Spain, on the 31st of December 2016 [12].

set has to track a desired state relative to another member and that the tracking control law must depend upon this relative state. The second point is described as the critical differentiation from a constellation, where the orbit corrections are solely based on an individual satellite's position and velocity [138]. Cappelletti, Battistini, and Malphrus [25] associate formations with small relative inter-satellite distances, on-board closed-loop control and inter-spacecraft communication.

In addition to distributing payload tasks, the miniaturization of satellites has revolutionized the way humans pursue spaceflight since the turn of the century. For decades, satellites expanded in size, mass, and complexity to adapt to their increasingly complex missions [76]. These monolithic satellites were expensive and could hardly be upgraded in orbit [97]. However, the advent of powerful, low-cost electronics and novel manufacturing techniques enabled the development of smaller and lighter satellites that could be manufactured more quickly and cheaply [119]. Consisting mainly of commercial off-the-shelf (COTS) parts, the functionality per unit mass significantly increased. This enabled new entities such as academic institutions, private companies, startups and developing countries to take their first ventures into the space business. Therefore, it is recognized as a powerful enabler of the commercialization of spaceflight[3].

A third trend in spaceflight emerged in the very recent past, namely the exploitation of the *Very Low Earth Orbit* (VLEO) regime, a subset of the traditional Low-Earth Orbit (LEO) regime, which might revolutionize spaceflight yet again. The approximate range of altitudes associated with VLEO can be stated as below 450 km [33], although no definitive standards have been established so far (see Fig. 1.2). The major challenge to be overcome for a sustained operation in this regime to become reality is the compensation of the atmospheric drag force acting on the spacecraft. Atmospheric drag, resulting from the interaction of residual atmospheric particles with

[3] Commonly referred to as 'NewSpace' or 'Space 2.0' [119].

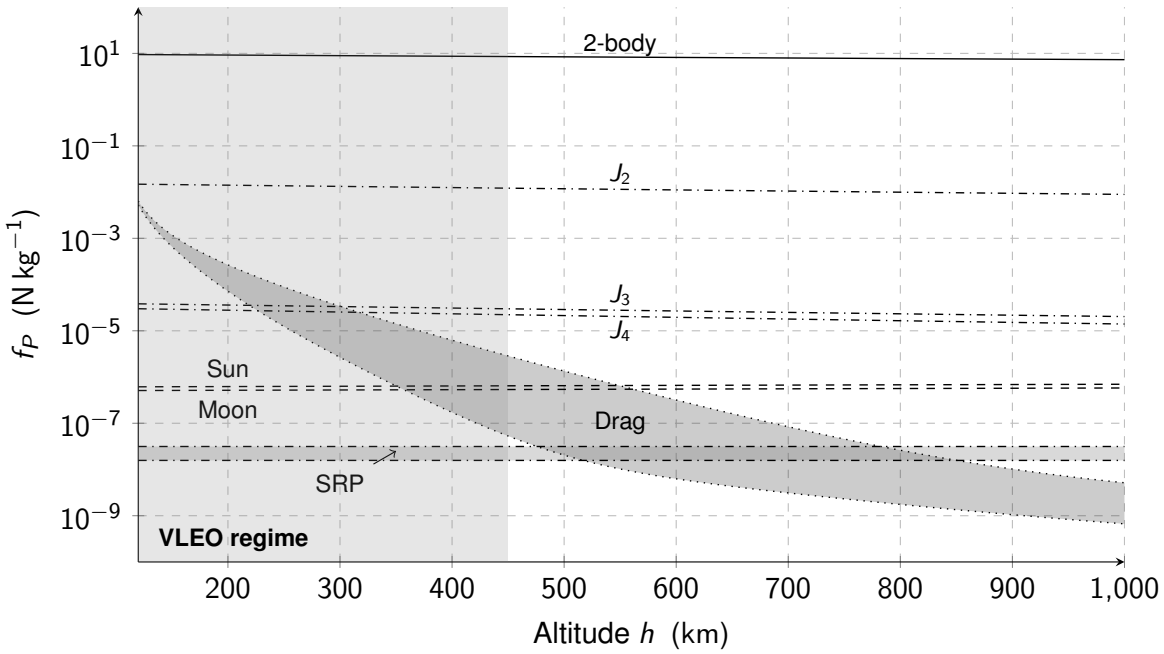

Figure 1.2: Order of magnitude of the specific perturbing forces f_p in the lower LEO regime over altitude (figure design adopted from Dell'Elce [37]).

the satellite's surface, continuously dissipates energy from the system and inevitably causes the satellite to slow down and re-enter in short time if no adequate countermeasures are being taken. In this regime, typical timespans to re-entry from orbital decay are often given in weeks, months or a few years at most for objects not sustained by drag-mitigating measures. Yet, similarly drag can be seen as an asset, as it ensures a rapid decay of debris particles and non-operational satellites, due to which the regime is attributed a 'self-cleaning characteristic'. With the traditional LEO regime being subjected to the very risk of becoming inaccessible in the near future due to the proliferation of satellite constellations and the accumulating orbital debris (see Fig. 1.3), many satellite operations in LEO could be relocated into the VLEO altitude range if sustained operations could be achieved through the development of new technologies and platform concepts. As illustrated in Fig. 1.4, an operation of spacecraft at lower altitudes promises a variety of potential benefits to future scientific and commercial space missions.

To establish, reconfigure and maintain satellite formations despite ever-present perturbing forces as well as to enable collision-avoidance maneuvers in case of an imminent close encounter with another object (active satellite and/or space debris), a method to exert control forces is indispensable. To this day, the state-of-the-art solution is to use chemical or electric propulsion systems. However, the stringent volume, mass and power budgets of miniaturized satellite systems make it increasingly difficult to accommodate these. In addition, reducing the respective launch costs through ride sharing imposes compelling requirements on the CubeSats that act as the secondary payloads, including limiting the amount and composition of stored fuel. Thus, alternative types of control mechanisms are desirable.

As far as natural resources are concerned, it is the major disturbance effect which should be exploited for actuation purposes. In the VLEO range, these are the Earth's oblateness and

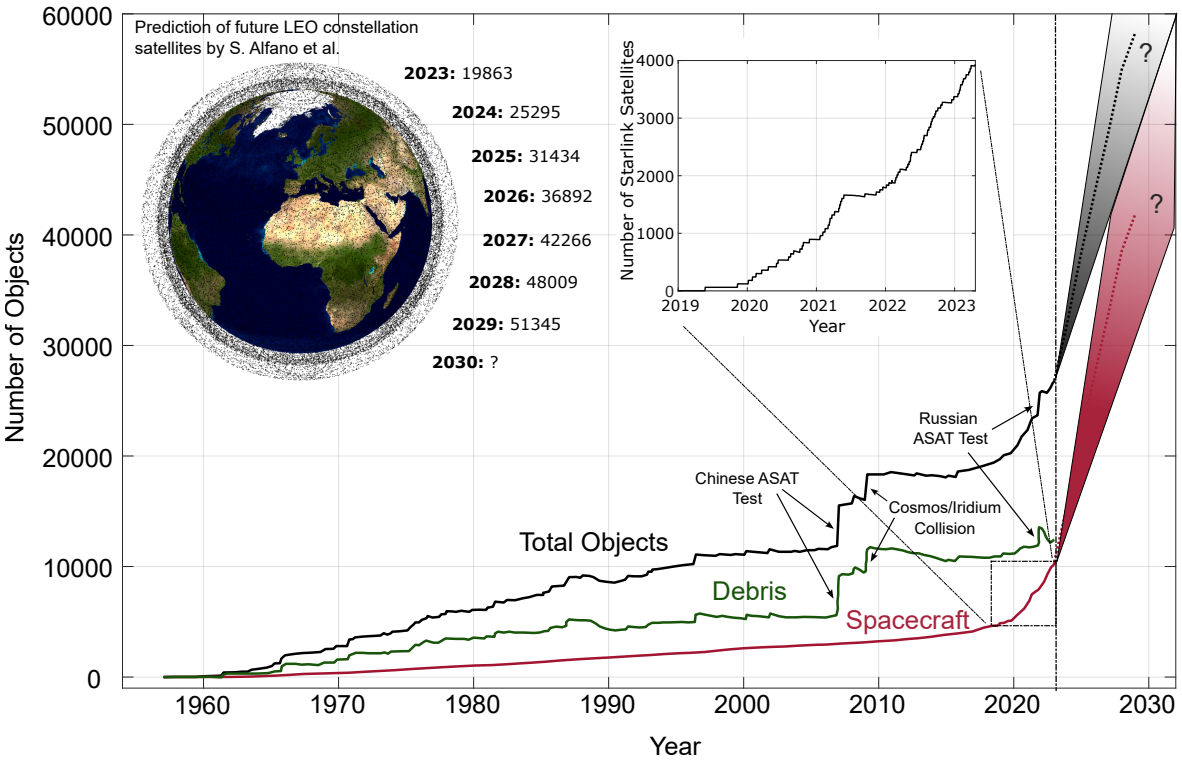

Figure 1.3: History and future of Earth orbiting objects, most in conventional Low Earth Orbit. Historic data extracted from NASA's orbital debris program office [56], SpaceX Starlink data from McDowell [107] and future data as predicted by Alfano, Oltrogge, and Shepperd [4]. (Credits: CRC ATLAS)

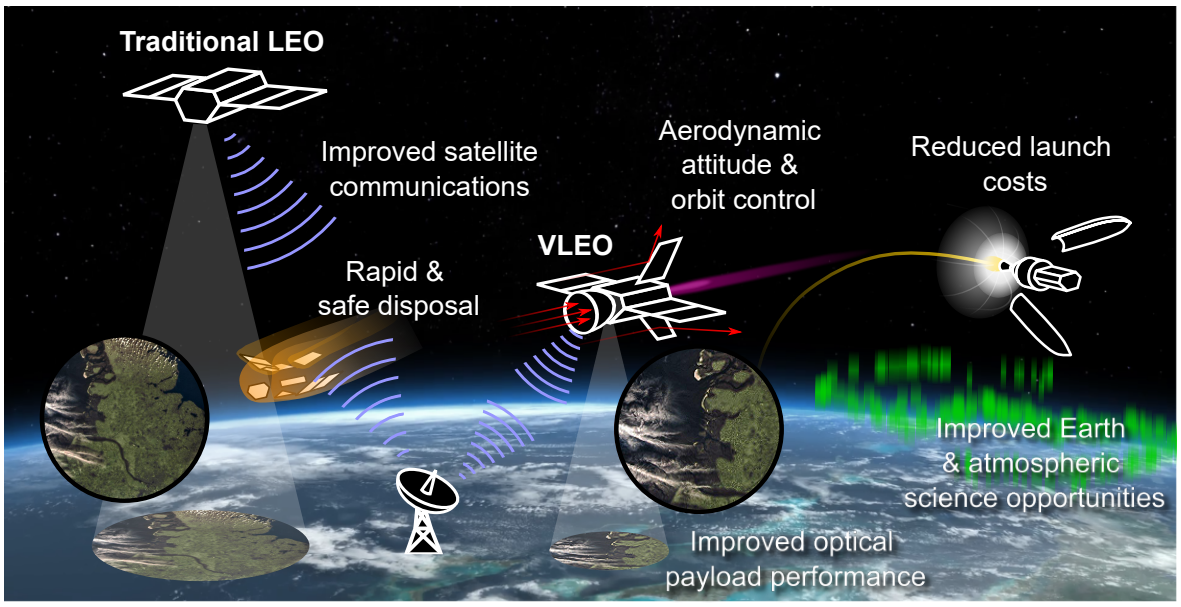

Figure 1.4: Illustration of benefits associated with sustainable VLEO utilisation. (Credits: A. Pagan, CRC ATLAS)

the aerodynamic drag (see Fig. 1.2). Since only the latter can be manipulated by the satellite, Leonard [90] introduced differential drag as a promising option for the propellant-less control of satellite formation flight (SFF) in the mid-eighties. In accordance with the introductory example of a murmuration of starlings, who coordinate the movement of the flock via dedicated adjustments of the individual bird's wings, this method comprises the adjustment of dedicated panels or the satellites' attitudes such that differences in the magnitudes of aerodynamic drag forces experienced by two spacecraft, referred to as differential drag forces, are intentionally induced. This propellantless alternative, which eliminates the need for complex propulsion systems and thus counteracts the difficulties mentioned above, has already been successfully demonstrated in orbit[4]. The major limitation of the methodology, however, is the fact that its control authority is basically limited to the in-plane relative motion control. As shown by Ben-Yaacov and Gurfil [10], the component of the drag force pointing in the out-of-plane direction[5] is unable to provide meaningful control authority. Thus, to enable three-dimensional relative motion control, forces perpendicular to the orbital plane, i.e., differences in the magnitude and/or direction of the residual aerodynamic lift forces, referred to as differential lift forces, are required.

Despite the promising benefits, differential lift has received only little attention in literature so far as frequently the aerodynamic lift forces of satellites, which by definition act perpendicular to drag, are considered to be negligible. This is due to a multitude of reasons, including that for satellites which are spinning or tumbling the effect of aerodynamic lift cancels out and that satellites with symmetrical shapes do not produce lift at all [62]. In addition, the lift coefficients C_L experienced by traditional satellites in orbit are noticeably smaller than the drag coefficients C_D and, according to the perturbation equation, perpendicular force components are significantly less effective in changing the orbit geometry. However, by intentionally maintaining a constant attitude with respect to the relative velocity vector, the effects of aerodynamic lift are shown to essentially build up over time and generate measurable effects on the satellite orbit. First studies of the effect of aerodynamic lift on satellite orbits by Cook [31] date back to 1964, yet an effect was first experienced during the analysis of the inclination of the S3-1 satellite in 1977 [28]. Moore [112] examined the effects of aerodynamic lift on near circular satellite orbits in closer detail in 1985. Therefore, this effect should also be exploitable for satellite relative motion control.

1.1 Scope

In line with the potentials and research gaps previously described, this dissertation aims to contribute to the research field by providing a comprehensive examination of the methodology of differential aerodynamic forces with a special focus on aerodynamic lift. The goal is to enable optimal simultaneous three-dimensional relative motion control for small satellites orbiting in the VLEO regime, as a combination of the three emerging trends (a short characterization is given in Appendix A) promises breakthroughs in numerous fields of application. Thus, the scope of

[4] By the ORBCOMM constellation [92], the AeroCube-4 CubeSats [50], Planet Labs CubeSast constellation [45] and the S-NET mission [194].

[5] Caused for any orbit with an inclination of $i \neq 0^\circ$ by the co-rotation of the atmosphere.

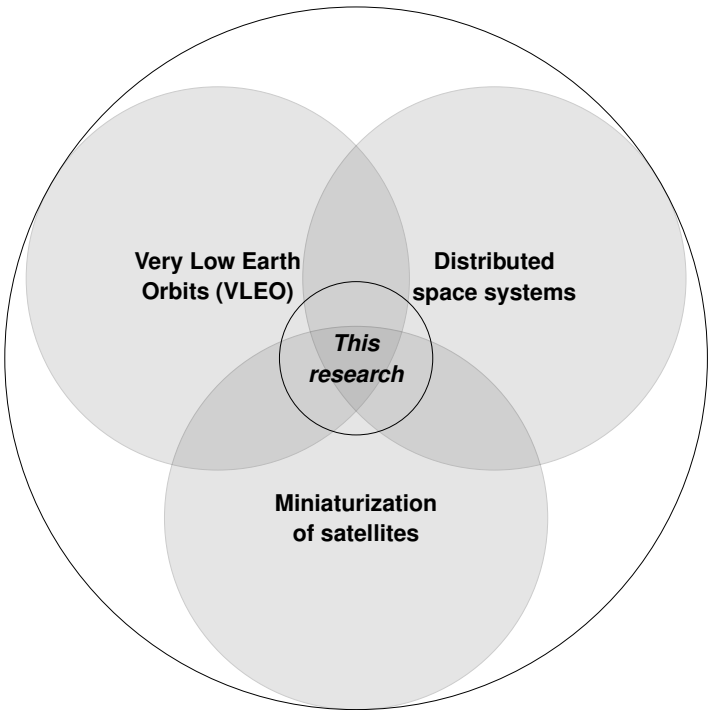

Figure 1.5: The scope of this research brings together three emerging areas in spaceflight.

this dissertation can be attributed to the intersection of the emerging areas discussed in the introductory section, corresponding to the inner circle in Fig. 1.5. Notably, all three areas have been receiving high attention across academic, agency and industrial sectors as by this means enabled satellite services surpass traditional possibilities and are indispensable for the preservation and further development of our modern knowledge, information and communication society.

1.1.1 Definition of the governing research question

Given the motivation and scope described in the previous sections, the governing research question to be answered within this dissertation can be formulated as:

Governing research question

How can optimal simultaneous three-dimensional relative motion control of satellite formations in VLEO be realized via differential lift and drag?

An initial consideration of the research question reveals that it is fraught with far-reaching challenges. The major challenge associated with exploiting aerodynamic forces for control purposes is caused by the dynamic, hostile and volatile nature of VLEO, which is unique in its properties and correspondingly challenging to handle, maintain and exploit in a sustainable fashion. Whereas it is already hard to measure and even harder to predict atmospheric drag forces, exploiting it for actuation purposes poses a very special challenge. Additionally, the methodology is subjected to drawbacks such as a lack of control authority and limited control magnitudes [67].

1.1.2 Definition of sub-research questions

Based on the governing research question and within the context described in the introductory section, the following sub-questions have been formulated:

1. *What are the relevant boundary conditions for an application of differential lift and drag of satellites in the VLEO regime?*
2. *How does the nature of the in- and out-of-plane relative motion differ and which implications does it have on the simultaneous control via differential lift and drag?*
3. *How do differential lift and drag compare?*
4. *Which mathematical tools and models are suitable for planning desired maneuver sequences precisely and efficiently?*
5. *Can critical parameters be identified to further develop the methodology?*
6. *What are the main limitations, drawbacks and challenges of the methodology and how can they be mitigated?*
7. *Can maneuvers be identified that are particularly suitable for the methodology?*

It is the aim of this dissertation to provide satisfactory answers to all of these questions.

1.2 Contributions

In a nutshell, the main contributions of this dissertation are:

- **Literature review:** The preparation of a comprehensive literature review of the theoretical background and the previous developments in the field. Based on this, the current state-of-the-art is derived and corresponding research gaps identified (Chapter 2 - 5, [170, 171]).
- **Planning tool for preliminary assessments:** The development of a flexible tool which allows for fast and efficient preliminary assessments of simplified maneuver trajectories and enables Monte Carlo analyses (Chapter 6, [21, 22, 189, 190]).
- **Optimal maneuver planning tool:** The development of a flexible and detailed planning tool for optimal maneuvering trajectories with minimal orbital decay based on a simultaneous application of differential lift and drag via yaw angle deviations $\delta\psi$ (Chapter 7, [167]).
- **Assessment of possible maneuver variants:** The identification of advantageous use cases and an illustration of the design space of possible maneuver variants (Chapter 8).
- **Optimal satellite designs:** The development of optimal satellite designs for an application in VLEO and for the methodology of differential aerodynamic lift and drag (Chapter 9, [58]).

Parts of these contributions have been peer-reviewed and published in: [22, 58, 167, 169, 171, 175, 177, 189].

1.3 Outline

Following its thematic division, this dissertation is structured into three parts: In a first part, including this introductory section (Chapter 1), the ***fundamentals*** are outlined. This comprises a description of the theoretical background in Chapter 2, the characterization of the Earth's at-

mosphere in Chapter 3 and the introduction of the relevant aspects of satellite aerodynamics in Chapter 4. This part was intentionally elaborated upon in detail to provide a substantive foundation for subsequent work in the field by consolidating the relevant literature. In the second part, denoted as ***research focus***, the methodology of differential lift and drag is introduced in detail (Chapter 5) and two different planning tools to schedule maneuver trajectories with different levels of fidelity presented in Chapter 6 and 7. The last part, ***analysis and optimization***, comprises an assessments on the nature of optimal simultaneous control in Chapter 8 before optimal satellite designs are presented and discussed in Chapter 9. Finally, in Chapter 10, responses to the sub-research questions are given before conclusions are drawn and future work topics revealed.

1.4 Remarks

Throughout this dissertation the generic masculine is used and any masculine designation is considered to entail females, too. Scalars are indicated without any additional identifier (x), vectors as bold symbols $(\boldsymbol{x})$, unit vectors as bold symbols with a hat $(\hat{\boldsymbol{x}})$ and matrices as bold symbols surrounded by squared brackets $\left([\boldsymbol{X}]\right)$. The eucledian norm of a vector $\boldsymbol{x} = (x_1,\ x_2,\ x_3)^T$, i.e., the square root of the sum of the squares of the coordinates of $\boldsymbol{x}$, is interchangeably indicated as x or $|\boldsymbol{x}|$, depending on which representation is more conducive to understanding. Similarly, derivatives with respect to time are interchangeably indicated as $\frac{dx}{dt} = \dot{x}$. Mean counterparts of oscillating orbital elements are indicated via a superscript bar ($\bar{\boldsymbol{\mathcal{E}}}$ for the Keplerian elements and $\bar{\boldsymbol{\mathcal{E}}}_{ns}$ for the non-singular elements, respectively). Simulations are run exclusively using an Intel® Core™ i7-7700HQ CPU @ 2.80GHz and MATLAB® R2018a.

Chapter 2

Theoretical background

2.1 Definition of relevant parameters

In the following, the reference frames employed are presented before the relevant attitude definitions and the concept of orbital elements are discussed.

2.1.1 Reference frames

The following main reference frames are employed throughout this dissertation:

Earth-centered inertial (ECI) frame $\mathcal{J}$ $\{\hat{\boldsymbol{I}}, \hat{\boldsymbol{J}}, \hat{\boldsymbol{K}}\}$: The geocentric equatorial coordinate system of mean equator and equinox of J2000 (EME2000), also Earth centered inertial (ECI) frame, has its origin at the Earth's center and the fundamental plane is the Earth's equator. The $\hat{\boldsymbol{I}}$ - and $\hat{\boldsymbol{K}}$ - axes point towards the vernal equinox and the North Pole at epoch January, 1st 2000@12:00 UTC [37, 179]. The $\hat{\boldsymbol{J}}$ - axis completes the right-hand frame and is located in the equatorial plane. The numerical integration of the non-linear spacecraft dynamics is performed in the $\mathcal{J}$ - frame.

True of date (ToD) frame $\mathcal{T}$ $\{{}^{\mathcal{T}}\hat{\boldsymbol{I}}, {}^{\mathcal{T}}\hat{\boldsymbol{J}}, {}^{\mathcal{T}}\hat{\boldsymbol{K}}\}$: The $\mathcal{T}$ - frame is analogous to the $\mathcal{J}$ - frame but accounts for the effects of precession and nutation [111]. Thus, the ${}^{\mathcal{T}}\hat{\boldsymbol{I}}$ and ${}^{\mathcal{T}}\hat{\boldsymbol{K}}$ - axes are directed towards the true equinox and North Pole at the current epoch. In accordance with the work of Dell'Elce [37], orbital elements are defined with respect to the $\mathcal{T}$ - frame within this work.

Local-vertical-local-horizontal (LVLH) frame $\mathcal{L}$ $\{\hat{\boldsymbol{x}}, \hat{\boldsymbol{y}}, \hat{\boldsymbol{z}}\}$: The unit vector triad of the $\mathcal{L}$ - frame is defined as follows: The $\hat{\boldsymbol{x}}$ - axis points from the Earth's center along the position vector ${}^{\mathcal{J}}\boldsymbol{r}$ towards the satellite. The $\hat{\boldsymbol{y}}$ - axis is perpendicular to the position vector and points in the direction of (not necessarily parallel to) the inertial velocity vector ${}^{\mathcal{J}}\boldsymbol{v}$. The $\hat{\boldsymbol{z}}$ - axis is normal to the orbital plane [179]. In the circular orbit special case, the $\hat{\boldsymbol{y}}$ - axis is constantly aligned with the velocity vector ${}^{\mathcal{J}}\boldsymbol{v}$. The mathematical expression is

$$\hat{\boldsymbol{x}} = \frac{{}^{\mathcal{J}}\boldsymbol{r}}{|{}^{\mathcal{J}}\boldsymbol{r}|}, \hat{\boldsymbol{z}} = \frac{{}^{\mathcal{J}}\boldsymbol{h}}{|{}^{\mathcal{J}}\boldsymbol{h}|}, \hat{\boldsymbol{y}} = \hat{\boldsymbol{z}} \times \hat{\boldsymbol{x}}, \tag{2.1}$$

where the specific angular momentum vector ${}^{\mathcal{J}}\boldsymbol{h}$ is defined as

$${}^{\mathcal{J}}\boldsymbol{h} = {}^{\mathcal{J}}\boldsymbol{r} \times {}^{\mathcal{J}}\boldsymbol{v}. \tag{2.2}$$

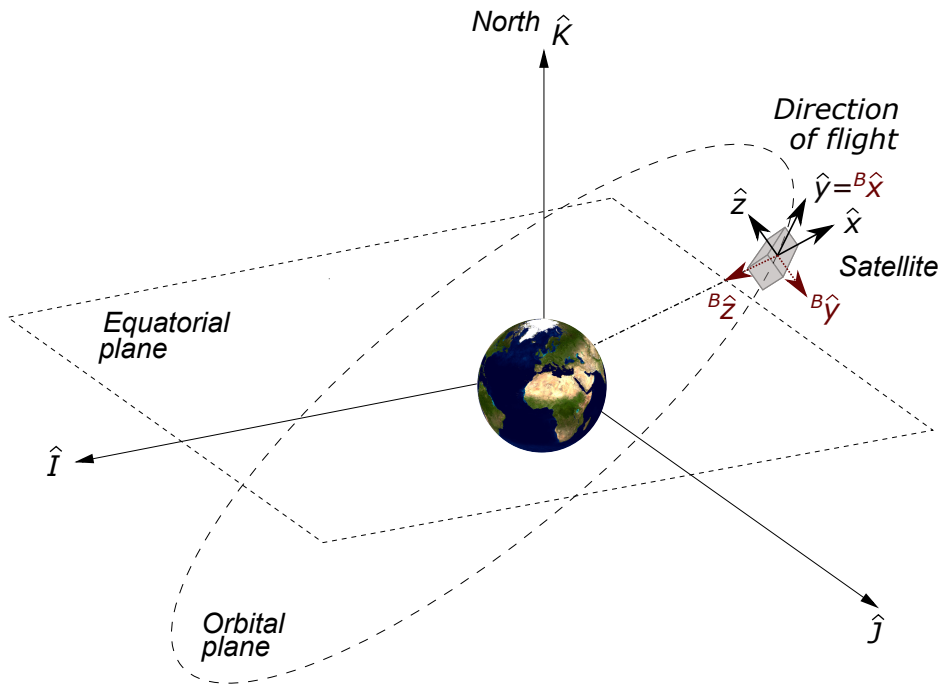

Figure 2.1: Graphical representation of the $\mathcal{J}$ -, $\mathcal{L}$- and $\mathcal{B}$ - frame of a satellite orbiting in its nominal configuration (in the circular orbit special case, the $\mathcal{L}$- and the $\mathcal{F}$ - frame are aligned).

The 3×3 rotation matrix $[{}^{\mathcal{L}}\boldsymbol{R}_{\mathcal{J}}]$ from $\mathcal{J}$ to $\mathcal{L}$ is given by

$$[{}^{\mathcal{L}}\boldsymbol{R}_{\mathcal{J}}] = [\hat{\boldsymbol{x}},\ \hat{\boldsymbol{y}},\ \hat{\boldsymbol{z}}]. \tag{2.3}$$

The $\mathcal{L}$ - frame is employed for a vivid description of the spacecraft relative motion.

Frenet frame $\mathcal{F}$ $\{\hat{\boldsymbol{n}}, \hat{\boldsymbol{t}}, \hat{\boldsymbol{w}}\}$: The $\mathcal{F}$ - frame has the $\hat{\boldsymbol{w}}$ - axis normal to the orbital plane, the $\hat{\boldsymbol{t}}$ - axis aligned with the velocity vector and the $\hat{\boldsymbol{n}}$ - axis normal to the inertial velocity vector ${}^{\mathcal{J}}\boldsymbol{v}$. In the circular orbit special case, the $\hat{\boldsymbol{n}}$ is aligned with ${}^{\mathcal{J}}\boldsymbol{r}$. The unit vector triad is

$$\hat{\boldsymbol{t}} = \frac{{}^{\mathcal{J}}\boldsymbol{v}}{|{}^{\mathcal{J}}\boldsymbol{v}|},\ \hat{\boldsymbol{w}} = \frac{{}^{\mathcal{J}}\boldsymbol{h}}{|{}^{\mathcal{J}}\boldsymbol{h}|},\ \hat{\boldsymbol{n}} = \hat{\boldsymbol{t}} \times \hat{\boldsymbol{w}}. \tag{2.4}$$

The 3×3 rotation matrix $[{}^{\mathcal{F}}\boldsymbol{R}_{\mathcal{J}}]$ from $\mathcal{J}$ to $\mathcal{F}$ is given by

$$[{}^{\mathcal{F}}\boldsymbol{R}_{\mathcal{J}}] = [\hat{\boldsymbol{n}},\ \hat{\boldsymbol{t}},\ \hat{\boldsymbol{w}}]. \tag{2.5}$$

This frame is convenient to assess the impacts of aerodynamic drag as, neglecting disturbing effects, it acts anti-parallel to ${}^{\mathcal{J}}\boldsymbol{v}$ and thus along $-\hat{\boldsymbol{t}}$.

Body fixed frame $\mathcal{B}$ $\{{}^{\mathcal{B}}\hat{\boldsymbol{x}}, {}^{\mathcal{B}}\hat{\boldsymbol{y}}, {}^{\mathcal{B}}\hat{\boldsymbol{z}}\}$: The $\mathcal{B}$ - frame is centered at the satellite's center of mass and the ${}^{\mathcal{B}}\hat{\boldsymbol{x}}$ -, ${}^{\mathcal{B}}\hat{\boldsymbol{y}}$ -, and ${}^{\mathcal{B}}\hat{\boldsymbol{z}}$ - axes are aligned with its principal axes forming a right-handed frame. Throughout this dissertation, the nominal satellite attitude is defined in a way that the $\mathcal{B}$ - frame tracks the $\mathcal{F}$ - frame so that the satellite's ${}^{\mathcal{B}}\hat{\boldsymbol{x}}$ is aligned with $\hat{\boldsymbol{t}}$, the ${}^{\mathcal{B}}\hat{\boldsymbol{z}}$ - axis is pointing towards $-\hat{\boldsymbol{n}}$ and ${}^{\mathcal{B}}\hat{\boldsymbol{y}}$ completes the right handed frame (see Fig. 2.1). The $\mathcal{B}$ - frame is required to define the attitude of the spacecraft with respect to inertial space.

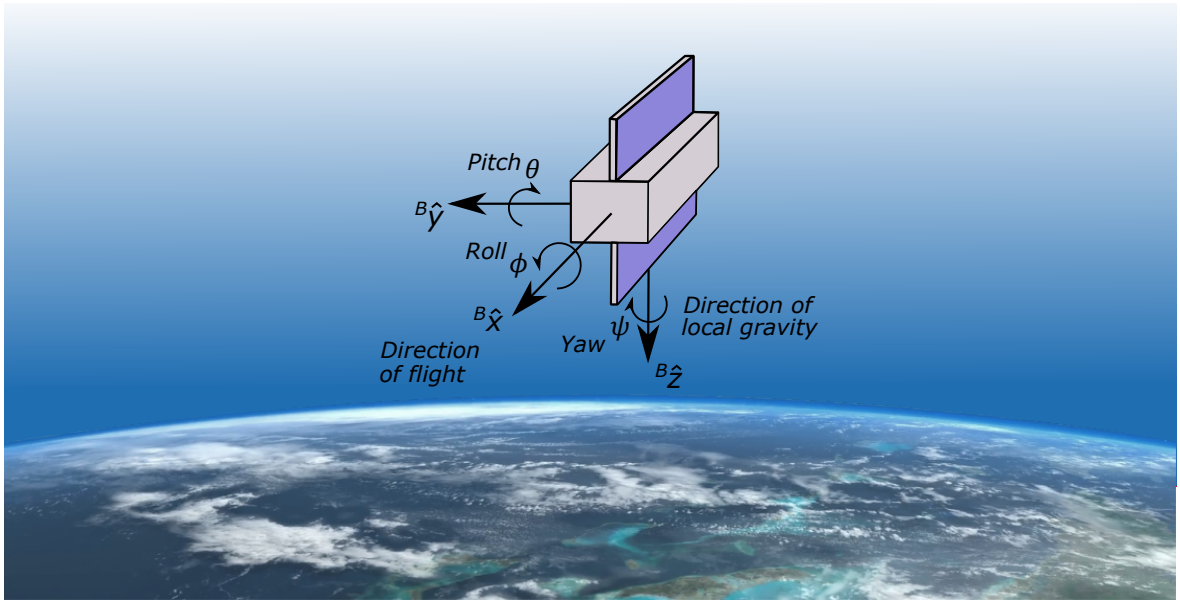

Figure 2.2: Graphical representation of the $\mathcal{B}$ - frame and the corresponding Euler angle definitions.

2.1.2 Attitude definitions

With respect to the attitude definitions, the orientation of the satellite with respect to inertial space and its orientation with respect to the surrounding flow are of particular interest.

Euler angles

In an Euler angle representation, a rotation from an initial to a final frame is expressed as three successive rotations specified by the so-called *Euler angles* ϕ, θ and ψ. In an asymmetric Euler angle sequence, these angles are often referred to as *roll*, *pitch* and *yaw*. [191] According to Markley and Crassidis [99], this terminology was historically used to describe the motion of ships and later on also applied for air- and spacecraft. Following their definitions, Euler angles are defined as follows throughout this dissertation (illustrated in Fig. 2.2) [99]:

- **Roll** ϕ: Roll defines a rotation around the vehicle body axis that is closest to the vehicle's predominant direction of motion (screwing motion) (the ${}^{\mathcal{B}}\hat{\boldsymbol{x}}$ - axis).
- **Pitch** θ: Pitch defines a rotation about the remaining vehicle body axis (${}^{\mathcal{B}}\hat{\boldsymbol{y}}$ - axis), and is often understood as a motion that points the vehicle up and down.
- **Yaw** ψ: Yaw defines a rotation about the body axis that is closest to the direction of local gravity (${}^{\mathcal{B}}\hat{\boldsymbol{z}}$ - axis) and often understood as a motion that points the spacecraft left or right.

Spacecraft orientation with respect to the flow

Due to the co-rotation of the atmosphere with the Earth and the presence of thermospheric winds, the satellite's velocity relative to the local atmosphere $\boldsymbol{v}_{rel}$ deviates from the inertial satellite velocity $\boldsymbol{v}$. Thus, a precise definition of the orientation of the body with respect to the flow requires the introduction of two additional angles, the angle of attack α_A and the angle of sideslip β_A.

In terms of the relative flow velocity components in the $\mathcal{B}$ - frame ${}^{\mathcal{B}}\boldsymbol{v}_{rel} = [{}^{\mathcal{B}}\boldsymbol{R}_{\mathcal{J}}]{}^{\mathcal{J}}\boldsymbol{v}_{rel} = \left({}^{\mathcal{B}}v_{rel,x},\ {}^{\mathcal{B}}v_{rel,y},\ {}^{\mathcal{B}}v_{rel,z}\right)^T$, these are defined as [113]

$$\alpha_A = \tan^{-1}\left(\frac{{}^{\mathcal{B}}v_{rel,x}}{{}^{\mathcal{B}}v_{rel,z}}\right), \tag{2.6}$$

$$\beta_A = \tan^{-1}\left(\frac{{}^{\mathcal{B}}v_{rel,y}}{{}^{\mathcal{B}}v_{rel,x}}\right). \tag{2.7}$$

Note: With perturbing effects being present, the angle of attack α_A deviates from the pitch angle θ and the angle of sideslip β_A deviates from the yaw angle ψ.

2.1.3 Orbital elements

Unlike Cartesian states $\{\boldsymbol{r}, \boldsymbol{v}\}$, Keplerian elements $\boldsymbol{\mathcal{E}} = (a, e, i, \Omega, \omega, \theta_k)^T$ are a representation of the state of the satellite that allow an intuitive geometric interpretation of its orbit (see Fig. 2.3). The size and shape of the orbit is defined by the semi-major axis a and the eccetricity e, whereas the inclination i, the right ascension of the ascending node (RAAN) Ω and the argument of perigee ω define the orientation of the orbital plane with respect to inertial space. Finally, the true anomaly θ_k defines the position of the spacecraft along its orbit. The latter can be replaced by the mean anomaly M_k. For true Keplerian orbits, the size, shape and orientation of the orbit is invariant and the true anomaly θ_k varies according to

$$\dot{\theta}_k = \frac{d\theta_k}{dt} = \frac{h}{r^2}. \tag{2.8}$$

In case of equatorial and circular orbits, however, Ω and ω are undefined. As quasi circular orbits are common for both spacecraft in VLEO and SFF, nearly-nonsingular (subscript *ns*) orbital elements $\boldsymbol{\mathcal{E}}_{ns}$ are the representation of choice within this dissertation[6]. With respect to the Keplerian elements $\boldsymbol{\mathcal{E}}$, the nearly-nonsingular version $\boldsymbol{\mathcal{E}}_{ns}$ is [132]

$$\boldsymbol{\mathcal{E}}_{ns} = \left(a,\ \lambda_{ns} = M_k + \omega,\ i,\ q_1 = e\cos(\omega),\ q_2 = e\sin(\omega),\ \Omega\right)^T, \tag{2.9}$$

where λ_{ns} is the mean argument of latitude which, in anology to the Keplerian elements, can be replaced by the true argument of latitude $u = \omega + \theta_k$.

2.2 Satellite dynamics

In this section, the absolute satellite dynamics is introduced first before in a second part the relative motion dynamics is elaborated.

[6] As the name suggests, for this set of elements Ω still remains undefined in case of equatorial orbits, for which equinoctial orbital elements $\boldsymbol{\mathcal{E}}_{eq}$ are the representation of choice [6].

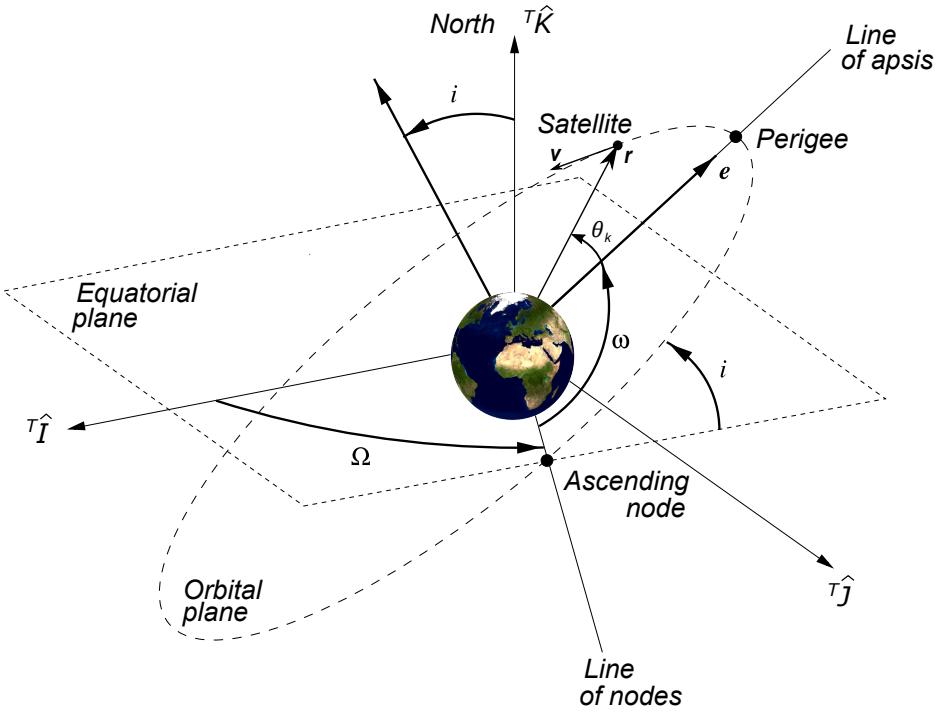

Figure 2.3: Graphical representation of six Keplerian elements of a spacecraft in an ellipctical Earth orbit (figure design adopted from Casella and Lovera [26]).

2.2.1 Satellite absolute motion

Keplerian orbits represent solutions to the two-body problem in which the only attraction acting on the satellite is the spherically symmetric gravitational potential of the central body[7] [6, 179]:

$$\ddot{\boldsymbol{r}} = -\frac{\mu_e}{r^3}\boldsymbol{r}. \tag{2.10}$$

Here, μ_e is the standard gravitational parameter of the Earth, obtained by multiplying the gravitational constant G with the Eath's mass m_e, $\boldsymbol{r}$ is the position vector of the satellite and $\ddot{\boldsymbol{r}}$ its second time derivative. The acceleration is proportional to the inverse square of the satellite distance r from the Earth's center. For Keplerian orbits, the specific mechanical energy ξ of a satellite, i.e., the sum of its kinetic and its potential energy divided by mass, is constant:

$$\xi = -\frac{\mu_e}{2a} = \frac{v^2}{2} - \frac{\mu_e}{r} = \text{const.} \tag{2.11}$$

It is noticeable that ξ is only dependent on the reciprocal semi-major axis. For the circular orbit special case ($r = a$), this yields a velocity of

$$v_{circ} = \sqrt{\frac{\mu_e}{a}}. \tag{2.12}$$

[7] Throughout this dissertation, the central body is the Earth and both designations are used interchangeably.

From Kepler's third law the following equation for the orbital period P results:

$$P = 2\pi\sqrt{\frac{a^3}{\mu_e}}. \tag{2.13}$$

From it, the mean motion n can be determined via

$$n = \frac{2\pi}{P} = \sqrt{\frac{\mu_e}{a^3}} = \dot{M}_k. \tag{2.14}$$

However, the shape and gravitational field of the Earth deviates from the simplified representation as ideally spherical, and various other forces must be considered. Thus, a more appropriate representation of the satellite dynamics is [36]

$$\ddot{\boldsymbol{r}} = -\frac{\mu}{r^3}\boldsymbol{r} + \boldsymbol{q} + \nabla\mathcal{R}, \tag{2.15}$$

in which $\boldsymbol{q}$ is the acceleration caused by non-conservative perturbing forces and $\mathcal{R}$ is a potential-like function, referred to as *disturbing function*. From it, the acceleration due to conservative perturbing forces can be derived. The disturbing function $\mathcal{R}$ is [36]

$$\mathcal{R} = -\frac{\Pi}{m}, \tag{2.16}$$

where m is the mass of the satellite and Π its potential energy. Non-conservative perturbing forces result from interactions between the satellite and the surrounding particles. [36]

Gauss' form of the variational equations

Within the context of this dissertation, Gauss' form of the variational equations (GVP), also referred to as variation-of-parameters (VOP) equations [6, 140], with respect to nearly-nonsingular orbital elements are employed. These indicate the rates of change of the orbital elements with respect themselves and to arbitrary perturbing forces ${}^{\mathcal{L}}\boldsymbol{f}_p = \left(f_{p,x}, f_{p,y}, f_{p,z}\right)^T$ [6, 132]:

$$\frac{da}{dt} = \frac{2a^2}{h}\left[\left(q_1\sin(u) - q_2\cos(u)\right)f_{p,x} + \frac{p_k}{r}f_{p,y}\right] \tag{2.17}$$

$$\begin{aligned}\frac{d\lambda_{ns}}{dt} = &\left[-\frac{p_k}{h(1+\eta)}\left(q_1\cos(u) + q_2\sin(u)\right) - \frac{2\eta r}{h}\right]f_{p,x} \\ &+ \frac{p_k + r}{h(1+\eta)}\left(q_1\sin(u) - q_2\cos(u)\right)f_{p,y} - \frac{r\sin(u)\cos(i)}{h\sin(i)}f_{p,z},\end{aligned} \tag{2.18}$$

$$\frac{di}{dt} = \frac{r\cos(u)}{h}f_{p,z}, \tag{2.19}$$

$$\frac{dq_1}{dt} = \frac{p_k\sin(u)}{h}f_{p,x} + \frac{1}{h}\left[(p_k + r)\cos(u) + rq_1\right]f_{p,y} + \frac{rq_2\sin(u)\cos(i)}{h\sin(i)}f_{p,z}, \tag{2.20}$$

$$\frac{dq_2}{dt} = -\frac{p_k\cos(u)}{h}f_{p,x} + \frac{1}{h}\left[(p_k + r)\sin(u) + rq_2\right]f_{p,y} - \frac{rq_1\sin(u)\cos(i)}{h\sin(i)}f_{p,z}, \tag{2.21}$$

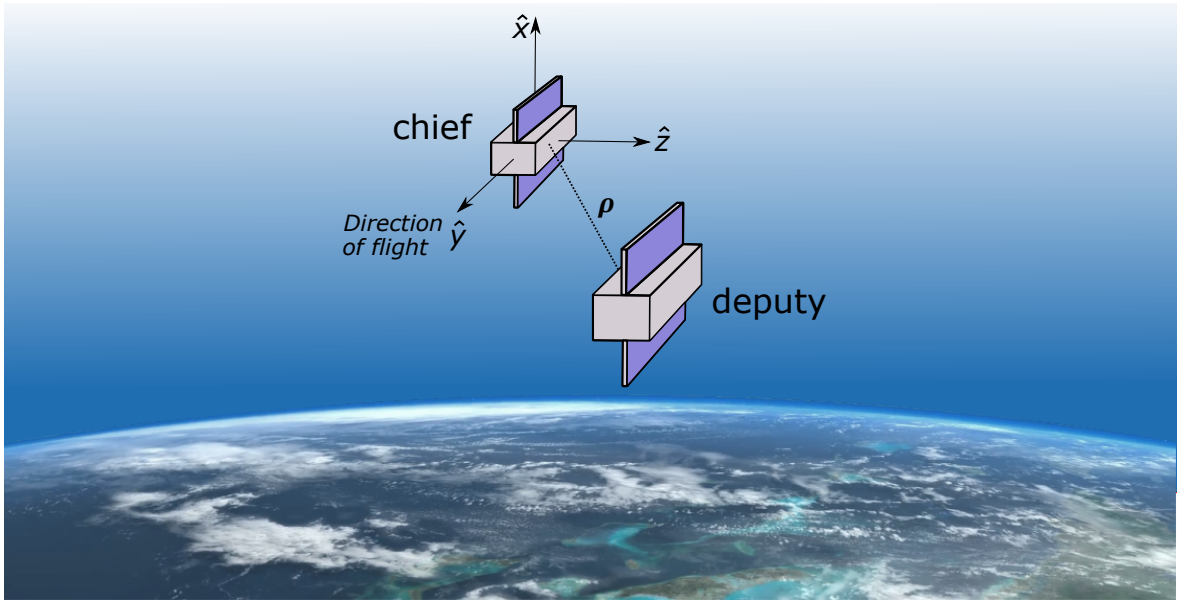

Figure 2.4: Graphical visualization of a satellite formation of two satellites and the relative position vector $\boldsymbol{\rho}$ expressed in the $\mathcal{L}$ - frame of the chief.

and

$$\frac{d\Omega}{dt} = \frac{r\sin(u)}{h\sin(i)} f_{p,z}. \tag{2.22}$$

Here, u is the true argument of latitude and p_k the semi-latus rectum (also semi-parameter). The orbit equation is [132]

$$r = \frac{a\eta^2}{1 + q_1\cos(u) + q_2\sin(u)}, \tag{2.23}$$

where η^2 is given by

$$\eta^2 = 1 - q_1^2 - q_2^2. \tag{2.24}$$

For equatorial orbits, the utilization of GVP in terms of equinoctial elements $\boldsymbol{\mathcal{E}}_{eq}$, which are non-singular except for rectilinear orbits and for orbits with $i = \pi$, is advised [6].

2.2.2 Satellite relative motion

Throughout this dissertation, the relative motion of a *deputy* (subscript d) with respect to a reference satellite, the so-called *chief* (subscript c), is considered (see Fig. 2.4). The contents of this subsection originate largely from the work of Roscoe et al. [132].

Non-linear relative motion dynamics

Since a depiction of the relative motion in inertial space is rather abstract, the dynamics are commonly expressed in the non-inertial $\mathcal{L}$ - frame centered at the chief. In the following, the Cartesian, rectilinear relative position and velocity of the deputy with respect to the chief in the $\mathcal{L}$ - frame of the chief are denoted as $\boldsymbol{\rho}$ and $\dot{\boldsymbol{\rho}}$. By applying the transport theorem twice, the unforced relative motion dynamics $\ddot{\boldsymbol{\rho}}$ can be expressed as

$$^{\mathcal{L}}\ddot{\boldsymbol{\rho}} = -\mu_e \left(\frac{^{\mathcal{L}}\boldsymbol{r}_c + {}^{\mathcal{L}}\boldsymbol{\rho}}{|^{\mathcal{L}}\boldsymbol{r}_c + {}^{\mathcal{L}}\boldsymbol{\rho}|^3} - \frac{^{\mathcal{L}}\boldsymbol{\rho}}{|^{\mathcal{L}}\boldsymbol{\rho}|^3} \right) - 2\,{}^{\mathcal{J}}\boldsymbol{\omega}_{\mathcal{L}} \times {}^{\mathcal{L}}\dot{\boldsymbol{\rho}} - {}^{\mathcal{J}}\boldsymbol{\omega}_{\mathcal{L}} \times ({}^{\mathcal{J}}\boldsymbol{\omega}_{\mathcal{L}} \times {}^{\mathcal{L}}\boldsymbol{\rho}) - {}^{\mathcal{J}}\dot{\boldsymbol{\omega}}_{\mathcal{L}} \times {}^{\mathcal{L}}\boldsymbol{\rho}, \quad (2.25)$$

where ${}^{\mathcal{J}}\boldsymbol{\omega}_{\mathcal{L}}$ represents the instantaneous rotational velocity of the $\mathcal{L}$ - frame of the chief with respect to the $\mathcal{J}$ - frame. In contrast to formation flying of planes, where arbitrary designs can be realized, in the case of satellites only so-called legal formations can be defined. The most striking explanation is provided by Yeh and Sparks [193], which is quoted verbatim:

> *"For example, one cannot require two satellites to 'fly' side by side forever. Their paths will cross each other before they finish one circle around the Earth. Nor can one require a satellite to 'fly' above or below another at the same speed. Satellites do not fly. They orbit. All orbits cross each other at some point because all orbit planes pass through the center of Earth, and the satellite in the lower orbit always travels faster."* [193]

Legal designs can be derived using a set of linearized equations of relative motion, which are introduced in the next subsection.

Linearized relative motion dynamics

The relative motion dynamics highly simplify for the circular chief orbit special case, where $r_c = a_c$, $\dot{r}_c = \ddot{r}_c = 0$, $|{}^{\mathcal{J}}\boldsymbol{\omega}_{\mathcal{L}}| = n$, and $|{}^{\mathcal{J}}\dot{\boldsymbol{\omega}}_{\mathcal{L}}| = \dot{n} = 0$ holds. After linearization, the well-known Hill [60] or Clohessy–Wiltshire (HCW) equations [30] result:

$$\begin{aligned} \ddot{x} &= 2n\dot{y} + 3n^2 x \\ \ddot{y} &= -2n\dot{x} \\ \ddot{z} &= -n^2 z. \end{aligned} \quad (2.26)$$

Due to their simple form, closed form solutions can be found. To ensure consistency, the notation of Roscoe et al. [132] is employed:

$$\begin{aligned} x(t) &= \rho_x \sin(nt + \bar{\alpha}_0) - \frac{2v_d}{3n} \\ y(t) &= 2\rho_x \cos(nt + \bar{\alpha}_0) + d + v_d(t - t_0) \\ z(t) &= \rho_z \sin(nt + \bar{\beta}_0). \end{aligned} \quad (2.27)$$

The solutions are uniquely defined by the set of parameters ${}^{\mathcal{L}}\bar{\boldsymbol{\alpha}} = \left\{ \rho_x,\ d,\ \rho_z,\ v_d,\ \bar{\alpha}_0,\ \bar{\beta}_0 \right\}$. Caused by a difference in the orientation of the orbital plane of the two satellites, the unforced out-of-plane motion is of sinusoidal nature and constantly bounded. The in-plane motion, however, is described by a pair of coupled second order ordinary differential equations and, besides a sinusoidal component, comprises an along-track and radial offset as well as an along-track secular drift. In Eq. 2.27, ρ_x and ρ_z correspond to the amplitude of the oscillating in-plane and

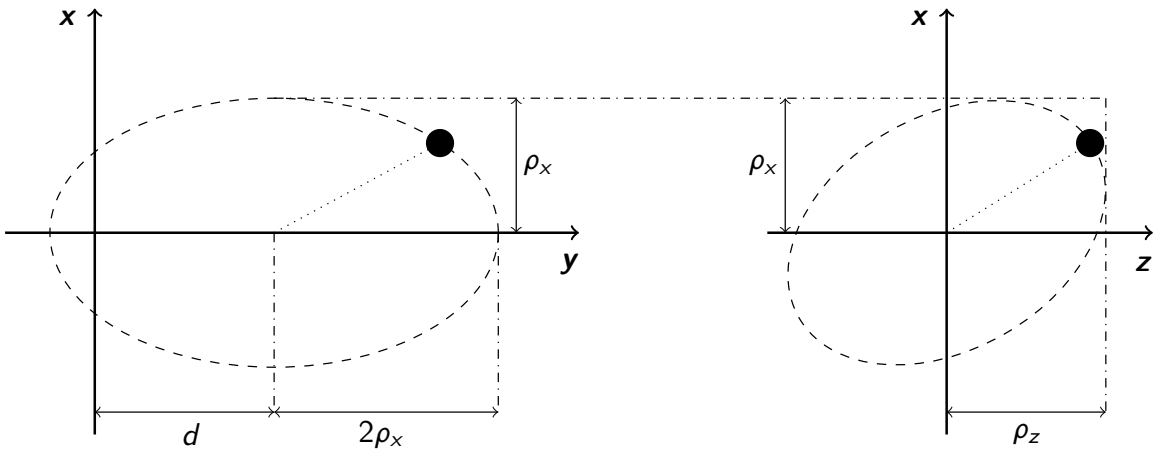

Figure 2.5: Projections of the solution of the HCW equations in the along-track/radial (left) and cross-track/radial (right) directions for formation with zero radial offset (figure design adopted from D'Amico [34]).

out-of-plane motion, d is the along-track offset of the initial in-plane ellipse and v_d is the along-track drift rate [132]. A stable formation design can be enforced via

$$\dot{y}_0 = -2nx_0, \tag{2.28}$$

which represents the Hill frame specialized bounded relative orbit constraint [140]. If this condition holds, the orbital periods of both spacecraft match and the relative orbit of the deputy with respect to the chief in the $\mathcal{L}$ - frame can be described by an ellipse of semi-major axis $2\rho_x$ in along-track direction and semi-minor axis ρ_x in radial direction (the so-called 2-1 ellipse, see Fig. 2.5). While ρ_x measures the size of the relative trajectory, the angle α_0 defines the relative pericenter. Whenever the sum of the argument of latitude u and α_0 equals $\pi/2$, the deputy is located right above the center of the 2-1 ellipse. The out-of-plane relative motion is described by a harmonic oscillation of amplitude ρ_z and phase angle $u + \beta_0$. Passively safe formations result when the initial phase angles are set so that the trajectory never crosses the along-track axis (maximum "safety" is ensured whenever $\beta_0 = \alpha_0 \pm \pi/2$ holds). [132, 148]

In case of elliptic orbits, the Tschauner-Hempel (TH) [172] or Lawden's [87] equations can be consulted [132]. A parametrization of the general solution to these equations in terms of nearly-nonsingular elements $\boldsymbol{\mathcal{E}}_{ns}$ has been derived by Sengupta and Vadali [148] and is recited for reference [132]:

$$\begin{aligned}
x(u) &= \rho_1 \sin(u + \tilde{\alpha}_0) - \frac{2v_d}{3n\eta^2}\left[\frac{r}{p_k} - \frac{3\left(q_1 \sin(u) - q_2 \cos(u)\right)}{2\eta^3} K(u)\right] \\
y(u) &= \frac{\rho_1 r}{p_k}\left(2 + q_1 \cos(u) + q_2 \sin(u)\right)\cos(u + \tilde{\alpha}_0) + \frac{\rho_2 r}{p_k} + \frac{v_d p_k}{r n \eta^5} K(u) \\
z(u) &= \frac{\rho_3 r}{p_k} \sin(u + \tilde{\beta}_0).
\end{aligned} \tag{2.29}$$

$K(u)$ is a function of the true argument of latitude:

$$K(u) = \lambda \; - \; \lambda_0 = n(t - t_0) \tag{2.30}$$

and $\eta = \sqrt{1 - e^2}$. Again, the set of parameters ${}^{\mathcal{L}}\tilde{\boldsymbol{\alpha}} = \left\{\rho_1,\ \rho_2,\ \rho_3,\ v_d,\ \tilde{\alpha}_0,\ \tilde{\beta}_0\right\}$ defines the relative trajectory: ρ_1 and ρ_3 are the amplitudes of the in-plane and out-of-plane motion, $\tilde{\alpha}_0$ and $\tilde{\beta}_0$ the initial phase angles, ρ_2 is the offset in the along-track direction, and v_d is again the along-track drift rate [132]. Notably, Eqs. 2.29 reduce to the HCW equations [30, 60] in the case of a circular chief orbit and the following relations with the parameterization of the TH equations hold: $\rho_1 = \rho_x$, $\rho_2 = d$, $\rho_3 = \rho_z$, $\tilde{\alpha}_0 = \bar{\alpha}_0$ and $\tilde{\beta}_0 = \bar{\beta}_0$ [132].

Nearly-nonsingular relative orbital element description

For the high-fidelity trajectory planning within this work, the motion of the deputy with respect to the chief is described by means of mean differential nearly-nonsingular orbital elements [132]

$$\delta\bar{\boldsymbol{\mathcal{E}}}_{ns} = \bar{\boldsymbol{\mathcal{E}}}_{ns,d} \; - \; \bar{\boldsymbol{\mathcal{E}}}_{ns,c} = \left(\delta a,\ \delta\lambda,\ \delta i,\ \delta q_1,\ \delta q_2,\ \delta\Omega\right)^T, \tag{2.31}$$

where $\bar{\boldsymbol{\mathcal{E}}}_{ns,c}$ and $\bar{\boldsymbol{\mathcal{E}}}_{ns,d}$ refer to the mean nearly-nonsingular orbital elements of the chief and the deputy, respectively. According to Schaub et al. [142], mean elements, i.e., orbit averaged values of the orbital elements, are advantageous over oscillating elements because the resulting motion follows the prescribed geometry more closely. Following the work of Dell'Elce [37], mean elements are calculated from their osculating counterparts by means of a first-order Brouwer-Lyddane contract transformation throughout this dissertation. This is indicated via the transformation function ζ [140]

$$\bar{\boldsymbol{\mathcal{E}}} = \zeta\left(\boldsymbol{\mathcal{E}}\right). \tag{2.32}$$

Relative motion dynamics in terms of mean differential nearly-nonsingular elements

With respect to mean differential nearly-nonsingular orbital elements $\delta\bar{\boldsymbol{\mathcal{E}}}_{ns}$, the relative motion dynamics are modeled using the linearized equations presented by Roscoe et al. [132]:

$$\delta\dot{\bar{\boldsymbol{\mathcal{E}}}}_{ns} \approx \left[\boldsymbol{A}(\bar{\boldsymbol{\mathcal{E}}}_{ns,c})\right]\delta\bar{\boldsymbol{\mathcal{E}}}_{ns} + \left[\boldsymbol{B}(\bar{\boldsymbol{\mathcal{E}}}_{ns,c})\right]\boldsymbol{u}. \tag{2.33}$$

$\left[\boldsymbol{B}(\bar{\boldsymbol{\mathcal{E}}}_{ns,c})\right]$ are Gauss's variational equations. $\left[\boldsymbol{A}(\bar{\boldsymbol{\mathcal{E}}}_{ns,c})\right]$ is the Jacobian of Lagrange's Planetary Equations (LPE) evaluated on the reference orbit [132]:

$$\left[\boldsymbol{A}(\bar{\boldsymbol{\mathcal{E}}}_{ns,c})\right] = \left[a_{ij}\right] = \left[\frac{\partial f_i}{\partial\bar{\boldsymbol{\mathcal{E}}}_{ns}}\right]. \tag{2.34}$$

The LPE are given in Chapter 7. With the constant parameter [142]

$$\epsilon = J_2\left(\frac{R_E}{p}\right)^2 n, \tag{2.35}$$

the elements of $\left[\boldsymbol{A}(\bar{\boldsymbol{\mathcal{E}}}_{ns,c})\right]$ which are non-zero are [132]

$$
\begin{aligned}
\frac{\partial f_\lambda}{\partial a} &= -\frac{3n}{2a} - \frac{21\epsilon}{8a}\left[\eta\left(3\cos^2(i)-1\right)+\left(5\cos^2(i)-1\right)\right],\\
\frac{\partial f_\lambda}{\partial i} &= -\frac{3\epsilon}{4}(3\eta+5)\sin(2i),\\
\frac{\partial f_\lambda}{\partial q_1} &= \frac{3\epsilon}{4\eta^2}\left[3\eta\left(3\cos^2(i)-1\right)+4\left(5\cos^2(i)-1\right)\right]q_1,\\
\frac{\partial f_\lambda}{\partial q_2} &= \frac{3\epsilon}{4\eta^2}\left[3\eta\left(3\cos^2(i)-1\right)+4\left(5\cos^2(i)-1\right)\right]q_2,\\
\frac{\partial f_{q_1}}{\partial a} &= \frac{21\epsilon}{8a}\left(5\cos^2(i)-1\right)q_2,\\
\frac{\partial f_{q_1}}{\partial i} &= \frac{15\epsilon}{4}q_2\sin(2i),\\
\frac{\partial f_{q_1}}{\partial q_1} &= -\frac{3\epsilon}{\eta^2}\left(5\cos^2(i)-1\right)q_1q_2,\\
\frac{\partial f_{q_1}}{\partial q_2} &= -\frac{3\epsilon}{4}\left(1+\frac{4q_2^2}{\eta^2}\right)\left(5\cos^2(i)-1\right),\\
\frac{\partial f_{q_2}}{\partial a} &= -\frac{21\epsilon}{8a}\left(5\cos^2(i)-1\right)q_1,\\
\frac{\partial f_{q_2}}{\partial i} &= -\frac{15\epsilon}{4}q_1\sin(2i),\\
\frac{\partial f_{q_2}}{\partial q_1} &= \frac{3\epsilon}{4}\left(1+\frac{4q_1^2}{\eta^2}\right)\left(5\cos^2(i)-1\right),\\
\frac{\partial f_{q_2}}{\partial q_2} &= \frac{3\epsilon}{\eta^2}\left(5\cos^2(i)-1\right)q_1q_2,\\
\frac{\partial f_\Omega}{\partial a} &= \frac{21\epsilon}{4a}\cos(i),\\
\frac{\partial f_\Omega}{\partial i} &= \frac{3\epsilon}{2}\sin(i),\\
\frac{\partial f_\Omega}{\partial q_1} &= -\frac{6\epsilon}{\eta^2}q_1\cos(i),\\
\frac{\partial f_\Omega}{\partial q_2} &= -\frac{6\epsilon}{\eta^2}q_2\cos(i).
\end{aligned}
$$

Mapping between CW parameters and mean differential orbital elements

To use the geometrical insights provided by the solutions to the TH and HCW equations, relationships to map the respective parameters ${}^{\mathcal{L}}\tilde{\boldsymbol{\alpha}} = \left\{\rho_1,\ \rho_2,\ \rho_3,\ v_d,\ \tilde{\alpha}_0,\ \tilde{\beta}_0\right\}$ into nearly-nonsingular element differences $\delta\bar{\boldsymbol{\mathcal{E}}}_{ns}$ are required. These are provided by Sengupta and Vadali [148][8]:

$$\delta a = -\frac{2\eta v_d}{3n}, \tag{2.36}$$

[8] **Note:** With the mapping presented in Eq. 2.36 - 2.41, the desired parameters are mapped into mean orbital elements $\delta\bar{\boldsymbol{\mathcal{E}}}_{ns}$ at $nt_0 = \lambda_0 = 0$.

$$\delta\lambda_0 = \frac{\rho_2}{p_k} - \delta\Omega\cos(i) \; - \; \frac{1+\eta+\eta^2}{1+\eta}\frac{\rho_1}{p_k}(q_1\cos(\tilde{\alpha}_0) - q_2\sin(\tilde{\alpha}_0)), \tag{2.37}$$

$$\delta i = \frac{\rho_3}{p_k}\cos(\tilde{\beta}_0), \tag{2.38}$$

$$\delta q_1 = -(1-q_1^2)\frac{\rho_1}{p_k}\sin(\tilde{\alpha}_0) + q_1 q_2\frac{\rho_1}{p_k}\cos(\tilde{\alpha}_0) \; - \; q_2\left(\frac{\rho_2}{p_k} \; - \; \delta\Omega\cos(i)\right), \tag{2.39}$$

$$\delta q_2 = -(1-q_2^2)\frac{\rho_1}{p_k}\cos(\tilde{\alpha}_0) + q_1 q_2\frac{\rho_1}{p_k}\sin(\tilde{\alpha}_0) + q_1\left(\frac{\rho_2}{p_k} \; - \; \delta\Omega\cos(i)\right), \tag{2.40}$$

$$\delta\Omega = -\frac{\rho_3}{p_k}\frac{\sin(\tilde{\beta}_0)}{\sin(i)}. \tag{2.41}$$

The necessary conditions for a bounded, centered relative motion of the deputy with respect to the chief are given by [148]

$$\delta a = 0\,\mathrm{m}, \tag{2.42}$$

$$\delta\lambda_0 = \; -\delta\Omega\cos(i). \tag{2.43}$$

Eqs. 2.36 - 2.41 are used to initialize formation designs in terms of $\delta\bar{\boldsymbol{\mathcal{E}}}_{ns}$ throughout this work.

Nearly-nonsingular orbital element differences to relative orbit position conversion

To allow for a intuitive graphical interpretation of the results, a mapping between mean differential nearly-nonsingular orbital elements $\delta\bar{\boldsymbol{\mathcal{E}}}_{ns}$ and Cartesian states $\boldsymbol{\rho}$ is required. This has been presented by Schaub and Junkins [140]:

$$\begin{aligned} x = {} & \frac{r}{a}\delta a + \frac{v_{ra}}{v_{tr}}r\delta u - \frac{r}{p_k}\left(2aq_1 + r\cos(u)\right)\delta q_1 \\ & - \frac{r}{p_k}\left(2aq_2 + r\sin(u)\right)\delta q_2, \end{aligned} \tag{2.44}$$

$$y = r\left(\delta u + \cos(i)\delta\Omega\right), \tag{2.45}$$

$$z = r\left(\sin(u)\delta i \; - \; \cos(u)\sin(i)\delta\Omega\right), \tag{2.46}$$

where the chief radial and transverse velocity components v_{ra} and v_{tr} can be calculated via

$$v_{ra} = \dot{r} = \frac{h}{p_k}\left(q_1\sin(u) - q_2\cos(u)\right), \tag{2.47}$$

$$v_{tr} = r\dot{u} = \frac{h}{p_k}\left(1 + q_1\cos(u) + q_2\sin(u)\right). \tag{2.48}$$

Throughout this dissertation, Eqs. 2.44 - 2.46 are employed to map mean differential nearly-nonsingular orbital elements $\delta\bar{\boldsymbol{\mathcal{E}}}_{ns}$ into Cartesian states $\boldsymbol{\rho}$.

Chapter 3

Earth's atmosphere

The Earth is surrounded by an envelope of gas that varies in space and time. Using thermal characteristics, chemical composition, movement, and density, five distinct layers have been identified: the *troposphere* (greek: 'tropos', "change", from the Earth's surface to about 8 - 14 km (the so-called tropopause)), the *stratosphere* (latin: 'stratum', "layered", from the tropopause to about 50 km (stratopause)), the *mesosphere* (greek: 'messos', "middle", from the stratopause to about 80 - 90 km (mesopause)), the *thermosphere* (greek: 'thermes', "heat", from the mesopause to around 400 - 600 km (thermopause)), and the *exosphere* (greek: 'exo', "outside", from the thermopause and extends to the interplanetary gases, or space). [44, 125] The boundaries between the different layers are defined by sharp changes in the temperature profile caused by the varying dominating energy sources and sinks present in the individual layers (see Fig. 3.1) [44].

Besides by the temperature profile, the Earth's atmosphere can also be stratified by molecular composition: below about 100 km, the so-called *homopause*, molecular diffusion is unable to rival the various mixing processes in the atmosphere and the molecular composition of the layer is well mixed with an almost uniform composition of gases [55]. Consequently, the regime is referred to as the *homosphere*. Above this threshold, there is a significant variation in composition and the vertical structure is governed by a balance between pressure and gravity. This balance is referred to as the hydrostatic equilibrium and the regime as the *heterosphere*. [39, 55]

In this chapter, which draws heavily from the excellent work of Doornbos [39], Livadiotti [93], Pisacane [125], and Prölss [128], the layer of interest within this dissertation, i.e., the thermosphere[9], is characterized. This is necessary to build an understanding of the critical boundary conditions of the methodology introduced in the later chapters.

3.1 Thermosphere

The thermosphere begins at the mesopause and extends to about 400 - 600 km in altitude, dependent on the current solar and geomagnetic activities. The temperature increases with altitude from around 180 - 200 K and asymptotically approaches a limiting value, the so-called

[9] Re-entry and launch activities are not discussed within the context of this dissertation. Also, this dissertation limits itself to neutral particles and a discussion of the ionosphere and aurora phenomena is omitted.

thermopause or exospheric temperature T_e. [111] The value is governed by the absorption of energy from the Sun and can vary between 600 - 2500 K [128]) (from 700 - 1800 K in [125], respectively). If not stated otherwise, the statements are based on the work of Doornbos [39].

3.1.1 Vertical structure

The hydrostatic equilibrium governs the vertical structure of the thermosphere, which is illustrated in Fig. 3.1. The balance can be expressed via the hydrostratic equation

$$\frac{dp_\infty}{dz} = -\rho(z)g(z). \tag{3.1}$$

p_∞ is the atmospheric pressure, z the height, $\rho(z)$ the atmospheric density $g(z)$ the gravitational attraction. In combination with the ideal gas law

$$p_\infty = \rho\frac{\mathcal{R}}{M}T_\infty, \tag{3.2}$$

where $\mathcal{R}$ is the universal gas constant, M the molar mass and T_∞ the atmospheric temperature, the vertical atmospheric density profile $\rho(z)$ can be determined by integrating over altitude:

$$\rho(z) = \rho(0)\exp\left(-\int_0^h \frac{1}{H^*}dz\right). \tag{3.3}$$

H^* is the density scale height defined as

$$\frac{1}{H^*} = \frac{1}{T(z)}\frac{dT_\infty(z)}{dz} + \frac{g(z)M(z)}{\mathcal{R}T_\infty(z)}, \tag{3.4}$$

representing the vertical distance over which the density decreases by $1/e$ (Euler's number). Assuming the temperature in the upper thermosphere to be constant and neglecting the height dependency of the gravitational attraction, Eq. 3.3 can be simplified to the *exponential density model* [128]:

$$\rho(h) = \rho_0\exp\left(-\frac{h-h_0}{H_0^*}\right). \tag{3.5}$$

Here, $\rho_0 = \rho(h_0)$ is the atmospheric density at the reference altitude h_0, also referred to as base density. H_0^* is the corresponding density scale height at the reference altitude. If the constant temperature assumption does not hold, the density profile can be approximated by a piecewise exponential density model. Hereby, the full altitude range is subdivided into a number of i segments and the respective parameters $h_{0,i}$, $H_{0,i}^*$ and $\rho_{0,i}$ are valid only within a respective range ($h_i < h < h_{i+1}$). Once the range is exceeded, they need to be updated accordingly [179].

Although the density of all constituent decreases almost exponentially with increasing altitude, Eq. 3.4 indicates that the respective rate depends on the molar mass M of the constituent of interest. Light gases have higher density scale heights and, therefore, decrease much more slowly than heavier gases. [111] As a result, the heterosphere has a distinct structure in which N_2 ($M_{N_2} = 28.0134\,\mathrm{g\,mol^{-1}}$) is the major thermospheric constituent below 170 km, O

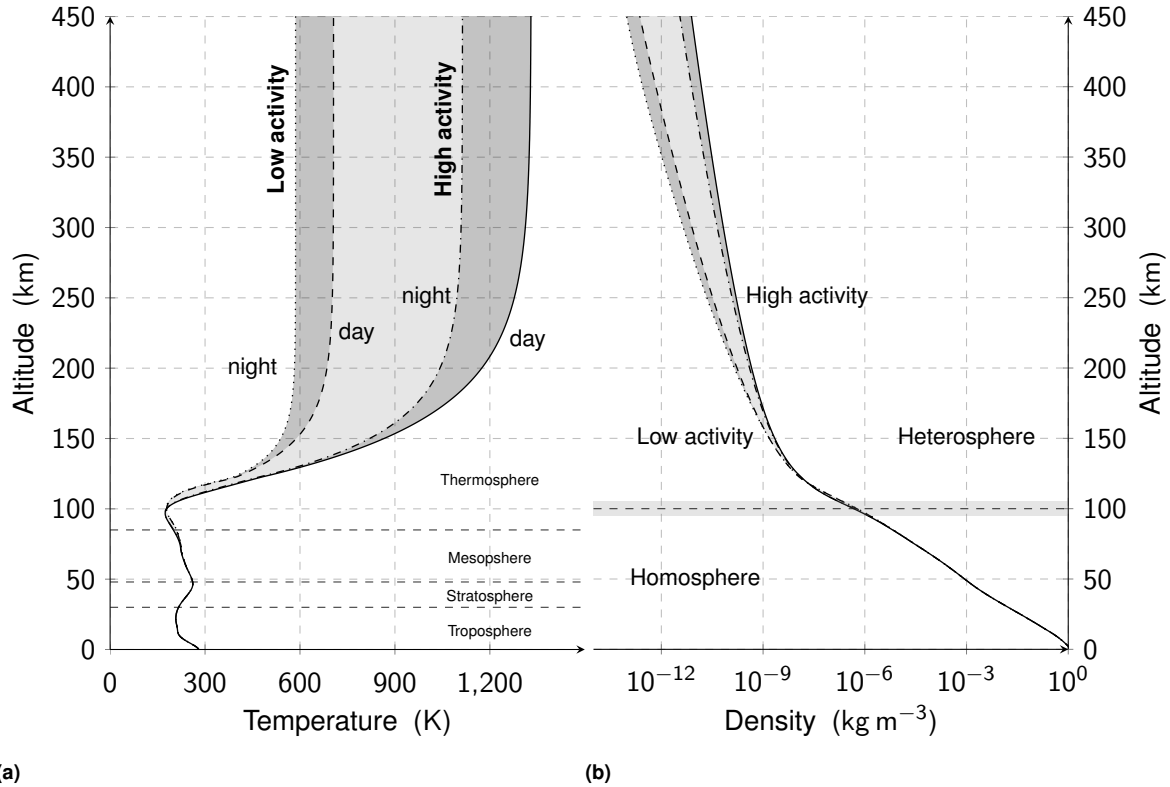

Figure 3.1: Temperature (left) and atmospheric mass density (right) vs. altitude over Stuttgart, Germany, plotted for different solar and geomagnetic activities according to Tab. 3.1 as a function of altitude using the NRLMSISE-00 environment model [122] (figure design adopted from Doornbos [39]).

($M_O = 15.999\,\mathrm{g\,mol^{-1}}$) in the range of 170 km and 500 - 600 km, He ($M_{He} = 4.002\,602\,\mathrm{g\,mol^{-1}}$) in in the range of 500 - 900 km and H ($M_H = 1.007\,84\,\mathrm{g\,mol^{-1}}$) at even higher altitudes [111]. This circumstance is displayed in Fig. 3.2, in which the species number density (top) and mass percentage (bottom) of all constituents are plotted over altitude for low (left) and high (right) levels of solar and geomagnetic activities according to the NRLMSISE-00[10] environment model [125]. In this range, it can be approximated that $T_\infty \simeq T_e$ and $\bar{M} \simeq M_O$. For a typical thermopause temperature of $T_e \simeq 1000\,\mathrm{K}$ and a mean gravitational acceleration of $\bar{g}(200 - 600\,\mathrm{km}) = 8.8\,\mathrm{m\,s^{-2}}$, the scale height of atomic oxygen H_O^* can be estimated as [128]

$$H_O^* = \frac{\mathcal{R}T_e}{\bar{g}M_O} \simeq 60\,\mathrm{km}. \tag{3.6}$$

Thus, in this region the total neutral density decreases by a factor of $1/e$ every $\approx 60\,\mathrm{km}$. [128].

3.1.2 Thermospheric winds and the co-rotation of the atmosphere

The geostrophic approximation, which stipulates that the pressure gradient force is balanced by the Coriolis force, holds up to the mesosphere and the wind in this region flows along isobars. In the upper thermosphere, however, the dominant driver of the flow are the pressure gradient force, ion drag and viscous diffusion, and the resulting wind flows across isobars. [105] The

[10] Naval Research Laboratory Mass Spectrometer and Incoherent Scatter Radar Exosphere (NRLMSISE).

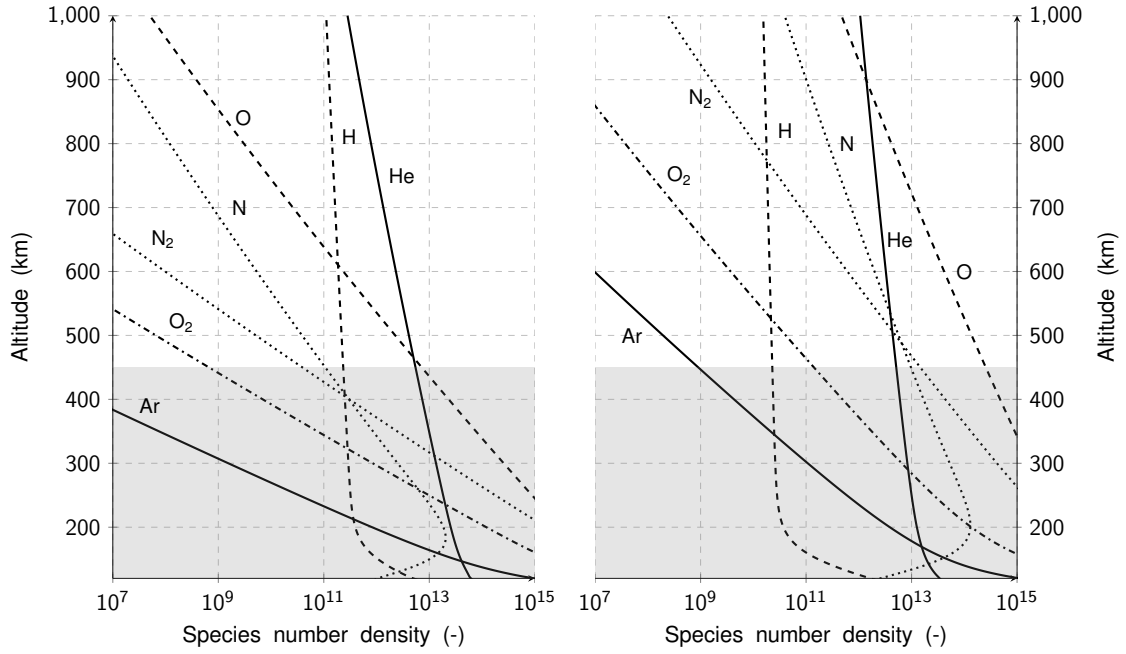

(a) Low activity conditions.

(b) High activity conditions.

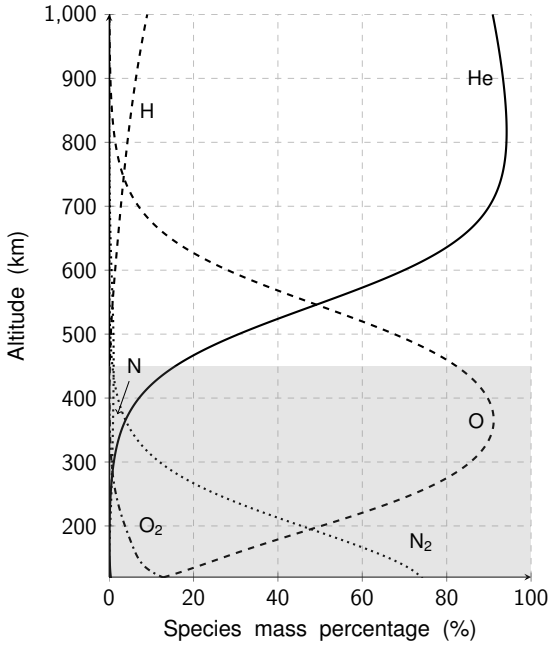

(c) Low activity conditions.

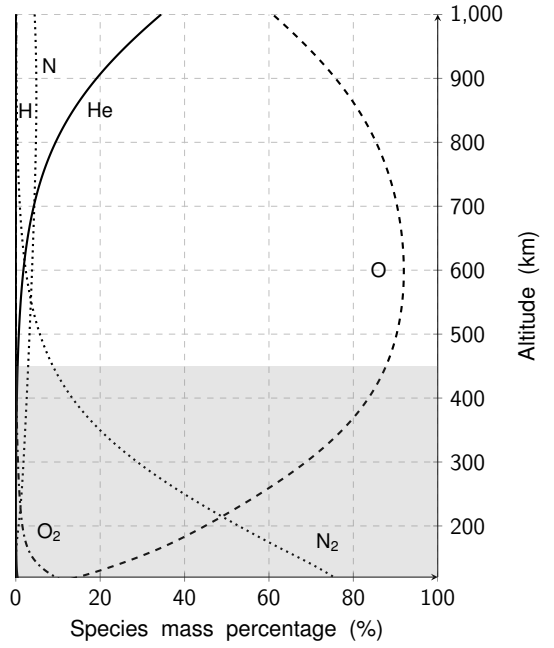

(d) High activity conditions.

Figure 3.2: Species number density (top) and mass percentage (bottom) over Stuttgart, Germany, plotted for low (left) and high (right) solar and geomagnetic activity conditions according to Tab. 3.1 as a function of altitude using the NRLMSISE-00 model [122] (figure design adopted from Doornbos [39]).

pressure gradients from the pressure bulge to low pressure regions (shifted by 12 hours) generate significant balancing winds which, due to their 24-hour periodicity, are referred to as tidal winds [128]. Additionally, there is a wind circulation from the summer to the winter hemisphere [105]. In general, vertical winds are smaller than the horizontal winds and frequently neglected. However, due to the strong vertical gradients, even small vertical wind speeds can have significant effects on the atmospheric composition. [86]

Thermospheric winds $\boldsymbol{v}_{rot}$ are superimposed to what is referred to as the co-rotation of the atmosphere, a motion *"[...] which is transferred to the outer gas envelope first by friction from the Earth's surface and subsequently by frictional forces between the individual gas layers."* [128] The co-rotational velocity of the atmosphere $\boldsymbol{v}_{rot}$ can be calculated in vector form via [179]

$$\boldsymbol{v}_{rot} = {}^{\mathcal{J}}\boldsymbol{\omega}_e \times \boldsymbol{r}, \tag{3.7}$$

where ${}^{\mathcal{J}}\boldsymbol{\omega}_e$ is the angular velocity vector of the Earth and $\boldsymbol{r}$ the satellite position vector.

3.1.3 Atomic oxygen in VLEO

Atomic oxygen is formed by photochemical dissociation of O_2 by shortwave EUV radiation emitted from the Sun ($< 190\,\mathrm{nm}$). Because the mean free path length at VLEO altitudes is long, the probability of recombination or O_3 formation is low and O is abundant. With respect to spacecrafts, the impact energy and high reactivity lead to oxidative erosion of materials. [125, 130]

3.2 Environmental drivers

The characteristic temperature profile which determines the delineation of the atmospheric layers is a result of the balance between energy sources and sinks [44]. In the following, the two dominant energy sources in the thermosphere are shortly described. If not stated otherwise, the statements are based on the work of Doornbos [39].

3.2.1 Solar EUV radiation

Extreme ultraviolet (EUV) radiation ($\lambda_{EUV} \leq 170\,\mathrm{nm}$) emitted by the Sun is the dominant driver of thermospheric heating, which can occur through excitation, dissociation and ionization [39]. The EUV emission of the Sun varies with the so-called 11-year solar activity cycle, a prediction of which is highly challenging. According to Brown et al. [17], the predictions for the next solar cycle (cycle 25) in the literature range from lower than the last to one of the largest cycles recorded. The last three maxima occurred in Nov. 1989, Nov. 2001, and April 2014 [17]. The amount of energy received from the Sun in terms of radiation at a wavelength of 10.7 cm (a frequency of 2.8 GHz), the so-called 10.7 cm radio flux $F_{10.7}$, correlates well with the thermospheric density. Measurements are in units of $1 \times 10^{-22}\,\mathrm{W\,m^{-2}\,s^{-1}}$, also referred to solar flux unit (sfu) [39]. In Fig. 3.3, the daily observed (black) and centered 81-day arithmetic average (red) of the $F_{10.7}$ flux is depicted for cycle 24 and the beginning of 25 (up until October 2022) along with a prediction for

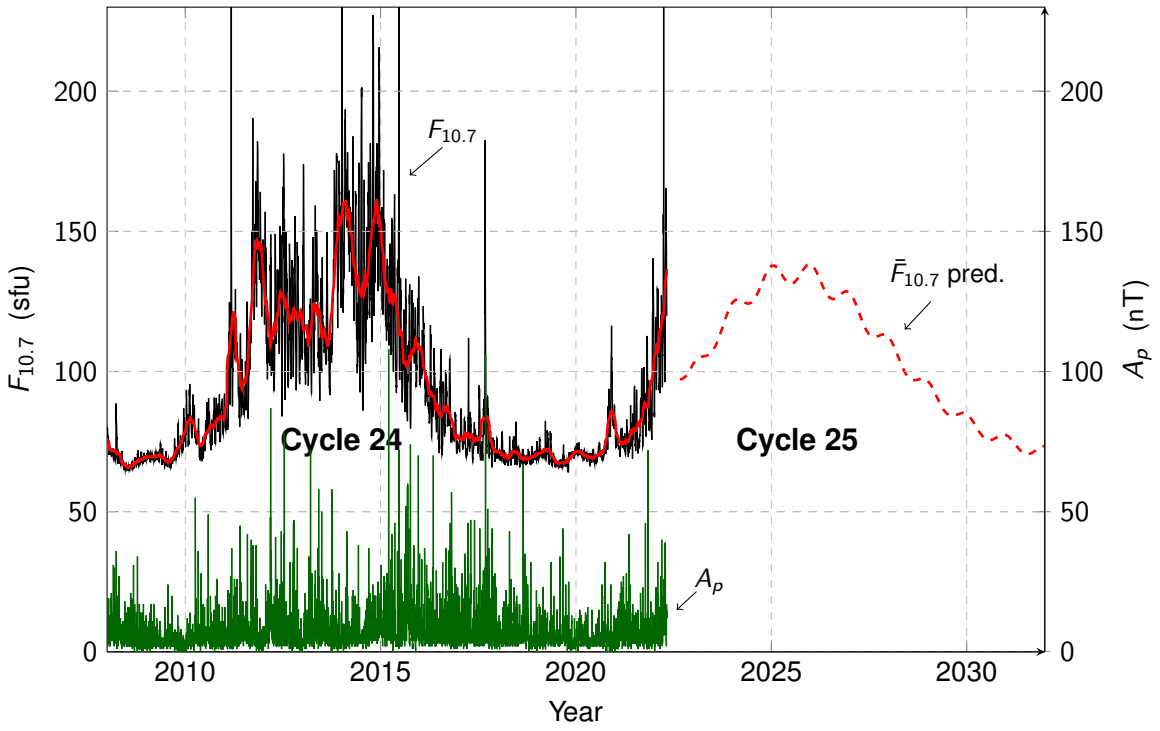

Figure 3.3: Daily observed (black), centered 81-day arithmetic average (red) and predicted 81-day arithmetic average (red dashed) 10.7-cm solar radio flux $F_{10.7}$ measured at Penticton at 2000 UT and daily A_p values [78].

the centered 81-day arithmetic average of cycle 25 (red dashed) [78]. During periods of minimum activity (2018-2020), the EUV output of the Sun along with its variability is low. During periods of high activity (2013-2015), its magnitude and variability is significantly higher [39]. In Fig. 3.4, the resulting density variations at $h = 350\,\text{km}$ as predicted by the NRLMSISE-00 model [122] is depicted, while Figs. 3.5 and 3.6 show diurnal and seasonal variations.

3.2.2 Charged particles and geomagnetic storms

Indirectly, solar activity introduces energy into the thermosphere through a stream of particles (mostly electrons and protons) called the *solar wind*. Near the Earth, the complex interactions between the solar wind, the magnetosphere, and the ionosphere can lead to large disturbances, referred to as *geomagnetic storms*. [39] To illustrate the effects with an example from the recent past: shortly after the SpaceX's launch of 49 Starlink satellites into an elliptical orbit with a perigee altitude of 210 km on Feb. 3, 2022[11], a geomagnetic storm (rated G1/G2 on a scale of G1 to G5) caused atmospheric density levels to rise (up to around 50 %), which resulted in the loss of mission of 38 of the 49 spacecraft [46]. To account for variations in geomagnetic activity, the K_p and a_p indices are commonly employed [39]. The K_p index is derived from measurements and can be converted to the planetary equivalent amplitude a_p, which is expressed in nano-Tesla (nT). The average of all eight a_p values in a UTC day results in the A_p index, which is depicted for cycle 24/25 in Fig. 3.3.

[11] The low perigee altitude was intentionally chosen so that a spacecraft that fails the initial tests after reaching orbit will quickly re-enter.

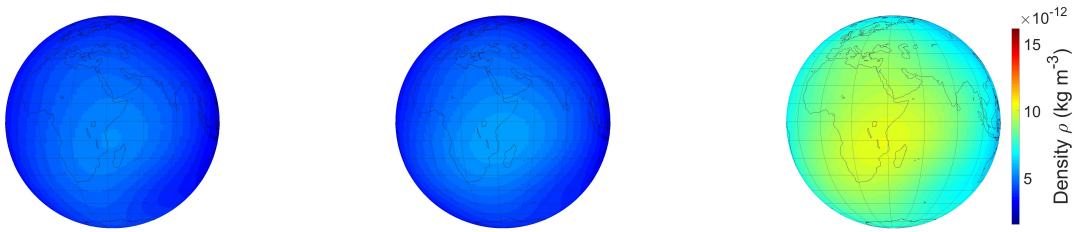

(a) March 1st, 2008 @ 12:00:00 UTC **(b)** March 1st, 2010 @ 12:00:00 UTC **(c)** March 1st, 2012 @ 12:00:00 UTC

(d) March 1st, 2014 @ 12:00:00 UTC **(e)** March 1st, 2016 @ 12:00:00 UTC **(f)** March 1st, 2018 @ 12:00:00 UTC

Figure 3.4: 11 - year density variation at $h = 350\,\mathrm{km}$ as predicted by the NRLMSISE-00 model [122] and using the 81-day arithmetic average 10.7-cm solar radio flux $F_{10.7}$ from Kelso [78] visualized in Fig. 3.3.

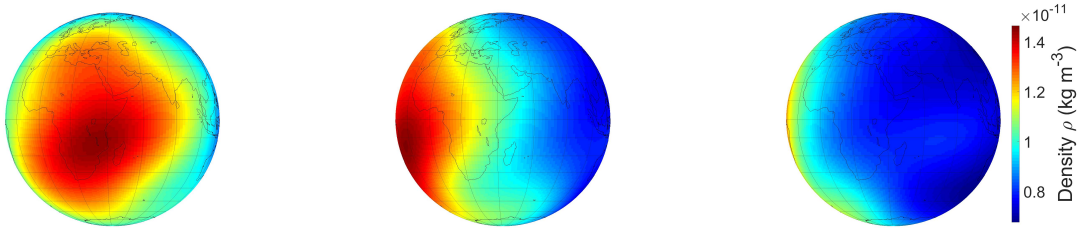

(a) March 1st, 2018 @ 12:00:00 UTC **(b)** March 1st, 2018 @ 16:00:00 UTC **(c)** March 1st, 2018 @ 20:00:00 UTC

(d) March 2nd, 2018 @ 00:00:00 UTC **(e)** March 2nd, 2018 @ 04:00:00 UTC **(f)** March 2st, 2018 @ 08:00:00 UTC

Figure 3.5: Daily density variation at $h = 350\,\mathrm{km}$ as predicted by the NRLMSISE-00 model [122] for moderate solar and geomagnetic activities according to Tab. 3.1.

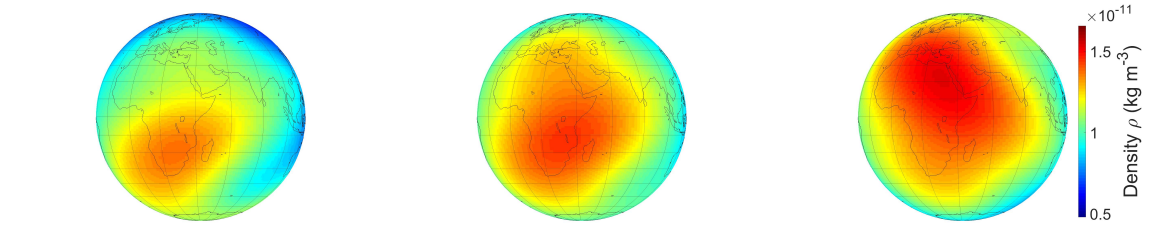

(a) January 1st, 2018 @ 12:00:00 UTC **(b)** March 1st, 2018 @ 12:00:00 UTC **(c)** May 1st, 2018 @ 12:00:00 UTC

(d) July 1st, 2018 @ 12:00:00 UTC **(e)** Sept. 1st, 2018 @ 12:00:00 UTC **(f)** Nov. 1st, 2018 @ 12:00:00 UTC

Figure 3.6: Yearly density variation at $h = 350$ km as predicted by the NRLMSISE-00 model [122] for moderate solar and geomagnetic activities according to Tab. 3.1.

Table 3.1: Standard solar activity scenarios [68].

	Low	**Moderate**	**Long term high**	**Short term high**
$F_{10.7}$ (sfu)	65	140	250	300
$\bar{F}_{10.7}$ (sfu)	65	140	250	250
a_p (nT)	0	15	45	240

3.3 Empirical modeling of the thermosphere

Over the years, three major empirical model families have emerged for the Earth's atmosphere:

1. The Jacchia models
2. The Drag-Temperature model (DTM)
3. The Mass Spectrometer and Incoherent Scatter (MSIS) models

Vallado and Finkleman [178] concluded that no model is advantageous for every application. Bruinsma et al. [19] state that Jaccia-Bowman 2008 [15] (JB2008) represents the most accurate model below 300 km, JB2008 and DTM 2009 [18] perform best in the 300 - 500 km altitude range and the NRLMSISE-00 [122] and DTM2009 models are the most accurate models above 500 km. Throughout this dissertation, the NRLMSISE-00 model [122] is the emperical model of choice. The decision has been taken based on the following reasoning:

1. The model requires a limited set of solar and geomagnetic indices ($F_{10.7}$, $\bar{F}_{10.7}$, a_p and A_p).
2. The parameter of the SESAM model [124] is fitted to the NRLMSISE-00 model and, according to Pilinski, Argrow, and Palo [124], is only valid in combination with said model.
3. A verified implementation of the model is accessible via MATLAB's aerospace toolbox [100].
4. The horizontal wind model (HWM) 14 [40] requires the same set of indices as input so that consistency between the model inputs can be ensured.

To facilitate the comparison of results, it is resorted to the distinct solar activity scenarios from the International Standard Report 14222 [68] listed in Tab. 3.1 throughout this dissertation.

Chapter 4

Satellite aerodynamics

4.1 Fundamentals of aerodynamic lift and drag

Satellite aerodynamics refers to the interaction of the satellite and the neutral atmospheric particles which retards the satellite's motion. As the residual gas in the thermosphere is no longer a continuum but a rarefied gas, spacecraft aerodynamics completely differs from aircraft aerodynamics [182]. The aerodynamic force acting on a spacecraft, which is non-conservative in nature, is generally subdivided into two components, namely *atmospheric drag*, $\boldsymbol{F}_D$, which acts anti-parallel to the relative velocity vector and *atmospheric lift*, $\boldsymbol{F}_L$, which acts in the plane perpendicular to drag. The total aerodynamic force $\boldsymbol{F}_A$ is the sum of both individual forces

$$\boldsymbol{F}_A = \boldsymbol{F}_D + \boldsymbol{F}_L. \tag{4.1}$$

In the context of satellite orbits, equations are usually expressed in terms of specific forces, indicated with a lower case symbol $\boldsymbol{f}$. A specific force has units of acceleration and is the inertial force per unit mass required to produce, in an inertial reference frame and following Newton's second law, the acceleration $\boldsymbol{a}$, i.e., the acceleration of a mass m proportional to $\boldsymbol{F}$.

4.1.1 Aerodynamic drag

Following the description of Vallado and McClain [179], the aerodynamic drag acting on a satellite can be expressed as

$$\boldsymbol{f}_D = -\frac{1}{2}\,\rho\,\frac{C_D A_{ref}}{m}|\boldsymbol{v}_{rel}|^2\frac{\boldsymbol{v}_{rel}}{|\boldsymbol{v}_{rel}|}. \tag{4.2}$$

Here, C_D is the drag coefficient of the spacecraft, m its mass and A_{ref} its cross-sectional area perpendicular to the relative velocity vector

$$\boldsymbol{v}_{rel} = \boldsymbol{v} - \boldsymbol{v}_{rot} - \boldsymbol{v}_w, \tag{4.3}$$

which is the satellite's velocity relative to the local atmosphere taking the atmospheric co-rotation with the Earth $\boldsymbol{v}_{rot}$ (see Eq. 3.7) and thermospheric winds $\boldsymbol{v}_w$ (see discussion in Subsection 3.1.2) into account [179]. The parameters which depend on the spacecraft design can be com-

bined to form the ballistic coefficient

$$\beta_D = \frac{m}{C_D A_{ref}}, \tag{4.4}$$

which indicates the sensitivity of a space object to perturbations by the drag force. β_D lends itself as means to assess the practical effect of spacecraft shape optimizations for VLEO applications, because satellites with a large A_{ref} can have a small C_D and vice versa, satellites with small A_{ref} can have comparatively large C_D. This will be discussed in closer detail in Section 9.1. The remaining terms of the drag equation represent the dynamic pressure

$$q = \frac{1}{2}\,\rho\,|\boldsymbol{v}_{rel}|^2. \tag{4.5}$$

In consequence, the magnitude of the specific drag force f_D can be subdivided into a term which is a function of the environment bulk properties and a second term related to the spacecraft geometry [182]:

$$f_D = \frac{q}{\beta_D}. \tag{4.6}$$

As the maximum specific drag force acts around perigee, drag causes a secular reduction in eccentricity, i.e., a circularization of an elliptical orbit. Similarly, it dissipates energy from the satellite, which inevitably reduces the semi-major axis (see Eq. 2.11). Without countermeasures, drag inevitably causes the re-entry of a spacecraft.

4.1.2 Aerodynamic lift

In case of aerodynamic lift, which by its fundamental definition acts perpendicular to drag, the magnitude is calculated similar to drag but the effective direction depends on the orientation of the surface under consideration:

$$\boldsymbol{f}_L = -\frac{1}{2}\,\rho\,\frac{C_L A_{ref}}{m}|\boldsymbol{v}_{rel}|^2\hat{\boldsymbol{u}}_L, \tag{4.7}$$

with the effective direction unit vector $\hat{\boldsymbol{u}}_L$ being defined as

$$\hat{\boldsymbol{u}}_L = \frac{(\boldsymbol{v}_{rel}\times\hat{\boldsymbol{n}})\times\boldsymbol{v}_{rel}}{|(\boldsymbol{v}_{rel}\times\hat{\boldsymbol{n}})\times\boldsymbol{v}_{rel}|}. \tag{4.8}$$

In Eqs. 4.7 and 4.8, C_L is the lift coefficient and $\hat{\boldsymbol{n}}$ the surface normal vector. In relevant literature, aerodynamic lift is predominantly considered to be negligible. This is because the effect of aerodynamic lift cancels out for satellites which are spinning or tumbling and non-rotating satellites with symmetrical shapes, e.g. spherical satellites such as Sputnik, do not produce lift at all [62]. In addition, the C_L experienced by traditional satellites in orbit are noticeably smaller than the C_D and, according to the perturbation equation, perpendicular force components are significantly less effective in changing the orbit geometry. However, by intentionally maintaining surfaces at a constant angle of attack α_A or angle of sideslip β_A with respect to $\boldsymbol{v}_{rel}$, measurable effects on the satellite's orbit can be created [32].

Table 4.1: General differentiation of the flow regimes by Knudsen number [182].

Knudsen number	Flow regime
$\mathrm{Kn} \geq 10$	Free molecular flow
$0.01 \leq \mathrm{Kn} < 10$	Transitional flow
$\mathrm{Kn} < 0.01$	Continuum flow

4.2 Free molecular flow

The atmosphere in the VLEO region is so rarefied that the average distance a particle travels between two consecutive collisions with other particles significantly exceeds the typical dimensions of a satellite. Thus, the rarefied gas represents a free molecular flow (FMF), where the atmosphere is considered to be particulate in nature with negligible inter-molecular collisions. This section as well as Section 4.3 draw heavily from the excellent work of Livadiotti [93], Mostaza Prieto, Graziano, and Roberts [114], and Virgili Llop [182].

4.2.1 Knudsen number

To distinguish between the different flow regimes, the non-dimensional Knudsen number

$$\mathrm{Kn} = \frac{\lambda}{L} \tag{4.9}$$

is consulted. It represents the ratio of the mean free path of the molecules λ and a characteristic length L of the body. Based on the Knudsen number, the three fundamentals regimes listed in Tab. 4.1 can be differentiated. Small Knudsen numbers are associated to the continuum regime, in which collisions between particles are the predominant mechanisms of interaction [94]. As the Knudsen number increases, so does the length traveled by the particles before interacting with others. Once the FMF condition holds, which is assumed throughout this work, the aerodynamic forces are governed by the gas-surface interactions (GSI), i.e., the interactions of the gas particles and the spacecraft surfaces. [182] An in-depth overview is given by Livadiotti [93].

4.2.2 Hypo- vs. hyperthermal flow

Due to the high gas temperatures and Knudsen numbers in this regime, each particle is attributed a random thermal velocity component superimposed to the bulk velocity of the flow [182]. The extend of the thermal velocity component can be quantified via the molecular speed ratio [114]

$$s = \frac{v_m}{v_t} = \frac{v_m}{\sqrt{\frac{2\mathcal{R}T_\infty}{\bar{M}}}}, \tag{4.10}$$

which relates the macroscopic gas velocity v_m to the most probable molecular thermal velocity according to a Maxwell-Boltzmann distribution

$$v_t = \sqrt{\frac{2\mathcal{R}T_\infty}{\bar{M}}}. \tag{4.11}$$

$\bar{M}$ is the mean molar mass which can be calculated from the individual particle number densities n_i and molar masses M_i of the N respective species via

$$\bar{M} = \frac{\sum_{i=1}^{N} (n_i M_i)}{\sum_{i=1}^{N} n_i}. \tag{4.12}$$

In Fig. 4.1, v_t and s are plotted over altitude for a circular orbiting spacecraft calculated via the NRLMSISE-00 model [122] and the different solar and geomagnetic activity scenarios listed in Tab. 3.1 over Stuttgart, Germany. In case of satellite aerodynamics, the gas macroscopic velocity corresponds to the satellite's velocity relative to the local atmosphere [94]. Based on s, it can be identified to which degree the flow behaves like a collimated beam, referred to as *hyperthermal flow*, or a chaotic drifting Maxwellian flow, the so-called *hypothermal flow* [114].

Hypothermal flow

For small speed ratios, generally considered to be valid for $s < 5$, the flow is referred to as *hypothermal* and all surfaces of a spacecraft may be hit by the molecules [114]. As the thermal velocity increases with altitude (see Fig. 4.1, (left)), this type of flow is attributed to larger altitudes.

Hyperthermal flow

For large speed ratios, generally considered to be valid for $s > 5$, the bulk velocity of the particles is predominant and the flow is referred to as *hyperthermal* [94]. This type of flow is attributed to VLEO altitudes (see Fig. 4.1).

4.3 Gas-surface interactions

In the FMF environment, the forces and torques acting on a spacecraft are the result of momentum and energy exchange between the incident gas particles and the external surfaces. This is commonly referred to as gas-surface interaction. [114] In that regard, two extreme cases of scattering mechanisms are differentiated (see Fig. 4.2):

- **Specular reflection**: The particles "remember" the information about their incoming condition and do not transfer energy at all ($T_{k,r} = T_{k,i}$).
- **Diffuse re-emission**: The particles "forget" the information about their incoming condition and accommodate their energy to the wall temperature ($T_{k,r} = T_w$).

$T_{k,i}$ and $T_{k,r}$ are the kinetic temperatures of the incident and reflected particles and T_w is the surface temperature [94]. Specular reflection is characterized by an equality of the angle of incident ψ_i and reflection ψ_r (see Fig. 4.2) [114]. In contrast, diffusely re-emitted particles leave the surface in a direction according to the Knudsen cosine law (around the surface normal vector) and at a velocity which in average, corresponds to the thermal velocity v_t at the surface temperature T_W [114]. The type of reflection that occurs depends on the physical parameters of the surface (i.e., roughness/cleanliness, molecular composition, lattice configuration and temperature) as well as the characteristics of the incident flow (i.e., composition, velocity and incident angle)

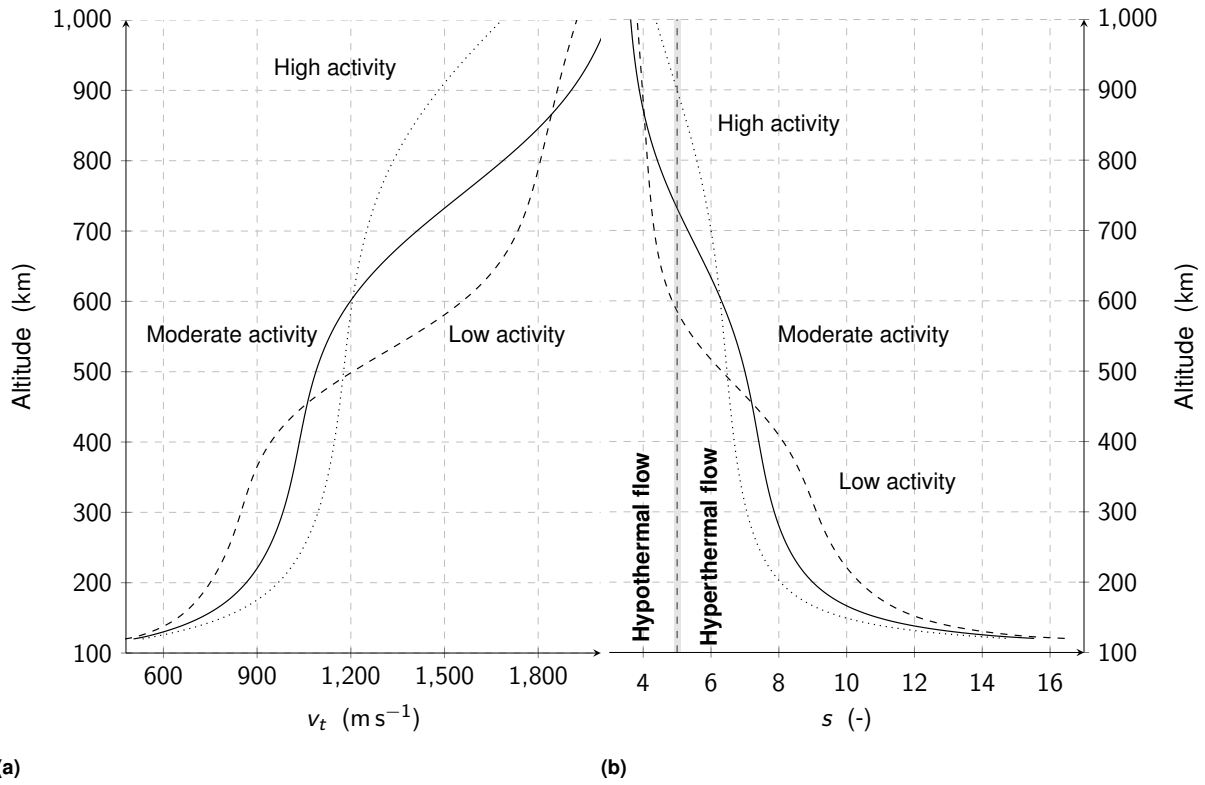

Figure 4.1: Most probable thermal velocity of the gas particles v_t (left) and molecular speed ratio s (right) over altitude assuming a circular orbiting spacecraft calculated via the NRLMSISE-00 model [122] and the different solar and geomagnetic activity scenarios listed in Tab. 3.1 over Stuttgart, Germany.

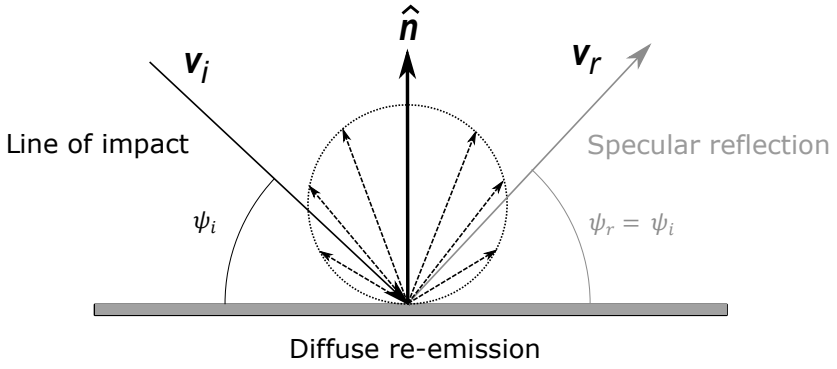

Figure 4.2: Extreme cases of scattering mechanisms.

[130]. Consequently, a prediction of the precise in-orbit conditions is challenging. As a rule of thump, however, the following description by Moe and Moe [108] can be consulted:

> *"When the incoming molecules strike a clean surface, they are reemitted near the specular angle with a partial loss of their incident kinetic energy. The fraction of the incident energy lost depends very much on the mass of the incoming molecule. However, when the surface becomes heavily contaminated with adsorbed molecules, the incident molecules are reemitted in a diffuse distribution, losing a large portion of their incident kinetic energy. Thus, adsorbed molecules increase energy accommodation and broaden the angular distribution of molecules reemitted from surfaces."* [108]

4.3.1 Gas-surface interaction parameters

To mathematically describe the nature of the gas-surface interactions, so-called accommodation coefficients are generally consulted.

Energy accommodation coefficient

The kinetic energy of a particle can be described as

$$E = \frac{1}{2} m_m v_m^2, \tag{4.13}$$

where v_m is the macroscopic velocity and m_m its the molecular mass[12]. The energy (or thermal) accommodation coefficient

$$\alpha_T = \frac{E_i - E_r}{E_i - E_w} = \frac{T_{k,i} - T_{k,r}}{T_{k,i} - T_w} \tag{4.14}$$

describes the energy exchange with the surface wall. E_i and E_r are the kinetic energies of the incident and the reflected particle. E_w describes the energy of the particle that would be carried away if re-emitted diffusely in complete thermal equilibrium with the wall. Consequently, $\alpha_T = 1$ describes complete thermal accommodation to the surface wall whereas $\alpha_T = 0$ indicates that no energy is exchanged. [94, 114] The energy transfer can be subdivided into the transfer normal and tangential to the surface. The normal energy accommodation coefficient α_n is defined as

$$\alpha_n = \frac{p_i^2 - p_r^2}{p_i^2 - p_w^2}, \tag{4.15}$$

where p_i is the normal momentum carried to the surface by the incident particle and p_r the normal momentum carried away from the surface by the reflected particle. p_w is the normal momentum that would be carried away from the surface by a particle that is in thermal equilibrium with the surface. Analogous, the tangential energy accommodation coefficient α_t is defined as

$$\alpha_t = \frac{\tau_i^2 - \tau_r^2}{\tau_i^2 - \tau_w^2} = \frac{\tau_i^2 - \tau_r^2}{\tau_i^2}, \tag{4.16}$$

[12] The molecular mass m_m, sometimes also referred to as molecule mass, is the mass of the molecule in units of kg and must not be confused with the molar mass M, which carries the unit g mol^{-1}.

where τ_i is the tangential momentum carried to the surface by the incident particle while τ_r is the tangential momentum carried away from the surface by the reflected particle. τ_w is the tangential momentum that would be carried away from the surface by a diffusely reflected particle that is in thermal equilibrium with the surface, which is zero per definition (the velocity distribution of the diffuse reflection is symmetrical around the surface normal). [93]

Based on the in-orbit data of seven spherical satellites, Pilinski, Argrow, and Palo [124] developed the *Semi-empirical model for the calculation of the satellite energy accommodation coefficients* (SESAM) which allows to avoid the constant coefficient assumption. Here, the energy accommodation coefficient of a VLEO satellite α_T is a function of the product of the number density of atomic oxygen and the atmospheric neutral temperature T_∞ [123, 124]. The most recent version of the model [123] is

$$\alpha_T\left(n_O, T_\infty\right) = \frac{4.98 \times 10^{-17} n_O T_\infty}{1 + 4.98 \times 10^{-17} n_O T_\infty}. \tag{4.17}$$

According to Pilinski, Argrow, and Palo [124], physically this equation holds for all values of $n_O T_\infty$ and satellite surface temperatures of $T_W \approx 300\,\mathrm{K}$ and its application is restricted to orbits with an eccentricity of $e \leq 0.07$, an altitude within the range of 100 - 500 km and values of $\alpha_T \in [0.85;\ 1.0]$ [124] due to the underlying orbital data. However, Doornbos [39] points out that the applicability of the isotherm function and the use of instantaneous and local empirical model values need to be further analyzed and confirmed in the future.

Momentum accommodation coefficients

The momentum of a particle can be described as

$$I = m_m v_m = \sqrt{p^2 + \tau^2}, \tag{4.18}$$

where τ represents the tangential and p the normal momentum. Thus, the accommodation coefficients for the tangential σ_t and the normal momentum σ_n exchange are [136]

$$\sigma_t = \frac{\tau_i - \tau_r}{\tau_i - \tau_w} = \frac{\tau_i - \tau_r}{\tau_i}, \tag{4.19}$$

$$\sigma_n = \frac{p_i - p_r}{p_i - p_w}. \tag{4.20}$$

All parameters remain as previously defined. Consequently, the following relation between the tangential momentum σ_t and energy accommodation α_t coefficient exists [184]:

$$\alpha_t = \sigma_t\left(2\ -\ \sigma_t\right). \tag{4.21}$$

For the conversion of the normal energy α_n to the momentum σ_n accommodation coefficient, however, no simple relation is available [184].

Conversions of accommodation coefficients

In the following, the conversions of α_T and f_M to σ_t, σ_n and α_n are presented [58, 98]. These are needed at a later stage to ensure the consistency of the input parameters for the different calculation tools. f_M is the Maxwell coefficient, which describes the fraction of molecules that are reflected diffusely [106]. For a particle of constant molecular mass m_m, the kinetic energy is proportional to the square of its momentum $E \propto I^2$. Thus, α_T can be expressed as

$$\alpha_T = \frac{I_i^2 \; - \; I_r^2}{I_i^2 \; - \; I_w^2} = \frac{\left(p_i^2 + \tau_i^2\right) \; - \; \left(p_r^2 + \tau_r^2\right)}{\left(p_i^2 + \tau_i^2\right) \; - \; \left(p_w^2 + \tau_w^2\right)}, \tag{4.22}$$

where I_i and I_r is the momentum carried by the incident and the reflected particles, while I_w denotes the momentum that would be carried by the reflected particle if complete thermal equilibrium was achieved. From it, the following expression for I_r can be derived:

$$I_r = \sqrt{I_i^2 \; - \; \alpha_T \left(I_i^2 \; - \; I_w^2\right)}. \tag{4.23}$$

For complete diffuse reflection, $\tau_r = 0$ holds and $p_r = I_r$ follows from the fundamental definition of the total momentum [149]. Considering specular reflections, incidence angle θ_i equals the reflection angle θ_r and the following relation holds:

$$\left|\frac{p_r}{p_i}\right| = \frac{\tau_r}{\tau_i} = \left|\frac{I_r}{I_i}\right|. \tag{4.24}$$

Next, τ_r and p_r are defined as a linear-combination of diffuse and specular reflection:

$$\tau_r = \left(1 \; - \; f_M\right) \tau_i \frac{I_r}{I_i}, \tag{4.25}$$

$$p_r = f I_r + \left(1 \; - \; f_M\right) p_i \frac{I_r}{I_i}. \tag{4.26}$$

Inserting the terms into Eqs. 4.19, 4.20 and 4.15, expressions for the desired parameters result:

$$\sigma_t = \frac{\tau_i \; - \; \left[\left(1 \; - \; f_M\right) \tau_i \frac{I_r}{I_i}\right]}{\tau_i}, \tag{4.27}$$

$$\sigma_n = \frac{p_i \; - \; \left[f_M I_r + \left(1 \; - \; f_M\right) p_i \frac{I_r}{I_i}\right]}{p_i \; - \; p_w}, \tag{4.28}$$

$$\alpha_n = \frac{p_i^2 - \left[f_M I_r + \left(1 \; - \; f_M\right) p_i \frac{I_r}{I_i}\right]^2}{p_i^2 - p_w^2}. \tag{4.29}$$

The total momentum of the reflected particles I_r has been defined in Eq. 4.23 and the total momentum of the incident particles I_i is defined via the fundamental definition

$$I_i = \sqrt{p_i^2 + \tau_i^2}. \tag{4.30}$$

Further, $I_w = p_w$ holds due to $\tau_w = 0$.

Now that the desired conversions have been derived, values for pending parameters τ_i, p_i and p_w need to be determined. To do so, the unitless auxiliary parameters τ_i', p_i' and p_w' are introduced, which were obtained from Sentman [149]:

$$\tau_i' = \vartheta \left[\varphi \left(1 + \operatorname{erf}(\varphi s)\right) + \frac{1}{s\sqrt{\pi}} \mathrm{e}^{-\varphi^2 s^2} \right] \propto \tau_i, \tag{4.31}$$

$$p_i' = \varphi \left[\varphi \left(1 + \operatorname{erf}(\varphi s)\right) + \frac{1}{s\sqrt{\pi}} \mathrm{e}^{-\varphi^2 s^2} \right] + \frac{1}{2s^2} \left(1 + \operatorname{erf}(\varphi s)\right) \propto p_i, \tag{4.32}$$

$$p_w' = \frac{1}{2} \sqrt{\frac{T_w}{T_i}} \left[\frac{\varphi\sqrt{\pi}}{s} \left(1 + \operatorname{erf}(\varphi s)\right) + \frac{1}{s^2} \mathrm{e}^{-\varphi^2 s^2} \right] \propto p_w. \tag{4.33}$$

Here, ϑ and φ are the direction cosines between the local x_S - and y_S - axes and the macroscopic velocity vector $\boldsymbol{v}_m$ and $\operatorname{erf}(x)$ the so-called error function which is defined in Eq. 4.40 in the next section. Whereas the auxiliary parameters τ_i', p_i' and p_w' do not correspond to the pending parameters themselves, these are proportional to the latter. As the proportionality constant is identical in any case, however, the desired ratios forming the accommodation coefficients can be formed from either the set of auxiliary parameters or the set of pending parameters (provided that the same set of parameters is applied throughout). Therefore, for the conversions performed within the context of this dissertation, the set of auxiliary variables is constantly resorted to.

4.3.2 Gas-surface interaction models

In literature, various GSI models with different levels of fidelity exist. In the following, the popular analytic models developed by Sentman [149] and Schamberg [137] are introduced.

Sentman's GSI model

Sentman's GSI model [149] *"[...] is the de-facto standard to compute spacecraft aerodynamic coefficients at low altitudes"* [182] and has been the GSI model of choice in a multitude of similar research activities [37, 39, 182]. Sentman's GSI model assumes that all incident particles hitting the surface are adsorbed and re-emitted diffusely in partial thermal equilibrium with the surface [182]. The normalized coefficients for a simple one-sided flat plate can be expressed as [162]

$$dC_D = \left[\frac{P}{\sqrt{\pi}} + \cos(\theta_i) Q Z + \frac{\cos(\theta_i)}{2} \frac{v_{r,mp}}{v_{rel}} \left(\cos(\theta_i) \sqrt{\pi} Z + P \right) \right] \frac{dA}{A_{ref,S}}, \tag{4.34}$$

$$dC_L = \left[\sin(\theta_i) G Z + \frac{\sin(\theta_i)}{2} \frac{v_{r,mp}}{v_{rel}} \left(\cos(\theta_i) \sqrt{\pi} Z + P \right) \right] \frac{dA}{A_{ref,S}}, \tag{4.35}$$

where

$$G = \frac{1}{2s^2}, \tag{4.36}$$

$$P = \frac{1}{s} e^{-\cos(\theta_i)^2 s^2}, \tag{4.37}$$

$$Q = 1 + G, \tag{4.38}$$

$$Z = 1 + \mathrm{erf}(\cos(\theta_i)\, s), \tag{4.39}$$

$$\mathrm{erf}(x) = \frac{2}{\sqrt{\pi}} \int_0^x e^{-y^2}\, dy. \tag{4.40}$$

The incident angle

$$\theta_i = \frac{\pi}{2} - \psi_i \tag{4.41}$$

is the angle between the incident flow $\boldsymbol{v}_{rel}$ and the local normal vector $\hat{\boldsymbol{n}}$ and consequently the complementary angle to ψ_i. $v_{r,mp}$ is the velocity of the re-emitted gas particles, v_{rel} the relative velocity between the spacecraft and the incident gas particles, $A_{ref,S}$ is an arbitrary chosen reference area, and s again the molecular speed ratio. The ratio r_{mp} of velocities of the re-emitted $v_{r,mp}$ and incident v_{rel} particles can be determined via [39, 83, 109]

$$r_{mp} = \frac{v_{r,mp}}{v_{rel}} = \sqrt{\frac{1}{2}\left[1 + \alpha_T \left(\frac{4\mathcal{R}T_w}{\bar{M} v_{rel}^2} - 1\right)\right]}, \tag{4.42}$$

The subscript 'mp' indicates that the re-emission velocity is the most probable velocity [129]. Sentman's GSI model is based on the hypothermal flow assumption.

Schamberg's GSI model

Schamberg's GSI model [137] is based on the hyperthermal flow assumption, i.e., all particles are assumed to have the same speed and direction. The normalized coefficients for a simple one-sided flat plate can be expressed as [162]

$$dC_D = \left[2\cos(\theta_i) + \frac{4}{3}\cos(\theta_i)^2\, r_{rms}\right] \frac{dA}{A_{ref,S}}, \tag{4.43}$$

$$dC_L = \left[\frac{4}{3}\cos(\theta_i)\sin(\theta_i)\, r_{rms}\right] \frac{dA}{A_{ref,S}}, \tag{4.44}$$

where r_{rms} refers to the ratio of the root-mean squared re-emission velocity $v_{r,rms}$ and incident velocity v_{rel} given by [82, 129]

$$r_{rms} = \frac{v_r}{v_{rel}} = \sqrt{1 + \alpha_T \left(\frac{3\mathcal{R}T_w}{\bar{M} v_{rel}^2} - 1\right)}. \tag{4.45}$$

Notably, Schamberg's GSI model uses root mean square (rms) velocity for the re-emission while Sentman's GSI model uses the most probable (mp) velocity [129].

Drag and lift coefficients of a flat plate

In the following, the results of Sentman's and Schamberg's GSI models for a one-sided flat plate as a function of the incident angle θ_i for varying boundary conditions are discussed. Unless otherwise noted, the parameters used for the calculations depicted in Figs. 4.3 - 4.5 are $A_{ref} = 1\,\mathrm{m}^2$, $T_w = 300\,\mathrm{K}$, $\alpha_T = 1$, $T_\infty = 1200\,\mathrm{K}$ and $\bar{M} = \bar{M}_\mathrm{O} = 16\,\mathrm{g\,mol}^{-1}$. The velocity $v_r = 7697\,\mathrm{m\,s}^{-1}$

corresponds to the circular orbital velocity of a satellite at a height of $h = 350\,\mathrm{km}$. It is immediately apparent that in all cases, C_L is significantly smaller than C_D, which is the norm for diffuse re-emission and follows from momentum conservation. The most important distinction between the models becomes observable for $\theta_i \to 90°$: in case of Sentman's GSI model, a residual value remains even for $\theta_i = 90°$. This is because Sentman's GSI model accounts for the random thermal motion of the atmospheric particles (hypothermal flow assumption). Thus, also panels which are parallel to or even facing away from the bulk flow contribute to drag. This effect, however, is not taken into account in Schamberg's GSI model, which is based on the hyperthermal flow assumption. Consequently, the coefficients approach zero for $\theta_i \to 90°$. Independent from the underlying GSI model, C_L shows a strong dependency on α_T. With respect to dependencies on $\bar{M}$ and T_∞, the model outputs differ: whereas in both cases C_D shows only slight dependencies, the effect of a variation in $\bar{M}$ on C_L is more pronounced for Sentman's GSI model (see Fig. 4.4). This can be attributed to the fact that $\bar{M}$ influences the speed ratio and the re-emission velocity. Whereas the latter is included in both sets of equations, s is only included in Sentman's GSI model. This also explains why T_∞ does not affect the results of Schamberg's GSI model at all, as it influences the nature of the flow via s: in general, the effects of the random thermal motion of the particles become more apparent with increasing T_∞ (see Fig. 4.5).

Note: *Given the fundamental definition of the two aerodynamic force components, there can be aerodynamic drag without lift, but never aerodynamic lift without drag.*

4.3.3 Panel method

To dynamically calculate the aerodynamic coefficients of convex satellite geometries within numerical integration, the so-called *panel method* is consulted within this work. Here, the geometry of the satellite is approximated by a discrete number of individual elements whose force coefficients are calculated using the equations for a simple one-sided plane plate before the individual coefficients are combined to form the coefficients of the entire satellite [123]. Assuming a total number of panels of N_P, the total C_D can be calculated via [123]

$$C_D = \frac{\sum_{k=1}^{N_p} \{C_{D,k} A_{plan,k}\}}{A_{ref}}, \tag{4.46}$$

in which $A_{plan,k}$ is the geometric area of the k'th panel and A_{ref} is the total cross-sectional area projected in the direction of the freestream velocity [123]

$$A_{ref} = \sum_{k=1}^{N_p} A_{proj,k}, \tag{4.47}$$

where

$$A_{proj,k} = \begin{cases} A_{plan,k} \, |\hat{\boldsymbol{n}}_k \cdot \hat{\boldsymbol{v}}_{rel}| \text{ if } \hat{\boldsymbol{n}}_k \cdot \hat{\boldsymbol{v}}_{rel} > 0, \text{ panel facing incoming flow} \\ 0 \text{ if } \hat{\boldsymbol{n}}_k \cdot \hat{\boldsymbol{v}}_{rel} \leq 0, \text{ panel facing away from flow.} \end{cases} \tag{4.48}$$

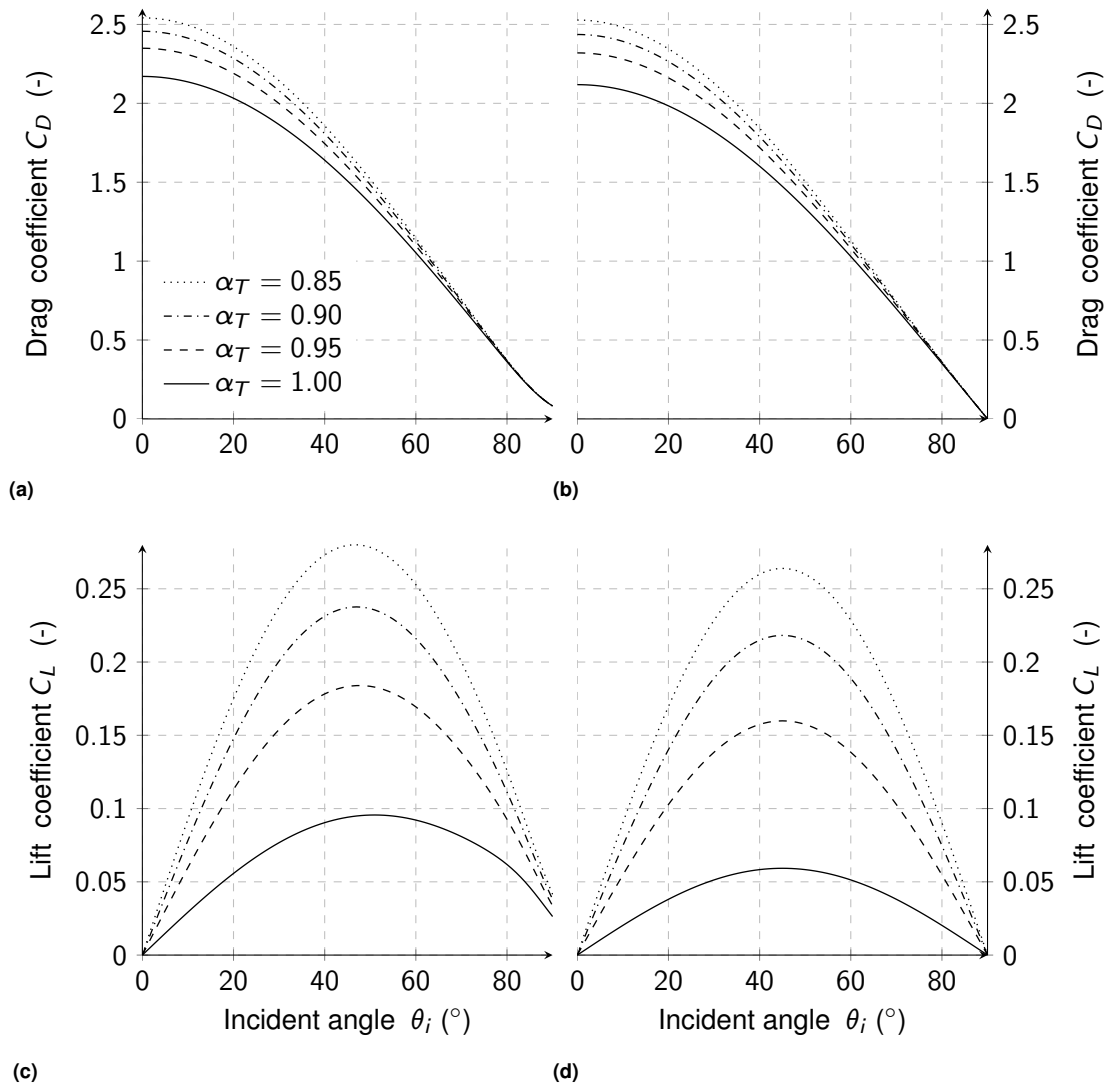

Figure 4.3: Drag (top) and lift (bottom) coefficients according to Sentman's (left) and Schamberg's (right) GSI model for a one-sided flat plate as a function of the incident angle θ_i for four different levels of energy accommodation α_T.

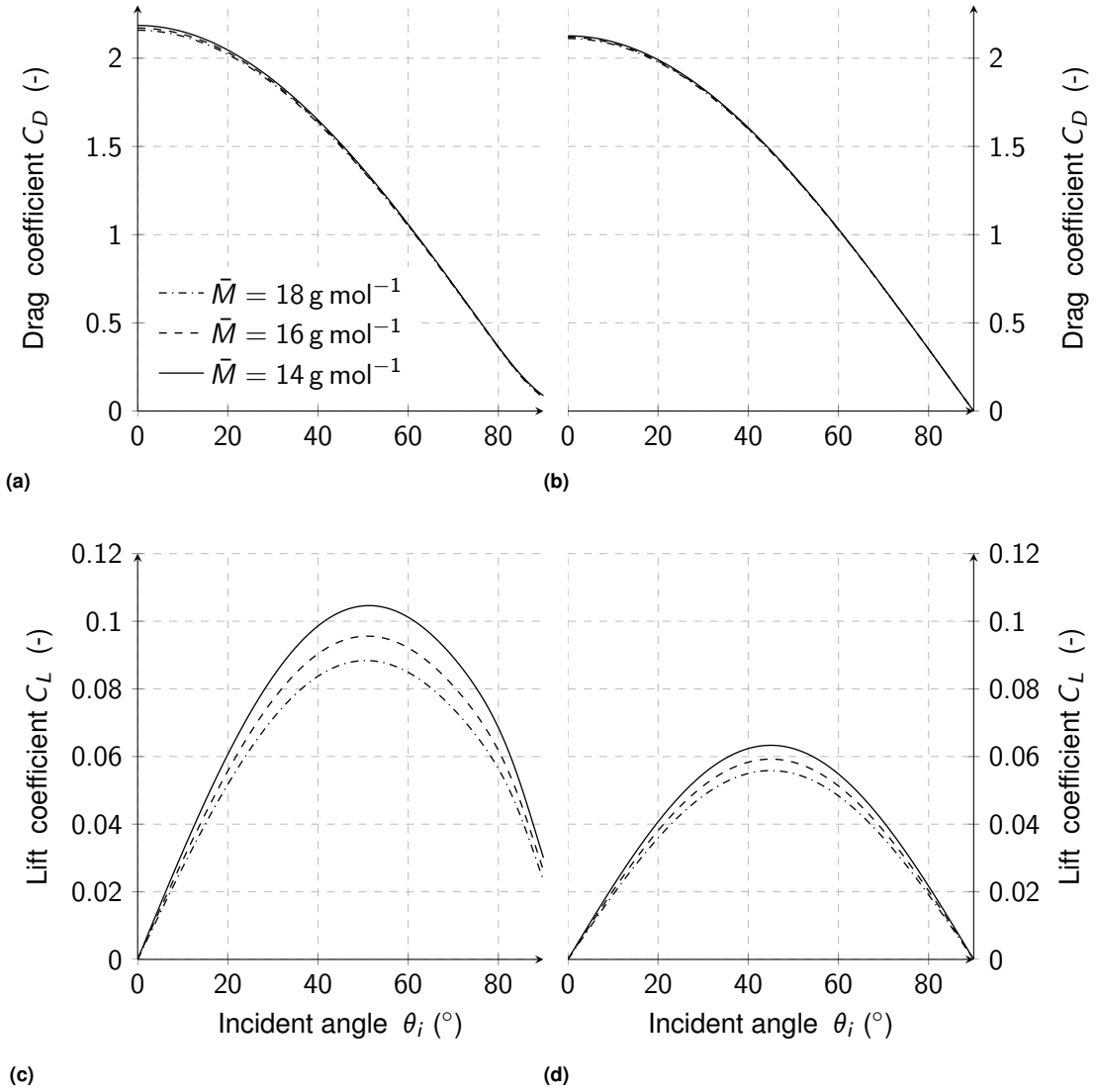

Figure 4.4: Drag (top) and lift (bottom) coefficients according to Sentman's (left) and Schamberg's (right) GSI model for a one-sided flat plate as a function of the incident angle θ_i for three different molar masses $\bar{M}$.

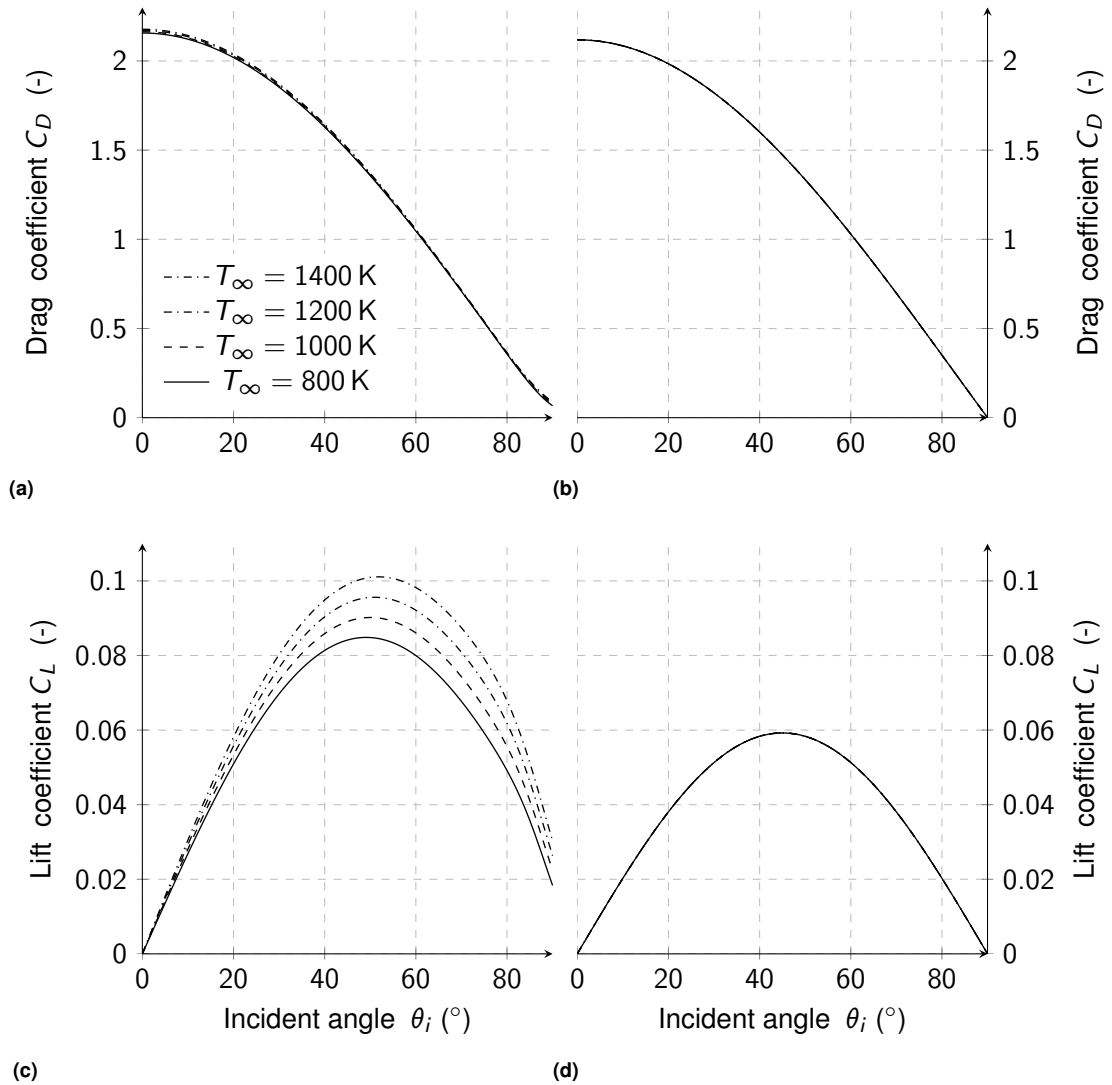

Figure 4.5: Drag (top) and lift (bottom) coefficients according to Sentman's (left) and Schamberg's (right) GSI model for a one-sided flat plate as a function of the incident angle θ_i for four different neutral atmospheric temperatures T.

For C_L, the contribution from each flat plate will be in a direction dependent on the reflection of molecules. Therefore, the calculation of the total normalized C_L requires a vector summation to resolve both the magnitude and direction [162]:

$$C_L \cdot \hat{\boldsymbol{u}}_L = \frac{\sum_{k=1}^{N_p} \left\{ C_{L,k} A_{plan,k} \hat{\boldsymbol{u}}_{L,k} \right\}}{A_{ref}}, \tag{4.49}$$

where $\hat{\boldsymbol{u}}_{L,k}$ is the unit vector

$$\hat{\boldsymbol{u}}_{L,k} = (\hat{\boldsymbol{v}}_{rel} \times \hat{\boldsymbol{n}}_k) \times \hat{\boldsymbol{v}}_{rel}. \tag{4.50}$$

The main limitation of this approach is that it cannot account for multiple reflections or shadowing. Nevertheless, the panel method allows to include the most important features of satellite aerodynamics in the analysis while avoiding the high computational costs of particle-based methods.

Part II

Research focus

Chapter 5

Differential lift and drag

"Power is nothing without control."
— Advertising slogan of the tire manufacturer Pirelli, 1974

The goal of this dissertation is to develop the necessary fundamentals to enable propellant-less, three-dimensional control of satellite formations orbiting in VLEO via differential aerodynamic forces. Before the methodology is comprehensively described, a short introduction to relative motion control is provided.

5.1 Relative motion control - an introductory overview

Control theory describes an interdisciplinary discipline that deals with influencing the behavior of a technical system in a satisfactory manner. Within the course of this dissertation, the system under investigation is the satellite formation. In highly perturbed environments like VLEO, active maintenance of a formation, commonly referred to as *formation keeping*, is required. Maintenance maneuvers can be necessitated by variations in the orbital elements, differential specific forces, hardware limitations or by any other anomaly [52]. Similarly, any adjustments to the formation design (*rendezvous* and/or *reconfiguration* maneuvers) require dedicated control inputs. During the Gravity Recovery and Climate Experiment (GRACE) mission, for example, an exchange of the leader/follower configuration had to be performed to compensate for surface erosion on the radar caused by O [35]. The conventional approach to exert control forces is to use onboard chemical or electric and/or cold gas thrusters. Consequently, the proposed control techniques range from continuous to impulsive [49]. Continuous control is applied for forced motion phases or if electric thrusters are employed [49]. For certain scientific measurements, however, impulsive control is preferred over continuous techniques because high-sensitive measurements might otherwise be disturbed by the lasting orbit correction maneuvers [49]. During synthetic aperture radar data takes, for example, even very minor effects such as non-modeled thruster performance errors can have detrimental effects on the measurement results [52].

5.2 Methodology of differential lift and drag

For satellite formations, long-term perturbation effects must be routinely compensated for, and the mission lifetime is frequently determined by the amount of stored propellant. This is especially critical for small satellites, which have very stringent mass and volume constraints. The need for dedicated propulsion systems can be overcome if natural resources are exploited. In the VLEO range, any residual difference in the specific aerodynamic forces experienced by two satellites

$$\delta \boldsymbol{f}_A = \boldsymbol{f}_{A,d} \; - \; \boldsymbol{f}_{A,c} \tag{5.1}$$

induces variations on the relative orbital elements $\delta \bar{\boldsymbol{\mathcal{E}}}_{ns}$. As a result, naturally long term stable formations require the use of largely identical satellites and attitude profiles. Conversely, a desired difference in the magnitude of the specific drag forces $\delta \boldsymbol{f}_D$, referred to as *differential drag*, can be intentionally applied for control purposes. Whilst by the fundamental definition of the aerodynamic drag force $\boldsymbol{f}_D$ its control authority is mainly restricted to the in-plane relative motion control[13], differences in the specific lift forces $\delta \boldsymbol{f}_L$, referred to as *differential lift*, can be applied to alter the motion perpendicular to the orbital plane. In this case, differences can be generated via differences in the magnitude and/or effective direction of lift $\hat{\boldsymbol{u}}_L$, which depends on the normal vector $\hat{\boldsymbol{n}}$ of the control surface under consideration. Differential aerodynamic forces can either be created by adjusting the attitude of non-symmetrical shaped satellites via dedicated attitude control systems, e.g. reaction wheels, or by rotating designated panels, which might otherwise serve as solar panels. Consequently, the methodology promises to allow any asymmetrically shaped VLEO satellite equipped with appropriate attitude control or with rotatable external panels to alter its motion with respect to any other real (or virtual) spatial object. Due to the sheer increase in the number of satellites planned in the LEO regime within the next ten years [4] (see Fig. 1.3), the ability to actively perform collision avoidance maneuvers will be critical for any satellite orbiting in this regime. Therefore, a significant increase in the relevance of the method is foreseen.

As differential lift has so far mostly been neglected, the focus of the studies was on the in-plane control. Thus, commanding pitch angles $\delta\theta$ deviations of two asymmetrically shaped satellites flying in formation is the method of choice to create differential drag. While in this case lift forces are generated aswell, these are also located within the orbital plane [22, 189]. Within this dissertation, deviations in the yaw angles $\delta\psi$ of the respective satellites are proposed to simultaneously create differential drag forces within the orbital plane and differential lift forces perpendicular to it, a practice which has recently also been investigated by Hu et al. [64]. Thereby, all translational degrees of freedom of a satellite formation orbiting in VLEO can be controlled simultaneously without the need for any thrusting device.

[13] As shown by Ben-Yaacov and Gurfil [10], the component of the drag force pointing in the out-of-plane direction due to the co-rotation of the atmosphere for any orbit with an inclination of $i \neq 0$ is two orders of magnitude smaller and unable to provide meaningful control authority.

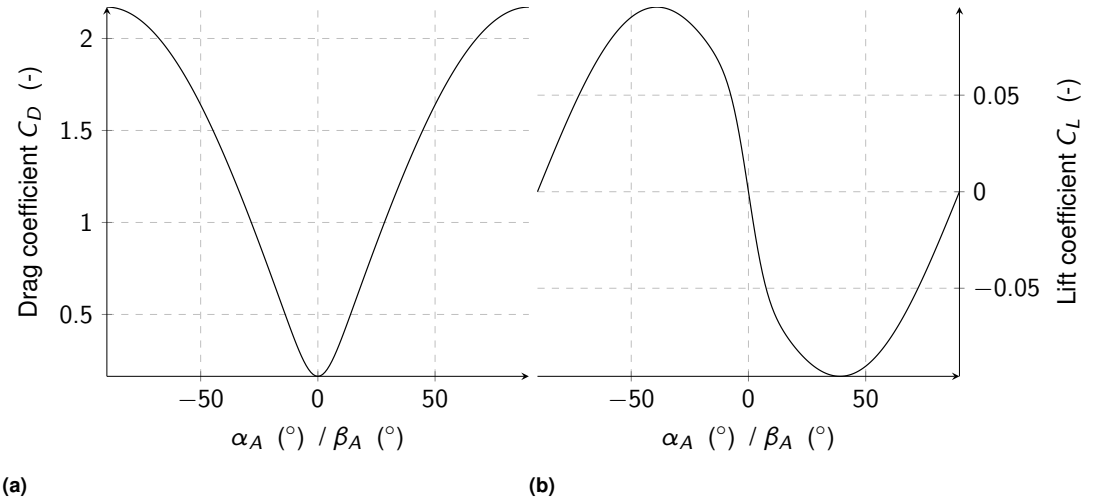

Figure 5.1: Drag (left) and lift (right) coefficient of a two sided flat plate according to Sentman's GSI model [149] and full energy accommodation ($\alpha_T = 1$).

5.2.1 Differential aerodynamic forces

To simplify and generalize, the introduction of the methodology is restricted to the circular orbit special case, in which the direction of the $\hat{\boldsymbol{y}}$ - unit vector points along the inertial satellite velocity vector $\boldsymbol{v}$. Neglecting the co-rotational velocity of the Earth's atmosphere and thermospheric winds ($\boldsymbol{v}_{rot} = \boldsymbol{v}_w = \mathbf{0}$ m s^{-1}), the satellite velocity relative to the local atmosphere matches its inertial velocity $\boldsymbol{v}_{rel} = \boldsymbol{v}$. In this case, the specific differential aerodynamic force in the $\hat{\boldsymbol{y}}$ - direction of the $\mathcal{L}$ - frame of the chief $\delta f_{A,y}$ is a result of differential drag δf_D only, whereas $\delta f_{A,x}$ and $\delta f_{A,z}$ are purely created via differential lift forces δf_L in the respective $\mathcal{L}$ - directions ($\delta f_{L,x}$ or $\delta f_{L,z}$). Through these simplifications, the pitch angle θ equals the angle of attack α_A and the yaw angle ψ equals the angle of sideslip β_A. Following the treatment by Horsley [62] and Smith [154], the aerodynamic characteristics of the spacecraft are approximated by a two-sided flat plate. While the actual aerodynamic properties of more complex shaped satellites differ from this simplified representation, this serves for the purpose of clarity. The profiles of $C_D(\alpha_A)$ (left) and $C_L(\alpha_A)$ (right), calculated using Sentman's GSI model [149] for $\alpha_T = 1$, are displayed in Fig. 5.1.

The drag coefficient profile $C_D(\alpha_A)$: The profile for $\alpha_A \in [-90°, 90°]$ is axisymmetric, so that a rotation in positive and negative direction results in the same value ($C_D(\alpha_A) = C_D(-\alpha_A)$). The coefficient has its minimum at $\alpha_A = 0°$ ($C_{D,min} = C_D(\alpha_A = 0°)$) and increases strictly monotonically with α_A up to its maximum value $C_{D,max} = C_D(|\alpha_A| = 90°)$.

The lift coefficient profile $C_L(\alpha_A)$: The profile for $\alpha_A \in [-90°, 90°]$ is point-symmetric, so that a rotation in positive and negative direction results in a C_L of similar value but different sign ($C_L(\alpha_A) = -C_L(-\alpha_A)$). The coefficient approaches zero at $\alpha_A = 0°$ and $|\alpha_A| = 90°$ ($C_{D,min} = C_D(\alpha_A = 0°) = C_D(\alpha_A = 90°) = 0$) and the maximum absolute value is achieved at $\alpha_A \approx \pm 45°$ ($C_{L,max} = C_L(|\alpha_A| \approx 45°)$).

Differential drag

The terminology differential drag describes the condition that the residual drag force acting on two satellites flying in formation differs. Starting from their nominal configuration[14], i.e., $\alpha_{A,c} = \beta_{A,c} = 0^\circ$ and $\alpha_{A,d} = \beta_{A,d} = 0^\circ$, differential drag can be created by commanding either pitch $\delta\theta$ (via a rotation around the ${}^{\mathcal{B}}\hat{\boldsymbol{y}}$ - axis) or yaw angle $\delta\psi$ deviations (via a rotation around the ${}^{\mathcal{B}}\hat{\boldsymbol{z}}$ - axis). For the latter, also the out-of-plane motion is inevitably affected (via differential lift $\delta f_{L,z}$ in the $\hat{\boldsymbol{z}}$ - direction) and literature consistently proposes the establishment of differential drag via pitch angle differences $\delta\theta$. Following the insights provided by Fig. 5.1:

- Maximum *positive* differential drag is reached when the chief satellite orbits in its maximum drag configuration (maximal sensitivity towards the aerodynamic drag force, i.e., $|\theta_c| = 90^\circ$) while the deputy aims to minimize the residual drag ($\theta_d = 0^\circ$).
- Maximum *negative* differential drag is accomplished when the chief minimizes drag ($\theta_c = 0^\circ$) while the deputy maximizes the residual drag ($|\theta_d| = 90^\circ$).
- *Zero* differential drag is achieved whenever the absolute value of the pitch angles of both satellites match $\left(|\theta_c| = |\theta_d|\right)$.

At these sets of discrete angle differences, referred to as *ternary drag states* in the following, no differential lift is created ($C_L\left(\theta = 0^\circ\right) = C_L\left(\theta = 90^\circ\right) = 0$)). A visualization of a maximum negative (top) and positive (bottom) differential drag configuration for a 3U CubeSat created via pitch angle deviations $\delta\theta$ is displayed in Fig. 5.2.

Differential lift

In terms of satellite aerodynamics, the direction of differential lift is per se not uniquely defined. Therefore, a distinction between the generation of differential lift in the radial (${}^{\mathcal{L}}\hat{\boldsymbol{x}}$) and in the out-of-plane (${}^{\mathcal{L}}\hat{\boldsymbol{z}}$) direction $\delta f_{L,x}$ and $\delta f_{L,z}$, respectively, has to be made.

Differential lift $\delta f_{L,x}$ in the $\hat{\boldsymbol{x}}$ - direction: Differential lift $\delta f_{L,x}$ in the $\hat{\boldsymbol{x}}$ - direction can be created by commanding pitch angle deviations $\delta\theta$ via rotations around the ${}^{\mathcal{B}}\hat{\boldsymbol{y}}$ - axes. Positive (negative) differential lift forces in the $\hat{\boldsymbol{x}}$ - direction result in case that the chief rotates in negative (positive) direction whereas the deputy rotates contrariwise to positive (negative) pitch angles. Following Fig. 5.1, maximum differential forces can be accomplished at $\theta_{C,d} \approx \pm 45^\circ$. A visualization of a maximum positive (a) and negative (b) differential lift $\delta f_{L,x}$ configuration in the $\hat{\boldsymbol{x}}$ - direction for a 3U CubeSat created via pitch angle deviations $\delta\theta$ is displayed in Fig. 5.3.

Differential lift $\delta f_{L,z}$ in the $\hat{\boldsymbol{z}}$ - direction: Differential lift $\delta f_{L,z}$ in the $\hat{\boldsymbol{z}}$ - direction can be created if the two satellites rotate contrariwise around their ${}^{\mathcal{B}}\hat{\boldsymbol{z}}$ - axes to apply yaw angle deviations $\delta\psi$. Positive (negative) differential lift forces in the $\hat{\boldsymbol{z}}$ - direction result in case that the chief rotates in positive (negative) direction whereas the deputy rotates contrariwise to negative (positive) yaw angles. Following Fig. 5.1, maximum absolute differential lift forces can be accomplished for rotating the satellites contrariwise to $\psi_{C,d} \approx \pm 45^\circ$. A visualization of a maximum negative (a) and positive (b) differential lift $\delta f_{L,z}$ configuration in the $\hat{\boldsymbol{z}}$ - direction for a 3U CubeSat created via yaw angle deviations $\delta\psi$ is displayed in Fig. 5.4.

[14] At this point, we limit ourselves to generating differential forces by rotating around a single axis.

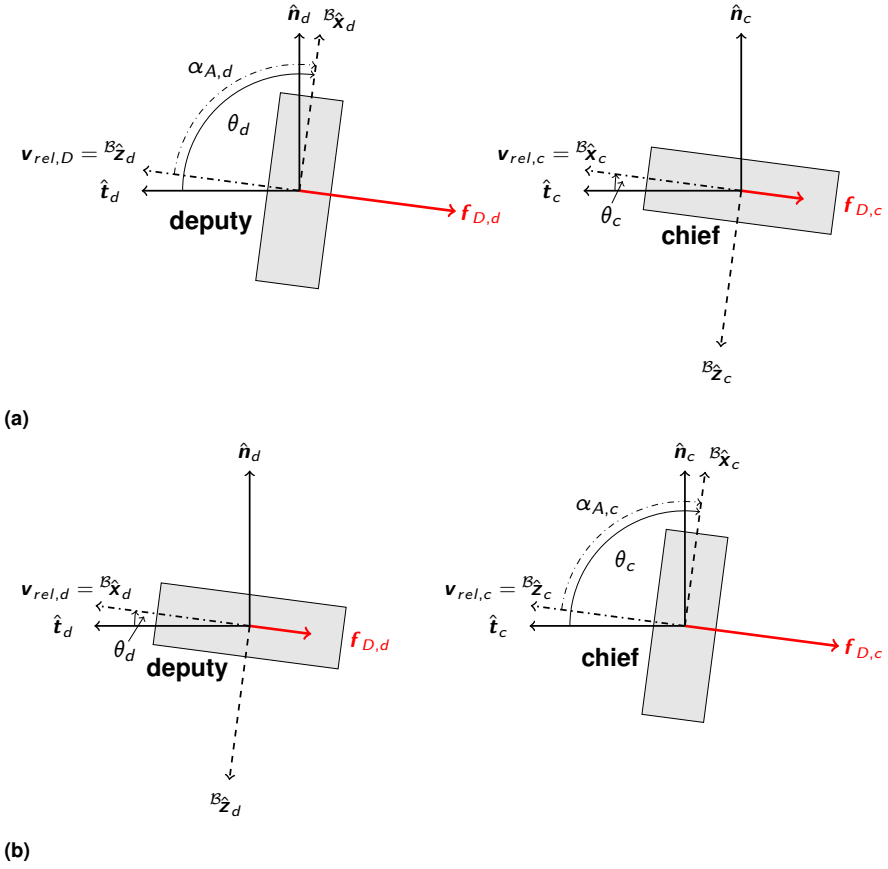

Figure 5.2: Visualization of a maximum negative (top, a)) and positive (bottom, b)) differential drag configuration for a 3U CubeSat via pitch angle deviations $\delta\theta$. At the ternary drag states, no differential lift is created.

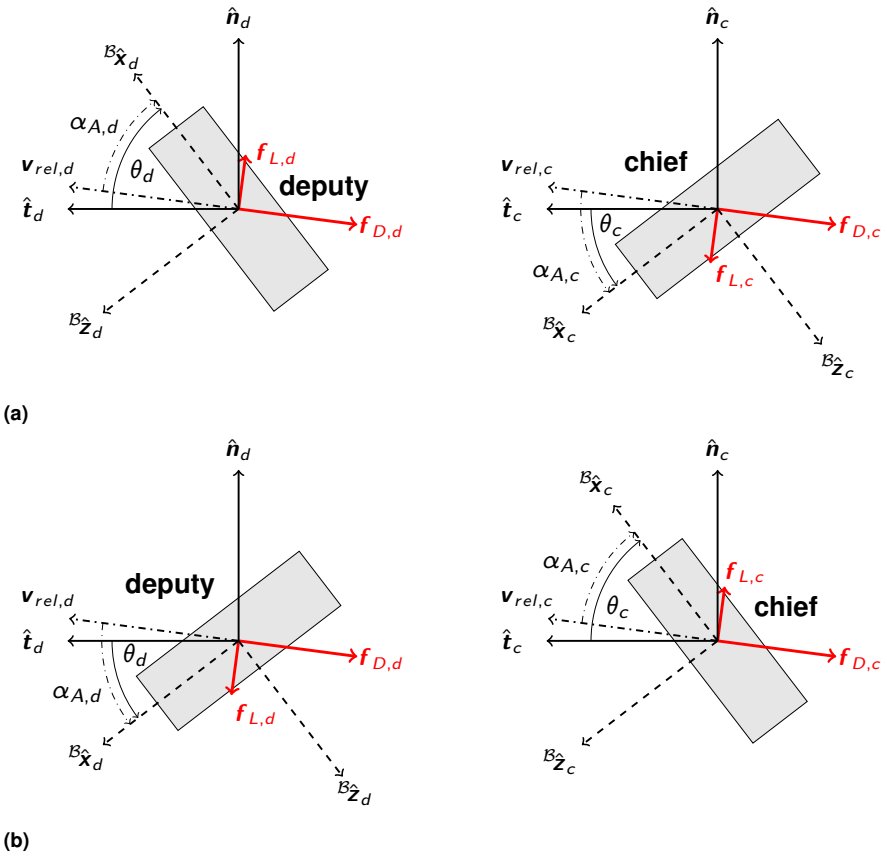

Figure 5.3: Visualization of a maximum positive (top, a)) and negative (bottom, b)) differential lift $\delta f_{L,x}$ configuration in the $\hat{x}$ - direction for a 3U CubeSat via pitch angle deviations $\delta\theta$. At the ternary lift states, no differential drag results.

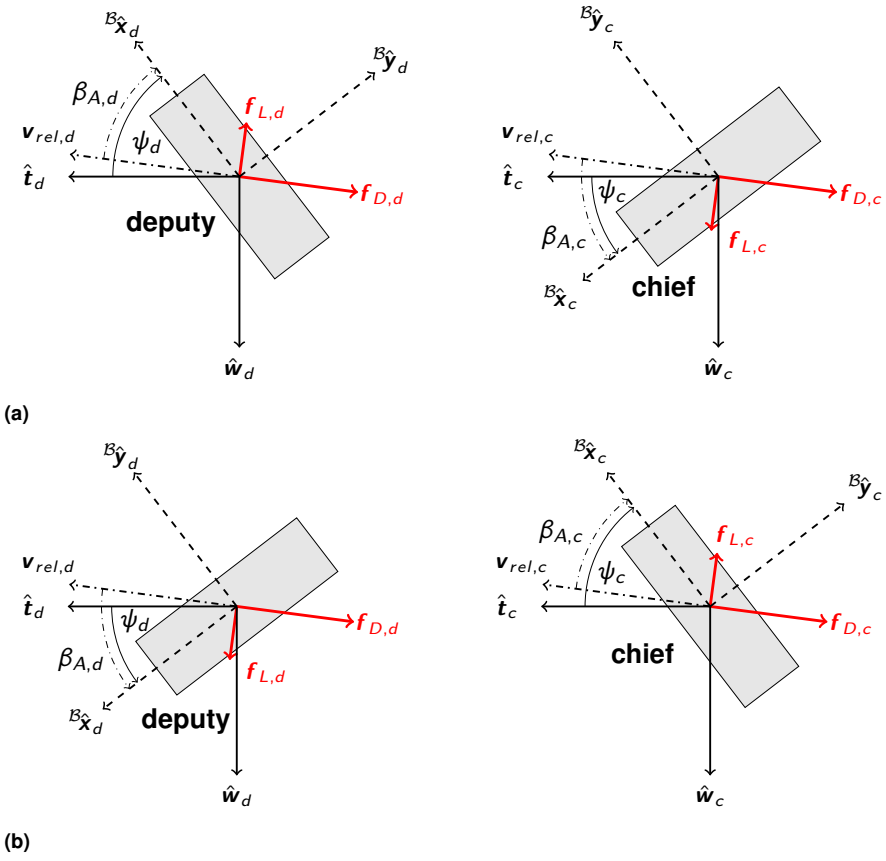

Figure 5.4: Visualization of a maximum negative (top, a)) and positive (bottom, b)) differential lift $\delta f_{L,z}$ configuration in the $\hat{z}$ - direction for a 3U CubeSat via yaw angle deviations $\delta\psi$. At the ternary lift states, no differential drag results.

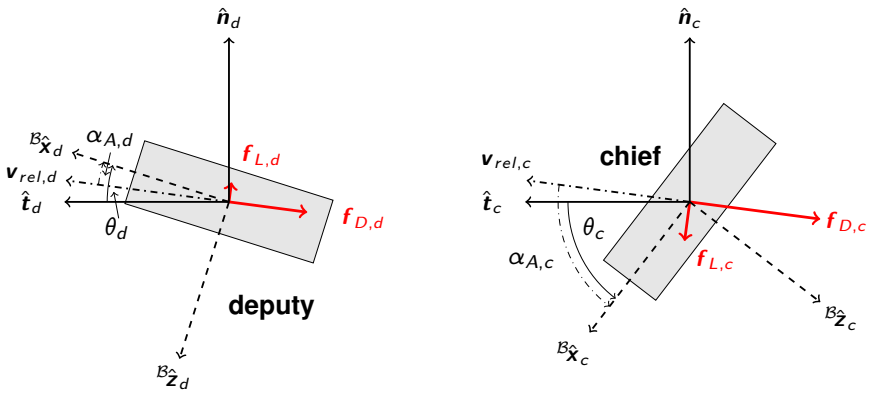

Figure 5.5: Visualization of a simultaneous positive differential lift $\delta f_{L,x}$ in the $\hat{x}$ - direction and positive differential drag configuration for a 3U CubeSat via pitch angle deviations $\delta\theta$.

At the set of discrete angle differences for which maximum and minimum differential lift forces can be accomplished ($|\theta_c| = |\theta_d| \approx 45°$ or $|\psi_c| = |\psi_d| \approx 45°$), referred to as *ternary lift states* in the following, no differential drag results as $C_D(\theta) = C_D(-\theta)$ and $C_D(\psi) = C_D(-\psi)$ holds. In any case, however, absolute drag is present, since there is no lift without drag. Zero differential lift in the respective direction is achieved whenever the pitch angles (radial direction) or the yaw angles (out-of-plane direction) of both satellites match ($\theta_c = \theta_d$ or $\psi_c = \psi_d$).

Differential lift and drag

Whether pitch $\delta\theta$ or yaw angle $\delta\psi$ deviations are applied, differential lift and drag can be created simultaneously if one refrains from ternary states and resorts to what will be referred to as *intermediate states*. This, however, directly implies that each respective control force can only be applied sub-optimally, as the individual optimum is reached at the ternary states.

Differential lift $\delta f_{L,x}$ and drag δf_D: By rotating around the ${}^{\mathcal{B}}\hat{y}$ - axes to command any pitch angle deviation except for the ternary states, differential lift $\delta f_{L,x}$ in the $\hat{x}$ - direction and differential drag δf_D are created simultaneously. As the direction of both forces is within the plane of motion, the authority of the control resulting from pitch angle deviations is limited to in-plane relative motion control. To enhance the effect of differential lift, the two satellites must rotate in opposite directions, while the magnitude of differential drag is defined by the difference between the absolute value of the commanded angles. A visualization of a simultaneous positive differential lift $\delta f_{L,x}$ in the $\hat{x}$ - direction and positive differential drag configuration for a 3U CubeSat created via pitch angle deviations $\delta\theta$ is displayed in Fig. 5.5.

Differential lift $\delta f_{L,z}$ and drag δf_D: By rotating around the ${}^{\mathcal{B}}\hat{z}$ - axes to command any yaw angle deviation $\delta\psi$ except for the ternary states, differential lift $\delta f_{L,z}$ in the $\hat{z}$ - direction as well as differential drag δf_D can be created simultaneously and three-dimensional relative motion control is enabled. Again, to increase the authority of differential lift, the two satellites are to rotate in opposite direction, while the magnitude of differential drag is defined by the difference between the absolute value of the commanded angles. A visualization of a simultaneous negative differential lift $\delta f_{L,z}$ in the $\hat{z}$ - direction and positive differential drag configuration for a 3U CubeSat created via yaw angle deviations $\delta\psi$ is displayed in Fig. 5.6.

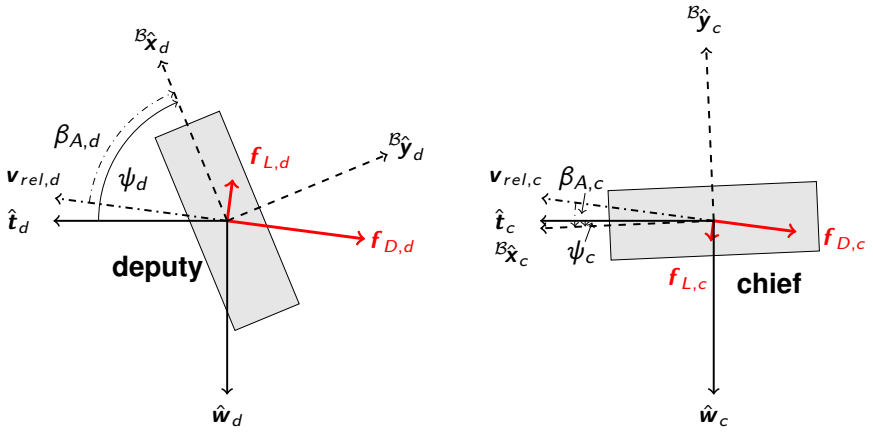

Figure 5.6: Visualization of a simultaneous negative differential lift $\delta f_{L,z}$ in the $\hat{z}$ - direction and positive differential drag configuration for a 3U CubeSat via yaw angle deviations $\delta\psi$.

5.2.2 Relative motion control via differential aerodynamic forces

Relative motion control via differential aerodynamic forces is introduced by referring to the forced CW equations including differential aerodynamic forces expressed the $\mathcal{L}$ - frame

$$\begin{aligned} \ddot{x} - 2n\dot{y} - 3n^2x &= \delta f_{L,x} \\ \ddot{y} + 2n\dot{x} &= \delta f_D \\ \ddot{z} + n^2 z &= \delta f_{L,z}, \end{aligned} \tag{5.2}$$

before these are put into context to $\delta\bar{\boldsymbol{\mathcal{E}}}_{ns}$. As the out-of-plane motion $(z,\ \dot{z})$ is decoupled from the in-plane motion $(x,\ y)$, the two control tasks can be handled separately.

In-plane relative motion control

Due to the coupled nature of the in-plane states, the motion can be altered either via differential lift $\delta f_{L,x}$ or drag δf_D. The coupled nature is caused by the fact that the orbital period P directly depends on the semi-major axis a, i.e., on the orbital radius in the circular orbit special case. Since aerodynamic drag dissipates energy from the satellite, it causes orbital decay while increasing the satellite's kinetic energy, a phenomena which is commonly referred to as *satellite drag paradox* [13]. With respect to the mean differential nearly-nonsingular orbital elements $\delta\bar{\boldsymbol{\mathcal{E}}}_{ns}$, this reflects itself in the coupling between the states δa and $\delta\lambda$, which represents the average in-plane motion. Although it can be influenced by both control forces, differential lift $\delta f_{L,x}$ and drag δf_D, the latter is clearly more influential due to its secular influence on δa. In descriptive terms, a spacecraft can catch up to another vehicle within its orbital plane by orbiting at a lower altitude. To stabilize the relative motion after the maneuver, i.e., to ensure a zero drift rate $v_d = 0\,\mathrm{m\,s^{-1}}$ via $\delta a = 0\,\mathrm{m}$, the second vehicle must lower its orbit accordingly, as the methodology does not provide a means to perform orbit raising. Superimposed to the average in-plane motion, an oscillating component δq_1 and δq_2, caused by differences in the eccentricities δe and arguments of perigee $\delta\omega$, is present, for which both control options represent a suitable means.

Out-of-plane relative motion control

The out-of-plane relative motion is of sinusoidal nature and follows the pattern of a harmonic oscillator. If a difference in the orientation of the orbital planes exists, both have a common line of intersection at which the residual out-of-plane distance is zero ($z = 0\,\mathrm{m}$, twice per orbit) whereas a maximum distance is reached quarter and three quarters of an orbit later ($|z| = z_{max} = \rho_z$). With respect to $\delta\bar{\boldsymbol{\mathcal{E}}}_{ns}$, the out-of-plane relative motion is a result of differences in the inclinations δi and in the ascending nodes $\delta\Omega$. Differences in inclination δi specify the out-of-plane distance as the satellite crosses the northern- or southernmost regions, whereas ascending node differences $\delta\Omega$ indicate the out-of-plane distance as the satellite crosses the equatorial plane [140]. Both, δi and $\delta\Omega$ can be altered solely by applying differential forces perpendicular to the orbital plane, which renders differential lift $\delta f_{L,z}$ the only suitable option to control the out-of-plane motion. Following the oscillating nature of the motion, the commanded differential lift force $\delta f_{L,z}$ must show alternating behavior and is required to change sign twice per orbit.

5.3 State-of-the-art

5.3.1 Literature review

Due to its promising benefits, differential drag methods have been investigated by different research groups worldwide since the pioneering work of Leonard [90] and have been demonstrated in-orbit[15]. To get a full picture of the developments and the current state-of-the-art, a comprehensive literature review has been published in 2020 [171]. Whereas the reader is advised to consult the original article for an overview of the historical developments in the field of differential drag[16], an up-to-date overview of the most important contributions in the field of differential lift and drag controlled SFF is included.

Analytic rendezvous algorithms

Horsley [62] and Horsley, Nikolaev, and Pertica [63] proposed to exploit differential lift as a means to control the out-of-plane motion in 2011. The proposed algorithms are based on the CW equations and the constant density assumption. In 2015, Shao et al. [152] replaced the CW equations with an intermediate set of the Schweighardt-Sedwick (SS) equations [145, 147] in order to account for the J_2 effect before in 2017, Smith et al. [156] rearranged the order in which rendezvous is achieved (to prevent collisions). In a more recent work, Smith [154] enabled simultaneous in- and out-of-plane control.

Sliding-mode and Lyapunov based control

In 2017, Shao et al. [151] presented a control approach based on Lyapunov principles [84] for the formation keeping task. In the same year, Sun et al. [160] investigated simultaneous translation

[15] In orbit demonstrations have been performed by the ORBCOMM constellation [92], the AeroCube-4 CubeSats [50], Planet Labs CubeSats constellation [45] and within the S-NET mission [194].

[16] Publications that have been identified upon completion of the article are: [5, 9, 16, 67, 70, 71, 72, 73, 110, 194].

and rotation control via sliding mode control. In follow-up publications, Sun et al. [158, 159] presented an adaptive neural networks-based sliding mode control method for the formation keeping task of spacecraft formation with coupled translational and rotational dynamics.

Linear-quadratic regulator (LQR) based control

In 2018, Ivanov, Kushniruk, and Ovchinnikov [69] presented a decentralized LQR based control algorithm for the formation reconfiguration task and for the maintenance task of a tetrahedral configuration [74]. In a follow up publication [75], the controller was applied to establish dedicated formation designs which provide graphic images in the sky visible from Earth. In the most recent publication [72], the control approach has been further refined and the influence of the initial launch conditions on the motion is studied. Only recently, Hu et al. [64] investigated the application of yaw angle deviation $\delta\psi$ to simultaneously control the in-plane and out-of-plane relative motion. For control of the in-plane motion, a LQR method is used to stabilize the system whereas a linear model predictive controller (MPC) is applied for the out-of-plane control.

Alternative propellant-less option

In literature, alternative options to either reduce or remove the need for on-board propellant have been proposed. These include *solar radiation pressure* [53, 85, 165, 180, 181, 192], *geomagnetic Lorentz forces* [66, 118, 127, 173, 161, 164, 163], *electromagnetic forces* [1, 2, 77, 81, 146], *inter-vehicle coulomb forces* [65, 80, 88, 133, 141] and *ionospheric drag forces* [154, 155].

5.3.2 Research gaps, goals and approach

Research gaps

In contrast to differential drag, for which considerable theoretical and practical progress has been made, differential lift was not considered until 2011, has received little attention since, and has not been applied or demonstrated in orbit. Therefore, a number of *research gaps* that need to be addressed to make the methodology a viable control option for future satellite missions have been identified:

- **Research gap #1:** So far, only the relative motion of generic satellite concepts with high area-to-mass ratios and a large number of external panels have been considered, which are not very realistic for a real-world application. Accordingly, the current state of knowledge of the available control forces as well as the resulting maneuver times is limited.
- **Research gap #2:** To date, there is little insight into how optimal three-dimensional control can be realized. This comprises primary research areas, such as optimal control profiles, but also an evaluation of secondary areas, such as optimal satellite designs. Furthermore, the question arises with respect to which parameter it should be optimized at all.
- **Research gap #3:** There is a lack of knowledge with regard to the influence of the aerodynamic characteristics of the satellites, of the dynamic variations in the atmospheric density as well as of more detailed effects, such as the atmospheric co-rotation with the Earth.

In summary, there is a lack of a comprehensive study that deals decidedly with the conception, the mathematical modeling and the subsequent analysis of a simultaneous exploitation of differential lift and drag for three-dimensional formation control purposes. In addition to these fundamentals, detailed considerations of aspects concerning real in-orbit demonstrations are still lacking (e.g. consideration of measurement errors (e.g. GPS sensor errors) or of communication as well as energy supply aspects). However, these aspects can only be worked out in a targeted manner once the fundamentals have successfully been established. Therefore, these are considered beyond the scope of this dissertation.

Research goals and approach

In line with the individual research gaps identified, the overall research goal of this thesis is to provide sound and comprehensive study, which is reflected in the governing research question as well as the sub-research questions defined in the introduction.

Research goal

The goal of this work is to provide a comprehensive and holistic
overall system view of the methodology of differential aerodynamic lift and drag.

The focus is on the maneuver planning process, which enables comprehensive system studies to investigate relationships between the satellite design, i.e., shape and surface material, the desired maneuver sequences, and a variety of external influencing factors.

However, although more advanced control methods have already been developed, rather simple (see e.g. the appraoch described by Yoon et al. [194]) control strategies have been applied for the in-orbit demonstrations in the field of differential drag to date. This is probably because the more advanced methods result in high demands in computing power which can hardly be met by the on-board resources of small satellites. To account for this, the maneuver planning efforts are subdivided into two complementary approaches:

1. **Maneuver planning tool for preliminary assessments:** In a first appraoach, existing shortcomings in the available analytic rendezvous algorithms are addressed and the applicability of the algorithms is extended to a variety of relevant formation flight cases. Ultimately, a flexible and powerful tool has been created, which is discussed in Chapter 6.
2. **Optimal maneuver planning:** In a second approach, a sophisticated and highly flexible planning tool for optimal and realistic maneuver sequences is developed. It allows for a simultaneous control of the in-plane and out-of-plane relative motion via differential drag and lift. The tool is discussed in detail in Chapter 7.

In the third part of this dissertation, ***analysis and optimization***, the developed approaches are applied within parameter studies to explore and outline the design space of possible maneuver variants and, thereby, to ultimately answering the guiding research question and the subquestions posed in the introductory section. Before the planning task of respective trajectories is addressed, however, *considerations with regard to practicability* are presented.

5.4 Considerations with regard to practicability

5.4.1 Maneuver objective

Optimal control aims to control the dynamical system within the maneuver time t_f from an initial state $\boldsymbol{x}_0$ to a desired final state $\boldsymbol{x}_f$ while minimizing a user-defined cost functional $\mathcal{J}(\boldsymbol{x}, \boldsymbol{u}, t_f)$. Regarding the differential drag methodology, different cost functionals have been proposed [37]:

- Oscillations $\left(\mathcal{J}_1(\boldsymbol{x}, \boldsymbol{u}, t_f) = \frac{1}{t_f} \int_0^{t_f} (\dot{r}_d - \dot{r}_c)^2 \, dt\right)$
- Differential drag $\left(\mathcal{J}_2(\boldsymbol{x}, \boldsymbol{u}, t_f) = \frac{1}{t_f} \int_0^{t_f} \delta f_D^2 \, dt\right)$

In addition, the maneuver time $\left(\mathcal{J}_3(\boldsymbol{x}, \boldsymbol{u}, t_f) = t_f\right)$ represents a natural choice. To date, however, optimal control theory has not been applied to minimize orbital decay during the maneuver, hereby defined as[17]

$$\Delta a = a_0 - a_f. \tag{5.3}$$

For satellites not equipped with any thrusting device, however, the orbital decay is the key determinant of the lifetime. Maneuver time, on the other hand, can be considered of secondary importance, as the methodology of differential aerodynamic forces is unlikely to be the preferred control option for time-critical maneuvers. Based on this reasoning, the following optimization goal is pursued throughout this dissertation:

Optimization goal
The optimization goal pursued throughout this dissertation is
the minimization of the resulting orbital decay during the maneuver.

This manifests itself in a holistic approach in which not only the maneuver trajectories but also the design of the satellites are optimized with this goal in mind. To the best of the authors' knowledge, this breaks completely new ground.

5.4.2 Further considerations

At this point, further considerations are made with respect to practicability. Whenever possible, the insights gained will be taken into account within the scope of this dissertation:

Attitude changes vs. external panels: Differential aerodynamic forces can be generated by changing the attitude of asymmetrically shaped satellites or by adjusting the orientation of external panels. While the latter strategy offers more flexibility, large external panels are uncommon for CubeSats, where solar panels are typically attached to the main body or deployed as needed. To account for this, satellite attitude adjustments are the control method of choice.

Bang-bang control pattern: Bang-bang patterns correspond to instantaneous changes in the attitude of the respective satellites. The highly accurate tracking of such a pattern places high demands on the attitude control system, and the pattern is not capable of providing two-sided maneuverability, so alternative control profiles are desired.

[17] Notably, Smith [154] already assessed the benefits of simultaneous differential lift and drag control in terms of a reduction in the specific mechanical energy loss.

Satellite parameters: The higher the area-to-mass ratio of the studied satellites, the higher the available control authority and the shorter the achievable maneuvering times. However, to obtain meaningful and representative results, ordinary 3U CubeSats augmented with folding panels serve as a basis within this work.

Proximity operations: The research presented in the literature to date has been almost exclusively limited to the special case of the rendezvous maneuver. While this serves as a well-defined example test case, close range maneuvers represent a very unlikely use case for differential drag and lift controlled SFF, since the underlying collision risk is caused by the dynamically varying control force, which is subject to a high degree of uncertainty. Therefore, alternative scenarios that avoid close proximity operations represent more realistic use cases for real mission scenarios. In this case, the control task is complicated as differential perturbations generally increase with the distance between the satellites.

Chapter 6

Fast and efficient maneuver planning

A common practice to schedule control patterns is via analytical algorithms based on linearized relative motion models and the assumption of a constant density. This trend was initiated by Leonard [90] and Leonard, Hollister, and Bergmann [91] in 1986 before Horsley [62] and Horsley, Nikolaev, and Pertica [63] proposed out-of-plane control via the introduction of differential lift in 2011. In 2015, the accuracy was increased by Shao et al. [152] by accounting for the J_2 effect before Smith et al. [156] presented an updated collision avoidance structure in 2017. While the accuracy of the resulting trajectories is limited, the algorithms provide an effective method for designing reference trajectories or estimating maneuver times. In addition, their computational efficiency allows the derivation of general results through the application of Monte Carlo methods. Thus, within this work, existing weaknesses of the original algorithms have been eliminated, new algorithms developed and the variety of feasible maneuvers has been significantly increased. Finally, the results of all efforts are bundled in a planning tool that allows for fast and efficient preliminary assessments of a variety of different maneuvers.

The contents of this chapter were developed in collaboration with Beck [8], Bühler [20], Friedrich [48], Homm [61], and Walther [188] and have been published in Refs. [22, 189].

6.1 Schweighardt-Sedwick equations

6.1.1 Differential form of the Schweighardt-Sedwick equations

To address the inaccuracy of the HCW equations arising from the non-spherical gravitational potential field, Schweighart and Sedwick [147] and Schweighart [145] developed a linear relative motion model, the so-called Schweighardt-Sedwick equations, that account for the J_2 effect. In analogy to Smith [154], the algorithms are based on predecessor to the final form of the equations in order to allow for a (largely) analytic treatment. Including specific differential aerodynamic forces ${}^{\mathcal{L}}\delta\boldsymbol{f}_A = (\delta f_{L,x}, \delta f_D, \delta f_{L,z})^T$, the differential equations are

$$\begin{aligned} \ddot{x} \; - \; 2(nc)\dot{y} \; - \; (5c^2 - 2)n^2 x &= \delta f_{L,x} \\ \ddot{y} + 2(nc)\dot{x} &= \delta f_{L,y} \\ \ddot{z} + (3c^2 - 2)n^2 z &= \delta f_{L,z}. \end{aligned} \tag{6.1}$$

Similar to the HCW equations, the chief spacecraft orbits the Earth in a circular orbit with a mean motion n and the co-rotational velocity of the Earth's atmosphere and thermospheric winds ($\boldsymbol{v}_{rot} = \boldsymbol{v}_w = \mathbf{0}\ \mathrm{m\,s^{-1}}$) are neglected. In Eq. 6.1, c is the so called Schweighardt-Sedwick coefficient defined as

$$c = \sqrt{1 + \frac{3J_2R_e^2}{8r_C^2}\left(1 + 3\cos(2i_C)\right)}. \tag{6.2}$$

In this case, the bounded relative orbit constraint to avoid secular drift is

$$\dot{y}_0 = -2ncx_0. \tag{6.3}$$

Notably, for $J_2 = 0$, the SS reduce to the HCW equations.

6.1.2 Solutions to the Schweighardt-Sedwick equations

Decomposing the in-plane motion into a double integrator modeling the average location of the deputy with respect to the chief $(\bar{x}, \bar{y})$ as well as a harmonic oscillator $\left(\alpha, \frac{\beta}{\sqrt{2cA_s}}\right)$ (see Fig. 6.1), the solutions to Eqs. 6.1 are

$$x(t) = \bar{x}(t) + \alpha(t), \tag{6.4}$$

$$y(t) = \bar{y}(t) + \beta(t), \tag{6.5}$$

$$z(t) = \left(z_0 - \frac{\delta f_{L,z}}{D_s^2 n^2}\right)\cos(D_s nt) + \frac{\dot{z}_0}{D_s n}\sin(D_s nt) + \frac{\delta f_{L,z}}{D_s^2 n^2}, \tag{6.6}$$

with $\bar{x}(t)$, $\bar{y}(t)$, $\alpha(t)$ and $\beta(t)$ being defined as

$$\bar{x}(t) = \bar{x}_0 + \frac{A_s}{n}\delta f_D t, \tag{6.7}$$

$$\bar{y}(t) = \bar{y}_0 + B_s n\bar{x}_0 t - \frac{A_s}{n}\delta f_{L,x} t + \frac{A_s B_s}{2}\delta f_D t^2, \tag{6.8}$$

$$\alpha(t) = \left(\alpha_0 - \frac{A_s\delta f_{L,x}}{2cn^2}\right)\cos\left(\sqrt{\frac{2c}{A_s}}nt\right) + \left(\frac{\beta_0}{\sqrt{2cA_s}} - \frac{A_s^2\delta f_D}{2n^2}\right)\sin\left(\sqrt{\frac{2c}{A_s}}nt\right) + \frac{A\delta f_{L,x}}{2cn^2}, \tag{6.9}$$

$$\frac{\beta(t)}{\sqrt{2cA_s}} = \left(\frac{\beta_0}{\sqrt{2cA_s}} - \frac{A_s^2\delta f_D}{2n^2}\right)\cos\left(\sqrt{\frac{2c}{A_s}}nt\right) + \left(\frac{A_s\delta f_{L,x}}{2cn^2} - \alpha_0\right)\sin\left(\sqrt{\frac{2c}{A_s}}nt\right) + \frac{A_s^2\delta f_D}{2n^2}, \tag{6.10}$$

and the coefficients A_s, B_s and D_s as

$$A_s = \frac{2c}{2 - c^2}, \tag{6.11}$$

$$B_s = \frac{2 - 5c^2}{2c}, \tag{6.12}$$

$$D_s = \sqrt{3c^2 - 2}. \tag{6.13}$$

The initial conditions are given by $\bar{x}_0$, $\bar{y}_0$, z_0, α_0, $\frac{\beta_0}{\sqrt{2cA_s}}$ and $\frac{\dot{z}_0}{D_s\omega}$.

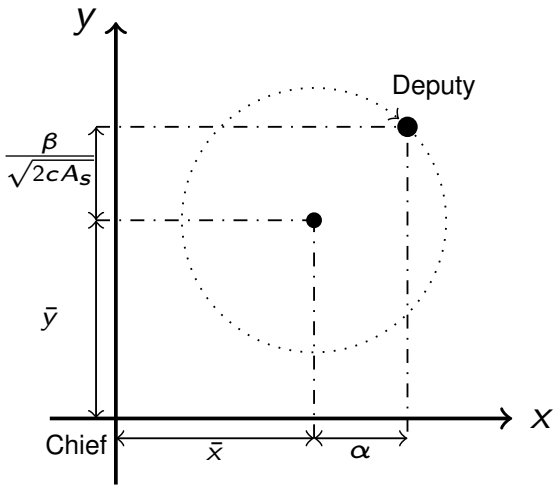

Figure 6.1: Graphical visualization of the decomposition of the in-plane relative state (x, y) into an average offset $(\bar{x}, \bar{y})$ as well as an harmonic oscillator $\left(\alpha, \frac{\beta}{\sqrt{2cA_s}}\right)$.

Polar representation of the oscillating states

Due to the harmonic nature of the oscillating states, it lends itself to express the $\left(\alpha, \frac{\beta}{\sqrt{2cA_s}}\right)$-states in polar coordinates $\left(e_{ip}, \theta_{ip}\right)$ where e_{ip}, in literature commonly referred to as the in-plane eccentricity, is the vector norm

$$e_{ip} = \sqrt{\alpha^2 + \left(\frac{\beta}{\sqrt{2cA_s}}\right)^2} \tag{6.14}$$

and $\theta_{ip} \in [0, 2\pi)$ represents the phase angle

$$\theta_{ip} = \tan^{-1}\left(\frac{\alpha\sqrt{2cA_s}}{\beta}\right). \tag{6.15}$$

If no control force is applied, the states circles around $(\bar{x}, \bar{y})$ at a constant distance of e_{ip} in a stable motion with a period of

$$T_{ip} = \frac{2\pi}{n}\sqrt{\frac{A_s}{2c}}. \tag{6.16}$$

Similarly, the harmonic oscillating out-of-plane motion (z,$\dot{z}$) can be scaled and transformed to a polar state representation $\left(e_{op}, \theta_{op}\right)$, where the out-of-plane eccentricity e_{op} is defined as

$$e_{op} = \sqrt{z^2 + \left(\frac{\dot{z}}{D_s n}\right)^2} \tag{6.17}$$

and the respective phase angle as $\theta_{op} \in [0, 2\pi)$

$$\theta_{op} = \tan^{-1}\left(\frac{zD_s n}{\dot{z}}\right). \tag{6.18}$$

To determine θ_{ip} and θ_{op}, the four-quadrant inverse tangent needs to be calculated, e.g. via MATLAB®'s *atan2* function [101]. The angles are defined in a mathematical negative sense to

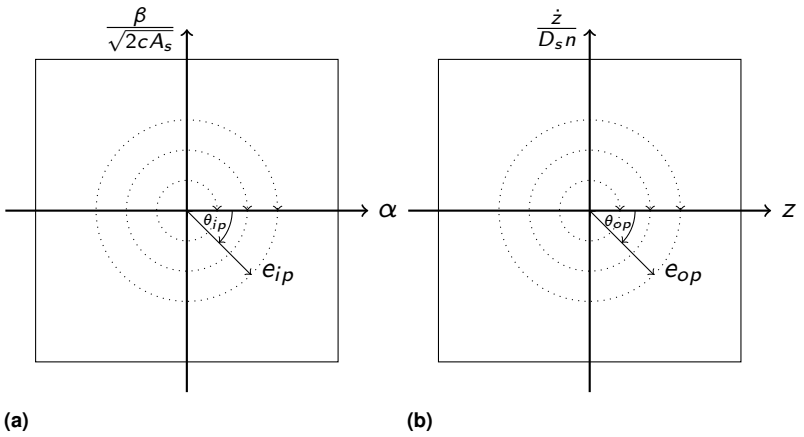

Figure 6.2: Graphical representation of the polar coordinates (e_{ip}, θ_{ip}) and (e_{op}, θ_{op}). If no control force is applied, the states coast along the dashed circles around the origin.

take the dynamic motion of the states into consideration. The period of the harmonic out-of-plane oscillation is

$$T_{op} = \frac{2\pi}{D_s n}. \tag{6.19}$$

Notably, T_{ip} and T_{op} match in the case of the HCW-equations ($c = 0$) but differ when accounting for the J_2 - effect. This causes any formation designs to deteriorate over time if no adequate means of control is applied.

Influence of control forces on the phase planes

The following elaboration of the algorithms is based on the assumption that the control forces in each of the three directions can take only one of the three following discrete states: maximum positive, maximum negative or zero, i.e. that the control is of *bang-bang type*. The influence of these constant specific differential lift and drag forces on the phase planes is displayed in Fig. 6.3. A differential lift force in the radial direction $\delta f_{L,x}$ shifts the center of the circular motion in the $\left(\alpha, \frac{\beta}{\sqrt{2cA_s}}\right)$ - plane by k_α in the α - direction:

$$k_\alpha = \frac{A_s^2 \delta f_{L,x}}{2cn^2}. \tag{6.20}$$

At the same time, this results in a secular variation on $\bar{y}$ which is proportional to the magnitude of $\delta f_{L,x}$. With no force being applied, the $\left(\alpha, \frac{\beta}{\sqrt{2cA_s}}\right)$ - states circulate around the origin at a distance of e_{ip} in a stable motion, which is depicted in Fig. 6.2. A differential drag force δf_D causes the $(\bar{x}, \bar{y})$ - state to move along the depicted parabolas in the phase plane. The parabolas passing through the origin are called switch curves, which are well-known from the time optimal control of a double integrator. At the same time, the force causes the state in the $\left(\alpha, \frac{\beta}{\sqrt{2cA_s}}\right)$ - plane to follow a circular motion with the circle's center being shifted in $\frac{\beta}{\sqrt{2cA_s}}$ - direction by

$$k_\beta = \frac{A_s^2 \delta f_D}{2n^2}. \tag{6.21}$$

As the out-of-plane motion is completely decoupled from the in-plane motion, differential lift $\delta f_{L,z}$ does not interfere with the in-plane motion and, vice versa, any in-plane control has no effects on the out-of-plane motion. Consequently, for a differential lift force $\delta f_{L,z}$, only the $\left(z, \frac{\dot{z}}{D_s n}\right)$ - plane is of interest. In this case, the centers of the circular motion are shifted by k_z along the z - axis:

$$k_z = \frac{\delta f_{L,z}}{(nD_s)^2}. \tag{6.22}$$

Notably, Fig. 6.3 displays the influence of *constant* differential forces, which cause the circles in the respective phase planes to be concentric. For varying forces, the centers of the respective circles shift accordingly.

6.2 Original three phased rendezvous algorithm

The original algorithm, which aims to achieve rendezvous between a deputy and a chief spacecraft, is divided into three separate control phases [62, 63, 152]. As the original control sequence inevitably causes collisions, Smith et al. [156] changed the order of the control phases. Accordingly, the following nomenclature is used throughout the remainder of this dissertation:

- **Phase #1**: Regulation of the $(\bar{x}, \bar{y})$ - states via differential drag (δf_D) .
- **Phase #2**: Regulation of the $\left(z, \frac{\dot{z}}{D_s n}\right)$ - states via differential lift $(\delta f_{L,z})$.
- **Phase #3**: Regulation of the $\left(\alpha, \frac{\beta}{\sqrt{2cA_s}}\right)$ - states via differential drag (δf_D) or lift $(\delta f_{L,x})$.

6.2.1 Phase #1: Regulation of the average in-plane states

In phase #1, the in-plane states $(\bar{x}, \bar{y})$ are regulated via differential drag and the well-known time-optimal solution for a double integrator. In a first step, the control force is applied for a time duration of $t_{P1,1}$ to guide states on a parabola towards the nearest switch curve (SC). Once this is reached, the direction of the control force is reversed for $t_{P1,2}$ to follow the SC into the origin. Which one of the two switch curves (positive or negative drag force) is the nearest depends on the region R_0 (see Fig. 6.3) in which the initial state $(\bar{x}_0, \bar{y}_0)$ is located in. If $R_0 = \text{A}$ ($R_0 = \text{B}$), the state is guided with a positive (negative) differential drag to the SC, where the commanded differential drag is reversed. The respective times $t_{P1,1}$ and $t_{P1,2}$ can be calculated via

$$t_{P1,1} = \delta_{SC} \frac{n}{A_s \delta f_D} \left(\bar{x}_{sc} - \bar{x}_0\right), \tag{6.23}$$

$$t_{P1,2} = \delta_{SC} \frac{n}{A_s \delta f_D} \bar{x}_{sc}. \tag{6.24}$$

$\bar{x}_{sc}$ represents the $\bar{x}$ - coordinate of the switch curve

$$\bar{x}_{sc} = \delta_{SC} \sqrt{\frac{A_s \delta f_D}{B_s n^2} \left(\frac{B_s n^2}{2 A_s \delta f_D} \bar{x}_0^2 - \bar{y}_0\right)} \tag{6.25}$$

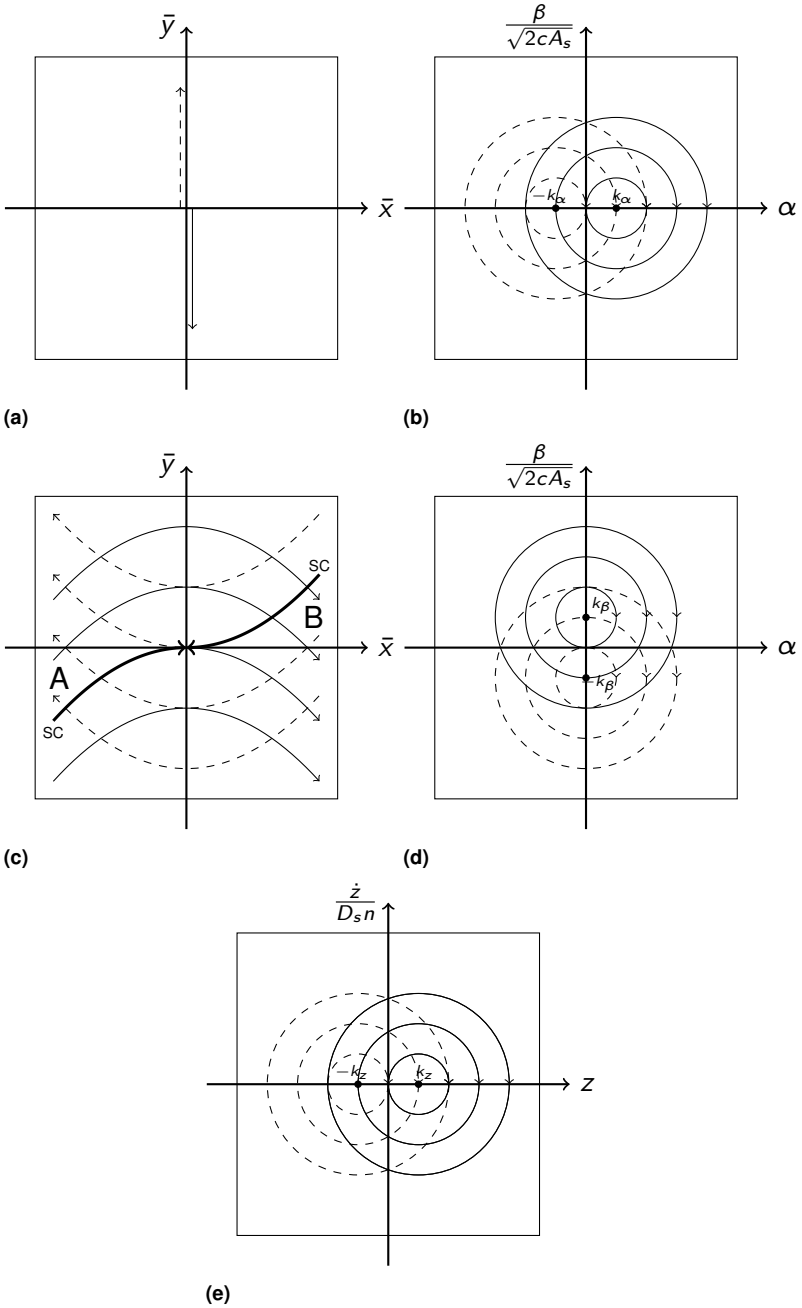

Figure 6.3: Phase plane for constant differential accelerations in all three $\mathcal{L}$-directions. A positive (negative) acceleration causes the state to move along the solid (dashed) trajectories.

and δ_{SC} accounts for the region R_0 (see Fig. 6.3):

$$\delta_{SC} = \begin{cases} +1 & R_0 = \text{A} \\ -1 & R_0 = \text{B}. \end{cases} \tag{6.26}$$

6.2.2 Phase #2: Regulation of the out-of-plane states

In the second phase, the out-of-plane states $\left(z_0, \frac{\dot{z}_0}{D_s n}\right)$ are regulated via differential lift $\delta f_{L,z}$. To do so, the deputy is guided from the initial state $\left(z_0, \frac{\dot{z}_0}{D_s n}\right)$ to a point on the z - axis $(z_{alt}, 0\,\text{m})$ with a predefined out-of-plane eccentricity of

$$e_{op,N} = z_{alt} = K_{op} \Delta e_{op,T_{op}}. \tag{6.27}$$

$\Delta e_{op,T_{op}}$ is the amount by which the out-of-plane eccentricity e_{op} can be reduced during a single orbital period T_{op} by an alternating differential lift force pattern in which the sign of $\delta f_{L,z}$ is switched whenever $\dot{z}$ switches sign, which is twice per orbit. A positive (negative) differential force is applied whenever $\dot{z} < 0$ ($\dot{z} > 0$). A value for $\Delta e_{op,T}$ can be calculated via

$$\Delta e_{op,T} = \frac{4 \delta f_{L,z}}{C_s^2 n^2}. \tag{6.28}$$

The alternating pattern has to be applied for a discrete number of K_{op} orbital revolutions until the states are completely zeroed out. Before the alternating sequence can be initiated, the initial states $\left(z_0, \frac{\dot{z}_0}{D_s n}\right)$ have to be guided to one of the possible starting points $\left(\pm K_{op} \Delta e_{op,T}, 0\,\text{m}\right)$ first. This can be achieved by a sequence of three consecutive phases: an initial coasting phase of $t_{P2,c}$, followed by two forced phases with reversed control force directions but a similar duration $t_{P2,I}$. Values for the required times $t_{P2,c}$ and $t_{P2,I}$ as well as the number of orbital revolutions K_{op} can be found by working backwards starting from the origin. The number of iterations K_{op} can be determined via

$$K_{op} = \left\lfloor \frac{e_{op,0}}{\Delta e_{op,T}} \right\rfloor. \tag{6.29}$$

The time $t_{P2,I}$ is found by numerically solving for the time required to guide the deputy from $\left(\pm K_{op} \Delta e_{op,T}, 0\,\text{m}\right)$ to an intermediate state $\left(z', \frac{\dot{z}'}{D_s n}\right)$, for which the in-plane eccentricity e'_{op} matches the initial value $e_{op,0}$. Notably, four different options can be envisaged as both possible points on the z - axis $\left(\pm K_{op} \Delta e_{op,T}, 0\,\text{m}\right)$ can be reached via a positive/negative (pn) or negative/positive (np) control sequence. To ensure a shortest overall maneuver duration, the respective times are calculated for all four possible options and the sequence with the shortest overall duration is used. Exemplary, the equation which has to be solved for a pn-sequence to $\left(+K_{op} \Delta e_{op,T}, 0\,\text{m}\right)$ is

$$e_{op,0} = \left(\left(\left(nk_{op} + \frac{k_{op}}{4} \right) \left(\cos\left(t_{P2,I} C_s n\right)^2 - \sin\left(t_{P2,I} C_s n\right)^2 \right) + \frac{k_{op}}{4} \left(1 - 2\cos\left(t_{P2,I} C_s n\right)\right) \right)^2 \dots \right.$$
$$\left. \dots + \left(2 \left(nk_{op} + \frac{k_{op}}{4} \right) \sin\left(t_{P2,I} C_s n\right) \cos\left(t_{P2,I} C_s n\right) - \frac{k_{op}}{2} \sin\left(t_{P2,I} C_s n\right) \right)^2 \right)^{\frac{1}{2}}. \tag{6.30}$$

In a last step, the time $t_{P2,c}$ to coast from the initial state $\left(z_0, \frac{\dot{z}_0}{D_s n}\right)$ to the intermediate state $\left(z', \frac{\dot{z}'}{D_s n}\right)$ needs to be determined via

$$t_{P_{2,1}} = \frac{\delta\theta_{c,op}}{D_s n}, \tag{6.31}$$

where $\delta\theta_{c,op}$ is the angular difference the deputy has to cover via coasting:

$$\delta\theta_{c,op} = \theta'_{op} \; - \; \theta_{op,0}. \tag{6.32}$$

Here, since $\theta_{c,op} \in [0, 2\pi)$ but $\frac{d\theta_{c,op}}{dt} \geq 0$, $\theta'_{op} = \theta'_{op} + 2\pi$ if $\theta'_{op} < \theta_{op,0}$.

6.2.3 Phase #3: Regulation of the oscillating in-plane states

In the third phase, the remaining in-plane eccentricity $e_{ip,0}$ is zeroed out via differential lift $\delta f_{L,x}$ or drag δf_D, respectively. As any in-plane control input also influences the $(\bar{x}, \bar{y})$ - plane, it needs to be ensured that the average in-plane states after the phase (subscript f) are zero again ($\bar{x}_f = \bar{y}_f = 0\,\mathrm{m}$). This can be achieved if the overall duration during which a positive differential force is commanded (t_+) matches the duration during which a negative force (t_-) is commanded:

$$\sum t_+ = \sum t_-. \tag{6.33}$$

Drag-based algorithm

The drag-based phase #3 control algorithm consists of an initial coasting period followed by three successive controlled segments during which differential drag forces are applied. The times of the three controlled segments are referred to as $t_{P3,d,1}$, $t_{P3,d,2}$ and $t_{P3,d,3}$ whereas the coasting period is referred to as $t_{P3,d,c}$. Depending on the initial states, either a positive/negative/positive (pnp) or negative/positive/negative (npn) control sequence leads to the shorter maneuver time. Since any drag control input direction causes the $(\bar{x}, \bar{y})$ - states to move on the parabola in the phase plane, the following conditions for the time periods must hold to fulfill Eq. 6.33:

$$t_{P3,d,1} \; - \; t_{P3,d,3} = 0\,\mathrm{s}, \tag{6.34}$$

$$t_{P3,d,2} \; - \; 2t_{P3,d,1} = 0\,\mathrm{s}. \tag{6.35}$$

As a consequence, it is sufficient to determine one of the three time periods and to determine the two others via Eqs. 6.34 and 6.35. Before the control sequence is initiated, a coasting period, in which no control input is commanded, is required. The four time periods are determined by applying a backwards sequence starting from the origin of the $\left(\alpha, \frac{\beta}{\sqrt{2cA_s}}\right)$ - phase plane and enforcing the final eccentricity after the controlled sequence to match the initial eccentricity $e_{ip,0}$. Whereas the technique of applying a backwards sequence to solve for the maneuver time and/or position has already been described by Smith [156], the equation which has to be solved for $t_{P3,d,1}$ has, to the authors knowledge, never appeared in the literature. For a pnp sequence, applying a backwards sequence of phase #3 maneuvers sequence results in Eq. 6.36 which needs to be solved for $\theta_{ip,d,1}$:

$$\begin{aligned} e_{ip,0} = \Bigg(\Bigg(& 2k_\beta \sin\left(\theta_{ip,d,1}\right) - 2k_\beta \sin\left(3\theta_{ip,d,1}\right) + k_\beta \cos\left(2\theta_{ip,d,1}\right) \sin\left(2\theta_{ip,d,1}\right) \dots \\ & \dots + k_\beta \sin\left(\theta_{ip,d,1}\right) \left(\cos^2\left(\theta_{ip,d,1}\right) - \sin^2\left(\theta_{ip,d,1}\right)\right) \Bigg)^2 \dots \\ & \dots + 4k_\beta^2 \Bigg(\frac{1}{2} \sin\left(\theta_{ip,d,1}\right) + \cos\left(3\theta_{ip,d,1}\right) - \cos\left(\theta_{ip,d,1}\right) \dots \\ & \dots - \frac{1}{2} \left(\cos\left(2\theta_{ip,d,1}\right) \left(\cos^2\left(\theta_{ip,d,1}\right) - \sin^2\left(\theta_{ip,d,1}\right)\right) \right) + \frac{1}{2} \Bigg)^2 \Bigg)^{\frac{1}{2}}. \end{aligned} \tag{6.36}$$

In a next step, the desired time $t_{P3,d,1}$ can be determined via

$$t_{P3,d,1} = \frac{\theta_{ip,d,1}}{n} \sqrt{\frac{A_s}{2c}}. \tag{6.37}$$

To determine the required coasting time $t_{P3,d,c}$, the coasting angle $\delta\theta_{c,ip,d}$ needs to be calculated first. In analogy to Eq. 6.38, this is defined as

$$\delta\theta_{c,ip,d} = \theta'_{ip} - \theta_{ip,0}. \tag{6.38}$$

In case of the in-plane motion, the respective coasting time $t_{P3,d,c}$ for a coasting angle of $\delta\theta_{c,ip,d}$ can be calculated via

$$t_{P3,d,c} = \frac{\delta\theta_{c,ip,d}}{n} \sqrt{\frac{A_s}{2c}}. \tag{6.39}$$

Here, since $\delta\theta_{c,ip,d} \in [0, 2\pi)$ but $\frac{d\delta\theta_{c,ip,d}}{dt} \geq 0$, $\theta'_{ip} = \theta'_{ip} + 2\pi$ if $\theta'_{ip} < \theta_{ip,0}$.

Lift-based algorithm

The lift-based phase #3 algorithm also consists of a set of three control inputs (pnp or npn) during which differential lift forces $\delta f_{L,x}$ are applied. The times of the controlled segments are $t_{P3,l,1}$, $t_{P3,l,2}$ and $t_{P3,l,3}$. To fulfill Eq. 6.33, the individual duration must be compliant with the following condition:

$$t_{P3,l,1} - t_{P3,l,2} + t_{P3,l,3} = 0\,\text{s}. \tag{6.40}$$

Table 6.1: Initial relative conditions of the reference maneuver published by Shao et al. [152].

x_0 (m)	y_0 (m)	z_0 (m)	$\dot{x}_0$ $\left(\mathrm{m\,s^{-1}}\right)$	$\dot{y}_0$ $\left(\mathrm{m\,s^{-1}}\right)$	$\dot{z}_0$ $\left(\mathrm{m\,s^{-1}}\right)$
82.50	-930.46	55.27	-0.17	-0.04	0.29

The times are determined by applying a backwards sequence from the origin. As $t_{P3,I,1}$ can differ from $t_{P3,I,3}$ due to the less restrictive condition stated in Eq. 6.40, two time periods have to be determined. For a pnp maneuver sequence, applying the backwards maneuver sequence results in the following system of equations which has to be solved for $\theta_{ip,I,1}$ and $\theta_{ip,I,3}$:

$$\alpha_{P3,0} = \left(2\cos\left(\theta_{ip,I,3}+2\theta_{ip,I,1}\right) - \cos\left(2\theta_{ip,I,3}+2\theta_{ip,I,1}\right) - 2\cos\left(\theta_{ip,I,1}\right)+1\right)\frac{A_s\delta f_{L,x}}{2cn^2}, \tag{6.41}$$

$$\frac{\beta_{P3,0}}{\sqrt{2cA_s}} = \left(2\sin\left(\theta_{ip,I,3}+2\theta_{ip,I,1}\right) - \sin\left(2\theta_{ip,I,3}+2\theta_{ip,I,1}\right) - 2\sin\left(\theta_{ip,I,1}\right)\right)\frac{A_s\delta f_{L,x}}{2cn^2}. \tag{6.42}$$

Finally, the respective times $t_{P3,I,1}$ and $t_{P3,I,3}$ can be determined via

$$t_{P3,I,i} = \frac{\theta_{ip,I,i}}{n}\sqrt{\frac{A_s}{2c}}. \tag{6.43}$$

Due to the much weaker symmetry constraints, no coasting segment is required and the maneuver can be executed immediately.

6.2.4 Verification

To verify the implementation of the original algorithms, the results for an example maneuver published by Shao et al. [152] are compared to the results published by [156]. The resulting maneuver times for each control phase are shown in Tab. 6.3 and show an excellent agreement. For the second control phase (referring to the original designation of Shao et al. [152]), the drag-based algorithm has been applied. The subphases of phase #3 (Shao et al. [152]) are defined in analogy to the work of Smith et al. [156]. The initial relative conditions and the boundary conditions are listed in Tabs. 6.1 and 6.2.

6.3 Modifications to the original algorithms

6.3.1 Modified phase #1: Adjustment of the average in-plane states

In order to account for the considerations on practicability and to avoid close proximity maneuvers, the original phase #1 algorithm is extended to enable the establishment of a stable in-plane formation (IPF) at an average offset of $\bar{y}_{IPF}$. To do so, an updated switch curve needs to be

Table 6.2: Boundary conditions of the reference maneuver published by Shao et al. [152].

Parameter	Unit	Value
r_c	m	6778137
i_c	°	10
J_2	-	0.0010826267
$\delta f_{L,x}$	$\mathrm{m\,s^{-2}}$	$0.9 \cdot 10^{-5}$
δf_D	$\mathrm{m\,s^{-2}}$	$4.0 \cdot 10^{-5}$
$\delta f_{L,z}$	$\mathrm{m\,s^{-2}}$	$0.9 \cdot 10^{-5}$

Table 6.3: Calculated control phase times for the reference maneuver published by Shao et al. [152].

Phase	**Shao et al.** [152]	**Smith et al.** [156]	**This work**
Phase $\#1_{Shao}$	10586.72 s	10586.72 s	10586.73 s
Phase $\#2_{Shao}$	4778.56 s	Not specified	4819.80 s
Phase $\#3.1_{Shao}$	1585.91 s	1544.68 s	1544.71 s
Phase $\#3.2_{Shao}/3.3_{Shao}$	1791.66 s	1791.65 s	1791.65 s
$\sum$ Phase $\#3_{Shao}$	55046.23 s	Not specified	55008.06 s
Overall maneuver	70414.51 s	70414.55 s	70414.59 s

targeted. In accordance with Eq. 6.25, $\bar{x}_{sc,IPF}$ can be determined for an in-plane offset of $\bar{y}_{IPF}$ via

$$\bar{x}_{sc,IPF} = \delta_{SC}\sqrt{\frac{A_s\delta f_D}{B_s n^2}\left(\frac{B_s n^2}{2A_s\delta f_D}\bar{x}_0^2 - \bar{y}_0 + \bar{y}_{IPF}\right)}. \tag{6.44}$$

Apart from this adaptation, the procedure of the original algorithm remains unchanged.

6.3.2 Modified phase #2: Regulation of the out-of-plane states

With respect to phase #2, a modified algorithm to zero out the out-of-plane relative states has been developed which, in a vast majority of cases, results in a shorter phase #2 maneuver time [189]. Whereas the general idea of the algorithm of Horsley [62] is adopted, the modified version is able to bypass the initial coasting period. It is obsolete as the sign of the differential force $\delta f_{L,z}$ required to reduce the out-of-plane eccentricity is ad hoc defined by the sign of $\dot{z}_{P2,0}$. Consequently, the modified algorithm immediately applies a positive (negative) control force $\delta f_{L,z}$ if $\dot{z}_{P2,0} < 0$ ($\dot{z}_{P2,0} > 0$) for a period of $t_{P2,1}$ after which the deputy intersects the z - axis at $(z_{P2,1}, 0\,\mathrm{m})$. As in the original algorithm, the control is reversed in an alternating fashion whenever $\dot{z}$ switches signs until the following condition holds (at $t_{P2,2}$ and $(z_{P2,2}, 0\,\mathrm{m})$):

$$|z_{P2,2}| \leq 2k_{op}. \tag{6.45}$$

Once the desired location $(z_{P2,2}, 0\,\mathrm{m})$ is reached, the sign of the current control force is maintained for an additional time period $t_{P2,3}$ until the state intersects one of the two semicircles

leading into origin at $\left(z_{P2,3}, \frac{\dot{z}_{P2,3}}{D_s n}\right)$. Once the respective point of intersection is reached, the control force is reversed for $t_{P2,4}$ to guide the deputy along the semicircle into the origin.

Close case: If the initial position is already within one of the two semicircles which pass through the origin, sub-phase one and two can be skipped ($t_{P2,1} = t_{P2,2} = 0\,\mathrm{s}$) and $t_{P2,3}$ and $t_{P2,4}$ can be calculated by applying a backward sequence from the origin.

6.3.3 Modified phase #3: Regulation of the oscillating in-plane states

By applying Monte Carlo methods, Smith et al. [156] discovered that the phase #3 algorithm is successful if and only if the initial in-plane eccentricity $e_{ip,0}$ is within a certain range, the so-called *feasibility range*[18]. If the initial eccentricity exceeds this range, the algorithm is not able to fully regulate the $\left(\alpha, \frac{\beta}{\sqrt{2cA_s}}\right)$ - states and the maneuver fails. In the following, modified phase #3 algorithms which are not subjected to any limiting size are presented. These have been developed by Bühler et al. [22].

Feasibility range determination

In this section, a fast and precise method to determine the size of the feasibility range $\Delta e_{ip,max}$ for differential drag and lift, which is required for the modified algorithm, is presented.

Differential drag δf_D: For differential drag, the desired value for $\Delta e_{ip,max,d}$, i.e. the size of the feasibility range for differential drag, can be calculated by maximizing the following function:

$$\Delta e_{ip,d}\left(\theta_{ip,d,1}\right) = \sqrt{\Delta\alpha_d\left(\theta_{ip,d,1}\right)^2 + \left(\frac{\Delta\beta_d\left(\theta_{ip,d,1}\right)}{\sqrt{2cA_s}}\right)^2}. \tag{6.46}$$

For an pnp maneuver sequence, $\Delta\alpha_l\left(\theta_{ip,d,1}\right)$ and $\Delta\beta_l\left(\theta_{ip,d,1}\right)$ can be expressed via

$$\begin{aligned}
&\Delta\alpha_d\left(\theta_{ip,d,1}\right) = \\
&\Bigg(2k_\beta \sin\left(\theta_{ip,d,1}\right) - 2k_\beta \sin\left(3\theta_{ip,d,1}\right) + k_\beta \cos\left(2\theta_{ip,d,1}\right)\sin\left(2\theta_{ip,d,1}\right) \ \ldots \\
&\ldots + k_\beta \sin\left(\theta_{ip,d,1}\right)\left(\cos^2\left(\theta_{ip,d,1}\right) - \sin^2\left(\theta_{ip,d,1}\right)\right),
\end{aligned} \tag{6.47}$$

$$\begin{aligned}
&\frac{\Delta\beta_d\left(\theta_{ip,d,1}\right)}{\sqrt{2cA_s}} = \\
&2k_\beta\Bigg(\frac{1}{2}\sin\left(\theta_{ip,d,1}\right) + \cos\left(3\theta_{ip,d,1}\right) - \cos\left(\theta_{ip,d,1}\right) \ \ldots \\
&\ldots\frac{1}{2}\left(\cos\left(2\theta_{ip,d,1}\right)\left(\cos^2\left(\theta_{ip,d,1}\right) - \sin^2\left(\theta_{ip,d,1}\right)\right)\right) + \frac{1}{2}\Bigg).
\end{aligned} \tag{6.48}$$

[18] Throughout this dissertation the terminology *feasibility range* refers to the maximum value of the initial eccentricity of phase #3 $\Delta e_{ip,max}$ for which the original algorithm leads to a successful rendezvous. As phase #3 can be controlled either via differential lift or drag, two different feasibility ranges need to be distinguished.

Table 6.4: Feasibility range comparison for differential drag.

Reference	$\Delta e_{max,d}$ Monte Carlo	$\Delta e_{max,d}$ Calculated
Walther et al. [189]	$\approx$ 326m	326.1m
Smith et al. [156]	$\approx$ 396m	396.7m
Bühler et al. [22]	$\approx$ 358m	357.7m

Throughout this dissertation, the respective value $\theta_{ip,d,1,max}$ is determined using MATLAB®'s *fminsearch* function [102]. From Eq. 6.46, it follows that the size is dependent on δf_D,c and n. From $\theta_{ip,1,max}$, the respective time $t_{P3,d,1,max}$ can be calculated from Eq. 6.37. The required phase angles $\theta_{0,\Delta e_{ip,max,d}}$, from which the maneuver has to be initiated, can be calculated via

$$\theta_{0,\Delta e_{ip,max,d}} = \tan^{-1}\left(\frac{\Delta\alpha_d\left(\theta_{ip,d,1,max}\right)\sqrt{2cA_s}}{\Delta\beta_d\left(\theta_{ip,d,1,max}\right)}\right). \tag{6.49}$$

Due to the symmetry of the two different possible sequences (pnp/npn), the complementary angle can simply be determined by adding π. In a last step, the final phase angle after an iteration $\theta_{f,\Delta e_{ip,max,d}}$ of both sequences (pnp/npn) is determined by applying a forward sequence from an auxiliary state $\left(e_{aux,d}, \theta_{0,\Delta e_{ip,max,d}}\right)$ with arbitrary eccentricity $e_{aux,d}$ larger than $\Delta e_{ip,max,d}$. Again, the complementary angle can be calculated taking advantage of the symmetry of the two different sequences (pnp/npn). In Tab. 6.4, the calculated feasibility ranges for differential drag are verified via a comparison with values extracted from literature, showing an excellent agreement.

Differential lift $\delta f_{L,x}$: In case of differential lift, the maximum possible reduction in in-plane eccentricity $\Delta e_{ip,max,l}$, i.e. the feasibility range for differential lift, can be calculated by maximizing the following equation:

$$\Delta e_{ip,l}\left(\theta_{ip,l,1},\theta_{ip,l,3}\right) = \sqrt{\Delta\alpha_l\left(\theta_{ip,l,1},\theta_{ip,l,3}\right)^2 + \left(\frac{\Delta\beta_l\left(\theta_{ip,l,1},\theta_{ip,l,3}\right)}{\sqrt{2cA_s}}\right)^2}. \tag{6.50}$$

For an pnp maneuver sequence, $\Delta\alpha_l\left(\theta_{ip,l,1},\theta_{ip,l,3}\right)$ and $\Delta\beta_l\left(\theta_{ip,l,1},\theta_{ip,l,3}\right)$ can be calculated via

$$\begin{aligned}&\Delta\alpha_l\left(\theta_{ip,l,1},\theta_{ip,l,3}\right) = \\ &\left(2\cos\left(\theta_{ip,l,3}+2\theta_{ip,l,1}\right) - \cos\left(2\theta_{ip,l,3}+2\theta_{ip,l,1}\right) - 2\cos\left(\theta_{ip,l,1}\right)+1\right)\frac{k_\alpha}{A_s},\end{aligned} \tag{6.51}$$

$$\begin{aligned}&\frac{\Delta\beta_l\left(\theta_{ip,l,1},\theta_{ip,l,3}\right)}{\sqrt{2cA_s}} = \\ &\left(2\sin\left(\theta_{ip,l,3}+2\theta_{ip,l,1}\right) - \sin\left(2\theta_{ip,l,3}+2\theta_{ip,l,1}\right) - 2\sin\left(\theta_{ip,l,1}\right)\right)\frac{k_\alpha}{A_s}.\end{aligned} \tag{6.52}$$

The value of $\Delta e_{ip,max,l}$ is dependent on $\delta f_{L,x}$, c and n. Again, the respective times $t_{P3,l,1,max}$

Table 6.5: Feasibility range comparison for differential lift.

Reference	$\Delta e_{max,I}$ Monte Carlo	$\Delta e_{max,I}$ Calculated
Walther et al. [189]	$\approx$ 20m $\times$ 18m	20.05m
Walther et al. [189]	$\approx$ 48m $\times$ 45m	47.96m
Walther et al. [189]	$\approx$ 86m $\times$ 81m	88.99m
Smith et al. [156]	$\approx$ 40m	39.7m
Bühler et al. [22]	$\approx$ 37m	36.58m

and $t_{P3,I,3,max}$ can be calculated from $\theta_{ip,I,1max}$ and $\theta_{ip,I,3,max}$ via Eq. 6.43. The required angles $\theta_{0,\Delta e_{ip,max,I}}$ to reach $\Delta e_{ip,max,I}$ can be calculated via

$$\theta_{0,\Delta e_{ip,max,I}} = \tan^{-1}\left(\frac{\Delta\alpha_I\left(\theta_{ip,I,1,max},\theta_{ip,I,3,max}\right)\sqrt{2cA_s}}{\Delta\beta_I\left(\theta_{ip,I,1,max},\theta_{ip,I,3,max}\right)}\right). \tag{6.53}$$

Again, the complementary angle can be calculated taking advantage of the symmetry of the two different sequences (pnp/npn). In a last step, the final phase angle after an iteration $\theta_{f,\Delta e_{ip,max,I}}$ of both sequences (pnp/npn) is determined by applying a forward sequence from an auxiliary state $\left(e_{aux,I},\theta_{0,\Delta e_{ip,max,I}}\right)$ with arbitrary eccentricity $e_{aux,I}$ larger than $\Delta e_{ip,max,I}$ and the complementary angle can be calculated by adding π. In Tab. 6.5, the calculated feasibility ranges for differential lift are compared with values extracted from Monte Carlo results from literature.

It is noticeable that for differential lift, the feasibility range in literature is no longer circular but has the shape of an ellipse. This is because the lift-based algorithm does not include any initial coasting period and the amount by which the eccentricity can be reduced depends on the phase angle. The new methodology, however, determines the largest possible reduction $\Delta e_{ip,max,I}$. While an angular dependency for differential drag exists as well, the optimal position can be reached in any case (due to the initial coasting period) and the feasibility range is circular.

Modified phase #3 algorithms

In analogy to the phase #2 algorithms, the modified algorithms gradually reduces the eccentricity e_{ip} by the maximum possible amount $\Delta e_{ip,max}$ until $e_{ip} < \Delta e_{ip,max}$ holds and the conventional algorithm is able to guide the states towards the origin[19].

Differential drag δf_D: In a first step, the number of iterations $K_{ip,d}$ is determined via

$$K_{ip,d} = \left\lceil \frac{e_{ip,0}}{\Delta e_{ip,max,d}} \right\rceil. \tag{6.54}$$

[19]Notably, the size of the feasible range is no physical quantity but solely a result of the structure of the original phase #3 algorithm, in which three successive control inputs (pnp/npn) are nested within each other. Therefore, the size of the range could be increased by increasing the number of nestings, which would avoid the coasting periods and likely result in shorter maneuver times. However, any additional nesting would only result in a larger range but not represent a solution to the problem. Therefore, this approach was not pursued further.

Table 6.6: Case distinction for determining the position of the deputy before the final drag-based approach.

	$\frac{2K_{ip,d}+1}{K_{ip,d}} \in \mathbb{Z}$	$\frac{2K_{ip,d}+1}{K_{ip,d}} \notin \mathbb{Z}$
$i_d = \text{pnp}$	$\alpha_{f,d} = \sin\left(\pi - \theta_{f,\Delta e_{ip,max,d,pnp}}\right) e_{ip,f,d}$	$\alpha_{f,d} = -\sin\left(\pi - \theta_{f,\Delta e_{ip,max,d,pnp}}\right) e_{ip,f,d}$
	$\frac{\beta_{f,d}}{\sqrt{2cA_s}} = -\cos\left(\pi - \theta_{f,\Delta e_{ip,max,d,pnp}}\right) e_{ip,f,d}$	$\frac{\beta_{f,d}}{\sqrt{2cA_s}} = \cos\left(\pi - \theta_{f,\Delta e_{ip,max,d,pnp}}\right) e_{ip,f,d}$
$i_d = \text{npn}$	$\alpha_{f,d} = -\sin\left(2\pi - \theta_{f,\Delta e_{ip,max,d,npn}}\right) e_{ip,f,d}$	$\alpha_{f,d} = \sin\left(2\pi - \theta_{f,\Delta e_{ip,max,d,pnp}}\right) e_{ip,f,d}$
	$\frac{\beta_{f,d}}{\sqrt{2cA_s}} = \cos\left(2\pi - \theta_{f,\Delta e_{ip,max,d,npn}}\right) e_{ip,f,d}$	$\frac{\beta_{f,d}}{\sqrt{2cA_s}} = -\cos\left(2\pi - \theta_{f,\Delta e_{ip,max,d,pnp}}\right) e_{ip,f,d}$

Notably, if the initial conditions are inside the feasible range (for $K_{ip,d} = 1$), the algorithm naturally reduces to the original phase #3 algorithm by Shao et al. [152]. Since the maximum reduction in eccentricity $\Delta e_{ip,max,d}$ for the drag-based phase #3 algorithm can only be achieved from one of the well-defined locations $\theta_{0,\Delta e_{ip,max,d}}$ (pnp/npn), the deputy is required to coast from its initial state $\left(e_{ip,0}, \theta_{ip,0}\right)$ to the next possible starting position $\left(e_{ip,0}, \theta_{0,\Delta e_{ip,max,d,i_0}}\right)$. Which of the two locations (pnp/npn) is the closest depends on the initial location $\theta_{ip,0}$ via

$$i_0 = \begin{cases} \theta_{0,\Delta e_{ip,max,d,pnp}} < \theta_{ip,0} \leq \theta_{0,\Delta e_{ip,max,d,npn}} & i_0 = \text{npn} \\ \text{else} & i_0 = \text{pnp}. \end{cases} \tag{6.55}$$

After the initial costing phase, the deputy is at $\left(e_{ip,0}, \theta_{0,\Delta e_{ip,max,d,i_0}}\right)$, from which the eccentricity can be reduced by $\Delta e_{ip,max,d,pnp}$ by applying a single iteration. After this, the deputy is located at $\left(e_{ip,0} - \Delta e_{ip,max,d,pnp}, \theta_{f,\Delta e_{ip,max,d,i_0}}\right)$, from which a connecting coasting phase for $t_{c,d}$ is required to reach the subsequent location from which an iteration can be initiated. Due to the symmetry of the two sequences, a pnp-type sequence is followed by an npn-type sequence as thereby a minimal coasting time is required. Vice versa, a pnp-type sequence follows an npn-type sequence. This procedure is repeated for $K_{ip,d}$ times after which $e_{ip,f,d} < \Delta e_{ip,max,d}$ holds and the final approach, calculated via the original drag-based algorithm from Shao et al. [152], is initiated. After a $\Delta e_{ip,max,d}$ reduction sequence, two final positions are possible. Thus, a value for the remaining eccentricity $e_{ip,f,d}$ and the information whether a pnp or npn-type maneuver sequence was performed before the final approach is required to calculate the initial state $\left(\alpha_{f,d}, \frac{\beta_{f,d}}{\sqrt{2cA_s}}\right)$ of the final approach. $e_{ip,f,d}$ can be determined by subtracting the sum of all $\Delta e_{ip,max,d}$ maneuvers from the initial eccentricity $e_{ip,0}$ first:

$$e_{ip,f,d} = e_{ip,0} - \Delta e_{ip,max,d}\left(K_{ip,d} - 1\right). \tag{6.56}$$

Whether the last $\Delta e_{ip,max,d}$ iteration is of pnp - or npn - type depends on the parity of $K_{ip,d}$, i.e. $\frac{2K_{ip,d}+1}{K_{ip,d}} \in \mathbb{Z}$ or $\frac{2K_{ip,d}+1}{K_{ip,d}} \notin \mathbb{Z}$, as well as the initial iteration. Via the case distinction listed in Tab. 6.6, the initial position of the final approach $\left(\alpha_{f,d}, \frac{\beta_{f,d}}{\sqrt{2cA_s}}\right)$ can be determined.

Differential lift $\delta f_{L,x}$: With the exception of the final approach, the structure of the modified algorithm for differential lift is analogous to one of differential drag, therefore it will not be repeated

Table 6.7: Case distinction for determining the position of the deputy before the final lift-based approach.

	$\frac{2K_{ip,I}+1}{K_{ip,I}} \in \mathbb{Z}$	$\frac{2K_{ip,I}+1}{K_{ip,I}} \notin \mathbb{Z}$
$i_I = \text{pnp}$	$\alpha_{f,I} = -\sin\left(2\pi - \theta_{f,\Delta e_{ip,max,I,pnp}}\right) e_{ip,f,I}$	$\alpha_{f,d} = \sin\left(2\pi - \theta_{f,\Delta e_{ip,max,I,pnp}}\right) e_{ip,f,I}$
	$\frac{\beta_{f,I}}{\sqrt{2cA_s}} = -\cos\left(2\pi - \theta_{f,\Delta e_{ip,max,I,pnp}}\right) e_{ip,f,I}$	$\frac{\beta_{f,I}}{\sqrt{2cA_s}} = \cos\left(2\pi - \theta_{f,\Delta e_{ip,max,I,pnp}}\right) e_{ip,f,I}$
$i_I = \text{npn}$	$\alpha_{f,I} = -\sin\left(\theta_{f,\Delta e_{ip,max,I,npn}}\right) e_{ip,f,I}$	$\alpha_{f,I} = -\sin\left(\theta_{f,\Delta e_{ip,max,I,pnp}}\right) e_{ip,f,I}$
	$\frac{\beta_{f,I}}{\sqrt{2cA_s}} = \cos\left(\theta_{f,\Delta e_{ip,max,I,npn}}\right) e_{ip,f,I}$	$\frac{\beta_{f,d}}{\sqrt{2cA_s}} = -\cos\left(\theta_{f,\Delta e_{ip,max,I,pnp}}\right) e_{ip,f,I}$

here. For the final phase, however, a mandatory coasting phase $t_{c,I}$ is added to guide the deputy to one of the respective locations $\theta_{0,\Delta e_{ip,max,I}}$ to ensure a successful maneuver. Otherwise, the algorithm might fail even though $e_{ip,f} < \Delta e_{ip,max,I}$ holds, as the maximum achievable eccentricity reduction from the current location would be too little due to the angular dependency of $\Delta e_{ip,max,I}$. In the drag-based case, a coasting period to the respective location is already included in the original form of the algorithm and therefore not required. Nevertheless, the final approach $e_{ip} < \Delta e_{ip,max,I}$ is calculated with the original lift-based algorithm from Shao et al. [152]. Similar to drag, two final positions after an $\Delta e_{ip,max,I}$ reduction sequence are possible. The case distinction for lift is depicted in Tab. 6.7.

6.4 Enhanced applications of the modified algorithms

Since the algorithms presented so far provide options for selectively influencing all three phase planes, they will serve as building blocks for sophisticated maneuvers in the following.

6.4.1 Simultaneous control

Smith [154] proposed to combine the three control phases into one overall phase by using intermediate angles of attack at which differential lift and drag can be generated simultaneously. While this practice leads to reduces magnitude in the available control forces, the increase in individual phase times is more than compensated for by the time saved due to the parallelization of the control task in most cases [154]. To avoid collisions whenever the in-plane movement is fully regulated before the out-of-plane movement, a semi-simultaneous method in which the control task is divided into two successive phases was derived by Homm [61]:

- **Phase #S1 - Regulation of the average in- and oscillating out-of-plane motion**: In the first phase, the average in- and the oscillating out-of-plane motion are regulated in parallel by using intermediate angles-of-attack. The average in-plane position is adjusted δf_D by applying the modified phase #1 algorithm (see 6.3.1) while simultaneously the out-of-plane states are regulated via $\delta f_{L,z}$ using the modified phase #2 algorithm (see 6.3.2) .
- **Phase #S2 - Regulation of the oscillating in-plane motion**: In the second phase, the remaining oscillating in plane states are regulated via δf_D or $\delta f_{L,x}$ via the modified phase #3 algorithms (see 6.3.3).

Table 6.8: Initial and final conditions of the verification case.

	$\bar{x}$ (m)	$\bar{y}$ (m)	α (m)	$\frac{\beta}{\sqrt{2cA}}$ (m)	z (m)	$\dot{z}$ $\left(\mathrm{m\,s^{-1}}\right)$
t_0	50	50	70.7107	141.4214	35.3553	0.040967
t_f	0	0	0	0	0	0

Table 6.9: Available differential forces of the verification case.

$\delta f_{L,x}$ $\left(\mathrm{m\,s^{-2}}\right)$	δf_D $\left(\mathrm{m\,s^{-2}}\right)$	$\delta f_{L,z}$ $\left(\mathrm{m\,s^{-2}}\right)$
4.51×10^{-5}	1.981×10^{-5}	4.51×10^{-5}

To verify the correct implementation of Smith's simultaneous algorithm [154], the resulting maneuver times are compared with sample data provided by B. Smith. The initial conditions are summarized in Tab. 6.8, the available differential forces in Tab. 6.9, an overview over the respective algorithms in Tab. 6.10 and the resulting maneuver times in Tab. 6.11. Again, the results are in excellent agreement so that a correct implementation can be safely postulated.

6.4.2 Ride sharing / ISS deployment special case

Given the increasing demand for miniaturized satellite systems, cost-effective launch options, such as ridesharing or deploying satellites from the International Space Station (ISS), are of great interest. Ridesharing programs provide a cost-effective way to launch small satellites into orbit along with payloads from other customers on the same launch vehicle. When multiple spacecraft are simultaneously released from the same launch vehicle or the ISS, their initial relative position and velocity vector are essentially zero, and a special control input is required to produce the desired formation geometry $\{\boldsymbol{\rho}_f, \dot{\boldsymbol{\rho}}_f\}$. For the modified phase algorithms presented in subsections 6.3.1 and 6.3.3, the general idea behind the maneuvers is to schedule a rendezvous from the desired state $\{\boldsymbol{\rho}_f, \dot{\boldsymbol{\rho}}_f\}$ and then command the resulting control pattern in reversed order. Nevertheless, adaptations to the respective task are required to ensure a successfully execution of the maneuvers. These have been developed by Friedrich [48] and are introduced in the following.

In the ridesharing / deployment from the ISS special case, the initial conditions regarding the desired average in-plane states $\bar{x}_0 = \bar{y}_0 = 0\,\mathrm{m}$ already fulfill the requirements for a projected circular formation / circular formation (PCF/CF), therefore only the desired oscillating motion has to be generated. To avoid collisions, the oscillating in-plane motion needs to be generated first,

Table 6.10: Applied algorithm for the verification case.

Regulated states	**Algorithm**
$(\bar{x}, \bar{y})$	time-optimal
$\left(z, \frac{\dot{z}}{D_s n}\right)$	conventional
$\left(\alpha, \frac{\beta}{\sqrt{2cA_s}}\right)$	drag-based

Table 6.11: Time comparison for the verification case of the simultaneous control approach.

Regulation	Smith	Calculated	Difference
In-plane	9618.59 s	9618.63 s	3.93×10^{-4} %
Out-of-plane	4515.09 s	4513.37 s	3.80×10^{-2} %

Table 6.12: Necessary adjustments to account for the symmetry of the SC leading to and from the origin.

Plane	Control	Desired state	Adjusted state
IP	Drag δf_D	$\left(\alpha_{int}, \frac{\beta_{int}}{\sqrt{2cA_s}}\right)$	$\left(-\alpha_{P3,0}, \frac{\beta_{P3,0}}{\sqrt{2cA_s}}\right)$
IP	Lift $\delta f_{L,x}$	$\left(\alpha_{int}, \frac{\beta_{int}}{\sqrt{2cA_s}}\right)$	$\left(\alpha_{P3,0}, -\frac{\beta_{P3,0}}{\sqrt{2cA_s}}\right)$

before the corresponding out-of-plane motion is created. For both tasks, the modified algorithms are employed and only minor adjustments are required. The first adaptation is necessary because, unlike a rendezvous maneuver, the dynamic evolution of the in-plane motion must be taken into account during the out-of-plane control phase. Moreover, both motions must be adequately synchronized to achieve the desired post-maneuver formation design $\left\{\boldsymbol{\rho}_{(P)CF}, \dot{\boldsymbol{\rho}}_{(P)CF}\right\}$. Therefore, an intermediate state $\left(\alpha_{int}, \frac{\beta_{int}}{\sqrt{2cA_s}}\right)$ is introduced. This represents the target state of the in-plane establishment maneuver taking the dynamic evolution of the states during the establishment of the out-of-plane motion into account. The state can be calculated by applying the unforced equations of motion backwards for the time period t_{op}, the duration of the out-of-plane maneuver. As a second necessary adaptation, the sign of one of the respective states needs to be changed depending on the control force to account for the symmetry of the SC leading to and from the origin (see Tab. 6.12). For the out-of-plane motion, the switch curve leading away from the origin is axis-symmetric to the switch curve leading towards the origin. To obtain the correct maneuver times for the desired location, the original calculation must therefore be carried out with an inverted initial out-of-plane velocity.

Circular formation: In a circular formation, the deputy is moving on a circular trajectory around the chief so that, in the unperturbed case, the relative distance between chief and deputy is constant at all times:

$$x^2(t) + y^2(t) + z^2(t) = r_{CF}^2 = \text{const.} \tag{6.57}$$

Notably, due to the J_2 - effect, the formation design deteriorates over time and in order to assure $r_{CF}(t) = \text{const.}$, adequate control is required. The CF is defined via a radius r_{CF} as well as a phasing angle φ_{CF}. With respect to Schweighardt-Sedwick parameters, the definition of x_{CF} and $\dot{x}_{CF}$ in dependence of the formation radius and phasing can be adopted from Sabol, Burns, and McLaughlin [134] without modification:

$$x_{CF} = \frac{r_{CF}}{2}\cos(\varphi_{CF}), \tag{6.58}$$

$$\dot{x}_{CF} = -n\frac{r_{CF}}{2}\sin(\varphi_{CF}). \tag{6.59}$$

Secular motion and constant offset terms are removed for the SS equations by defining y_f and $\dot{y}_f$ according to

$$y_{CF} = \frac{2}{n}\frac{c}{2 - c^2}\dot{x}_{CF}, \tag{6.60}$$

$$\dot{y}_{CF} = -2ncx_{CF}. \tag{6.61}$$

Consequently, for the oscillating in-plane states, it simply follows

$$\alpha_{CF} = A_s B_s x_{CF} - \frac{A_s}{n}\dot{y}_{CF} = x_{CF}, \tag{6.62}$$

$$\beta_{CF} = \frac{A_s}{n}\dot{x}_{CF} = y_{CF}, \tag{6.63}$$

which is a direct consequence from Eqs. 6.4 and 6.5 for $\bar{x}_{CF} = \bar{y}_{CF} = 0\,\mathrm{m}$. For z_{CF} and $\dot{z}_{CF}$, two different options are available. The respective conditions are

$$z_{CF} = \pm\sqrt{3}x_{CF}, \tag{6.64}$$

$$\dot{z}_{CF} = \pm\sqrt{3}D_s\dot{x}_{CF}, \tag{6.65}$$

where the signs must match for a given scenario.

Projected circular formation: The design of the projected circular formation (PCF) is very similar to that of the circular formation. In this case, though, the trajectory of the deputy with respect to the chief is of elliptic shape and the distance between the two spacecraft is no longer constant. However, if the deputy's elliptical trajectory is projected onto the along-track/cross-track (y, z) - plane, the projected trajectory is of circular shape:

$$y^2(t) + z^2(t) = r_{PCF}^2 = \text{const.} \tag{6.66}$$

Again, in the perturbed case, the formation design deteriorates over time and adequate means of control, i.e. differential aerodynamic forces, are required to ensure $r_{PCF}(t) = \text{const}$. Similarly to the CF, the formation is defined by the variable r_{PCF} and a phasing angle φ_{PCF}. The initial in plane states α_{PCF} and β_{PCF} are defined analogous to the CF case (again $\bar{x}_{PCF} = \bar{y}_{PCF} = 0\,\mathrm{m}$). In terms of the out-of-plane motion, two solutions for the definition of z_{PCF} and $\dot{z}_{PCF}$ exist:

$$z_{PCF} = \pm 2x_{PCF}, \tag{6.67}$$

$$\dot{z}_{PCF} = \pm 2D_s\dot{x}_{PCF}. \tag{6.68}$$

Here, the signs must again match for a given scenario. The major advantage of the PCF design is the fixed distance between chief and deputy in the along-track/cross-track plane [134], which is a desirable feature, e.g. for Earth observation missions.

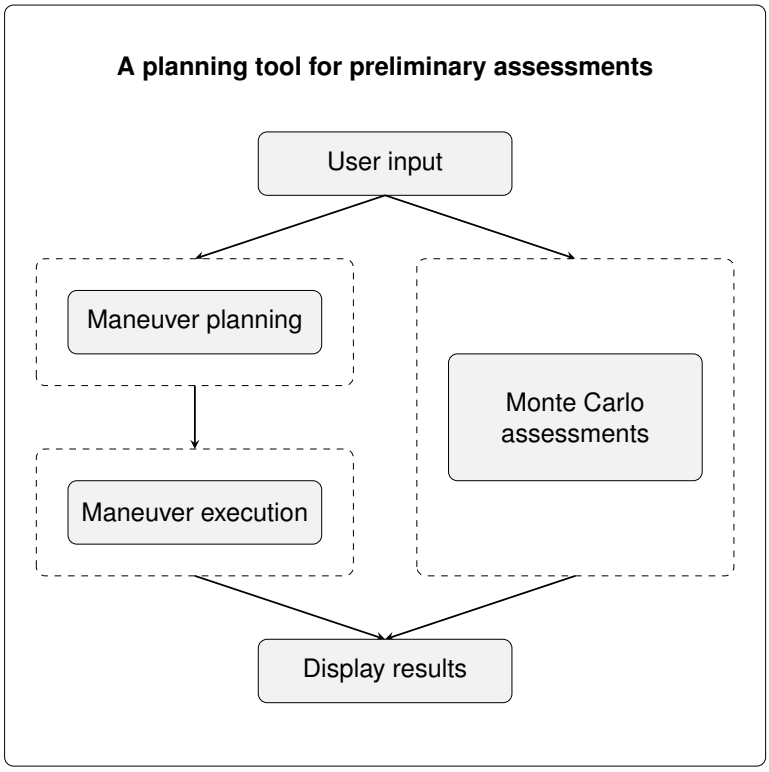

Figure 6.4: Schematic overview of the planning tool for preliminary assessments.

6.4.3 Monte Carlo methods

As first proposed and demonstrated by Smith et al. [156], the computational efficiency of the algorithms just introduced enables to perform a large number of simulations with varying initial conditions from which general conclusions can be drawn by applying Monte Carlo (MC) methods. In the context of this dissertation, the term "Monte Carlo methods" refers to the concept of combining results from a large number of experiments with randomly chosen initial conditions to gain insight into the general behavior of a system. In particular, individual maneuvers are computed from a large number of randomly generated initial conditions. This allows to derive more general conclusions about the influences of boundary conditions and to enable parameter studies aimed at exploring and outlining the design space of possible maneuver variants. In addition, general statements about time savings by modified maneuver algorithms can be made.

6.5 An analysis tool for preliminary assessments

To make the multitude of developed maneuver algorithms accessible for scientific analyses, Beck [8] combined them into a dedicated MATLAB®-based tool for a fast and flexible evaluation of different maneuver scenarios. The tool allows to evaluate either single maneuver trajectories or Monte Carlo results. An overview of the optimal maneuver planning tool is displayed in Fig. 6.4. In the following, the two different evaluation options are described and exemplary results are shown. To establish comparability, all maneuver results are calculated using the boundary conditions from Shao et al. [152] listed in Tab. 6.2.

Table 6.13: Initial and final states for the in-plane formation establishment maneuver.

	x (m)	y (m)	z (m)	$\dot{x}$ $\left(\mathrm{m\,s^{-1}}\right)$	$\dot{y}$ $\left(\mathrm{m\,s^{-1}}\right)$	$\dot{z}$ $\left(\mathrm{m\,s^{-1}}\right)$
t_0	-50	-500	150	-0.2	-0.01	0.12
t_f	0	2500	0	0	0	0

Table 6.14: Initial and final states for the circular formation establishment maneuver after ride sharing. The final states correspond to a CF with $r_{CF} = 500\,\mathrm{m}$ and $\varphi_{CF} = 0^\circ$.

	x (m)	y (m)	z (m)	$\dot{x}$ $\left(\mathrm{m\,s^{-1}}\right)$	$\dot{y}$ $\left(\mathrm{m\,s^{-1}}\right)$	$\dot{z}$ $\left(\mathrm{m\,s^{-1}}\right)$
t_0	0	0	0	0	0	0
t_f	250	0	433.01	0	-0.5661	0

6.5.1 Individual maneuver trajectories

When evaluating individual maneuver trajectories, the user is presented with all available maneuver options for selection. Based on the selection as well as the respective constraints, the control pattern to achieve the maneuver task is planned. In a second step, the forced SS equations are numerically integrated in differential form with the scheduled control pattern as open-loop input. By separating the computation of the control pattern and the generation of the trajectory, the validity of the results is ensured. In a final step, the most relevant results are displayed. For a single maneuver, this is the resulting maneuver trajectory as well as the respective control pattern. In each case, the total maneuver time t_f, the number of control switches n_s and the maneuver option with the shortest maneuver time are displayed.

Exemplary individual maneuver results

As exemplary individual maneuvers cases, two fundamentally different maneuvers, namely (a) an in-plane formation establishment maneuver and (b) a circular formation establishment maneuver after ISS deployment, are presented. The maneuver details are listed in Tabs. 6.13 and 6.14. In both cases, the third phase is scheduled for both available options, i.e. differential drag δf_D and lift $\delta f_{L,x}$. The fundamental maneuver results are summarized in Tabs. 6.15 and 6.16 and the dynamic evolution of the $\mathcal{L}$ - states along with the respective control pattern in Figs. 6.5 - 6.8. In Tabs. 6.15 and 6.16, t_f is the final maneuver time, n_s the number of control switches and $t_{comp.}$ the computational time required to schedule the control pattern.

Table 6.15: Fundamental maneuver results for the in-plane formation establishment maneuver.

Phase #3	t_f (h)	n_s $(-)$	$t_{comp.}$ (s)
δf_D	13.74	21	0.61
$\delta f_{L,x}$	25.12	41	0.60

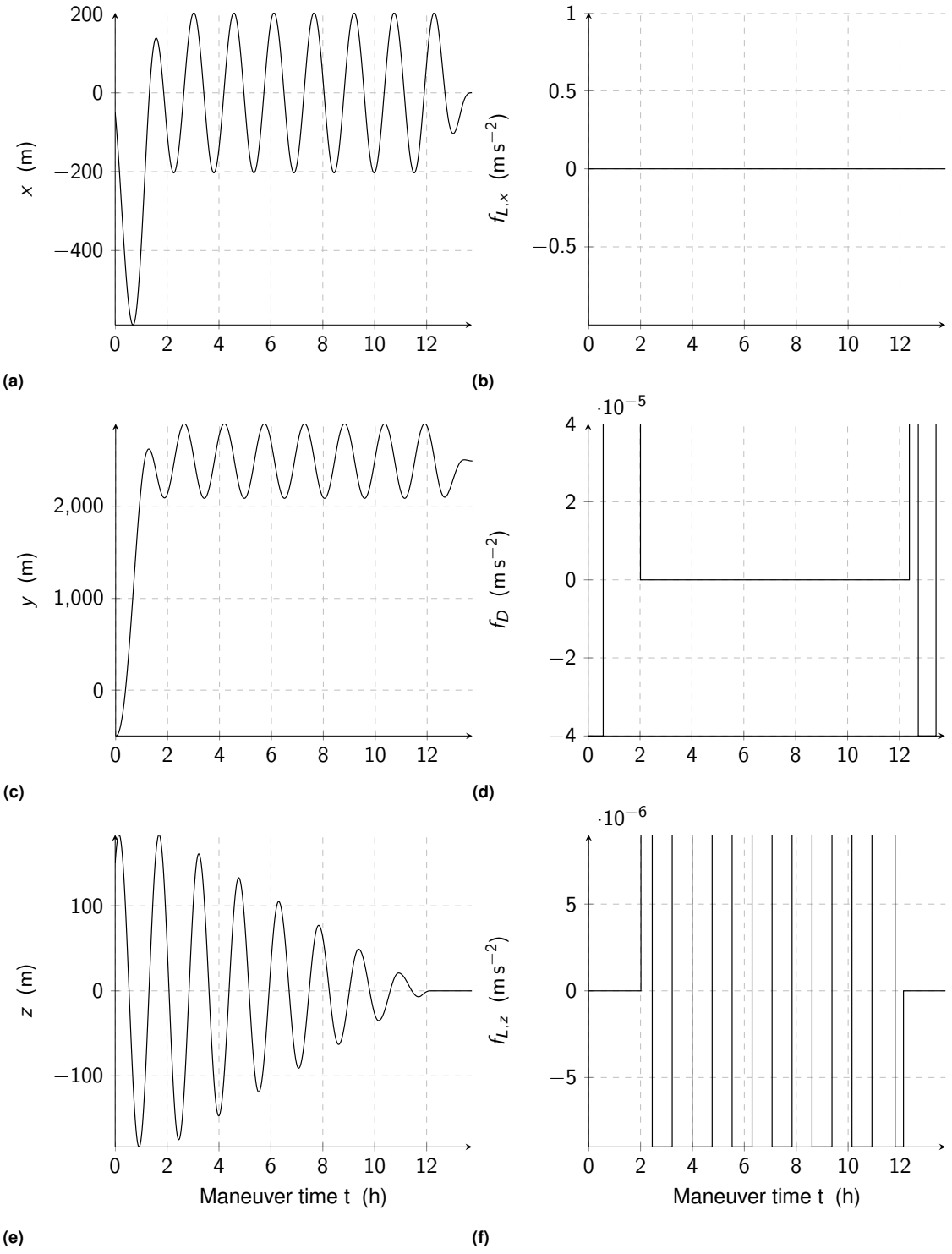

Figure 6.5: Dynamic evolution of the $\mathcal{L}$ - states along with the respective control pattern for the in-plane formation establishment maneuver and a differential drag-based third phase δf_D .

Table 6.16: Fundamental maneuver results for the circular formation establishment maneuver after ride sharing.

Phase #3	t_f (h)	n_s $(-)$	$t_{comp.}$ (s)
δf_D	25.47	35	0.69
$\delta f_{L,x}$	39.63	59	0.60

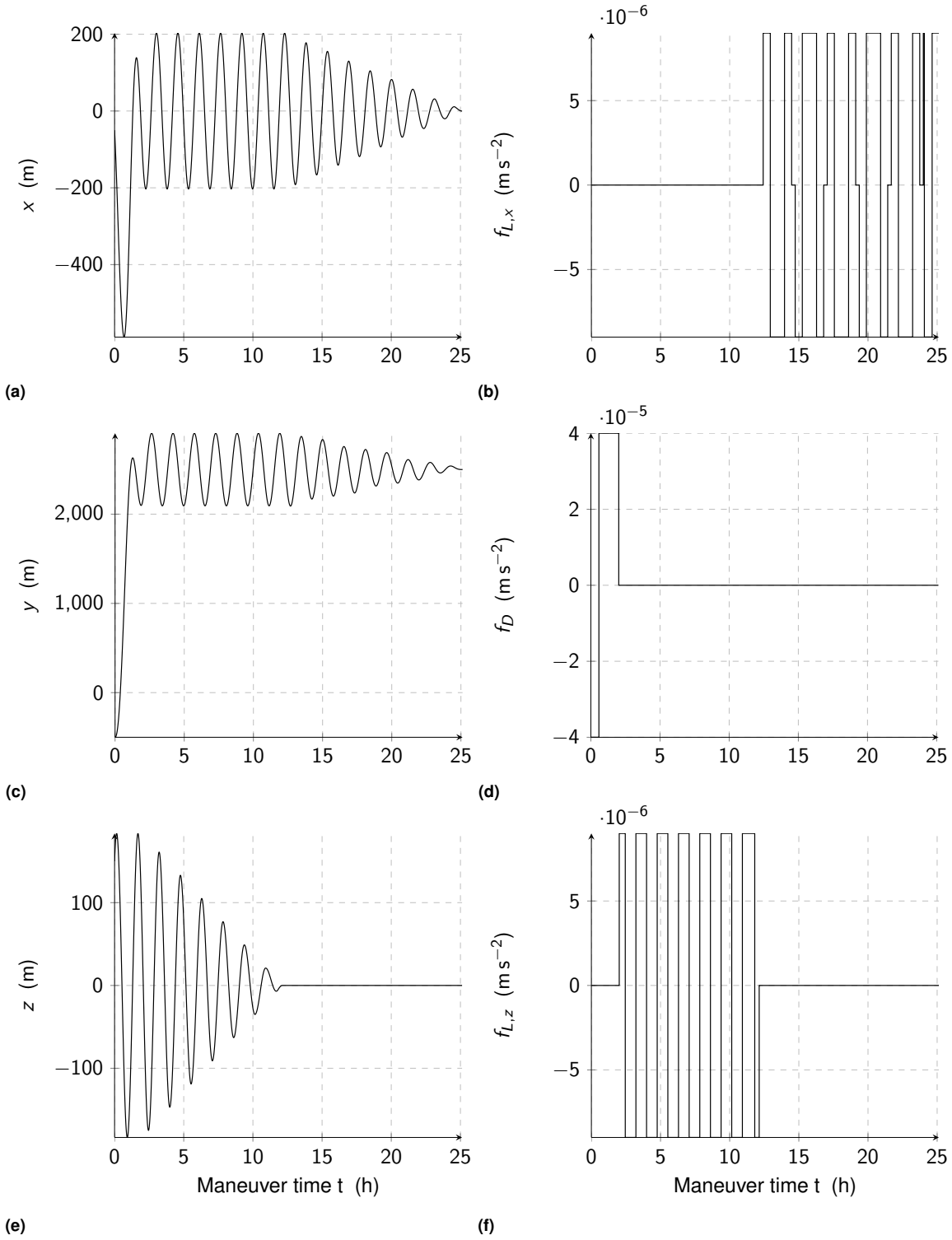

Figure 6.6: Dynamic evolution of the $\mathcal{L}$ - states along with the respective control pattern for the in-plane formation establishment maneuver and a differential lift-based third phase $\delta f_{L,x}$.

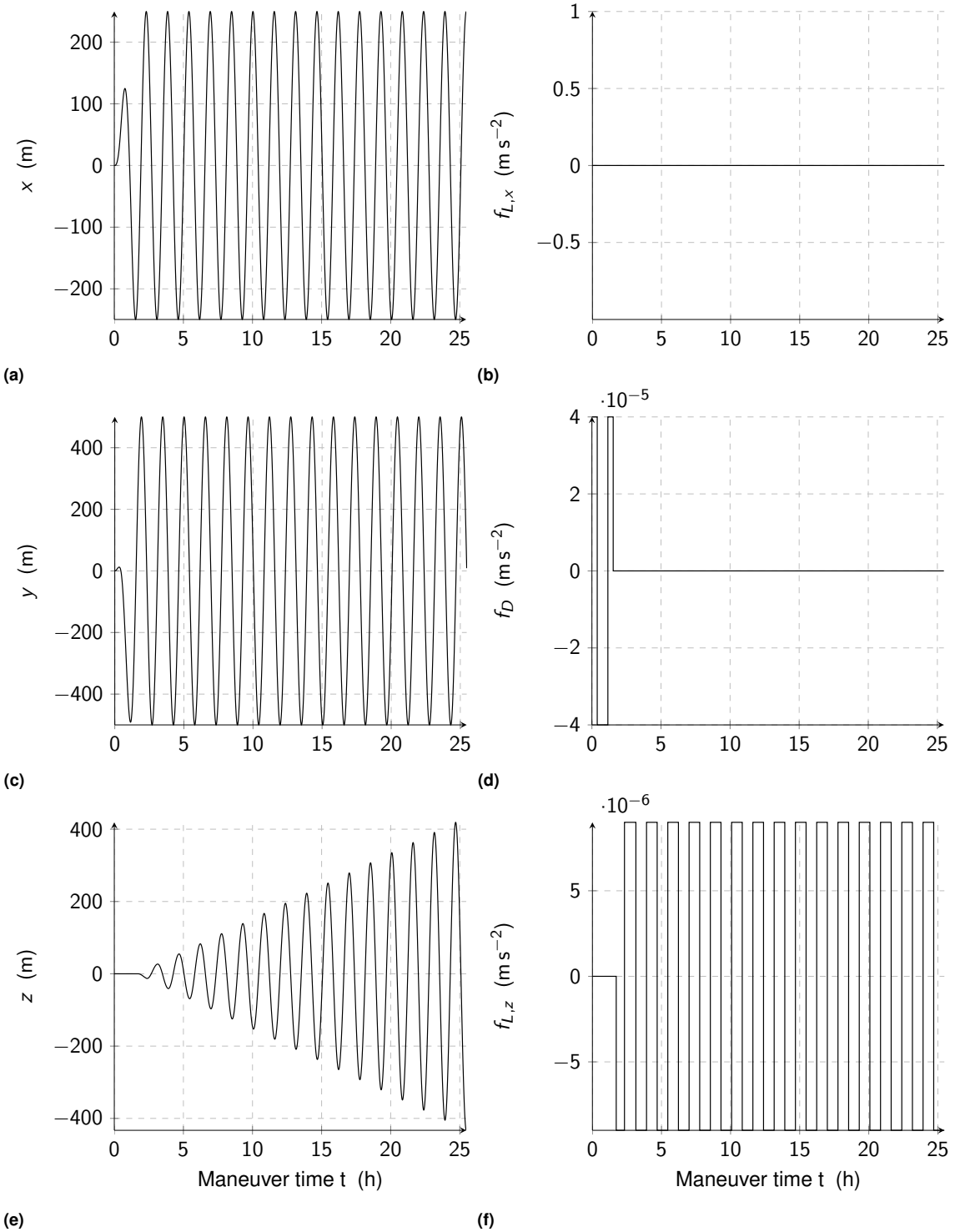

Figure 6.7: Dynamic evolution of the $\mathcal{L}$ - states along with the respective control pattern for the circular formation establishment maneuver after ride sharing and a differential drag-based third phase δf_D.

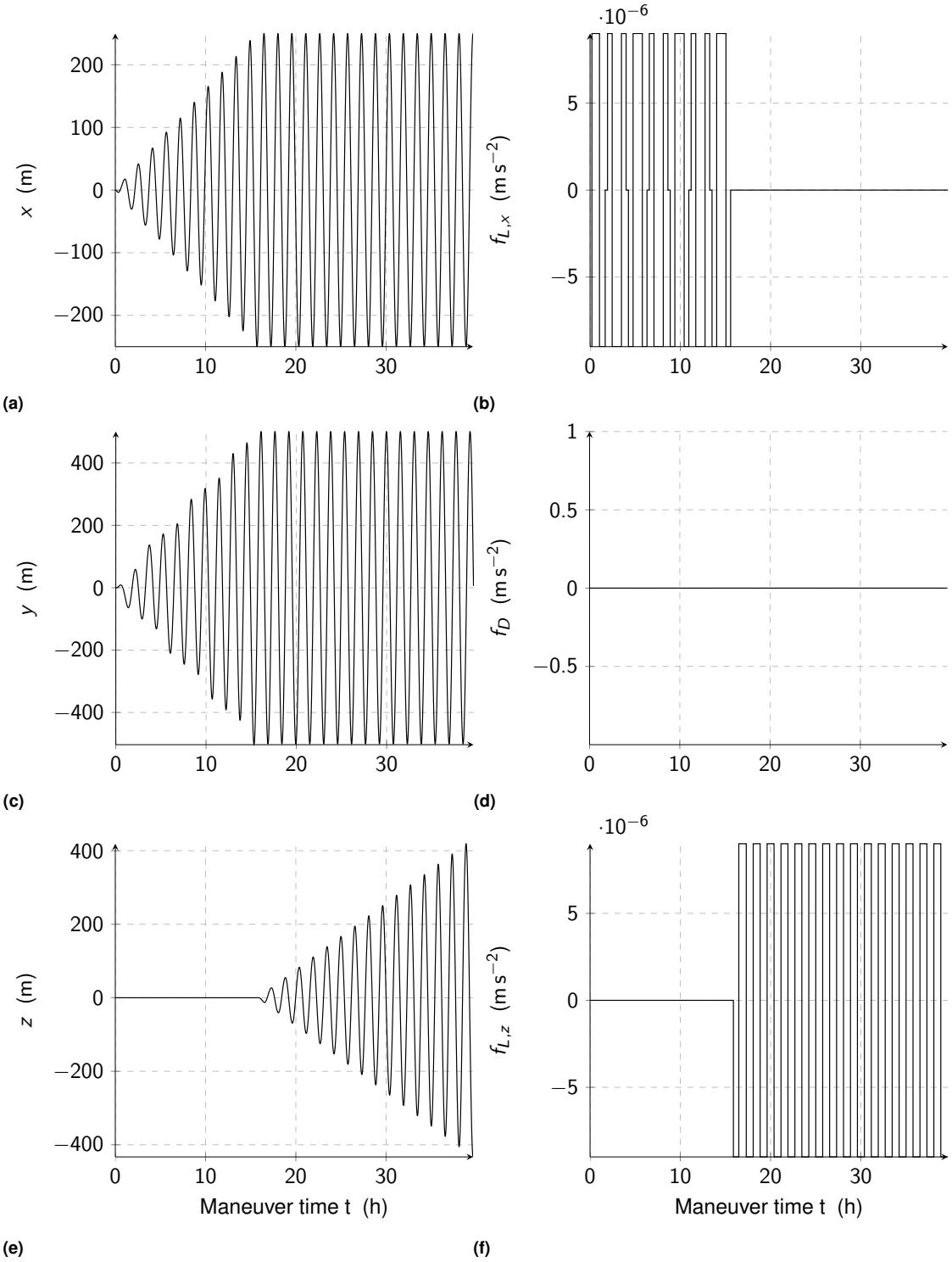

Figure 6.8: Dynamic evolution of the $\mathcal{L}$ - states along with the respective control pattern for the circular formation establishment maneuver after ride sharing and a differential lift-based third phase $\delta f_{L,x}$.

Table 6.17: Employed parameter ranges for the comparison of a rendezvous maneuver and an in-plane formation establishment maneuver.

$\bar{x}_0$ (m)	$\bar{y}_0$ (m)	α_0 (m)	β_0 (m)	z_0 (m)	$\dot{z}_0 \left(\mathrm{m\,s^{-1}}\right)$
$[-500, 500]$	$[-3000, 3000]$	$[-250, 250]$	$[-500, 500]$	$[-150, 150]$	$[-0.1, 0.1]$

Table 6.18: Employed parameter ranges for the comparison of the establishment maneuvers for a CF and PCF formation designs for both available phase three control options (δf_D and $\delta f_{L,x}$).

$r_{(P)CF}$ (m)	$\varphi_{(P)CF}$ (°)
$[10, 500]$	$[0, 360]$

6.5.2 Monte Carlo assessments

With respect to Monte Carlo evaluations, the user must first select the desired maneuver case. Based on the selection as well as the respective boundary conditions, the control pattern to achieve the maneuver task is planned for a desired number of iterations n_{MC} from random initial conditions within a user-defined range. In a second step, the graphical representation of the results is performed, which allows a descriptive evaluation of the results. Since different parameters are of interest for different maneuvers, the exact representation depends on the particular maneuver. In a final step, the results are displayed. For the Monte Carlo case, these are the average time for each subphase $\bar{t}_{P1}$, $\bar{t}_{P2}$, $\bar{t}_{P3}$, the average total maneuver time $\bar{t}_f$, the average number of control switches $\bar{n}_s$ per maneuver, and the total computational time required $t_{comp.}$.

Exemplary Monte Carlo results

In case of Monte Carlo methods, two exemplary assessment cases are discussed in the following:

1. A comparison of a rendezvous maneuver using the original out-of-plane algorithm by Shao et al. [152] and the modified differential drag-based phase three algorithm and an in-plane formation establishment maneuver with $\bar{y}_f = 2500\,\mathrm{m}$ employing the modified out-of-plane algorithm and the modified differential lift-based phase three algorithm.
2. A comparison of the establishment maneuvers for a CF and PCF formation designs for both available phase three control options (δf_D and $\delta f_{L,x}$).

The employed parameter ranges are listed in Tabs. 6.17 and 6.18 and the most fundamental average maneuver results are summarized in Tabs. 6.19 and 6.20. Notably, CF and PCF establishment maneuvers with a differential lift $\delta f_{L,x}$ controlled phase #3 represent unique maneuver cases which are purely differential lift δf_L controlled (no differential drag required). To the best of the author's knowledge, a pure differential lift maneuver has never been presented in literature.

The results depicted in Tabs. 6.19 and 6.20 as well as the graphical visualization depicted in Fig. 6.9 further validate that, in average, the maneuver time for phase #2 using the modified algorithm is shorter than when applying Shao et al.'s [152] original algorithm. For the given boundary conditions, the average phase #2 time could by reduced from $\bar{t}_{P2} = 5.76\,\mathrm{h}$ to $\bar{t}_{P2} =$

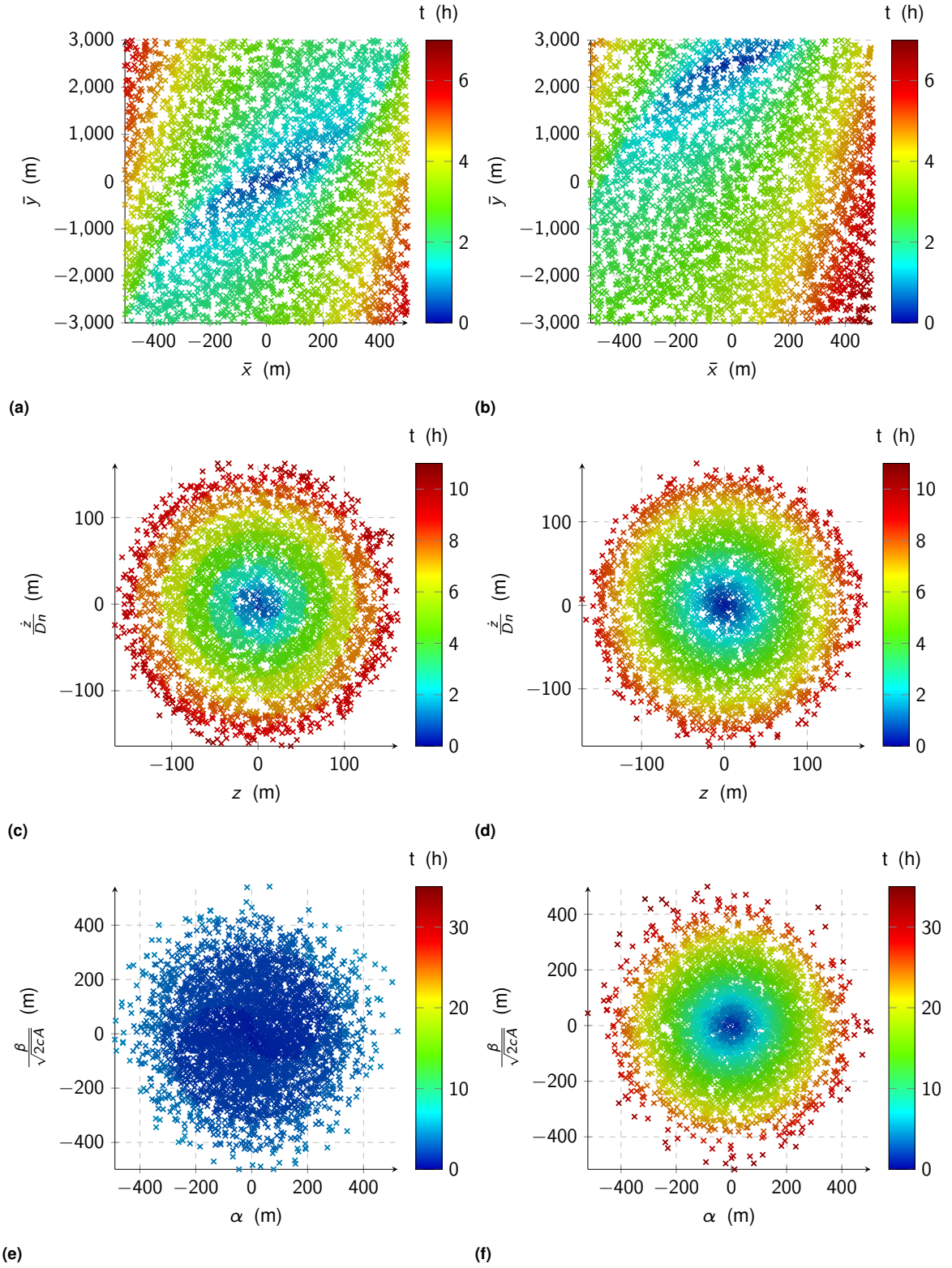

Figure 6.9: Comparison of a rendezvous maneuver using the original out-of-plane algorithm by Shao et al. [152] and the modified differential drag-based phase three algorithm (left) and an in-plane formation establishment maneuver with $\bar{y}_f = 2500\,\mathrm{m}$ employing the modified out-of-plane algorithm and the modified differential lift-based phase three algorithm (right). For reasons of clarity, only every third data point is depicted.

Table 6.19: Averaged maneuver results for the rendezvous using the original out-of-plane algorithm by Shao et al. [152] and the modified differential drag-based phase three algorithm.

$\bar{t}_{P1}$ (h)	$\bar{t}_{P2}$ (h)	$\bar{t}_{P3}$ (h)	$\bar{t}_f$ (h)	$\bar{n}_s$ (−)	n_{MC} (−)	$t_{comp.}$ (h)
2.74	5.76	2.05	10.54	15.39	10,000	1.55

Table 6.20: Averaged maneuver results for the in-plane formation establishment maneuver with $\bar{y}_f = 2500$ m employing the modified out-of-plane algorithm and the modified differential lift-based phase three algorithm.

$\bar{t}_{P1}$ (h)	$\bar{t}_{P2}$ (h)	$\bar{t}_{P3}$ (h)	$\bar{t}_f$ (h)	$\bar{n}_s$ (−)	n_{MC} (−)	$t_{comp.}$ (h)
3.08 h	5.19 h	14.74 h	23.01 h	37.39	10,000	1.43 h

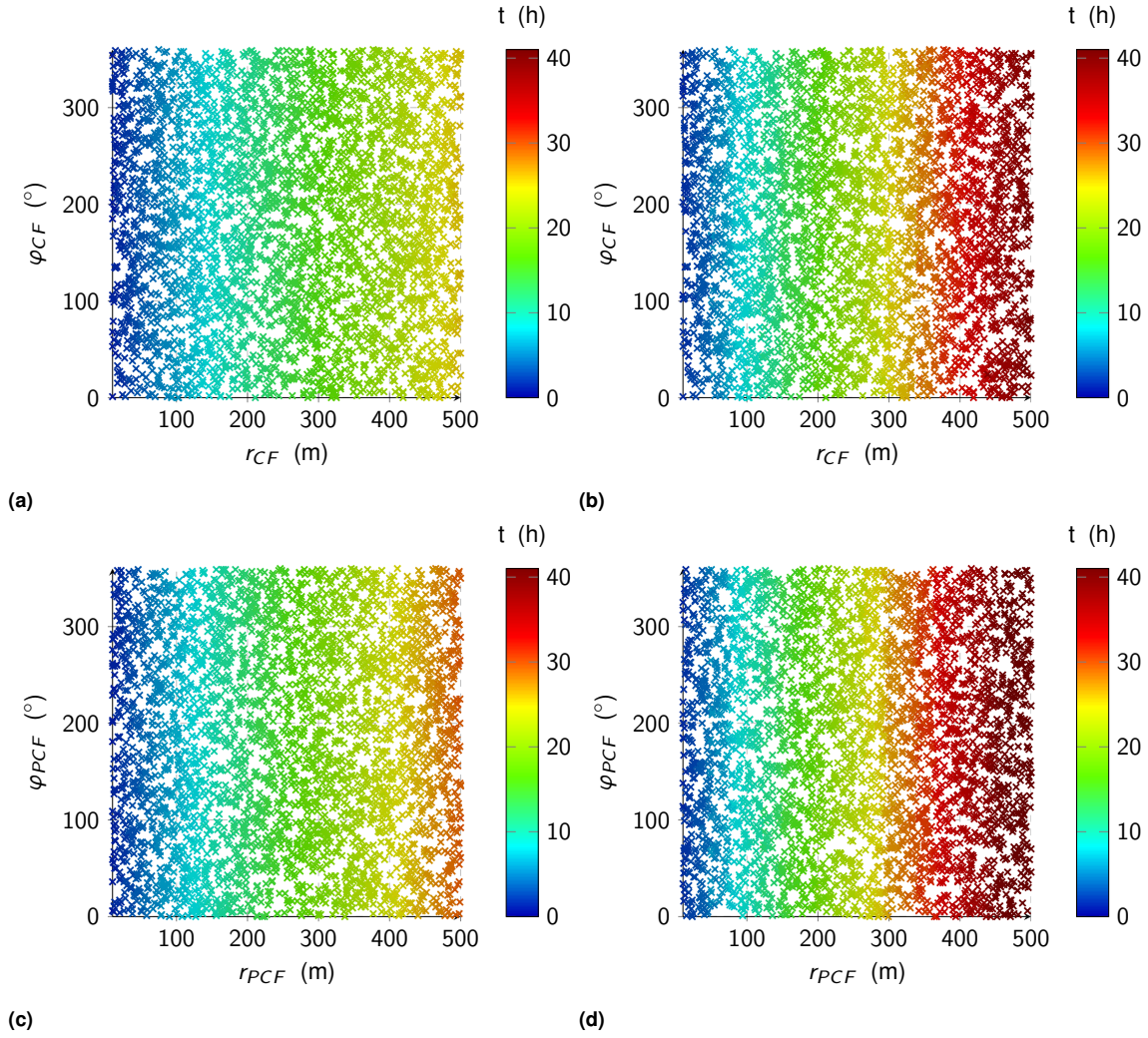

Figure 6.10: A comparison of the establishment maneuvers for a CF (top) and PCF (bottom) formation designs for both available phase three control options (δf_D (left) and $\delta f_{L,x}$ (right)). For reasons of clarity, only every third data point is depicted.

Table 6.21: Average maneuver results for the CF establishment maneuvers.

Phase #3	$\bar{t}_{P1}$ (h)	$\bar{t}_{P2}$ (h)	$\bar{t}_{P3}$ (h)	$\bar{t}_f$ (h)	$\bar{n}_s$ (−)	n_{MC} (−)	$t_{comp.}$ (h)
δf_D	-	12.12	1.5	13.61	20.69	10,000	1.53
$\delta f_{L,x}$	-	12.12	8.55	20.67	32.58	10,000	1.52

Table 6.22: Average maneuver results for the PCF establishment maneuvers.

Phase #3	$\bar{t}_{P1}$ (h)	$\bar{t}_{P2}$ (h)	$\bar{t}_{P3}$ (h)	$\bar{t}_f$ (h)	$\bar{n}_s$ (−)	n_{MC} (−)	$t_{comp.}$ (h)
δf_D	-	13.99	1.5	15.49	23.12	10,000	1.47
$\delta f_{L,x}$	-	13.98	8.54	22.53	34.97	10,000	1.45

5.19 h, representing a time saving of $\Delta\bar{t}_{P2} = 0.48$ h (an average time saving of around 8.34 %). In addition, it is vividly displayed that for phase #3 and for the given boundary conditions, applying differential drag results in *significantly* shorter maneuver times than applying differential lift ($\bar{t}_{P3} = 2.05$ h for differential drag compared to $\bar{t}_{P3} = 14.74$ h for differential lift (an average time saving of $\Delta\bar{t}_{P3} = 12.69$ h)). The results of the CF/PCF establishment maneuvers are listed in Tabs. 6.21 and 6.22 and illustrated in Fig. 6.10. The establishment of PCFs results in 9.0 % - 13.8 % longer t_f than of CF and no dependency on $\varphi_{P(CF)}$ is observed. In any case, differential drag represents the superior control option with respect to t_f.

6.6 Limitations and conclusion

6.6.1 Inaccuracies, limitations and assumptions

To render the problem analytically manageable, the presented algorithms are based on far-reaching assumptions and the equations of motion have a number of limitations:

1. The available control forces are known and constant.
2. The application is limited to the circular chief orbit special case.
3. The relative distance must be small compared to the orbit radius of the chief r_c.
4. The co-rotation of the atmosphere and thermospheric wind effects are neglected.
5. The control is of bang-bang type, i.e. instantaneous attitude changes are assumed.

Therefore, interpreting the results or drawing appropriate conclusions can only be meaningful if these limitations and their implications are taken into consideration.

6.6.2 Concluding remarks on the planning tool for preliminary assessments

In this chapter, the major limitations of analytic algorithms from literature were eliminated and their applicability significantly extended. While so far only the special case of the rendezvous maneuver was considered, a multitude of relevant use cases are now feasible. Subsequently, the resulting algorithms have been combined in a planning tool which allows the user to perform flexible preliminary assessments. This includes individual maneuver trajectories as well as Monte Carlo analysis. The algorithms were verified and the capabilities of the tool were demonstrated in exemplary analyses. However, due to the analytical nature of the algorithms, the resulting maneuvers are subject to some limitations, which have been clearly communicated. To mitigate some of these and to achieve a higher generality of the results, a more sophisticated planning tool is presented in Chapter 7.

Chapter 7

Optimal maneuver planning

While the planning tool presented in Chapter 6 allows for a fast and computationally efficient maneuver design and evaluation, its analytical nature requires a number of simplifications and assumptions. In addition, the user has no ability to include constraints in the planning process and the designed maneuvers are by no means optimal. In this chapter, a novel planning tool for optimal three-dimensional formation flight maneuvers of satellites in VLEO using aerodynamic forces is proposed and its capabilities are described.

The planning tool is based on the work of Dell'Elce [37] and Dell'Elce and Kerschen [38] and the contents of this chapter has been published in Ref. [167].

7.1 Background

The planning of practicable, three-dimensional maneuver sequences controlled by differential drag or lift is the focus of this dissertation. First efforts following Lyapunov principles[20] were published in 2020 [169]. In the same publication, the significant influence of the satellite surface material on the achievable differential lift forces and, consequently, on the overall result of the maneuver was indicated. However, the approach only allowed to apply either differential drag or differential lift but not both forces simultaneously. In addition, the approach was quite inflexible and resulted in a "bang-bang" control pattern. Due to these limitations, any further pursuit of this approach was discarded. Subsequently, a more flexible and improved approach was pursued [168]. This enables to plan formation flight maneuvers of two cooperating satellites in the same plane using differential drag via pitch angle deviations $\delta\theta$ and is based on the original approach developed by Dell'Elce [37] and Dell'Elce and Kerschen [38]. As this approach proved to be very promising in terms of flexibility, it forms the basis for further developments within the framework of this dissertation. The original approach [37, 38], which aimed at the planning and execution of an in-plane rendezvous maneuver between an active deputy as well as a non-cooperative target satellite via differential drag, consisted of three phases:

- **Phase #1 - Drag estimator:** The ballistic coefficient β_D of the active satellite is fitted in-orbit for different pitch angles θ via a least mean squared error approach.

[20] Based on the excellent developments of Pérez and Bevilacqua [120].

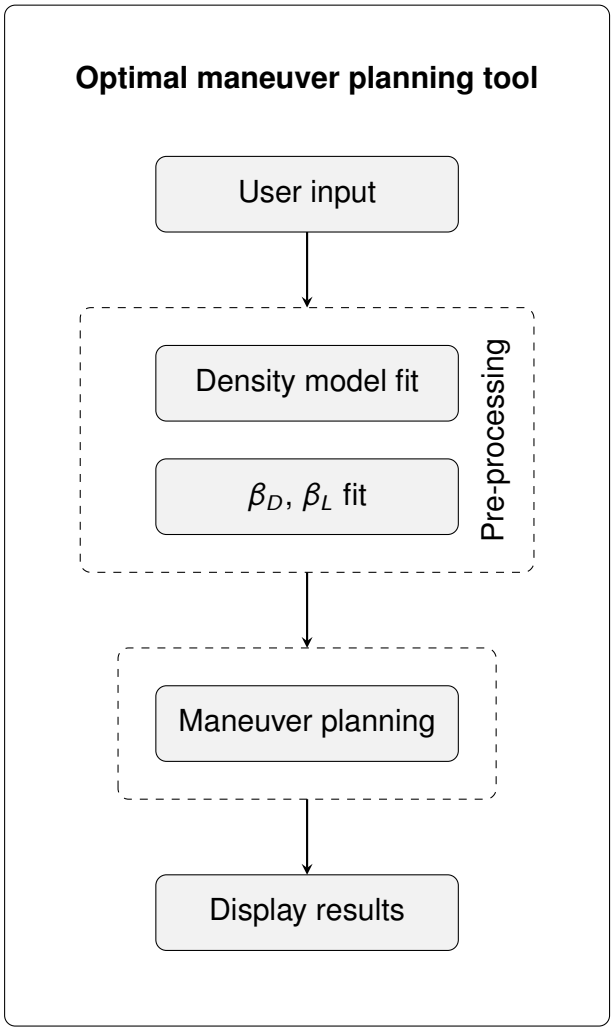

Figure 7.1: Schematic overview of the optimal maneuver planning process.

- **Phase #2 - Maneuver planner:** The maneuver is scheduled via optimal control theory.
- **Phase #3 - On-line compensator:** The maneuver is executed while an on-line compensator accounted for uncertainties and un-modeled dynamics.

Answering the fundamental research questions of this dissertation requires a flexible and sophisticated planning tool for optimal maneuver sequences that enables parameter studies to explore and sketch the design space of possible maneuver variants. Therefore, the focus of this chapter is only on the second phase, the *maneuver planning process*. Consequently, the development of sophisticated methods able to cope with the challenges such as uncertainties and measurement noise with manageable demands on available computational resources is left for future work.

7.2 Optimal maneuver planning tool

In this section, the optimal planning tool is presented and discussed in detail. An overview is displayed in Fig. 7.1.

7.2.1 Pre-processing

The computational burden of the planning process can be significantly decreased if some pre-processing prior to the planning process is performed. The pre-processing steps are adopted from the work of Dell'Elce [37] and Dell'Elce and Kerschen [38].

Fitting of the coefficients of the analytic density model

The most significant limitation of the simplified maneuver trajectories presented in Chapter 6 in terms of achievable accuracy is the constant density assumption. In reality, the density of the upper atmosphere is subject to a variety of variations. To account for dynamic variations within the numerical orbital propagation, empirical density models are the method of choice. However, their incorporation in the planning process would significantly slow down the computation, as this requires a series of coordinate transformations for each iteration and at each collocation point. A suitable representation of density along the trajectory that requires only a fraction of the computational effort is provided by [37, 38]

$$\rho\left(u, i, r, A_\rho, B_\rho, C_\rho, D_\rho\right) = A_\rho\left(1 + B_\rho \cos\left(u - C_\rho\right)\right) \exp\left(\frac{r - R_e\,\sqrt{1 - e_e^2 \sin(i)^2 \sin(u)^2}}{D_\rho}\right), \tag{7.1}$$

which has already been applied by Dell'Elce [37]. The four coefficients (A_ρ,B_ρ,C_ρ,D_ρ) are orbit and epoch dependent and fitted to the NRLMSISE-00 environmental model [122]. In Eq. 7.1, R_e is the Earth's mean equatorial radius and e_e the Earth's eccentricity. The fitting of the coefficients is performed so that the mean squared error

$$e_{MSE} = \frac{1}{n}\sum_{i=1}^{n}\left(\rho_{i,AM} - \rho_{i,ref}\right)^2 \tag{7.2}$$

between the values predicted by the analytic model (subscript *AM*) and the NRLMSISE-00 model [122] (subscript *ref*) is minimized. While fitting the model coefficients accounts for influences such as the epoch and the solar and geomagnetic activities, the model is able to take the exponential vertical structure, the day/night bulge, and the Earth's oblateness into account [37, 38].

Fitting of the aerodynamic properties of the spacecraft

Applying the panel method requires an evaluation of the respective GSI model equations for each panel of the surface mesh for each iteration and at each collocation point. Additionally, knowledge of the current environmental conditions is required. To adapt the aerodynamic calculations to the satellites under investigation while keeping the computational effort low, the profile of the ballistic coefficients β_D (β_A) and β_L (β_A) are fitted to the reference data calculated with the panel method and Sentman's GSI model. The environmental parameters, i.e., thermospheric temperature T_∞, mean molar mass $\bar{M}$, and particle number density of atomic oxygen n_O, are included as orbit-averaged values for the orbit under study and calculated via the NRLMSISE-00 model [122].

7.2.2 Maneuver planner

Optimal control aims to guide the dynamical system $\dot{\boldsymbol{x}} = f(\boldsymbol{x}, \boldsymbol{u}, t)$, in which $\boldsymbol{x}$ are the states and $\boldsymbol{u}$ the control variables, within the maneuver time t_f from an initial state $\boldsymbol{x}(t = 0) = \boldsymbol{x}_0$ to a desired final state $\boldsymbol{x}(t_f) = \boldsymbol{x}_f$ while minimizing the cost functional

$$\mathcal{J}(\boldsymbol{x}, \boldsymbol{u}, t_f) = \mathcal{M}(t_f) + \int_0^{t_f} \mathcal{L}(\boldsymbol{x}, \boldsymbol{u}, t)\, dt \tag{7.3}$$

and satisfying the inequality constraints $g(\boldsymbol{x}, \boldsymbol{u}, t) \leq 0$ [37]. In summary, this results in the following *Bolza problem* [37]:

$$\begin{aligned} [\boldsymbol{x}^*, \boldsymbol{u}^*] = \arg \Big[\min_{\boldsymbol{x(t)}, \boldsymbol{u(t)}, t \in [0, t_f]} \mathcal{J}(\boldsymbol{x}, \boldsymbol{u}, t_f) \Big] \; s.t. \\ \dot{\boldsymbol{x}} = f(\boldsymbol{x}, \boldsymbol{u}, t) \quad \forall t \in [0, t_f] \\ g(\boldsymbol{x}, \boldsymbol{u}, t) \leq 0 \quad \forall t \in [0, t_f] \\ \boldsymbol{x}(t_0) = \boldsymbol{x}_0 \\ \boldsymbol{x}(t_f) = \boldsymbol{x}_f. \end{aligned} \tag{7.4}$$

Hereafter, the respective definitions for the problem under investigation are introduced.

Dynamical system

The state vector $\boldsymbol{x}$ considered in the control plant is

$$\boldsymbol{x} = \begin{bmatrix} \delta\bar{\boldsymbol{\mathcal{E}}}_{ns} \\ \bar{\boldsymbol{\mathcal{E}}}_{ns,c} \\ \psi_c \\ \dot{\psi}_c \\ \psi_d \\ \dot{\psi}_d \end{bmatrix}, \tag{7.5}$$

which consists of the mean differential nearly-nonsingular orbital elements $\delta\bar{\boldsymbol{\mathcal{E}}}_{ns}$, the mean nearly-nonsingular elements of the chief $\bar{\boldsymbol{\mathcal{E}}}_{ns,c}$, the yaw angles $\psi_{c,d}$ of both satellites and their corresponding time derivatives $\dot{\psi}_{c,d}$. By including the mean nearly-singular elements of the chief $\bar{\boldsymbol{\mathcal{E}}}_{ns,c}$ in the state vector, the respective counterparts of the deputy $\bar{\boldsymbol{\mathcal{E}}}_{ns,d}$ can be calculated via

$$\bar{\boldsymbol{\mathcal{E}}}_{ns,d} = \bar{\boldsymbol{\mathcal{E}}}_{ns,c} + \delta\bar{\boldsymbol{\mathcal{E}}}_{ns} \tag{7.6}$$

so that the full absolute and relative states of the two spacecraft are known at all times. From the mean non-singular elements $\bar{\boldsymbol{\mathcal{E}}}_{ns}$, mean Keplerian elements $\bar{\boldsymbol{\mathcal{E}}}$ and their osculating counterparts $\boldsymbol{\mathcal{E}}$ can be obtained. In a last conversion, these can be mapped into the osculating inertial position ${}^{\mathcal{T}}\boldsymbol{r}$ and velocity ${}^{\mathcal{T}}\boldsymbol{v}$ in the $\mathcal{T}$ - frame, which are used to calculate the aerodynamic forces acting

on the satellites. For the methodology under investigation, the control vector $\boldsymbol{u}$ is the arithmetic difference of the specific aerodynamic forces acting on the satellites $\delta \boldsymbol{f}_A$ expressed in the $\mathcal{L}$ - frame of the chief

$$ {}^{\mathcal{L}}\delta \boldsymbol{f}_A = {}^{\mathcal{L}}\boldsymbol{f}_{A,d} \; - \; {}^{\mathcal{L}}\boldsymbol{f}_{A,c} = \left(f_{A,x},\; f_{A,y},\; f_{A,z}\right)^T . \tag{7.7} $$

Since the gradient of the contract transformation is close to the identity matrix according to Schaub et al. [142], the instantaneous specific aerodynamic forces ${}^{\mathcal{L}}\boldsymbol{f}_{A,D}$ and ${}^{\mathcal{L}}\boldsymbol{f}_{A,D}$ are used to calculate this difference [37, 142]. These are calculated for each spacecraft via Eqs. 4.1, 4.2 and 4.7, respectively. In Eqs. 4.2 and 4.7, the local atmospheric density is calculated using the analytic density model and the relative velocity vector $\boldsymbol{v}_{rel}$ is calculated via Eq. 4.3, in which thermospheric wind effects are neglected ($\boldsymbol{v}_w = \boldsymbol{0}\ \mathrm{m\,s^{-1}}$). The sensitivity of the satellites towards the aerodynamic forces are incorporated in the equations via the fitted functions for $\beta = f(\beta_A)$ and $\beta_L = f(\beta_A)$. As, by the definition of the yaw angle, the body fixed frame is rotated with respect to the Frenet - frame by an angle of ψ around the ${}^{\mathcal{B}}\hat{\boldsymbol{z}}$ – axis, the orientation of the satellite with respect to the flow, i.e., the angle of sideslip β_A, can be determined at all times.

The absolute motion dynamics of the chief in terms of mean nearly-nonsingular orbital elements $\bar{\boldsymbol{\mathcal{E}}}_{ns,c}$ is calculated using the Lagrange's Planetary Equations (LPE) and Gauss's Variational Equations (see Subsection 2.2.1). To determine mean element changes, technically the osculating-mean transformation must be applied [132]. However, as the sensitivities of mean element changes with respect to osculating element changes are shown to be of at most $\mathcal{O}(J_2)$ [139, 142], the following approximation is used in analogy to the work of Roscoe et al. [132]:

$$ \dot{\bar{\boldsymbol{\mathcal{E}}}}_{ns,c} \approx \boldsymbol{f}(\bar{\boldsymbol{\mathcal{E}}}_{ns,c}) + \left[\boldsymbol{B}(\bar{\boldsymbol{\mathcal{E}}}_{ns,c})\right] {}^{\mathcal{L}}\boldsymbol{f}_{A,c}. \tag{7.8} $$

The unforced dynamics $\boldsymbol{f}(\bar{\boldsymbol{\mathcal{E}}}_{ns,c})$ including the perturbing effect caused by J_2 is given by [132]

$$ \boldsymbol{f}(\bar{\boldsymbol{\mathcal{E}}}_{ns,c}) = \begin{bmatrix} 0 \\ n + \frac{3}{4} J_2 \left(\frac{R_e}{p}\right)^2 n \left[\eta(3\cos^2(i) - 1) + (5\cos^2(i) - 1)\right] \\ 0 \\ -\frac{3}{4} J_2 \left(\frac{R_e}{p}\right)^2 n(3\cos^2(i) - 1) q_2 \\ +\frac{3}{4} J_2 \left(\frac{R_e}{p}\right)^2 n(3\cos^2(i) - 1) q_1 \\ -\frac{3}{2} J_2 \left(\frac{R_e}{p}\right)^2 n\cos(i) \end{bmatrix} . \tag{7.9} $$

The rotational dynamics of both spacecraft around their ${}^{\mathcal{B}}\hat{\boldsymbol{z}}$ - axes are included in a simplified form neglecting any perturbing effects and cross-term couplings. These are included to ensure a smooth and realistic profile of the yaw angles $\psi_{c,d}(t)$ avoiding bang-bang type control switches:

$$ \ddot{\psi}_c = -I_{z,c} u_c, \tag{7.10} $$

$$ \ddot{\psi}_d = -I_{z,d} u_c. \tag{7.11} $$

I_z is the moment of inertia around the ${}^{\mathcal{B}}\hat{\boldsymbol{z}}$ - axis of the satellite and u the control variable which is

the torque commanded to the reaction wheel. Due to the simplified rotational dynamics, not the resulting torque but the resulting yaw angle profiles $\psi_c^\star$ and $\psi_d^\star$ are considered the results of the planner. In a real maneuver application, it is the task of the attitude control systems to ensure a proper profile tracking.

Cost function

As elaborated in Subsection 5.4.1, reducing the resulting orbital decay is the focus throughout this dissertation. This reflects itself in the choice of the cost functional $\mathcal{J}(\boldsymbol{x}, \boldsymbol{u}, t_f)$, which is defined throughout this dissertation as

$$\mathcal{J}(\boldsymbol{x}, \boldsymbol{u}, t_f) = -\bar{a}_{c,f}. \tag{7.12}$$

Thus, the scheduled control profile is optimal in a sense that it maximizes the mean semi major axis of the chief $\bar{a}_{c,f}$ after the maneuver (at t_f).

Constraints

Constraints are the admissible value range of the yaw angles of both satellites $\psi_{c,d}$, their minimum and maximum angular velocity $\dot{\psi}_{c,d}$, and the absolute value of the maximum torque commanded to the reaction wheels $T_{W,max}$:

$$\psi_{c,d} \in [\psi_{min},\ \psi_{max}] \ \ \forall t \in [0, t_f], \tag{7.13}$$

$$\dot{\psi}_{c,d} \in [\dot{\psi}_{min},\ \dot{\psi}_{max}] \ \ \forall t \in [0, t_f], \tag{7.14}$$

$$u_{c,d} \in [-T_{W,max},\ T_{W,max}] \ \ \forall t \in [0, t_f]. \tag{7.15}$$

An exact value for the maneuver time t_f is not prescribed to broaden the solution space. However, limits are included to facilitate the solution finding process ($t_f \in [t_{f,min},\ t_{f,max}]$). During the maneuver, no constraints on the absolute $\dot{\tilde{\boldsymbol{\varepsilon}}}_{ns,c}$ or relative states $\delta\dot{\tilde{\boldsymbol{\varepsilon}}}_{ns}$ are set. The initial absolute $\dot{\tilde{\boldsymbol{\varepsilon}}}_{ns,C,0}$ and relative states $\delta\dot{\tilde{\boldsymbol{\varepsilon}}}_{ns,0}$ as well as the formation geometry after the maneuver $\delta\dot{\tilde{\boldsymbol{\varepsilon}}}_{ns,f}$ are fixed. The final absolute states of the chief, however, $\dot{\tilde{\boldsymbol{\varepsilon}}}_{ns,C,f}$ remain unconstrained.

Programming and solution

The continuous-time problem is transformed into a nonlinear programming problem by means of direct transcription via the 'General Purpose OPtimal Control Software' (GPOPS-II) [117] and the optimization is performed using the nonlinear program solver 'Interior Point OPTimizer' (IPOPT) [183]. Additional insights can be found in the work of Dell'Elce [37]. To ensure an efficient solution finding process, the programming is designed in a way that all calculations are realized as vector-matrix-product and no computational expensive loops have to be executed. To enable the required coordinate transformations, the rotation matrices are adapted accordingly via MATLAB®'s *reshape* function [104]. To avoid numerical difficulties, all translational states except δa and a_c are scaled by R_e.

7.3 Exemplary maneuver results

7.3.1 Maneuver setup

To simplify and generalize, throughout this chapter formation flight maneuvers of two satellites are considered and close proximity operations are avoided. The satellites under investigation, identical in design[21], are 3U CubeSats augmented with two additional external panels each. The panels, which can be solar panels, are oriented so that the control authority of both differential forces (lift and drag) is increased (see Fig. 2.4). The satellite design ensures that multiple reflections or shadowing effects are avoided. The satellite bodies consist of 30 x 10 x 10 cm (length/width/height) cuboids. The panels have a size of 30 x 0.5 x 12.5 cm each and are attached directly to the body. Each satellite has a total mass of $m_c = m_d = 5\,\mathrm{kg}$ and neither of them is equipped with any thrusting device. The corresponding symmetric moments of inertia tensor $[\boldsymbol{I}]$ expressed in the body fixed coordinate frame is

$$[\boldsymbol{I}] = \begin{bmatrix} I_x & 0 & 0 \\ 0 & I_y & 0 \\ 0 & 0 & I_z \end{bmatrix} = \begin{bmatrix} 0.0152 & 0 & 0 \\ 0 & 0.0490 & 0 \\ 0 & 0 & 0.0412 \end{bmatrix} \mathrm{kg\,m^2}. \tag{7.16}$$

In terms of attitude control, the satellites are equipped with three Astrofein RW1 Type A reaction wheels [43] with a moment of inertia of $694.5 \times 10^{-9}\,\mathrm{kg\,m^2}$, a nominal maximum torque of $23 \times 10^{-6}\,\mathrm{N\,m}$ and a maximum rotational velocity of 16 380 rpm. The maximum torque of the reaction wheels is used as the limit $T_{W,max}$ for the control variable in the maneuver planner (see Eq. 7.15). In addition, the admissible yaw angle range is $\psi_{c,d} \in [-90°, 90°]$ and the angular velocity of the satellites limited to $\dot{\psi}_{c,d} \in \left[-0.1\,^\circ\,\mathrm{s}^{-1}, 0.1\,^\circ\,\mathrm{s}^{-1}\right]$. Thereby, it is ensured that an attitude change of a satellite from a minimum to a maximum drag configuration (from 0° to 90°) requires at least 15 minutes and unwanted effects like chattering or bang-bang type control switches are avoided. Constant and moderate solar and geomagnetic activities are assumed according to ISO 14222 [68]. The maneuver parameters, valid for all subsequent cases, are summarized in Tab. 7.1. The initial absolute states of the chief are invariant and included in Tab. 7.1. The initial $\{\boldsymbol{\rho}_0, \dot{\boldsymbol{\rho}}_0\}$ and desired final $\{\boldsymbol{\rho}_f, \dot{\boldsymbol{\rho}}_f\}$ relative states vary with the maneuver cases and are stated in the individual subsections. For all maneuvers, the initial guess for the maneuver time $t_{f,g}$ is arbitrarily defined to $n_i = 16$ orbital periods of the initial chief orbit $P_{c,0} = 2\pi\sqrt{a_{c,0}/\mu_e}$. This results in $t_{f,g} = 24.1\,\mathrm{h}$. The limits are set to $n_{i,min} = n_i - 1/2$ and $n_{i,max} = n_i + 1/2$ which results in $t_{f,min} = 23.4\,\mathrm{h}$ and $t_{f,max} = 24.9\,\mathrm{h}$. The settings of the GPOPS-II software employed to schedule the optimal maneuver trajectory are listed in Tab. 7.2.

7.3.2 Pre-processing results

In the first of the two pre-processing steps, the parameters A_ρ, B_ρ, C_ρ, D_ρ are fitted. Fig. 7.2 shows a comparison between the values predicted as well as the reference data calculated via the NRLMSISE-00 model [122] over one orbital period of the chief $P_{c,0}$. Whereas some mis-

[21] A common strategy to facilitate the formation maintenance task.

Table 7.1: Relevant maneuver parameters which are valid for all subsequently discussed maneuver cases.

Parameter	Unit	Value
$a_{c,0}$	km	6678.137
$e_{c,0}$	–	0.001
$i_{c,0}$	°	98
$\Omega_{c,0}$	°	10
$\omega_{c,0}$	°	30
$\theta_{k,c,0}$	°	60
$\psi_{c,d,0}$	°	0
$\dot{\psi}_{c,d,0}$	°	0
$\psi_{c,d,f}$	°	0
$\dot{\psi}_{c,d,f}$	°	0
$F_{10.7} = \bar{F}_{10.7}$	sfu	140
$A_p = a_p$	nT	15
$t_{f,min}$	h	23.4
$t_{f,max}$	h	24.9
$t_{f,g}$	h	24.1
Epoch	-	22/10/2016 00:00:00 (UTC)

Table 7.2: Settings of the GPOPS-II software employed to schedule the optimal maneuver trajectory.

Parameter	Setting
Max. iterations	4
Method	Hp-LiuRao
Tolerance	5e-4
Colpointsmin	6
Colpointsmax	20
R	1.6
IPOPT tolerance	1e-10
Derivatives supplier	SparseFD
Derivatives level	First
Derivatives dependencies	sparseNaN
Derivatives stepsize	1e-10
Scales numsamples	200

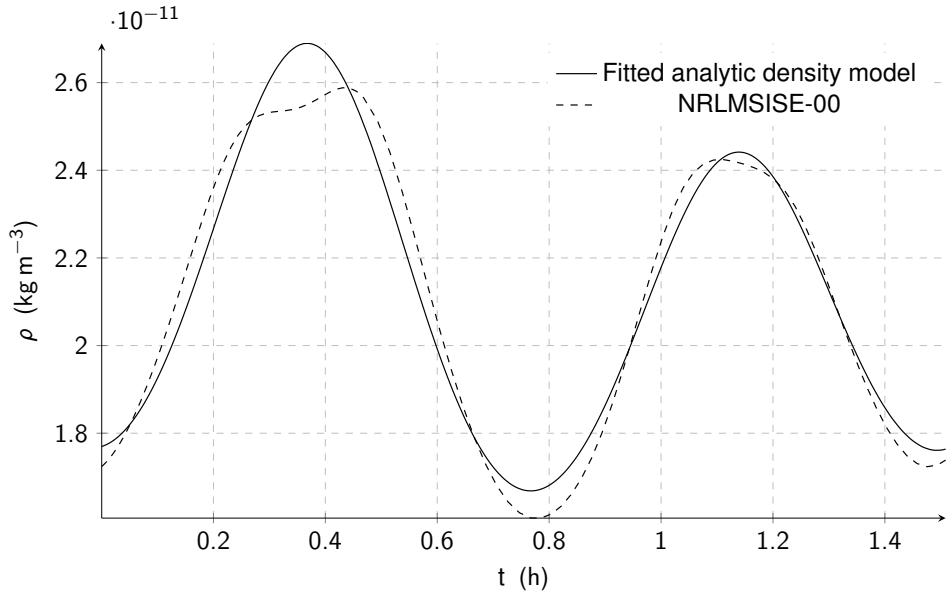

Figure 7.2: Comparison of the output of the fitted analytic density model and the reference data, which is produced using the NRLMSISE-00 environmental model [122, 167].

matches in the predicted density values are inevitable, the model is able to depict the most relevant dynamic variations with a significantly reduced computational burden.

In the second pre-processing step, the aerodynamic properties of the spacecraft, represented by $\beta_D = f(\beta_A)$ and $\beta_L = f(\beta_A)$, are fitted to the reference data calculated via the panel method applied with Sentman's GSI model for an angle of sideslip range of $\beta_A \in [0°, 90°]$. The results and the reference data are plotted in Fig. 7.3. Notably, the values are plotted reciprocally ($\beta_D^{-1}(\beta_A)$ and $\beta_L^{-1}(\beta_A)$) for a more vivid depiction of the aerodynamic sensitivity: an increase in β_D^{-1} indicates a higher sensitivity towards the aerodynamic drag force and, in analogy, an increase in β_L^{-1} indicates a higher sensitivity towards the aerodynamic lift force. Due to the symmetrical shape of the spacecraft, a similar profile results for a rotation in the opposite direction.

7.3.3 Maneuver results

In this subsection, the results for the following cases are presented:

- **Case #1:** Re-phasing maneuver with simultaneous out-of-plane regulation.
- **Case #2:** In-plane formation into centered, bounded relative motion maneuver.
- **Case #3:** Centered, bounded relative motion variation maneuver.

As these are of fundamental difference, the vast range of applicability and powerfulness of the developed approach is indicated. At this stage, only a description of the main results will be provided. A detailed analysis of the maneuvers will be given in Subsection 8.1.1. Over all, the tool is able to successfully schedule these reference cases, which represents an added value to the research field.

To increase the vividness of the desired maneuvers, the inital and final relative states of the deputy with respect to the chief are expressed in terms of the set of parameters $\left\{\rho_x,\ d,\ \rho_z,\ v_d,\ \bar{\alpha}_0,\ \bar{\beta}_0\right\}$ well known from the solutions to the CW equations. The resulting ma-

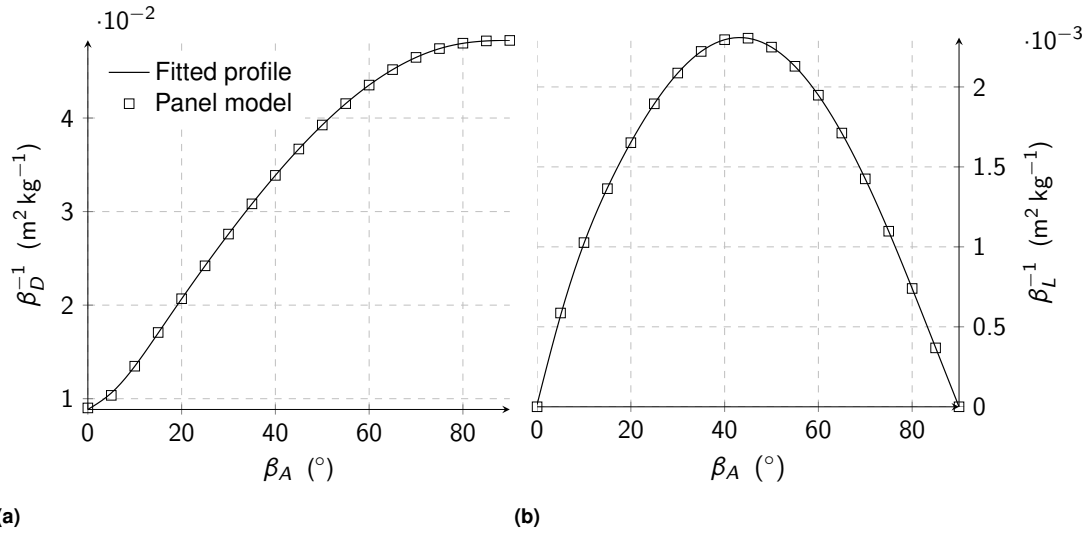

Figure 7.3: Comparison of the fitted and reference ballistic coefficient β_D (left) and ballistic lift coefficient β_L (right) of the chief spacecraft. The reference data is calculated using the panel method with Sentman's GSI model [149, 167].

Table 7.3: Initial and final formation design for case #1.

	$\boldsymbol{v_t}\left(\mathrm{m\,s^{-2}}\right)$	$\boldsymbol{\rho_x}\,(\mathrm{m})$	$\bar{\boldsymbol{\alpha}}_{\mathbf{0}}\,(^\circ)$	$\boldsymbol{\rho_z}\,(\mathrm{m})$	$\bar{\boldsymbol{\beta}}_{\mathbf{0}}\,(^\circ)$	$\boldsymbol{d}\,(\mathrm{km})$
t_0	0	0	0	80	90	30
t_f	0	0	0	0	0	-1

neuver trajectories are displayed in terms of relative Cartesian states $\boldsymbol{\rho}$, which are calculated from the nearly-nonsingular elements $\delta\bar{\boldsymbol{\mathcal{E}}}_{ns}$ and $\bar{\boldsymbol{\mathcal{E}}}_{ns,c}$ via the mapping presented in Subsection 2.2.2. For each case, the main results of the maneuver, that is the final maneuver time t_f, the resulting orbital decay of the chief Δa_c and the required computational time to find the optimal solution $t_{comp.}$ are summarized in a respective table. Δa_c is defined as

$$\Delta a_c = a_{c,0} \; - \; a_{c,f}. \tag{7.17}$$

Case #1: Re-phasing maneuver with simultaneous out-of-plane regulation

In case #1, a re-phasing maneuver of an in-plane formation during which the order of the leader - follower configuration is switched is conducted. Simultaneously, a residual initial out-of-plane motion $\rho_{z,0} \neq 0$ is regulated. The initial and final states of the deputy with respect to the chief are summarized in Tab. 7.3. The resulting three-dimensional relative maneuver trajectory of the deputy with respect to the chief in the $\mathcal{L}$ - frame of the chief is plotted in Fig. 7.4, where the color bar indicates the maneuver time. In addition, the in-plane maneuver trajectory is shown in Fig. 7.5 and the corresponding yaw angle $\psi(t)$ and angle of sideslip profiles $\beta_A(t)$ for both satellites are depicted in Fig. 7.6. The main results of the maneuver are summarized in Tab. 7.4.

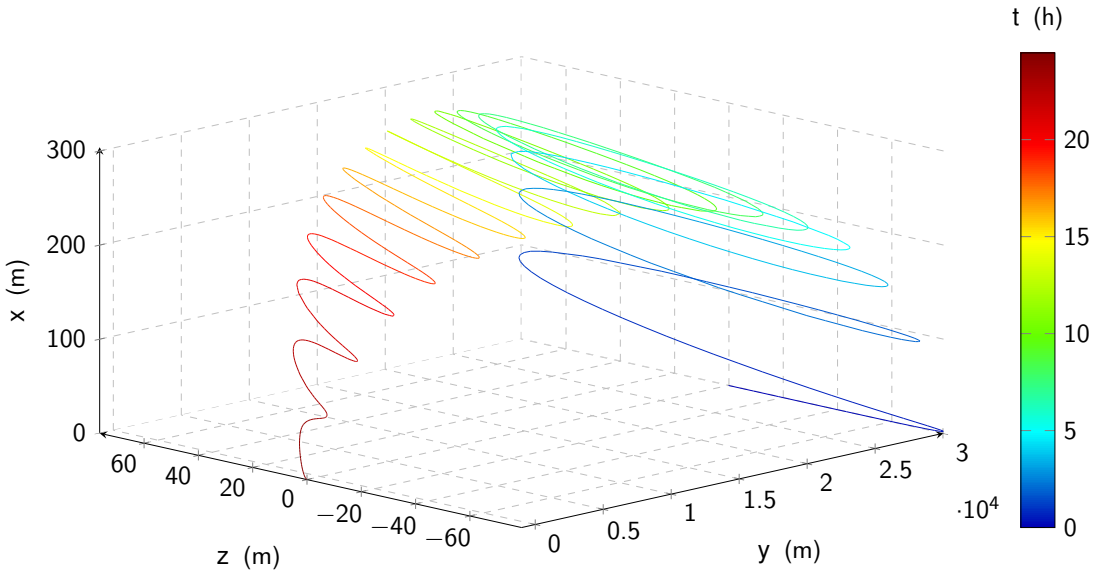

Figure 7.4: Relative maneuver trajectory of the deputy with respect to the chief plotted in the $\mathcal{L}$ - frame of the chief for an in-plane formation re-phasing maneuver with simultaneous out-of-plane regulation [167].

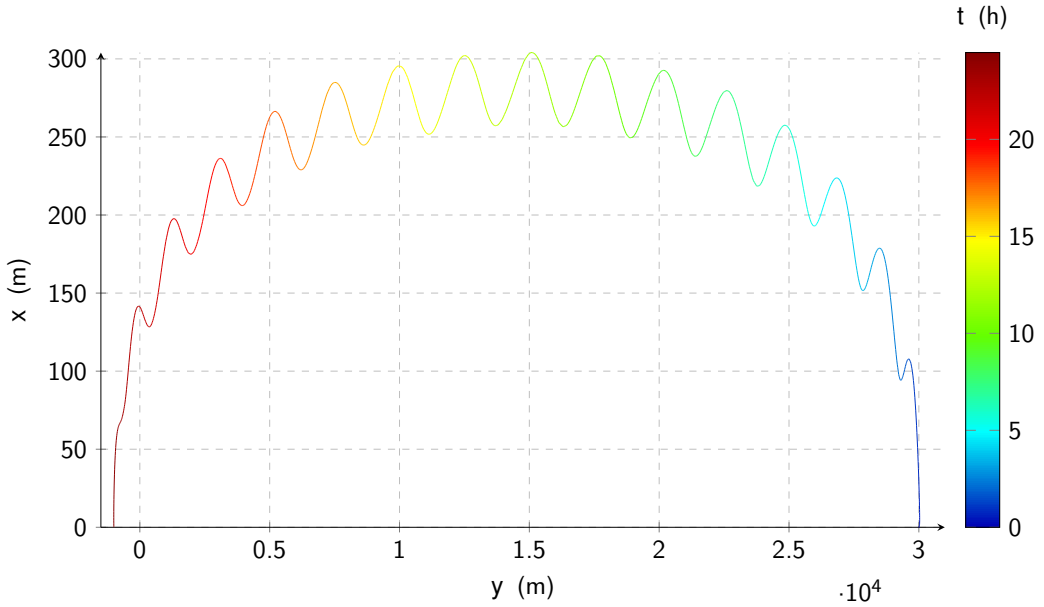

Figure 7.5: Relative in-plane trajectory of the deputy with respect to the chief plotted in the $\mathcal{L}$ - frame of the chief for an in-plane formation re-phasing maneuver with simultaneous out-of-plane regulation [167].

Table 7.4: Main results for case #1.

t_f (h)	Δa_c (m)	$t_{comp.}$ (h)
24.49	1717.32	3.62

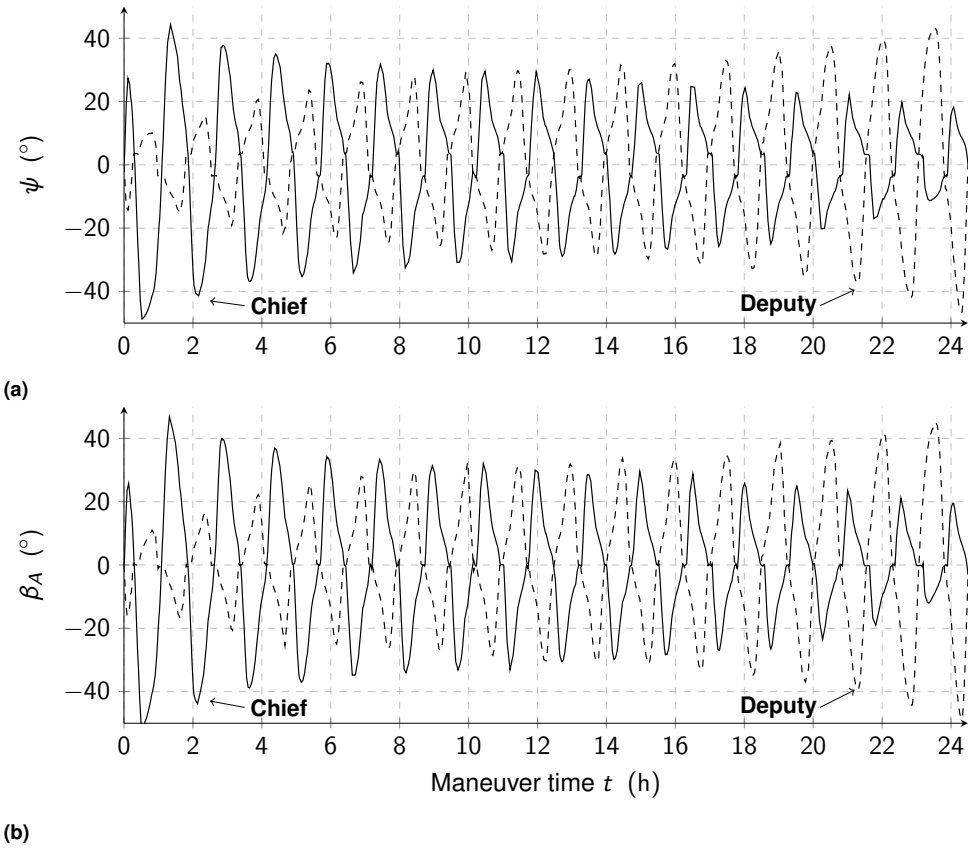

Figure 7.6: Resulting yaw angle $\psi(t)$ (top, a)) and angle of sideslip $\beta_A(t)$ (bottom, b)) profile of both satellites for an in-plane formation re-phasing maneuver with simultaneous out-of-plane regulation [167].

Table 7.5: Initial and final formation design for case #2.

	$v_t \left(\mathrm{m\,s^{-2}}\right)$	ρ_x (m)	$\bar{\alpha}_0$ (°)	ρ_z (m)	$\bar{\beta}_0$ (°)	d (km)
t_0	0	0	0	0	0	-30
t_f	0	125	0	80	90	0

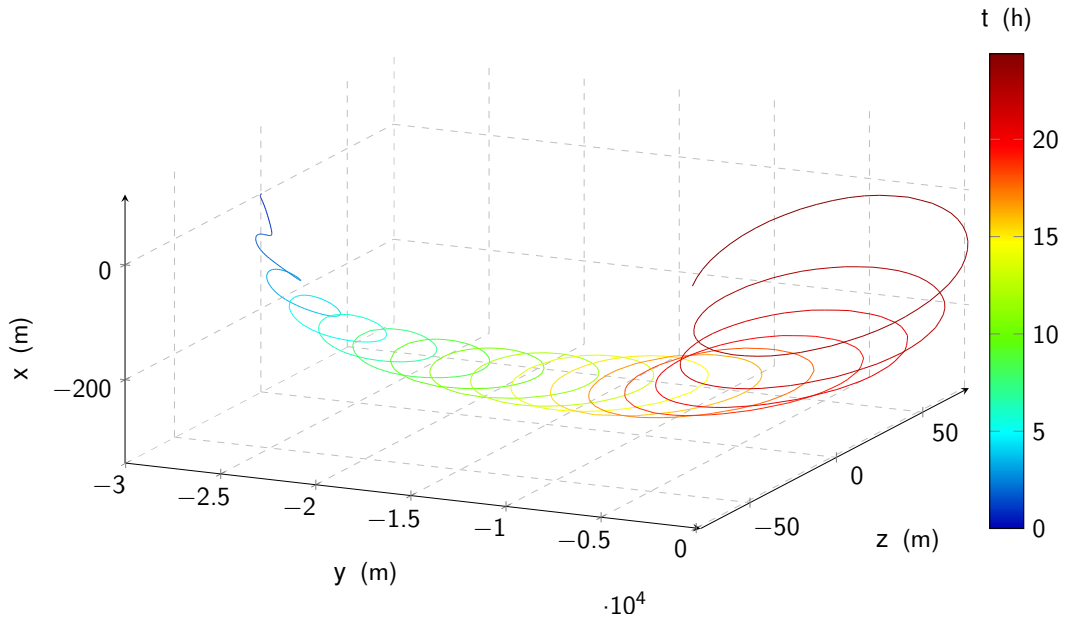

Figure 7.7: Relative maneuver trajectory of the deputy with respect to the chief plotted in the $\mathcal{L}$ - frame of the chief for an in-plane formation into a centred, bounded relative motion maneuver [167].

Case #2: In-plane formation into centered, bounded relative motion maneuver

In case #2, the satellites are guided from an in-plane formation into a centered, bounded relative motion ellipse. The initial and final states of the deputy with respect to the chief are listed in Tab. 7.5. The resulting three-dimensional relative maneuver trajectories of the deputy with respect to the chief plotted in the $\mathcal{L}$ - frame of the chief are depicted in Fig. 7.7, the in-plane relative motion trajectory in Fig. 7.8 and the yaw angle $\psi(t)$ and angle of sideslip $\beta_A(t)$ profiles for both satellites are depicted in Fig. 7.9. The main results of the maneuver are summarized in Tab. 7.6.

Table 7.6: Main results for case #2.

t_f (h)	Δa_c (m)	$t_{comp.}$ (h)
24.41	1669.47	3.04

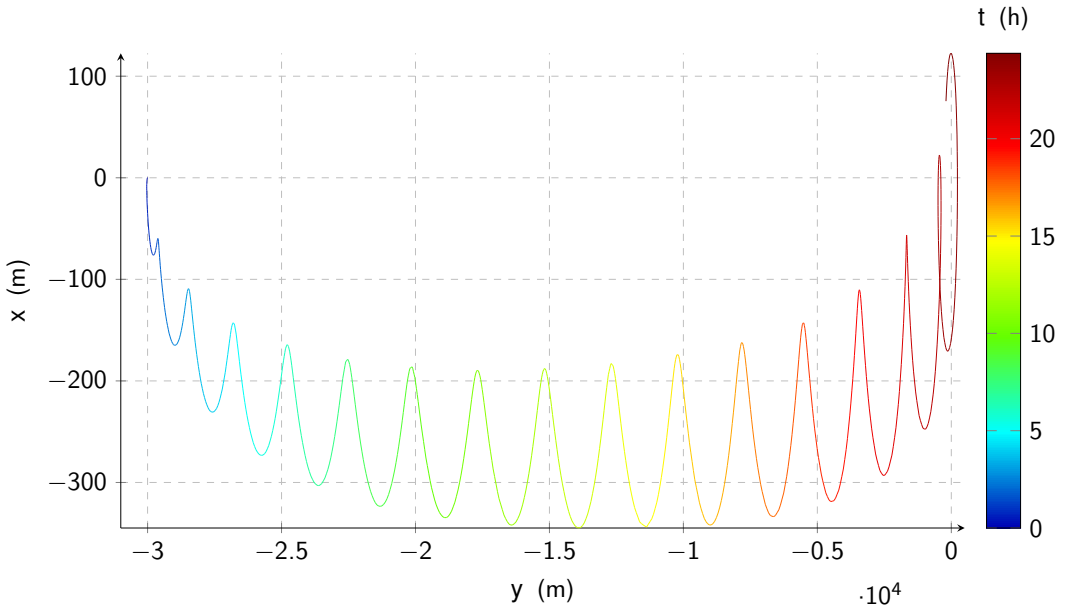

Figure 7.8: Relative in-plane trajectory of the deputy with respect to the chief plotted in the $\mathcal{L}$ - frame of the chief for an in-plane formation into a centred, bounded relative motion maneuver [167].

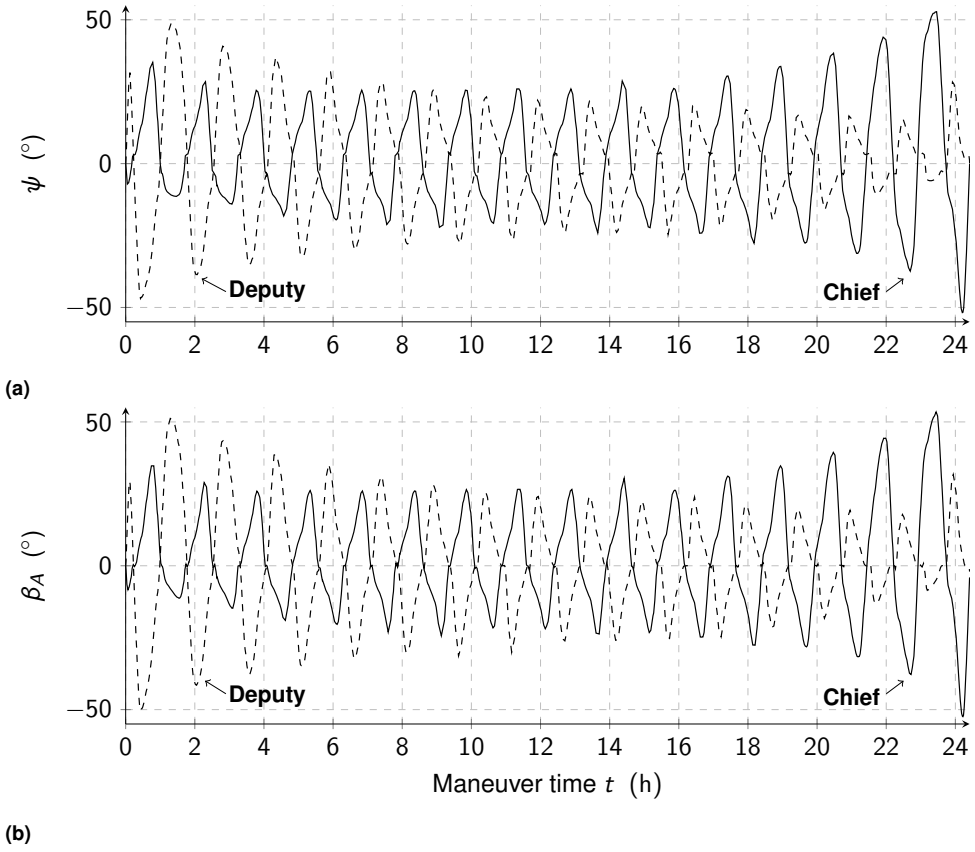

Figure 7.9: Resulting yaw angle $\psi(t)$ (top, a)) and angle of sideslip $\beta_A(t)$ (bottom, b)) profile of both satellites for an in-plane formation into a centred, bounded relative motion maneuver [167].

Table 7.7: Initial and final formation design for case #3.

	$v_t \left(\mathrm{m\,s^{-2}}\right)$	ρ_x (m)	$\bar{\alpha}_0$ (°)	ρ_z (m)	$\bar{\beta}_0$ (°)	d (km)
t_0	0	125	0	80	90	0
t_f	0	125	0	120	90	0

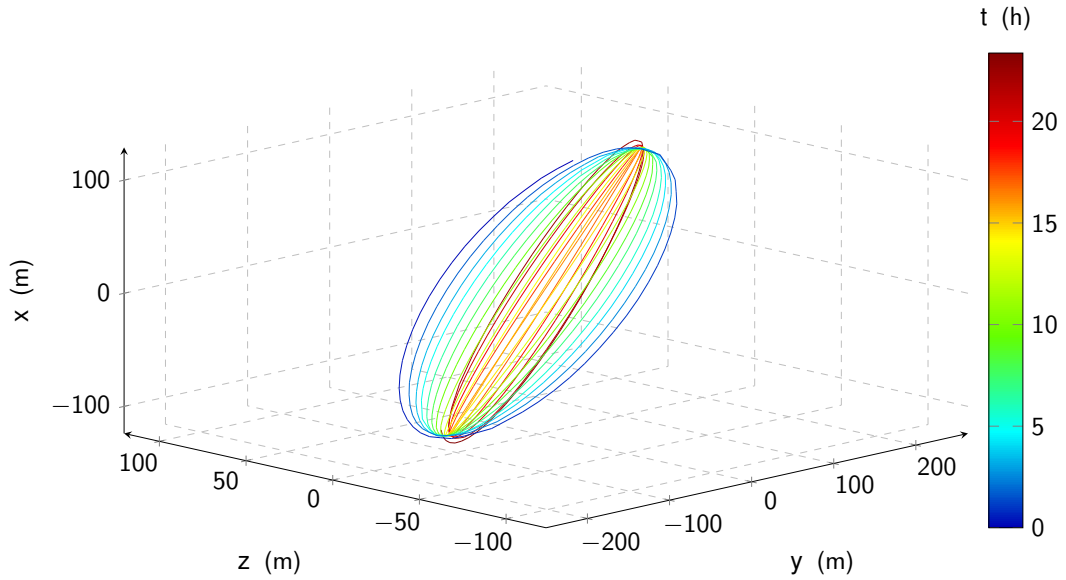

Figure 7.10: Relative maneuver trajectory of the deputy with respect to the chief plotted in the $\mathcal{L}$ - frame of the chief for a centered, bounded relative motion variation maneuver [167].

Case #3: Centered, bounded relative motion variation maneuver

In case #3, the out-of-plane motion of a centered, bounded relative motion ellipse is adjusted while the in-plane formation design remains unaltered. The initial and final states of the deputy with respect to the chief are listed in Tab. 7.7. The resulting three-dimensional relative maneuver trajectory is plotted in Fig. 7.10 and the in-plane relative motion trajectory in Fig. 7.11. The yaw angle $\psi(t)$ and angle of sideslip $\beta_A(t)$ profiles for both satellites are depicted in Fig. 7.12. Again, the phase angles of the initial and final formation design are chosen so that the formation is passively safe. The main results of the maneuver are summarized in Tab. 7.8.

Table 7.8: Main results for case #3.

t_f (h)	Δa_c (m)	$t_{comp.}$ (h)
23.38	1372.79	5.10

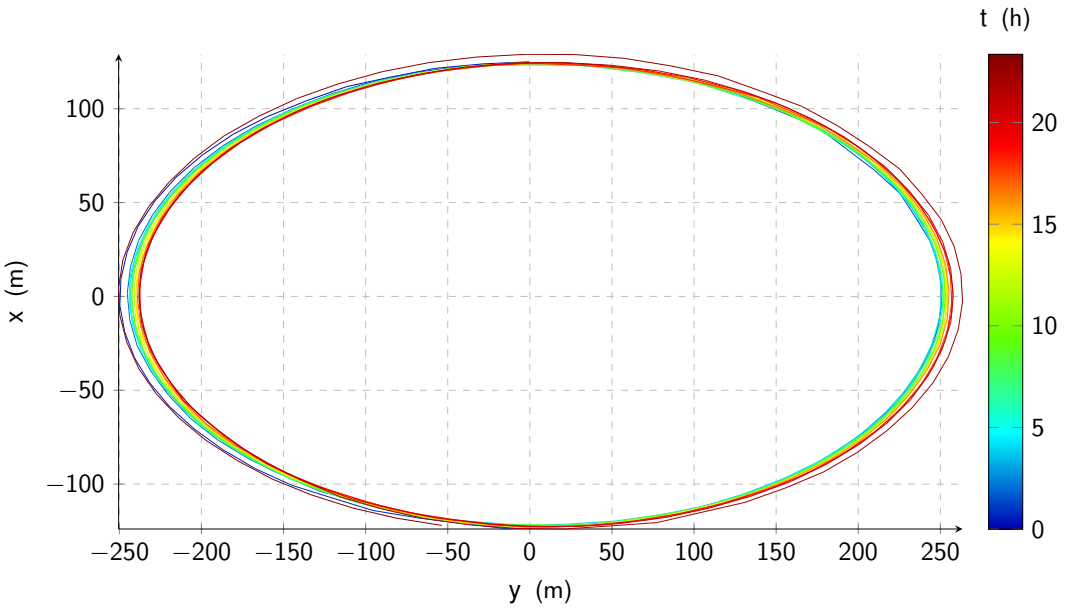

Figure 7.11: Relative in-plane trajectory of the deputy with respect to the chief plotted in the $\mathcal{L}$ - frame of the chief for a centered, bounded relative motion variation maneuver [167].

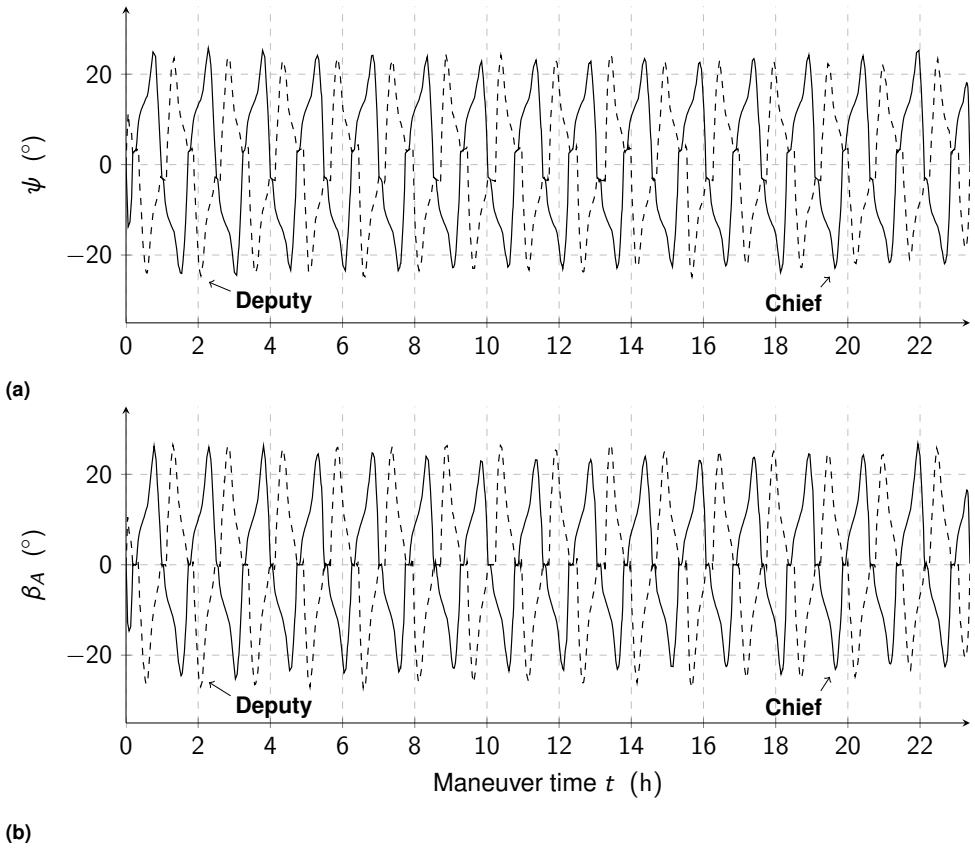

Figure 7.12: Resulting yaw angle $\psi(t)$ (top, a)) and angle of sideslip $\beta_A(t)$ (bottom, b)) profile of both satellites for a centered, bounded relative motion variation maneuver [167].

7.4 Open-loop control performance in a perturbed environment

To assess the performance of the maneuvers in a perturbed environment, the planned trajectory is compared to a 'real' trajectory generated by commanding the resulting yaw angle profiles $\psi_c^\star(t)$ and $\psi_d^\star(t)$ as open-loop control input. The 'real' relative motion is calculated from the individual, non-linear dynamics of both spacecraft simulated via an in-house built MATLAB® based 6-DoF propagator according to Cowell's method [179], in which the kinematics and dynamics are numerically integrated using MATLAB®'s *ode113* integrator [103]. Coordinate changes due to precession, nutation and polar motion are modeled according to Montenbruck and Gill [111]. Perturbing forces caused by third-body effects of the Sun and the Moon, solar-radiation pressure and higher harmonics of the Earth's gravitational potential up to order and degree six (EGM96)[89] are included. To calculate the aerodynamic properties of the satellites, the panel method in combination with Sentman's GSI model is used [149]. The energy accommodation coefficient α_T is dynamically calculated using the SESAM [124] model. The environmental conditions are calculated via the NRLMSISE-00 model [122]. The co-rotation of the atmosphere as well as horizontal winds ${}^{\mathcal{J}}\boldsymbol{v}_{wind}$, modeled via the Horizontal Wind Model (HWM14), are taken into account [40]. Attitude control is performed using three reaction wheels which are de-saturated using three-axis magnetic coils. The torques commanded to the reaction wheels to ensure an adequate tracking of the desired yaw angle profiles $\psi_c^\star(t)$ and $\psi_d^\star(t)$ as well as to compensate for perturbing torques are calculated via the quaternion feedback controller from Wie [191]. Momentum dumping is performed using the method proposed by Markley and Crassidis [99]. The World Magnetic Model is used to calculate the Earth's magnetic field [29]. Considered perturbing torques are gravity gradient torque and aerodynamic torque.

Exemplary, the case #2 maneuver presented in Subsection 7.3.3 will serve as the reference case which is assessed here in closer detail. In Fig. 7.13, the dynamic evolution of the real (full) and planned (dash dotted) relative $\mathcal{L}$ - states over the maneuver time is depicted. Qualitatively, the planned dynamic evolution of all states corresponds very well with the real evolution and all characteristic features of the real trajectory are replicated in the planned trajectory. Nevertheless, quantitative differences arise over time, especially with respect to the in-plane states. Due to their coupled nature, any miss-match between the real and the planned differential drag forces results in quantitative differences in δa which causes a secular drift in δu. The maneuver planner, however, is not able to model all occurring forces exactly. The following major differences between the planning process and the 6-DoF propagation need to be noted:

1. During the planning process a fit for $\beta_D(\beta_A)$ and $\beta_L(\beta_A)$ is used whereas within the 6-DoF propagator the panel method is dynamically applied.
2. The planner uses a linearized relative motion model whereas the 6-DoF propagator integrates the non-linear dynamics.
3. The 6-DoF propagator includes far more disturbing effects (e.g. third-body, solar radiation pressure, higher-order harmonics).
4. During the planning process the analytical density model is applied whereas within the 6-DoF propagator the NRLMSISE-00 model is employed.

5. Within the 6-DoF propagation, the desired yaw angle profile is not directly commanded but tracked via a quaternion feedback controller. Therefore, a slight delay is observable.

As an example, the inclusion of horizontal winds ${}^{\mathcal{J}}\boldsymbol{v}_{wind}$ causes changes in magnitude and direction of the residual differential drag and lift forces which, on the long term, results in a residual drift. To better assess the quality of the planner's modeling capabilities, Figs. 7.14 and 7.16 depict the dynamic evolution of relevant planned (dashed) and real (full) parameters over maneuver time t for the chief and the deputy satellite, respectively, whereas Figs. 7.15 and 7.17 display the resulting specific drag and lift forces[22]. Although the planner is able to replicate the dynamic processes, deviations are present over the duration of the maneuver. Prominent is the discrepancy in the magnitude of the relative velocity v_{rel}, which is caused by the thermospheric winds. With respect to out-of-plane relative motion, no secular drift occurs but a slight drift between the phases of the oscillatory motion can be observed. The peak distances, however, are modeled with sub-meter accuracy. To conclude, Fig. 7.18 shows the real (solid, black) and the planned (dash-dotted, colored) relative in-plane trajectories and Fig. 7.19 the real (full, black) and the planned (dash-dotted, colored) relative trajectories for comparison. More accurate tracking in a perturbed environment can hardly be achieved by open-loop control methods, but closed-loop robust methods are required. This becomes especially important when further uncertainties are added, such as the measurement noise of the GPS sensors.

7.5 Summary

In this chapter, a planning tool for three-dimensional satellite formation flight maneuvers using differential aerodynamic forces has been presented. Efforts were made to take all practicability considerations into account during the development. In summary, the main advantages of the presented planning tool are:

1. Differential lift and drag can be applied *simultaneously* via yaw angle $\delta\psi$ deviations.
2. The maneuver is planned optimal in the sense that the decay of the chief satellite Δa_c during the maneuver is minimized.
3. The resulting control profile avoids chattering or bang-bang type control switches.
4. Arbitrary formation flight maneuvers within the bounds of possibilities can be planned and the desired initial and final relative states defined via the descriptive set of parameters ${}^{\mathcal{L}}\bar{\boldsymbol{\alpha}} = \left\{\rho_x,\ d,\ \rho_z,\ v_d,\ \bar{\alpha}_0,\ \bar{\beta}_0\right\}$ which are well known from the solutions to the CW equations.
5. Mean differential nearly-nonsingular orbital elements $\delta\bar{\boldsymbol{\varepsilon}}_{ns}$ and mean nearly-nonsingular orbital elements $\bar{\boldsymbol{\varepsilon}}_{ns}$ are employed, which are well suited for near-circular orbits.

In addition, the planning tool takes all dominant perturbation effects in VLEO into account, i.e., the J_2 effect and aerodynamic forces. For aerodynamic forces, varying atmospheric densities, the co-rotation of the Earth, and the fundamentals of gas-surface interactions are taken into account. The boundary conditions can be varied in a highly flexible manner, allowing parameter studies aimed at exploring and outlining the design space of possible maneuver variants. These are included in the third part of this dissertation, denoted as ***analysis and optimization***.

[22] For clarity, not the entire maneuver is shown but only the first 5 h.

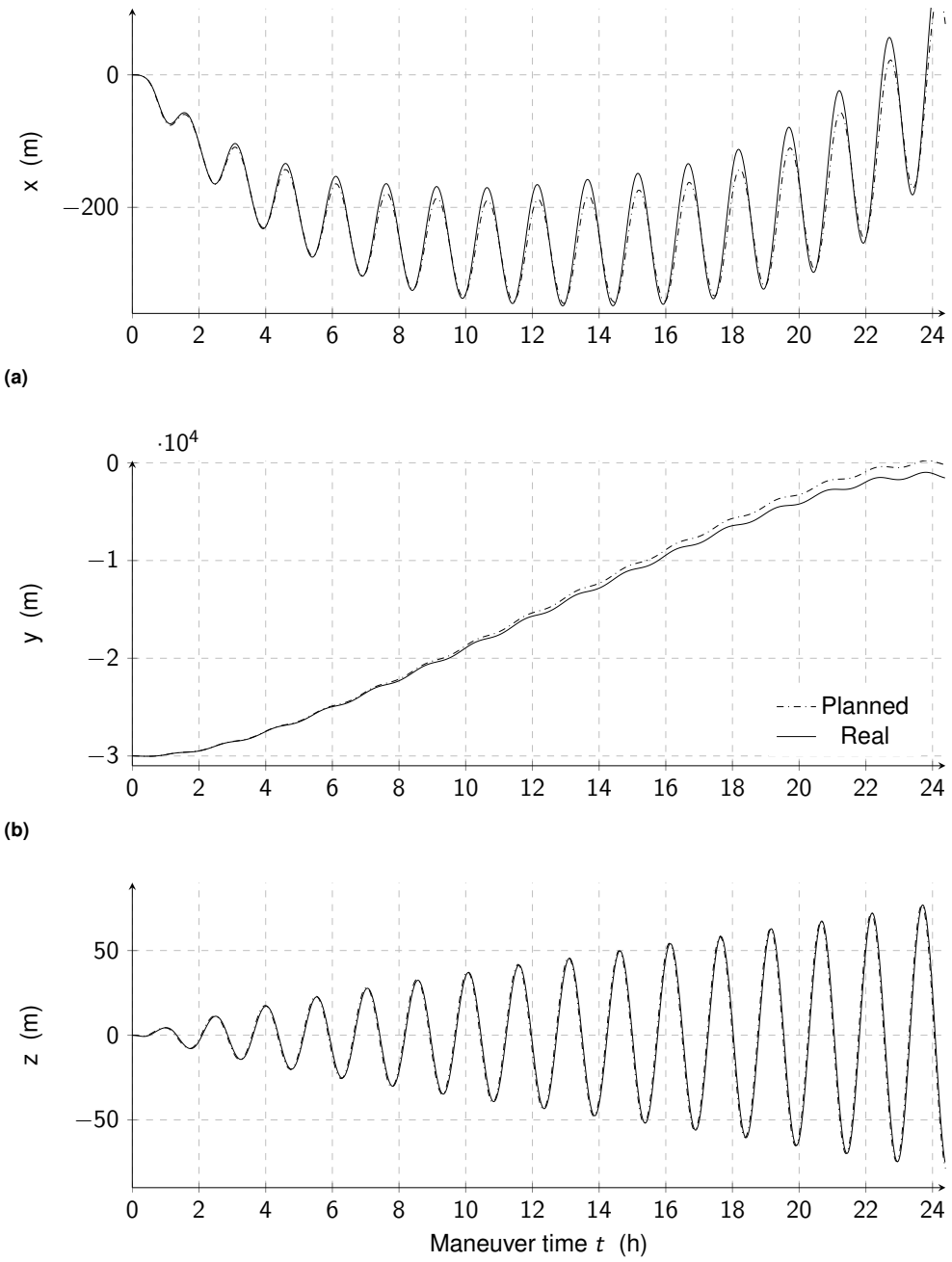

Figure 7.13: Dynamic evolution of the real (full) and planned (dash dotted) relative $\mathcal{L}$ - states over the maneuver time.

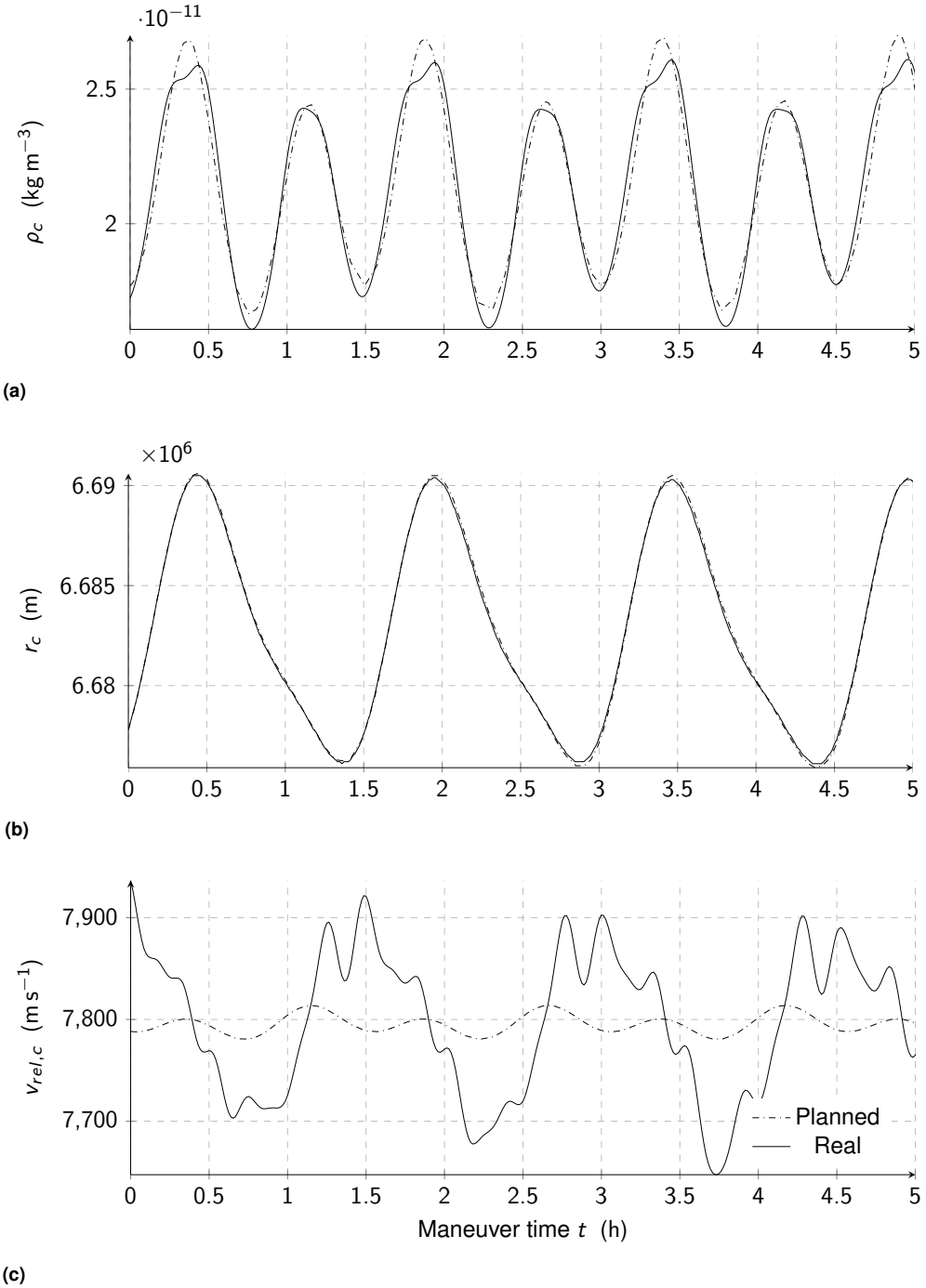

Figure 7.14: Dynamic evolution of planned (dashed) and real (full) maneuver parameters over maneuver time for the chief satellite.

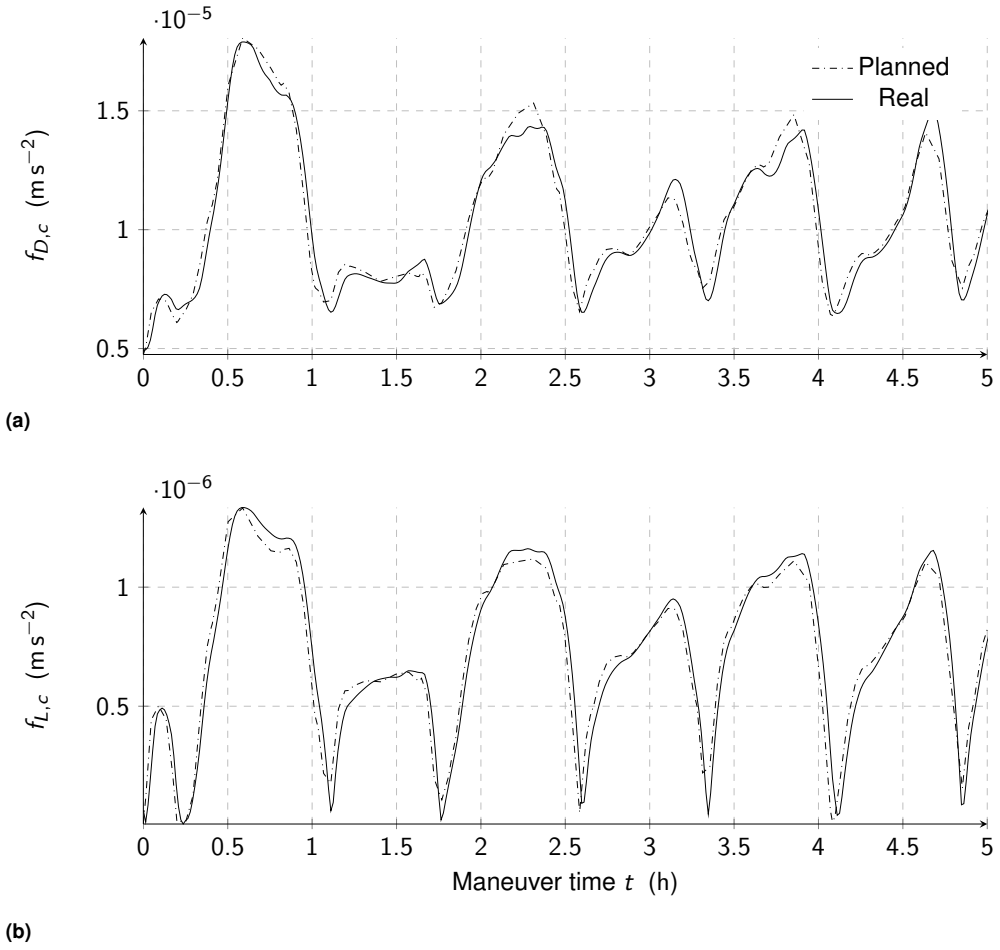

Figure 7.15: Dynamic evolution of the planned (dashed) and real (full) specific drag (top) and lift (bottom) force over maneuver time for the chief satellite.

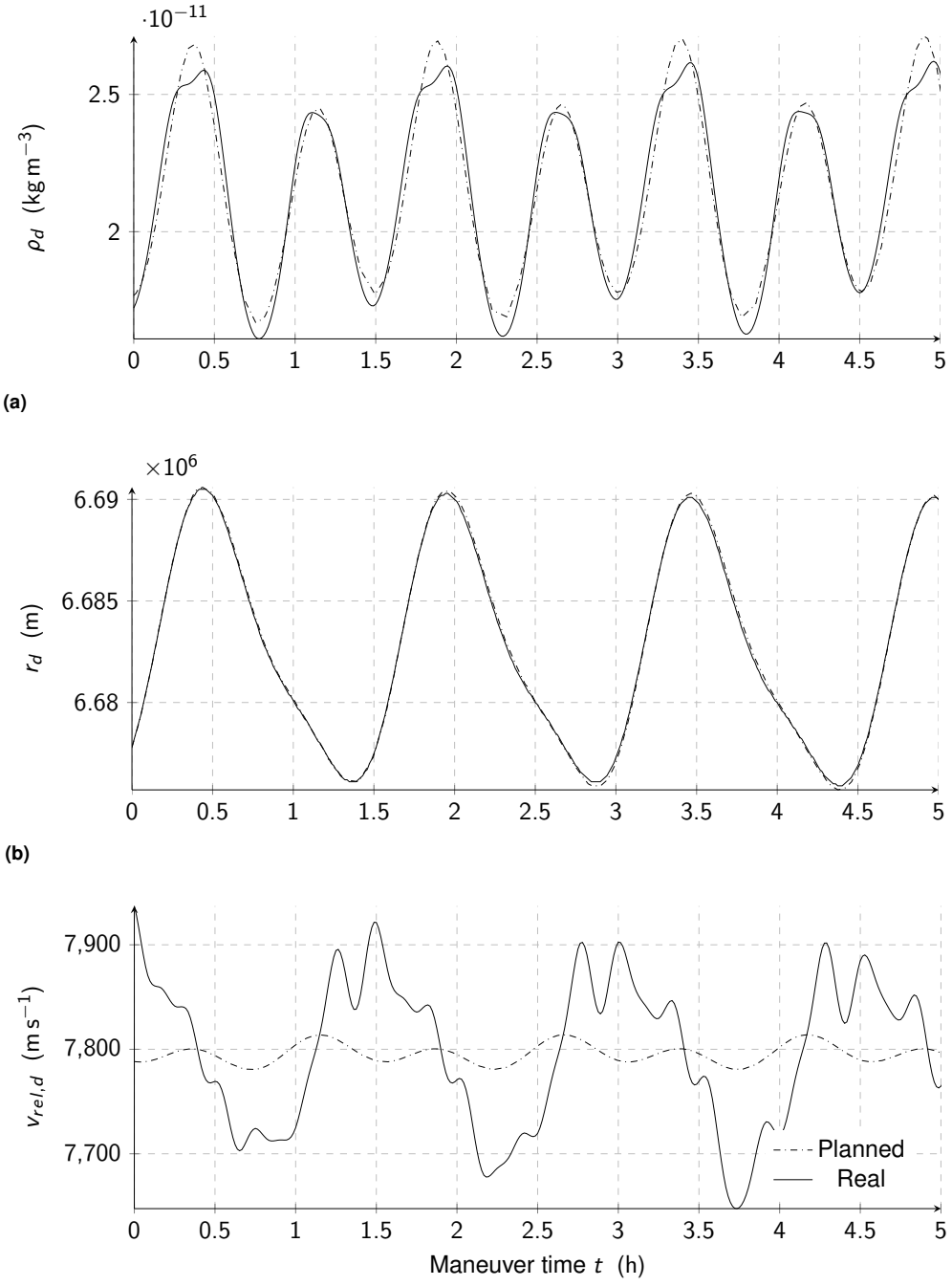

Figure 7.16: Dynamic evolution of relevant planned (dashed) and real (full) maneuver parameters over maneuver time for the deputy satellite.

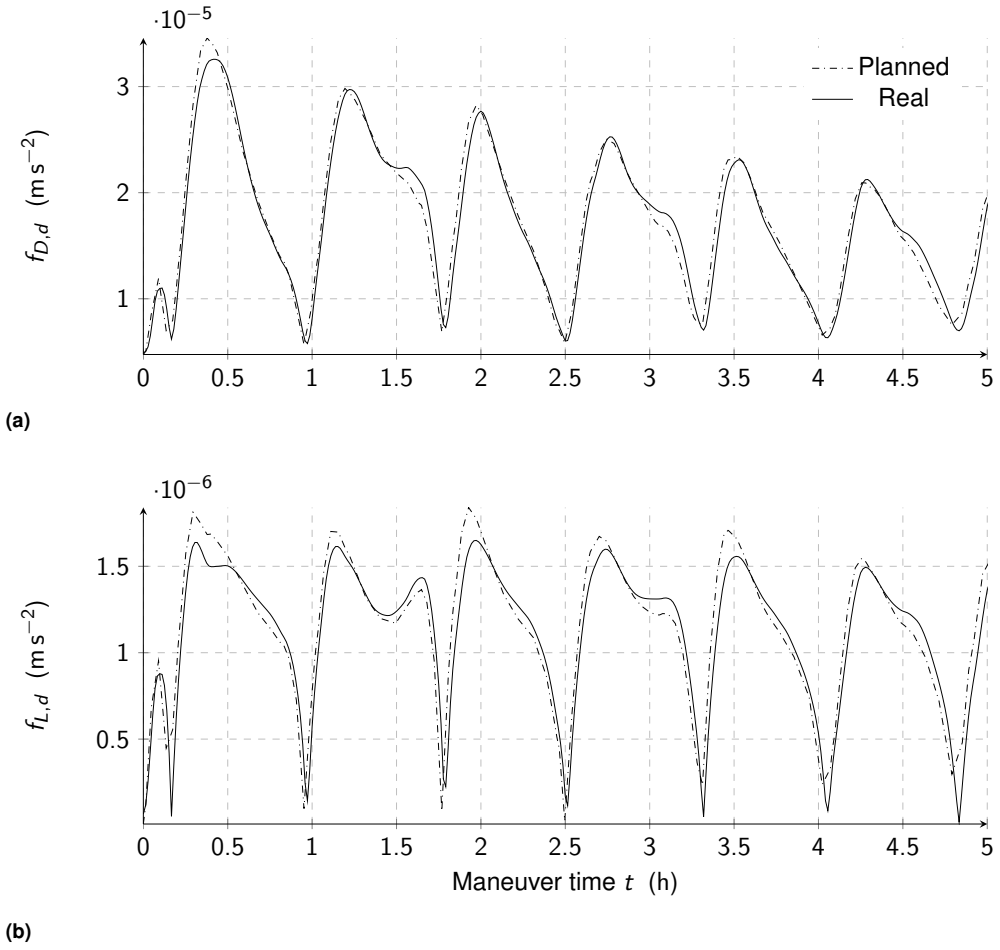

Figure 7.17: Dynamic evolution of the planned (dashed) and real (full) specific drag (top) and lift (bottom) force over maneuver time for the deputy satellite.

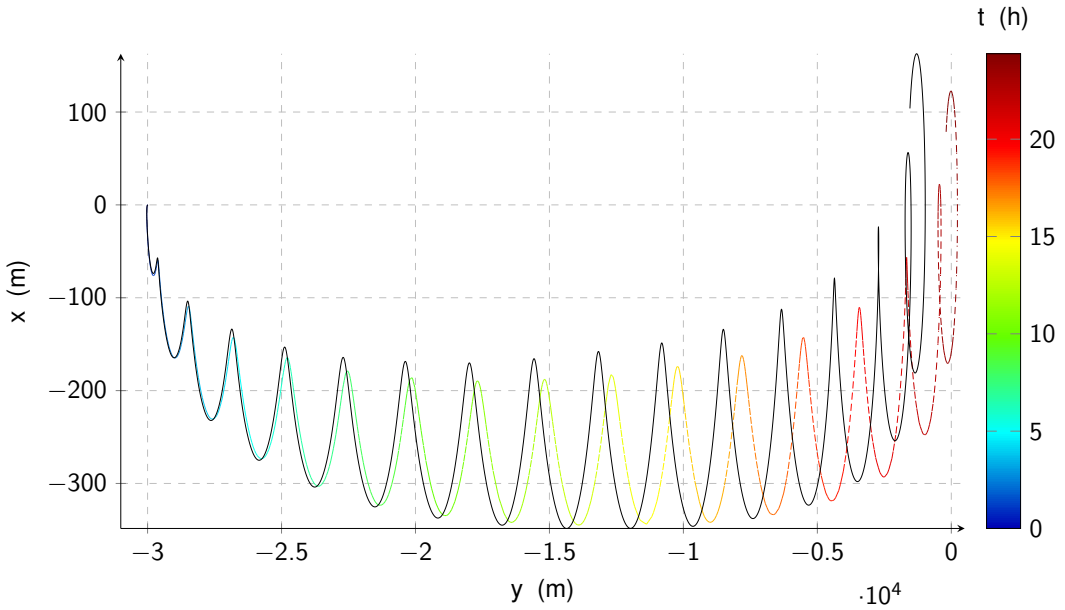

Figure 7.18: Planned (dash dotted, colored) and executed (full, black) relative in-plane trajectory of the deputy with respect to the chief plotted in the $\mathcal{L}$ - frame of the chief for an in-plane formation into a centred, bounded relative motion maneuver (case #2).

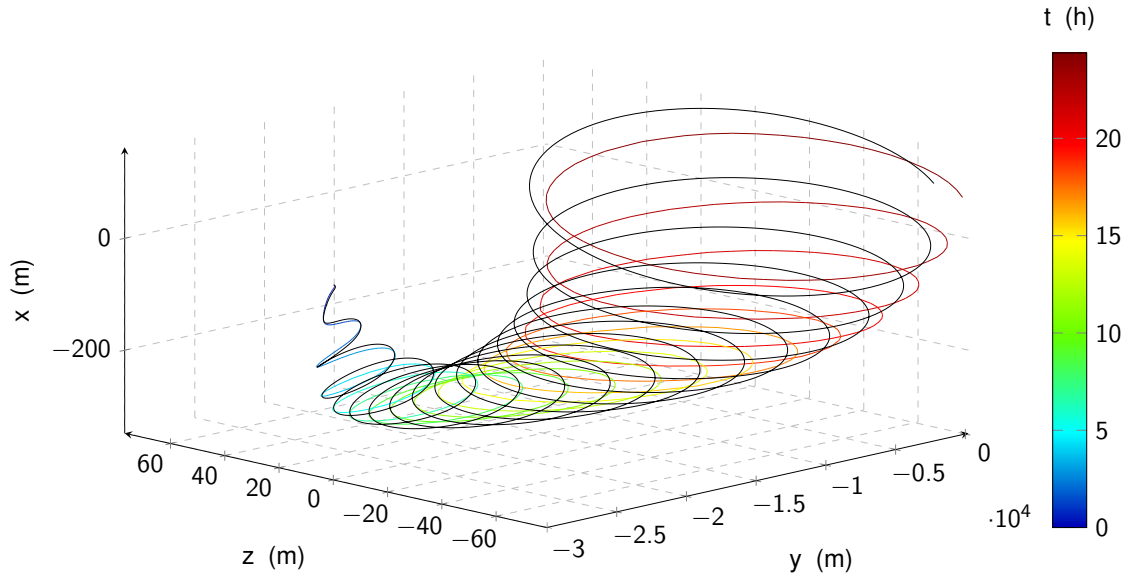

Figure 7.19: Planned (dash dotted, colored) and executed (full, black) relative trajectory of the deputy with respect to the chief plotted in the $\mathcal{L}$ - frame of the chief for an in-plane formation into a centred, bounded relative motion maneuver (case #2).

Part III

Analysis and optimization

Chapter 8

Analysis and discussion

"Any fool can know. The point is to understand."

— Albert Einstein

8.1 Analysis

In this section, optimal simultaneous in- and out-of-plane control via yaw angle deviations $\delta\psi$ is comprehensively characterized and discussed.

8.1.1 Optimal simultaneous control with minimal decay

Achieving optimal simultaneous in- and out-of-plane control

The variety of maneuver cases presented in Subsection 7.3.3 (case #1 - #3) provides insights on how an optimal simultaneous control of the in- and out-of-plane relative motion via yaw angle deviations $\delta\psi$ can be achieved:

Case #1: Case #1 serves as a representative example. In the initial formation design, the deputy is leading the in-plane formation by $d_0 = 30\,\mathrm{km}$. As during the maneuver the order of the two spacecraft is to be switched ($d_f = -1\,\mathrm{km}$), the chief has to catch up with respect to the deputy, which can be achieved by orbiting at a lower altitude with a shorter orbital period P. To do so, the chief needs to lose altitude with respect to the deputy. Thus, larger absolute angles of sideslip values are commanded to the chief with respect to those commanded to the deputy (see Fig. 7.6). As a consequence, the absolute value of the chief's rate of decay $|\dot{a}_c|$ surpasses the one of the deputy $|\dot{a}_d|$ and the difference in the semi-major axes δa increases accordingly (note the negative sign due to sign $(\delta\dot{a}) < 0$). However, as during the maneuver also the remaining out-of-plane motion is to be regulated, the satellites are forced to change the sign of the respective sideslip angles $\beta_A(t)$ in an oscillatory, coordinated and counter-rotating manner. According to the nature of the out-of-plane relative motion, the sign changes twice per orbit. In the course of the maneuver, the absolute values of the angles of sideslip of the chief gradually decrease while, conversely, the corresponding values for the deputy increase. This is required to establish a

stable formation at the end of the maneuver, for which the semi-major axes of the two spacecraft must be adjusted accordingly ($\delta a\left(t_f\right) = 0\,\mathrm{m}$).

Case #2: Case #2 differs from case #1 in the sense that the order of the initial formation design is reversed. Therefore the deputy is *trailing* the in-plane formation at the beginning ($d_0 = -30\,\mathrm{km}$). In addition, the final formation design consists of a passively stable, three-dimensional relative motion ellipse ($d_f = 0\,\mathrm{m}$ but $\rho_{x,f}, \rho_{z,f} \neq 0\,\mathrm{m}$). Accordingly, the general course of the angle of sideslip profile $\beta_A(t)$ shown in Fig. 7.9 is opposite to the profile shown in Fig. 7.6. However, as the difficulty of the maneuver tasks, i.e., the in-plane maneuvering distance Δd and the desired out-of-plane adjustments $\Delta\rho_z$ with respect to the available maneuvering time t_f, is in a comparable range to case #1, the absolute values of $\beta_A(t)$ largely correspond. Only in the beginning of the maneuver, an asymmetric profile for the chief is apparent which differs from the profile in case #1. This is required to initiate the oscillating in-plane motion. In any case, a stable formation after the maneuver is ensured by adjusting the semi-major axes of both spacecraft.

Case #3: Case #3 substantially differs from case #1 and case #2 because the center of the bounded relative ellipse of motion of the deputy before and after the maneuver is located right at the chief $d_0 = d_f = 0\,\mathrm{m}$ and, consequently, no in-plane distance is to be covered ($\Delta d = 0\,\mathrm{m}$). To achieve an adjustment of the out-of-plane motion while maintaining the in-plane formation design, only differential lift but little to no differential drag is required. This can be achieved by rotating both satellites in opposite directions to similar angles of sideslip values ($\beta_{A,c}(t) \approx -\beta_{A,d}(t)$), which is illustrated in Fig. 7.12.

Implications of the cost function on the control profile

This subsection examines how the goal of reducing the decay during the maneuver affects the evolution of the control profile. In this respect, the overall (or total, subscript t) decay Δa_t is subdivided into the following three types of decay:

$$\Delta a_t = \Delta a_n + \Delta a_i + \Delta a_e. \tag{8.1}$$

- **Type #1 - Natural decay Δa_n:** The minimum level of decay a satellite orbiting in VLEO experiences for a given maneuver time t_f, i.e., when orbiting for t_f in its minimum drag configuration ($\beta_A\left(t\right) = 0^\circ = \text{const.}$).
- **Type #2 - Induced decay Δa_i:** Additional decay generated by the associated drag forces resulting from purposely commanded differential lift control inputs (out-of-plane control).
- **Type #3 - Exploited decay Δa_e:** Additional decay generated by the increased drag forces resulting from purposely commanded differential drag control inputs (in-plane control).

Based on these definitions optimal maneuver strategies, the associated control profiles as well as their implications on the resulting decay are assessed in the following.

Pure in-plane control: In the case of pure in-plane control, a desired secular drift rate has been established by purposely reducing the orbital altitude of the satellite, which represents exploited decay by definition. To minimize the overall decay, the minimal level of exploited decay

required to successfully perform the maneuver task in the given maneuver time t_f is commanded. Consequently, in analogy to the fuel-optimal control of a double integrator for a given maneuver time, the longer the available maneuver time t_f the less exploited decay is required whereas, vice versa, achieving shorter maneuver times requires larger values of exploited decay (in the borderline case, the in-plane control corresponds to the bang-bang control pattern for the time-optimal control of a double integrator). Once the desired drift rate is established, both satellites orbit in their minimum drag configuration. Then, they passively drift until a second control intervention zeros this drift out again (in analogy to the differential drag maneuvers presented in [167]). During these passive phases, nothing but natural decay is observed. In case of differential drag, having both satellites deviate from the minimum drag configuration at the same time neither augments the available differential drag force nor minimizes the resulting overall decay, so that both requirements are complementary.

Pure out-of-plane control: In the case of pure out-of-plane control, both satellites actively oscillate in opposite directions to similar angle of sideslip values ($\beta_{A,c}(t) \approx -\beta_{A,d}(t)$) as a result of the sinusoidal nature of the dynamics. As there is no lift without drag, induced drag, which represents an unwanted byproduct, is constantly produced. The most effective means to minimize the overall decay is to limit the peak angles of sideslip values to the minimum which is sufficient for the control task within t_f. The value is dependent on the difficulty of the task, i.e., on the out-of-plane distance to be adjusted $\Delta\rho_z$ with respect to t_f. In case of differential lift, allowing both satellites to deviate from the minimum drag configuration augments the available differential lift force but, vice versa, has detrimental effects on the resulting overall decay so that both are contradictory requirements.

Simultaneous in- and out-of-plane control: In case of optimal simultaneous in- and out-of-plane control, the challenge is to combine the competing requirements as good as possible. To characterize an optimal maneuver, a brief recall of the fundamental difference between the induced Δa_i and exploited Δa_e decay is required. Whereas induced decay represents an undesirable by-product which inevitably results from differential lift control inputs, exploited decay is intentionally generated for in-plane control purposes. Taking this difference into account, an ideal maneuver can be defined. A maneuver is ideal, i.e., the simultaneous control maximum efficient, when (a) the induced decay resulting from the out-of-plane control is minimized and (b) it is effectively exploited for the in-plane control purpose. Both requirements are met if only one satellite deviates from the minimal drag configuration and the range of the commanded angle of sideslip values is within the range of $|\beta_A| \in [0°, \approx 45°]$. If this is the case, the in-plane control task determines which satellite is to rotate, whereas the out-of-plane control task determines the direction of rotation[23]. The values of the respective angles of sideslip are dependent on the difficulty of the maneuver task. Such an ideal maneuver, however, can only be accomplished if both control tasks are well balanced and simple enough to be achieved with only a fraction of the maximum available control forces. Since these insights represent a key result of this dissertation, this shall be elaborated in closer detail.

[23] If it is sufficient to rotate only one satellite, the out-of-plane control task can be accomplished via a rotation of either one of the satellites as this can be accounted for via the direction of rotation.

To fulfill condition (a), only one of the satellites is allowed to deviate from the minimal drag configuration. As this directly reduces the magnitude of the available differential lift force, it is only a suitable option if the out-of-plane control task can be completed in the given maneuver time. The higher the demands on the out-of-plane control task, the more it must be deviated from this practice. In this case, it is inevitable that both satellites rotate contrariwise to achieve sufficiently large control forces. However, for pure differential lift control inputs, large levels of decay are induced which do not support the in-plane control task at all.

To fulfill condition (b), the level of induced decay must match the level of decay required to accomplish the in-plane control task as good as possible. If this is the case, no dedicated exploited decay is required and the overall decay is minimized. A secondary condition is that the maneuver can be accomplished with angles of sideslips between $\beta_A = 0°$ and the value at which the maximum lift force can be achieved, at $|\beta_A| \approx 45°$. If the in-plane control task is more demanding, it must be deviated from this procedure and resorted to larger angles of sideslip $|\beta_A| > 45°$. If this is the case, however, requirement (a) can no longer be met, as the level of induced decay is by no means minimal. In the worst case, ternary drag states ($|\beta_A| = 90°$) are required, for which no differential lift is produced at all. Whenever this is the case, dedicated exploited decay is commanded and no efficient simultaneous control realized.

Key finding: In summary, ideal simultaneous in- and out-of-plane control can be realized whenever the maneuver requirements can be met with (a) only one satellite deviating from the minimum drag configuration and (b) angles of sideslip within the range of $|\beta_A| \in [0°, \approx 45°]$. In this case, the induced decay is at a minimum and effectively exploited for in-plane control purposes. With respect to the control profile, the in-plane task determines which satellite is to rotate, whereas the out-of-plane control task determines the direction of rotation. The ideal case, however, is more a theoretical concept, as it represents a special case for which the demands on both control tasks are relaxed and perfectly balanced. If these requirements are almost met, which represents a more practicable condition, the maneuver is referred to as quasi-ideal. In any case, the simultaneous control is achieved efficiently whenever the induced decay can be exploited for in-plane control purposes. Vice versa, maneuvers become very inefficient when both control tasks are clearly imbalanced or when the overall maneuver task is too demanding. At some point it even becomes inevitable to resort to the ternary states, which are optimal for the individual control task but by no means for the simultaneous control. As a consequence, the resulting overall decay strongly depends on nature of the maneuver task, i.e., the balance of the difficulty of the out-of-plane control task $\Delta\rho_z$ with respect to the difficulty of the in-plane task Δd for a given maneuver time t_f, which will be assessed in closer detail in the following subsections.

8.1.2 Exploring the design space of possible maneuver variants

The developed tools and methods enable to perform parameter studies to explore and outline the design space of possible maneuver variants. In this subsection, the results of selected assessments are presented. To ensure comparability, case #2 from Subsection 7.3.3 is employed as a reference case on the basis of which the influence of various parameters is assessed.

Table 8.1: General results for the parameter study assessing the implications of $\rho_z(t_f)$ variations on the resulting orbital decay Δa_c for maneuver case #2.

$\Delta\rho_z$ (m)	Δa_c (m)	t_f (h)	$+\Delta a_c$ (m)	$+\Delta a_c$ (%)
0	1127.11	24.80	-	-
20	1169.17	24.87	42.06	3.73
40	1393.53	24.59	266.42	23.64
60	1406.35	24.38	279.24	24.77
80	1669.47	24.41	542.36	48.12
100	2129.97	23.42	1002.86	88.98
120	2556.75	24.04	1429.64	126.84

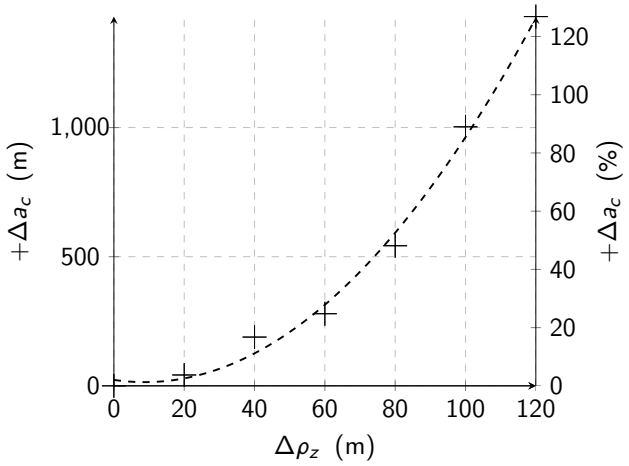

Figure 8.1: Increase in the resulting decay Δa_c for the case #2 maneuver with increasing demand on the out-of-plane control task with respect to the case with $\rho_z(t_f) = 0$ m. The dashed curve represents the squared fit.

The influence of the nature of the maneuver task

In this subsection, the influence of the nature of the maneuver task is assessed, i.e., the balance of the difficulty of the out-of-plane with respect to the difficulty of the in-plane control task. To do so, the parameter governing the difficulty of the out-of-plane task $\Delta\rho_z$ is increased in discrete steps of $+\Delta\rho_z = 20$ m from $\Delta\rho_z = 0$ m to $\Delta\rho_z = 120$ m to successively shift the characteristics of the maneuver task from being basically purely in-plane towards including a demanding out-of-plane component. To ensure comparability, all other boundary conditions remain unchanged. The general results of this parameter study are summarized in Tab. 8.1 and depicted in Fig. 8.1[24]. For less demanding out-of-plane adjustments, simultaneous control can be achieved very efficiently, e.g. with an increase in overall decay of $+\Delta a_c = 3.73\,\%$ for $\Delta\rho_z = 20$ m, as a large part of the induced decay resulting from the out-of-plane control can be exploited for in-plane control purposes. The higher the demands on the out-of-plane adjustments, however, the more dedicated and pure differential lift control inputs are needed, which induces additional decay that

[24]Notably, a maneuver with $\Delta\rho_z = 0$ m does not correspond to a pure in-plane control maneuver, as in this case $\rho_z z(t_f)$ would remain unconstrained.

Table 8.2: Increase in decay for different maneuver times with respect to the global minimum of $\Delta a_{c,min} = 1659.76\,\text{m}$ achieved at $t_f = 24.89\,\text{h}$ for maneuver case #2.

n_i	t_f (h)	Δa_c (m)	$+\Delta a_c$ (m)	$+\Delta a_c$ (%)
13	18.91	1938.37	278.61	16.79
14	20.37	1757.76	98.00	5.90
15	22.97	1697.01	37.25	2.24
16	24.41	1669.47	9.71	0.59
17	24.89	1659.76	-	-
18	26.40	1677.85	18.09	1.09
19	27.91	1685.97	26.21	1.58
20	30.38	1721.23	61.48	3.70
23	35.12	1828.98	169.22	10.20
26	38.47	2004.12	344.36	20.75

does not serve to fulfill the in-plane task. Consequently, the overall decay significantly increases. At this point, the different dimensions of the control possibilities must be emphasized: while an in-plane distance of $\Delta d = 30\,\text{km}$ is covered, the explored range in the out-of-plane direction is $\Delta\rho_z \in [0\,\text{m}, 120\,\text{m}]$, which represents $0 - 0.4\,\%$ of the in-plane distance. Nevertheless, the out-of-plane adjustments result in an increase in the resulting decay of up to 126.84 %.

Key finding: In orbital mechanics, any change to the orientation of the orbital plane, i.e., to Ω and/or i, requires large control inputs. This circumstance combined with the low lift coefficients experienced in orbit so far drastically limits the possibilities for out-of-plane adjustments via differential lift. Moreover, the low lift to drag ratios C_L/C_D render it very expensive in terms of the resulting decay. Vice versa, efficient long distance in-plane maneuvers can be scheduled by exploiting its instable nature.

The influence of the maneuver time t_f

A critical parameter determining the difficulty of the maneuver is the available maneuver time t_f. Shorter maneuver times necessitate larger control inputs and levels in exploited and induced decay. Longer maneuver times require less control inputs and result in larger levels in natural decay. Thus, the question arises for which maneuver time t_f the global minimum in overall decay can be achieved. In addition, more in-depth insights into the dependence of the available maneuver time t_f and the resulting decay $\Delta a_c(t_f)$ are desired. Thus, case #2 has been re-scheduled for different $t_{f,g}$ in the range of $t_{f,g} = n_i P_{c,O}$ with $n_i = [13, 26]$ and a resulting admissible range of $t_{f,min} = \left(n_i - 1/2\right) P_{c,O}$ and $t_{f,max} = \left(n_i + 1/2\right) P_{c,O}$ each. The results of this study are listed in Tab. 8.2 and depicted in Fig. 8.2 (left, (a)).

The global minimum in terms of the overall decay for case #2 under the given boundary conditions is $\Delta a_{c,min} = 1659.76\,\text{m}$ and can be achieved at $t_f = 24.89\,\text{h}$. For shorter maneuver

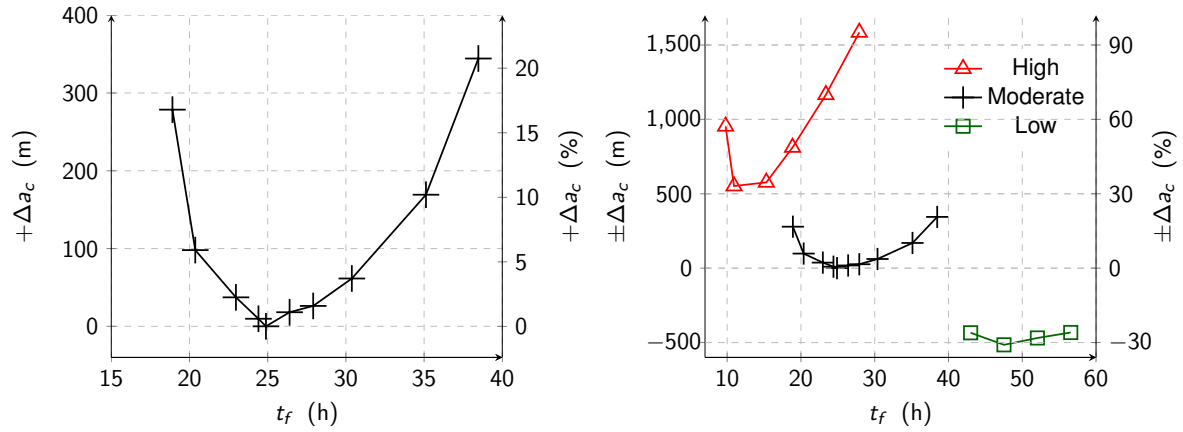

(a) **(b)**

Figure 8.2: Influence of the maneuver time t_f on the resulting decay Δa_c with respect to the global minimum of $\Delta a_{c,min} = 1659.76$ m achieved at $t_f = 24.89$ h for maneuver case #2 for moderate conditions (left) and for long term high, moderate and low space weather conditions (right).

times, the overall decay increases as more severe control inputs are required (increased levels of exploited and induced decay), which prevents an efficient application of simultaneous control. In this case, the two control tasks are addressed rather individually, resulting in a control pattern which is separated into different sections during which the individual optimal control for the respective tasks is applied. For longer maneuver times, however, contrary to the ordinary fuel-optimal control approach of a double integrator, the overall decay increases alike. This is because, even during coasting periods, atmospheric drag is constantly acting upon the satellites and causing them to naturally decay (representing natural decay by definition).

Note: This discussion also emphasizes that a comprehensive examination of the methodology requires an equal consideration of the relative and absolute motion. This is enabled with the developed planning tool and represents an essential contribution.

The influence of the solar and geomagnetic activity

The magnitude of the specific aerodynamic drag and lift forces acting on any satellite in VLEO depends on the environmental bulk properties (summarized in q) and spacecraft design-depending parameters (summarized in β_D or β_L, respectively). Whereas any effort targeting the optimization of the spacecraft design directly influences the profile of β_D and β_L, the environmental bulk properties are a result of the orbit design (via $\boldsymbol{v}$ and ρ) and the current thermospheric conditions (primarily via ρ), for which there is little to no possibility to act upon them externally. Consequently, they represent a critical boundary condition in mission planning. To analyze the effects of this boundary condition case #2 has been re-scheduled for the two extreme cases listed in Tab. 3.1.

With respect to the discussions on the different types of decay from the previous subsections, the environmental conditions have a direct impact on the natural decay only. While these correspondingly also influence the available authority of both control forces, the effects on the level of induced and exploited decay can be intercepted via a yaw angle profile adjustment.

Table 8.3: Increase in decay for the case #2 maneuver for long term high space weather conditions with respect to the minimum of $\Delta a_{c,min} = 1659.76\,\text{m}$ achieved at $t_f = 24.89\,\text{h}$ for maneuver case #2 under moderate conditions.

n_i	t_f (h)	Δa_c (m)	$+\Delta a_c$ (m)	$+\Delta a_c$ (%)
6	9.79	2613.02	953.26	57.43
7	10.93	2211.76	552.01	33.26
10	15.31	2236.24	576.48	34.73
13	18.86	2471.09	811.33	48.88
16	23.38	2825.28	1165.52	70.22
19	27.91	3244.21	1584.46	95.46

Table 8.4: Decrease in decay for the case #2 maneuver for low space weather conditions with respect to the minimum of $\Delta a_{c,min} = 1659.76\,\text{m}$ achieved at $t_f = 24.89\,\text{h}$ for maneuver case #2 under moderate conditions.

n_i	t_f (h)	Δa_c (m)	$+\Delta a_c$ (m)	$+\Delta a_c$ (%)
29	43.00	1225.35	-434.40	-26.17
32	47.52	1144.39	-515.37	-31.05
35	52.05	1190.44	-469.31	-28.28
38	56.57	1227.27	-432.49	-26.06

Tabs. 8.3 and 8.4 list the results for long term high and low levels of space weather activity, which are illustrated in Fig. 8.2 (right, (b)). To illustrate the scope of the influence of varying space weather activities on the maneuver characteristics, Fig. 8.3 depicts the optimal relative in-plane trajectory of the deputy with respect to the chief plotted in the $\mathcal{L}$ - frame of the chief for case #2 for long term high (a) and low (b) solar activities.

High space weather conditions: High space weather conditions have such a severe influence on the thermospheric bulk properties (primarily via ρ) that natural decay becomes a dominant driver. Thus, shorter maneuver durations as under moderate conditions are advantageous. This, however, requires additional control inputs and directly results in increased levels of exploited and induced decay. Consequently, independent of the maneuver time, the overall level in decay increases significantly with respect to the maneuvers under moderate conditions. Apart from that, a similar dependency on the maneuver time is observed. For too short maneuver times, the maneuver tasks are so demanding that no efficient simultaneous control can be achieved and large levels of exploited and induced decay result. For too long maneuver times, the large levels of natural decay become the dominant driver. For long term high conditions, a minimal level of $\Delta a_{c,min} = 2211.76\,\text{m}$ has been obtained at $t_f = 10.93\,\text{h}$, which represents an increase of $+\Delta a_c = 33.26\,\%$ with respect to the global optimum under moderate conditions at 43.91 % of the original maneuver time. Notably, an advantage of high space weather activity levels is the increase in available control authorities.

Low space weather conditions: For low space weather conditions, the effects of natural decay become less important and longer maneuver times become beneficial. Nevertheless,

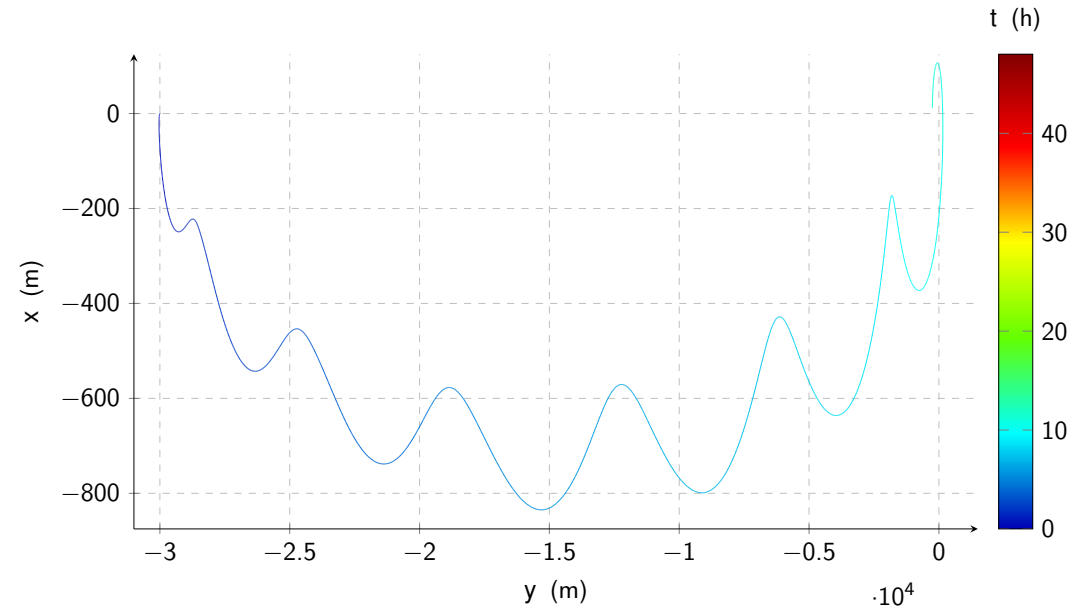

(a)

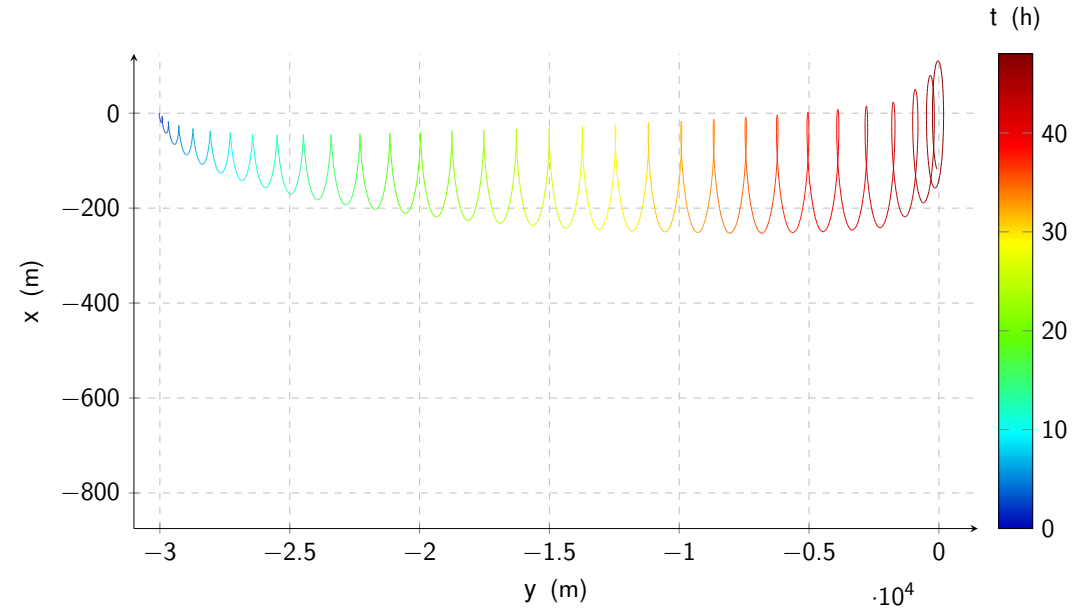

(b)

Figure 8.3: Relative in-plane trajectory of the deputy with respect to the chief plotted in the $\mathcal{L}$ - frame of the chief for the case #2 maneuver for long term high (top, (a)) and low (bottom, (b))) solar activities.

a similar dependency on the maneuver time is observed. For too short maneuver times, the maneuver tasks become so demanding that no efficient simultaneous control can be realized and exploited and induced decay are produced separately, which causes the overall levels of decay to increase. Vice versa, for too long maneuver times, the increase in natural decay becomes a dominant driver, even though to a lower extent as compared to the moderate not to speak the long term high conditions. For low conditions, a minimal level of $\Delta a_{c,min} = 1144.39\,\mathrm{m}$ has been obtained at $t_f = 47.52\,\mathrm{h}$, which represents a decrease of $+\Delta a_c = -31.05\,\%$ with respect to the global optimum under moderate conditions at 190.92 % of the original maneuver time. Whereas the reduced levels in decay per se represent an advantage, the respective decrease in the available control authority must be recognized, which (a) causes the achievable maneuver times to increase considerably and (b), in the worst case, causes the maneuver to become infeasible. To give an example of the implications of these results: if project delays which cause a significantly delayed launch were to occur, mission planning would have to adjust the maneuver accordingly to guarantee successful execution, e.g. by counteracting a variation in solar and geomagnetic activity by adjusting the target orbital altitude.

Key findings: As shown by Traub, Fasoulas, and Herdrich [168], the statements on variations in solar and geomagnetic activities equally apply to all other parameters that have an effect on the dynamic pressure q and therefore on the natural decay, e.g. the orbital altitude. So it can be concluded that any advantages in the available control forces resulting from the increase in the dynamic pressure q are inevitably detrimental to the resulting overall decay. Conversely, for reduced dynamic pressures, the available control forces reduce and the achievable maneuver times increase accordingly, but there are advantages in terms of the resulting decay. Consequently, the only suitable means to improve the control authority while maintaining a similar or achieving even a reduction in the level of decay is an optimization of the design of the spacecraft under investigation. With respect to the different types of decay, satellites designs with the following specifications would contribute to a significant improvement of the methodology:

- **Specification #1:** Increased maximum ballistic coefficients $\beta_{D,max}$ but fairly constant minimum ballistic coefficients $\beta_{D,min}$ would reduce the levels of natural decay and increase the available in-plane control authority.
- **Specification #2:** Increased lift to drag ratios C_L/C_D would reduce the levels of induced decay and render out-of-place adjustments more efficiently.

In this regard, specification #1 is essentially the exact opposite of previous practices in the field, in which the available differential drag control forces were generally increased by decreasing the minimum ballistic coefficient $\beta_{D,min}$. Since this is easier to achieve (e.g. by increasing the surface area of control panels), it is the natural choice when orbital decay is disregarded.

Exploited decay is defined as to be purposefully generated to fulfill the given maneuver task and is not per se dependent on the satellite design. However, a lower level of natural decay also directly reduces the requirement for exploited decay, as longer maneuver times with lower control requirements can be accepted. The ultimate goal in optimizing satellite design for differential lift and drag applications is thus to find an optimal trade-off between (a) the achievable control

authority, which must undoubtedly be maintained to some degree in order to perform collision avoidance or other unexpected maneuvers, (b) the maneuver time, and (c) the resulting orbital decay. This will especially increase the feasibility of missions where frequent maneuvers are foreseen. In this case, any reduction in decay per maneuver will ultimately contribute to a significant increase in the overall lifetime of the satellite. In Chapter 9, efforts to design satellites with the given characteristics are elaborated.

The effect of the co-rotating atmosphere

For demanding out-of-plane control tasks, the oscillating pattern in the yaw angle profiles $\psi(t)$ is thoroughly governed by the control task. If only slight adjustments are desired, however, a second cause of oscillations becomes observable. In this case, it is optimal in terms of the resulting decay if only one of the satellite induces control while the other satellite orbits in its minimum drag configuration, i.e., at $\beta_A(t) = 0^\circ$. This, however, does not imply $\psi(t) = 0^\circ = \text{const.}$, as the effect of the co-rotating atmosphere has to be accounted for. In particular, it requires a harmonic oscillation in the yaw angle profile $\psi(t)$[25]. This is depicted in Fig. 8.4, showing the yaw angle $\psi_d(t)$ (top, (a)) and angle of sideslip $\beta_{A,d}(t)$ (bottom, (b)) profile of the deputy for case #2 with $\rho_z(t_f) = 0\,\text{m}$. As only very slight out-of-plane adjustments are required, the satellite transitions from the pattern governed by the out-of-plane control task (indicated in the black rectangle) into its minimum drag configuration, indicated via $\beta_{A,d}(t) = 0^\circ = \text{const.}$ and the harmonic oscillations in $\psi_d(t)$ (indicated in the red rectangle). Obtaining such insights into the methodology would not be feasible without the developed tool.

8.2 Discussion

This section examines challenges and further perspectives of differential lift before discussing a possible potential of superior control via roll, pitch and yaw angle deviations.

8.2.1 Challenges and further perspectives of differential lift

Through the intensive study of the methodology of differential aerodynamic forces throughout this dissertation, a number of causes why differential lift is currently inferior to drag and why the possibilities for out-of-plane control via differential lift are limited have been revealed:

- **Cause #1:** The C_L experienced in orbit with traditional satellite surface materials are significantly lower than the C_D due to the diffuse re-emission of the incident particles. This is explained by the assumed deposition of O on the surfaces (Figs. 4.3 - 4.5). It not only limits the achievable control authority in the out-of-plan direction but also causes large levels of induced decay due to the low C_L/C_D ratios.
- **Cause #2:** For differential lift, the maximum control authority is exerted when both satellites deviate from the minimum drag configuration (see Figs. 5.2 - 5.6), which is contrary to the optimum for reducing the overall decay.

[25] In any case besides for equatorial orbits (i.e., for $i = 0^\circ$).

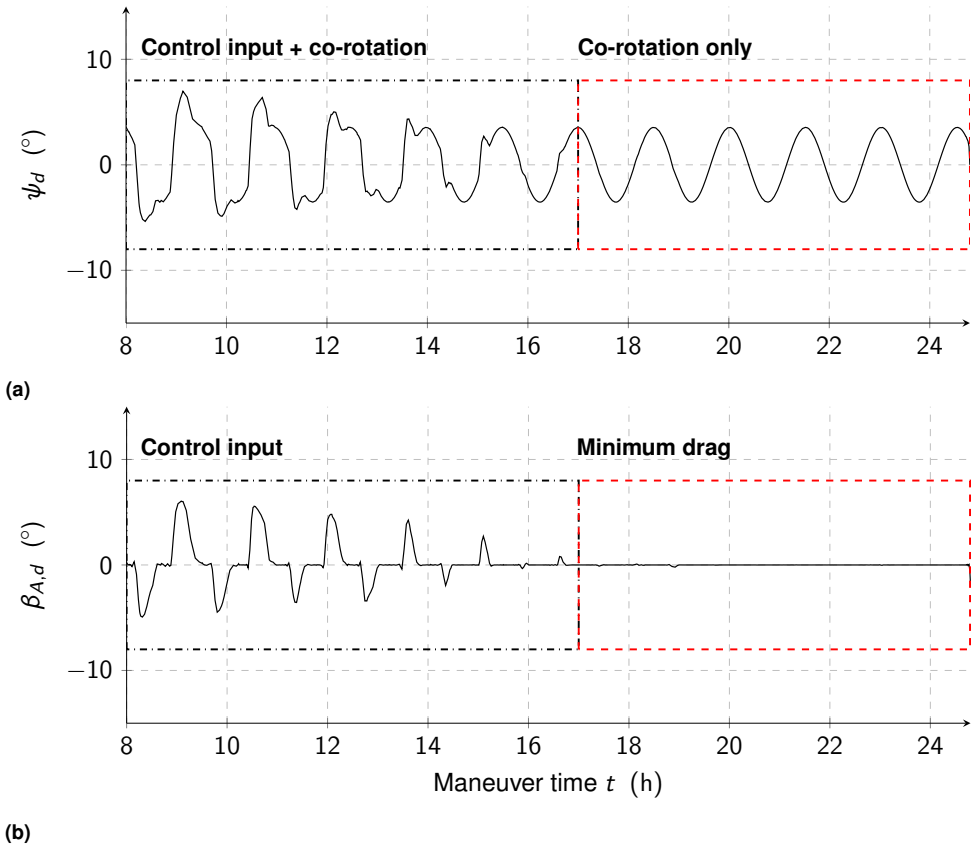

Figure 8.4: Resulting yaw angle $\psi(t)$ (top, a)) and angle of sideslip $\beta_A(t)$ (bottom, b)) profile of the deputy for an in-plane formation into a centred, bounded relative motion maneuver with $z(t_f) = 0\,\mathrm{m}$.

- **Cause #3:** Due to the high absolute spacecraft velocities, any changes to the orientation of the orbital plane, i and Ω, require large control inputs. The out-of-plane relative motion, however, is a result of differences in just these two parameters.
- **Cause #4:** The sinusoidal nature of the out-of-plane motion, resulting from the fact that the orbital planes of the satellites cross twice per orbit, generally requires *active* rotations of both satellites throughout the maneuver. This poses challenges to the attitude control system and could disturb sensitive measurement campaigns.

In a critical evaluation, it must therefore be concluded that although differential lift is indispensable for the three-dimensional control of satellite formations in VLEO, the possibilities of out-of-plane adjustments are currently very limited and associated to high levels of decay. Consequently, this method may find only limited application in the immediate future. However, should specular or quasi-specular reflecting materials be identified, a re-evaluation of the statement would be required. Indeed, in case of the in-plane motion, a certain level of decay cannot be prevented as this represents the actual means of control (representing exploited decay by definition). Consequently, the only effective means to optimize the methodology further in terms of the resulting decay is to reduce the level of natural decay via satellite shape optimization and to accept longer maneuver times. In case of differential lift, on the other hand, which per se is not responsible for any loss of energy of the satellite (but yet is again the decay induced by the associated drag), the practicability of the methodology will profit severely from any increase in the available C_L/C_D ratios. Therefore, the potential for improvement through design optimization is enormous.

8.2.2 On the potential of superior control via roll, pitch and yaw angle deviations

The control strategies proposed for differential aerodynamic force generation by a rotation of asymmetrically shaped satellites so far include the generation of differential drag for in-plane relative motion control via variations of pitch angles $\delta\theta$ or, as proposed in this work, the simultaneous exploitation of differential lift and drag via yaw angle variations $\delta\psi$. However, the simultaneous control of two of the three - not to say all - Euler angles has not been considered so far. Therefore, the question arises whether the simultaneous consideration of more than one Euler angle could possibly lead to better maneuvering procedures. As stated in Subsection 5.2.2, the control of satellite formations involves two subtasks, the control of in- and out-of-plane relative motion. The in-plane relative motion is highly unstable and, due to the coupling of the two states, can be controlled either by differential lift (in the radial direction), differential drag (antiparallel to the relative velocity vector), or by any superposition of the two specific forces. According to the VOP equations, a perpendicular force component is much less effective in changing the orbital geometry than the force component running along the orbit and the C_L experienced in orbit so far are much smaller than the corresponding C_D. Thus, differential drag is currently the undisputed control method of choice for in-plane relative motion [154, 156, 189]. For out-of-plane relative motion, however, the only suitable aerodynamic control option is the application of differential lift forces perpendicular to the orbital plane. For this reason, the application of yaw angle differences is arguably the most suitable option to achieve three-dimensional relative motion control with only one control variable. Since the control competence of differential lift is very low anyway,

a less than optimal application would make the methodology practically infeasible. This does not imply, however, that in certain cases controlling more than one Euler angle and thus generating differential forces in every possible direction could not lead to improved (or at least more flexible) maneuvering procedures. Enabling simultaneous control of multiple Euler angles, and a subsequent in-depth evaluation of possible benefits based on dynamic simulations, is therefore considered as part of future work. Since a problem to be solved with GPOPS-II does not need to be linear, the optimal planning tool provides a perfect basis for future extension.

Chapter 9

Satellite design optimization

In this chapter, optimal satellite designs for differential lift and drag controlled satellite formations are developed. In a first step, a tool is presented for the optimization of satellite designs with regard to minimizing the residual specific drag. In a second step, dedicated adjustments are made to the resulting designs in order to optimize them with respect to the specifications worked out in the previous chapter. A design optimization of satellites for the corresponding methodology is not available in the literature so far and breaks completely new ground.

9.1 Optimal designs for satellites in VLEO

To enable sustained operation in VLEO without constant resupply or on-board storage of large amounts of propellant, the specific aerodynamic drag force acting on the satellite must be (passively) mitigated or (actively) compensated. As far as passive means are concerned, optimizing the satellite design with respect to minimizing drag is arguably the most effective strategy. Any reduction in residual drag force directly increases the lifetime of passively orbiting satellites or reduces the propulsion requirements. Therefore, minimizing drag through design optimization is a critical need for sustained VLEO operation. For satellites orbiting the Earth in a circular orbit, the orbital lifetime t_L can be approximated via[26] [187]

$$t_L = \frac{\beta_D H_0}{\rho_0 \sqrt{\mu_e a_0}} \left(1 - \exp\left(-\frac{h_0}{H_0}\right)\left(1 + \frac{h_0}{2a_0}\right)\right), \tag{9.1}$$

in which ρ_0 is the density at the initial altitude h_0, H_0 is the atmospheric scale height just below the initial altitude and a_0 is the initial semi-major axis of the orbit. Equation 9.1 indicates that the satellite lifetime is linearly dependent on the ballistic coefficient β_D. Consequently, the ultimate task to passively increase the satellite lifetime is to maximize the ballistic coefficient $\beta_{D,max}$, defined in Eq. 4.4, via a minimization of the product $C_D A$ [27]. However, which strategy is most effective in achieving this goal depends heavily on the nature of the GSI that occurs.

[26] This represents a slight overestimation as it determines the time from the initial value down to $h = 0$ m.

[27] Technically, increasing the satellite mass is also a suitable means to achieve this goal. Since in the case of satellites, mass is one of the largest cost drivers, this practice will not be considered further in this dissertation.

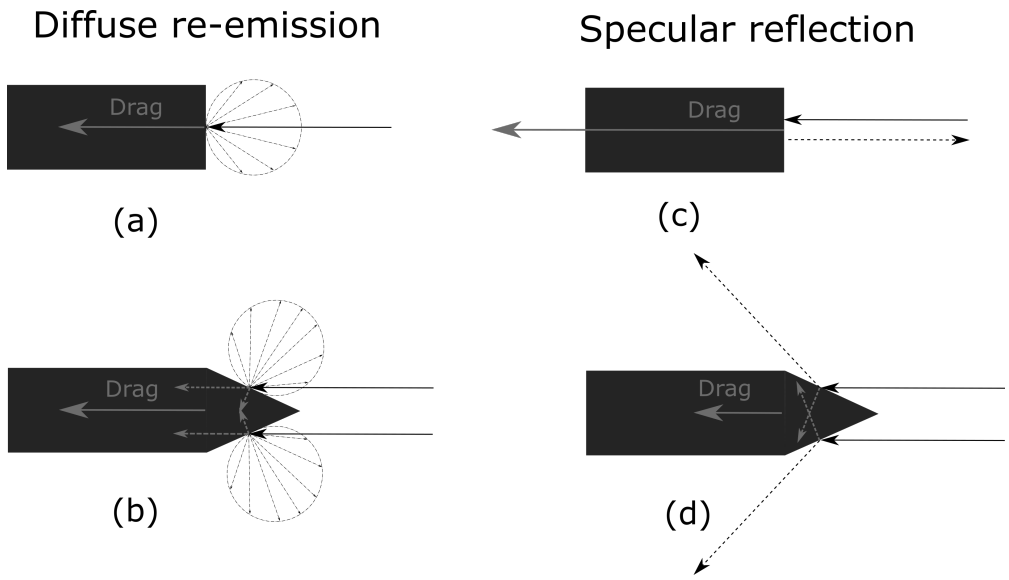

Figure 9.1: Resulting drag force due to energy and momentum exchange for diffuse re-emission ((a), (b)) and specular reflection ((c), (d)) for satellite shapes without ((a), (c)) and with ((b), (d)) nose cones geometries.

9.1.1 Theoretical background

Assuming that diffuse scattering is the predominant mechanism of re-emission, as it is the case for satellites in VLEO orbits with conventional surface materials, any surface facing the flow contributes to drag, essentially independent from its orientation. Thus, the most promising design decision is to reduce the surface area perpendicular to the flow as best as possible. This is indicated in Fig. 9.1 (a) and (b), where a dedicated nose cone does not alter the residual drag so that only a reduction of the frontal area would constitute a suitable measure for drag reduction. The rationale just described led to the compact and slender design of the GOCE satellite, which serves as a prime example of a satellite shape for VLEO applications assuming highly accommodated diffuse re-emission. This changes when specularly reflective materials are considered where momentum exchange is perpendicular to the surface. Here, an exposure of larger areas perpendicular to the flow can be compensated by a corresponding slope of frontmost elements [116, 185]. Accordingly, these offer far more design possibilities. This is depicted in Fig. 9.1 (c) and (d), where either a significant increase (c) or decrease (d) of the residual drag can be accomplished by the proper choice of the incident angle θ_i. While this discussion is aimed at developing measures to minimize drag, an intentional increase in residual drag may be desirable for effective end-of-life solutions. By tilting the surfaces at shallow angles to the flow, a reduction of the drag by one order of magnitude is possible [130].

A second means of reducing drag is available under hypothermal flow conditions, where the probability of collisions with surfaces not directly exposed to the flow can increase significantly [114]. Especially for satellites with elongated shapes, this effect can be mitigated by including dedicated tapering tail profiles. According to Walsh, Berthoud, and Allen [186], the slope of the profile can be limited to 8°, which represents the Mach angle of the atmospheric constitutes.

Table 9.1: Overview of the available literature in the field of satellite design optimization [58].

	Park et al. [116]	**Walsh and Berthoud** [185]	**Yu and Fan** [195]	**Walsh et al.** [186]
Nose geometry	Yes	Yes	Yes	Yes
Rear geometry	No	Yes	No	Yes
Constant volume	No	No	No	No
Altitude (km)	200, 300	250	250	200
Published in	2014	2017	2020	2021

9.1.2 Gap analysis

Different options for satellite shape optimizations are discussed in the available literature, namely adjusting the nose and tail geometry of the satellite individually and in combination. An overview of the available literature in satellites design optimization is given in Tab. 9.1. For the given boundary and environmental conditions, a drag reduction of up to 35 % could be achieved for an elongated body by optimizing the nose and tail geometries. However, both options come at the expense of the internal volume and can only be considered if the associated volume loss is acceptable. In addition, the results of the optimized profiles are poorly comparable in quality to the results of the reference design. In summary, no strategy for optimizing satellite designs while maintaining its volume exists. This critical lack is closed within this subsection.

9.1.3 Optimal designs for VLEO satellites

In this subsection, which incorporates the results from the master's thesis of Hild [57] and the contents of which has been published in Refs. [58, 59], a two-step optimization approach for satellite shapes with regard to a passive drag minimization is presented:

- **Step #1 - 2D profile generation:** A new type of 2D profile optimizer is used to generate an optimal profile, taking into account the current GSI properties.
- **Step #2 - PICLas simulations:** High fidelity simulations of the extended optimal 3D bodies are performed by means of the DSMC method using the open-source plasma suite PICLas[28] [41].

Before presenting and discussing the two steps, the design of the reference satellite is presented, which serves as the basis for the analysis of the improvement.

Reference satellite

In analogy to the geometry of the GOCE satellite, the reference satellite is of elongated cylindrical shape. It has an internal volume of $V_b = 0.004\,\mathrm{m}^3$ and a length of $l = 0.5\,\mathrm{m}$. The mass is set to $m = 4\,\mathrm{kg}$ and its surface temperature to $T_w = 300\,\mathrm{K}$. Throughout this subsection, the satellite is assumed to orbit in a circular orbit at $h = 350\,\mathrm{km}$.

[28] Available on GitHub via: https://github.com/piclas-framework/piclas.

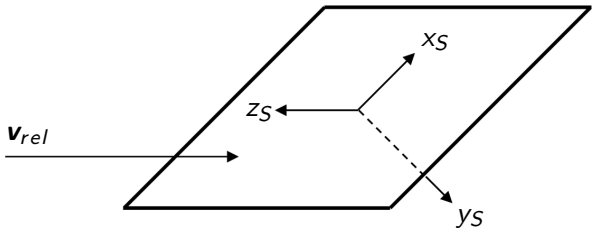

Figure 9.2: Local coordinate system on an area element according to Sentman [149].

2D profile generation

The goal of the 2D profile optimizer is to determine an optimal satellite profile $f^*(x)$. This is defined as the longitudinal section along the direction of the incident velocity vector. The profile is optimal in the sense that the residual drag force is minimized while the internal volume of the satellite remains constant. To do so, the profile is sub-divided into a total number of n linear sections for which the drag force is determined. Therefore, knowledge about the dimensionless coefficient of the total force component of a surface element dC/dA is required, which is provided by Sentman [149]. If only two dimensions are considered, the following relation holds:

$$\begin{aligned}\frac{dC}{dA} = \frac{1}{A_{ref,S}} \Bigg\{ &\left[\sigma_t \left(\vartheta k_S + \chi t_S\right) + \left(2 - \sigma_n\right)\varphi l_S\right] \left[\varphi\left(1 + \operatorname{erf}(\varphi s)\right) + \frac{1}{s\sqrt{\pi}} \mathrm{e}^{-\varphi^2 s^2}\right] \\ &+ \frac{\left(2 - \sigma_n\right) l_S}{2s^2}\left(1 + \operatorname{erf}(\varphi s)\right) \frac{\sigma_n l_S}{2}\sqrt{\frac{T_w}{T_i}} \left[\frac{\varphi\sqrt{\pi}}{s}\left(1 + \operatorname{erf}(\varphi s)\right) + \frac{1}{s^2}\mathrm{e}^{-\varphi^2 s^2}\right] \Bigg\}.\end{aligned} \tag{9.2}$$

Here, k_S, l_S and t_S are the direction cosines between the force direction and the axes of the local frame $\{x_S, y_S, z_S\}$ of the element of surface area. y_S is defined as the inward directed surface normal and x_S and z_S tangential to the surface element (see Fig. 9.2). ϑ, φ and χ are the direction cosines between the local axes and the macroscopic velocity vector $\boldsymbol{v}_m = \boldsymbol{v}_{rel}$. T_i is the neutral temperature of the incident particles and erf the error function. In addition, a body axes coordinate frame $\{X_S, Y_S, Z_S\}$ is introduced, which is stationary and the gas molecules move relative to it [149]. As the optimization is limited to two-dimensions $\chi = t_S = 0$ holds. For the aerodynamic force acting on an area element $\frac{dF_A}{dA}$ it follows:

$$\frac{dF_A}{dA} = \frac{1}{2}\rho v_{rel}^2 A_{ref,S} \frac{dC}{dA}. \tag{9.3}$$

The infinitesimal area element dA inclined at an angle α_S can be approximated as

$$dA = dX_S\sqrt{dX_S^2 + \left(f' dX_S\right)^2} = dZ_S dX_S \sqrt{1 + f'^2}, \tag{9.4}$$

assuming that X_S points along the direction of the incident velocity vector, Y_S points in direction of the body height and Z_S completes the right handed frame. dX_S is the dimension of the area element in the global X_S direction while dZ_S represents the third spatial dimension. f' is defined as the slope of the area element with $f' = \tan\left(\alpha_S\right)$. By inserting Eq. 9.4 into Eq. 9.3 and

integrating in X_S direction the following relation can be obtained:

$$\begin{aligned}\frac{dF_A}{dZ_S} &= \int_0^{X_{S,max}} \frac{1}{2}\rho v_{rel}^2 A_{ref,S} \frac{dC}{dA}\sqrt{1+f'^2}\,dX_S \\ &= \underbrace{\frac{1}{2}\rho v_{rel}^2}_{q} \underbrace{\int_0^{X_{S,max}} A_{ref,S}\frac{dC}{dA}\sqrt{1+f'^2}\,dX_S}_{\mathcal{J}_D}\,.\end{aligned} \tag{9.5}$$

Notably, Eq. 9.5 is only applicable for finite values of f'. If an existing frontal area perpendicular to the incident velocity vector is being considered, i.e., $f(0) \neq 0$, the element area can be calculated by $dA = dZ_S f(0)$. Since the dynamic pressure q is considered constant throughout the optimization process, the total force varies only with the term $\mathcal{J}_D$. Approximating the profile $f(X_S)$ with a piecewise linear function by introducing the discretised profile points $f_i(X_{S,i})$, the cost functional $\mathcal{J}_D$ to be minimized can be defined as

$$\mathcal{J}_D = \frac{dC}{dA}A_{ref,S}\cdot f_1 + \sum_{i=2}^{n+1}\left[\frac{dC}{dA}A_{ref,S}\sqrt{1+\left(\frac{f_i - f_{i-1}}{\delta X_S}\right)^2}\,\delta X_S\right], \tag{9.6}$$

where δX_S represents the dimension of each area element in the X_S - direction. In a subsequent step, the set of f_i for which $\mathcal{J}_D$ is minimized is determined via numerical optimization. Linear and non-linear constraints are included to account for (a) the maximum dimensions of the body, (b) to assure the constant satellite volume, (c) to ensure convex surfaces and (d) to avoid surfaces that are shaded from the incident flow. A convex surface implies that the slope of a profile section is not greater than the slope of the previous section:

$$\forall i : f_{i+1} - f_i \geqq f_{i+2} - f_{i+1}. \tag{9.7}$$

Non-shaded areas imply that the slope of a section is non-negative:

$$\forall i : f_{i+1} \geqq f_i. \tag{9.8}$$

Exemplary optimal 2D profiles for $\alpha_T = f_M = 0.95, 0.80, 0.65$ and the averaged atmospheric conditions at an altitude of 350 km listed in Tab. 9.2 are indicated in Fig. 9.3. To further mitigate the effects caused by the random thermal motion of the particles, tapered tail geometries are desired. Since the effect of shaded panels cannot be taken into account with the presented approach, the rear part is designed as a constant tapered profile and only the nose geometry is optimized accordingly. In any case, following the findings of Walsh, Berthoud, and Allen [186], an angle of 8° is defined as a fixed tail angle. Finally, three-dimensional satellite geometries are derived from the resulting optimal 2D profiles by (a) rotation, (b) extrusion, or (c) an overlap of both. Renderings of exemplary optimal 3D bodies including tail variations are shown in Fig. 9.4.

Table 9.2: Atmospheric data at 350 km altitude according to the NRLMSISE-00 model [122].

Parameter	Unit	Value
T_∞	K	1056.6
ρ	$\mathrm{kg\,m^{-3}}$	9.15×10^{-12}
n_O	$\mathrm{m^{-3}}$	2.64×10^{14}
$n_{\mathrm{N_2}}$	$\mathrm{m^{-3}}$	4.18×10^{13}
n_He	$\mathrm{m^{-3}}$	4.88×10^{12}
n_N	$\mathrm{m^{-3}}$	4.44×10^{12}
$n_{\mathrm{O_2}}$	$\mathrm{m^{-3}}$	1.09×10^{12}
n_H	$\mathrm{m^{-3}}$	8.53×10^{10}
n_Ar	$\mathrm{m^{-3}}$	8.63×10^{9}
v_{rel}	$\mathrm{m\,s^{-1}}$	7697.1
$\bar{M}$	$\mathrm{kg\,mol^{-1}}$	0.0174
s	–	7.66

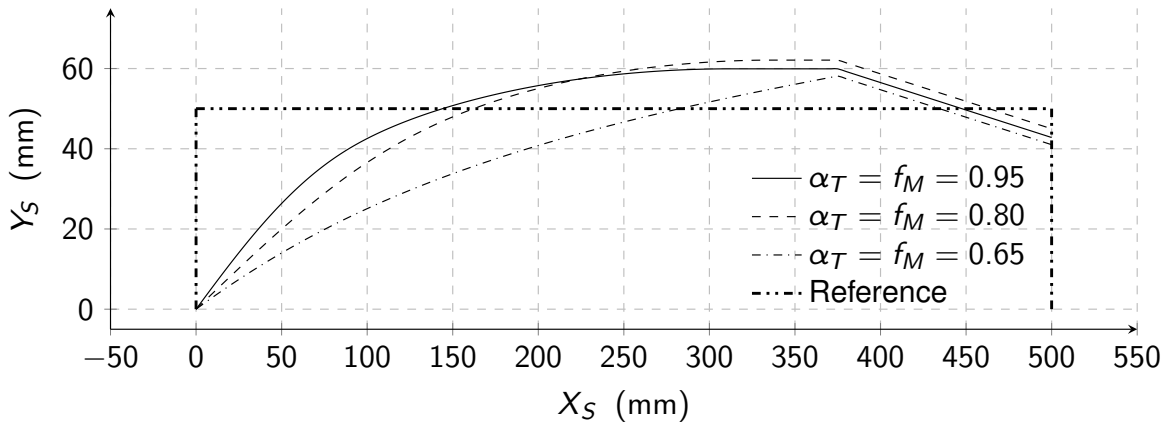

Figure 9.3: Optimal satellite profile for $\alpha_T = f_M = 0.95$ (solid, shape (a)), $\alpha_T = f_M = 0.80$ (dashed, shape (b)) and $\alpha_T = f_M = 0.95$ (dash dotted, shape (c)) with 25 % tail length [58].

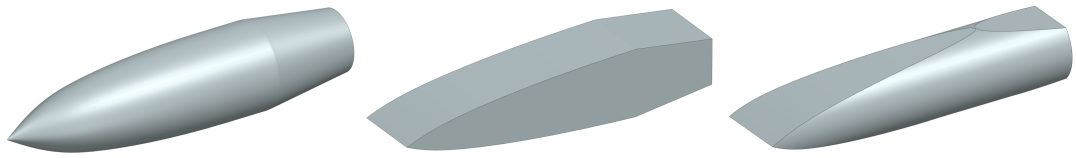

(a) Rotated. **(b)** Extruded. **(c)** Overlap.

Figure 9.4: The three basic three-dimensional shapes of the optimized profiles with 25 % tail length: (a) rotated, (b) extruded, (c) overlap of the both [58].

Table 9.3: Results for the optimized bodies including 25 % tail length compared to the reference case.

$\alpha_T = f_M$	Shape	$A\ \left(\mathrm{m}^2\right)$	$C_D\ (-)$	$\beta_D\ \left(\mathrm{kg\,m^{-2}}\right)$	$\Delta t_L\ (\%)$	Δt_L (d)
0.95	(a)	1.10×10^{-2}	2.40	151.0	+13.0	+21.7
0.80	(a)	1.21×10^{-2}	1.99	166.0	+24.2	+40.5
0.65	(c)	1.06×10^{-2}	1.93	195.5	+46.3	+77.3

PICLas gas kinetic simulations

In a second step, the aerodynamic characteristics of the resulting optimal 3D bodies have been obtained by means of the DSMC method using the open-source plasma suite PICLas [41]. Figure 9.5 shows the particle number density in the surrounding area for (a) the reference satellite, (b) the optimized rotated profile, and (c) optimized rotated profile with a tail of 25 % total length for $\alpha_T = f_M = 0.95$. The environmental conditions are set according to NRLMSISE-00 model [122] for moderate solar and geomagnetic activities according to Tab. 3.1. With the optimized nose shapes, less particles accumulate in the front of the body. With regard to the optimum profile with variations in the rear geometry, the wake behind the body is reduced by adjusting the rear. Figure 9.6 compares the results of the drag force per area over the body lengths for the different tail lengths for shape (a). While for the reference body the force per area decreases abruptly due to the sharp edge on the cylinder, a slower decrease can be seen for all optimized bodies due to the slowly decreasing incident angle. It can further be observed that the force per area acting on the front surface of the reference satellite is larger than for the optimized bodies. In general, the force per area decreases with the accommodation coefficient, especially in the front region. For the bodies including tail variations, a sharp decrease in the force becomes observable. This is due to the low amount of particles impinging on the posterior surfaces that are shadowed by the incident flow. As the tail length increases, however, the force on the front part of the satellite increases due to the constant volume constraint. The best results for $\alpha_T = f_M = 0.95, 0.80, 0.65$ could be achieved with the geometries depicted in Fig. 9.3. With the optimized profiles, lifetime improvements of 13.0 %, 24.2 % and 46.3 % with respect to the reference satellite could be achieved. The results for the optimal satellite designs are summarized in Tab. 9.3.

9.2 Optimal designs for differential lift and drag applications

In this section, which incorporates the results from the master's thesis of Marianowski [98], it is built upon the efforts from Section 9.1 to design satellites which are optimal for a differential lift and drag application.

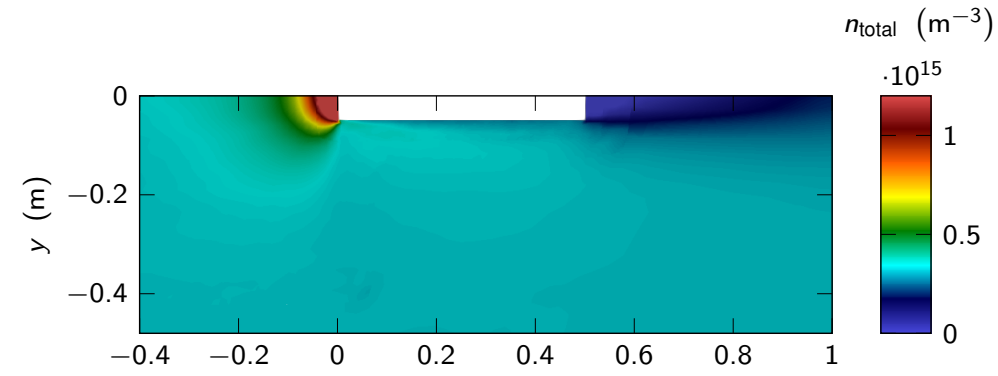

(a) Reference.

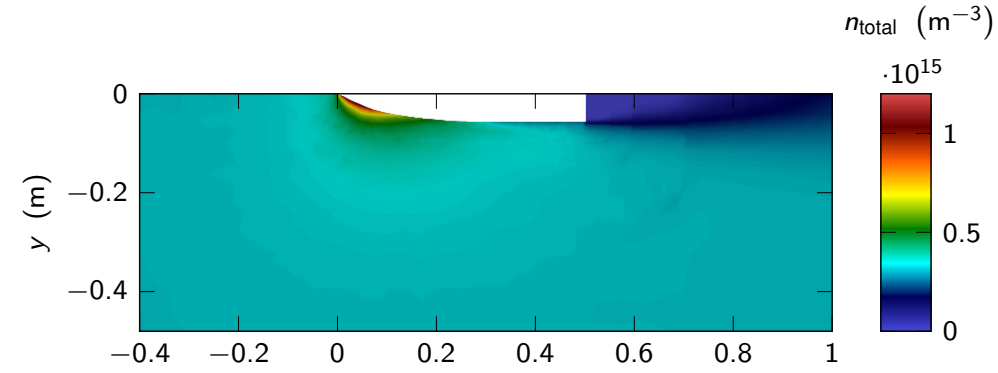

(b) Optimal (no tail).

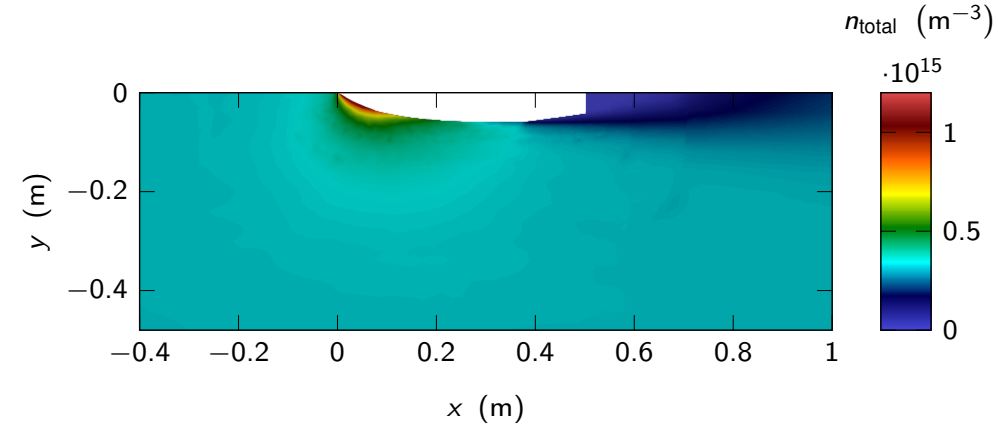

(c) Optimal (with 25 % tail length).

Figure 9.5: Number density of atmospheric particles in the surrounding area for (a) the reference satellite, (b) the optimized rotated profile and (c) the optimized rotated profile with a tail length of 25 % for $\alpha_T = f_M = 0.95$ [58].

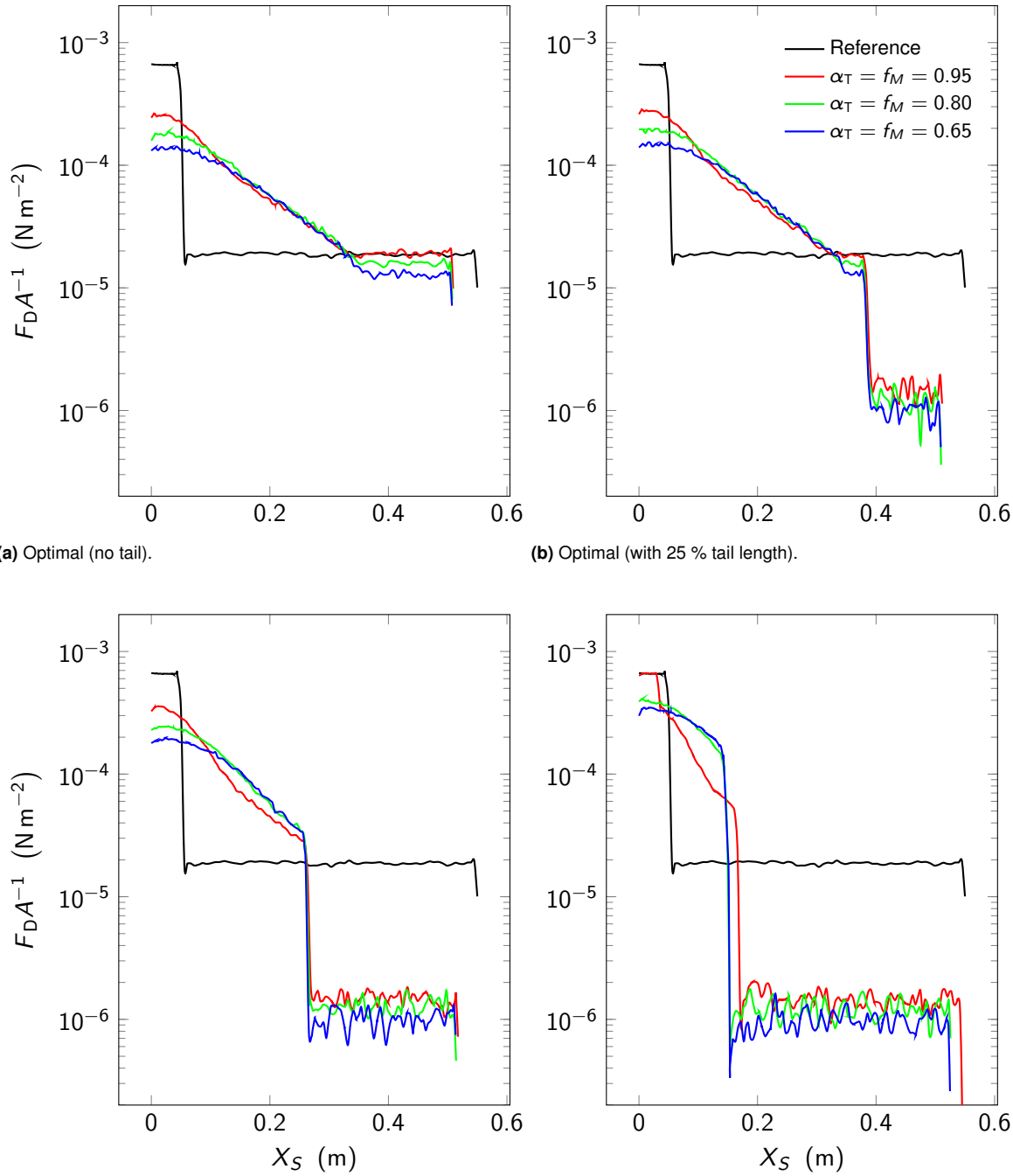

(a) Optimal (no tail).

(b) Optimal (with 25 % tail length).

(c) Optimal (with 50 % tail length).

(d) Optimal (with 75 % tail length).

Figure 9.6: Simulation results for the drag force per area acting on the optimized rotated profiles (a) without tail, (b) with 25 %, (c) 50 % and (d) 75 % tail length, compared to the reference body [58].

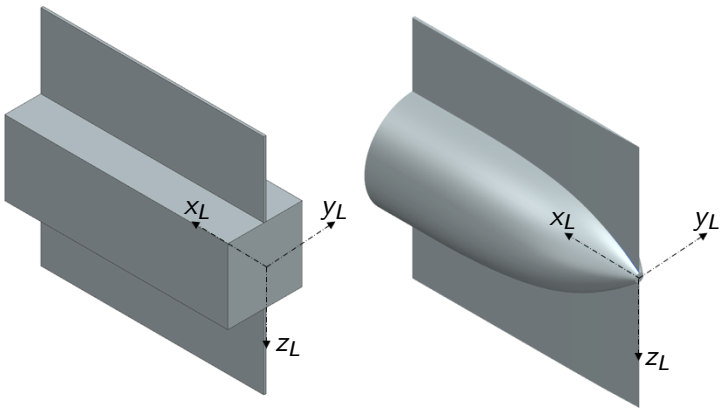

Figure 9.7: 3D renderings of the reference satellite (left) and an exemplary bullet-shaped satellite (right).

9.2.1 Theoretical background

Definition of the optimization priorities

When optimizing the satellite design for a differential lift and drag application, the most natural objective is a maximization of the available control authority as any increase in the available control forces would directly result in shorter maneuvering times and to a higher robustness towards disturbance forces. This explains why very lightweight satellites with high surface-to-mass ratios have been considered in the literature so far. These efforts, however, have not taken the resulting decay into consideration. Even for satellite formations controlled via differential lift and drag, though, it is expected that the satellites will spend most of their service life oriented in their nominal configuration. Consequently, in line with the governing optimization goal within this dissertation, minimizing the residual atmospheric drag in this configuration is retained as the prime objective and design adjustments to increase the achievable control forces are considered as secondary objectives. The goal is to develop the best possible design for a simultaneous application of differential lift and drag, so that a second level of prioritization needs to be added. In line with the desired focus on advancing the methodology of differential lift throughout this dissertation, improvements in differential lift are prioritized over drag. Consequently, the priorities underlying all decisions within this subsection are set as follows:

- **Priority #1:** Increased lifetime $+\Delta t_L$
- **Priority #2:** Increased differential lift $+\Delta\delta f_L$
- **Priority #3:** Increased differential drag $+\Delta\delta f_D$

In the next subsection, promising options for design improvements are identified. Subsequently, their benefits with respect to a reference satellite are assessed. To ensure comparability, all environmental conditions were set according to Tab. 9.2.

Theoretical considerations on design options

At this point, theoretical considerations are made to illustrate why an increased lifetime in nominal configuration generally counteracts the goal of increased differential drag forces by resorting to the examples shown in Fig. 9.7. In Fig. 9.8, the particle reflections for diffuse and specular

reflecting surfaces are illustrated for the two satellite designs depicted in Fig. 9.7 in (a) the minimum drag configuration, (b) the maximum drag configuration, and (c) the maximum lift configuration. As depicted in Fig. 9.8 (a), the larger share of surface elements aligned perpendicular to the flow results in a larger residual drag force (left) compared to the bullet-shaped satellite in the nominal flight configuration (right). This is more pronounced for specular reflecting surfaces (blue), where the direction of the normal momentum is reversed, than for diffuse re-emitting surfaces (red), were the particles are largely accommodated to the surface. While exactly this condition is exploited to minimize the drag in the nominal configuration, increased drag forces in the maximum drag configuration are desired to increase the control authority of differential drag. In this respect, however, the optimized design is less advantageous. The rounded profile equally reduces the residual drag force in the maximum configuration, which is graphically visualized in Fig. 9.8 (b). In this configuration, a largest possible share of surface elements perpendicular to the flow would be beneficial. Consequently, the challenge is to combine the contradictory requirements as best as possible. From Fig. 9.8 (c), it is also apparent how a diffuse re-emission limits the achievable lift forces compared to the specular reflecting case. This is due to the cosine distribution of the re-emitted particles and their thermal adaption to the wall. Due to this, the potential for geometric optimizations for differential lift and drag applications for traditional surface materials is limited. The following design variations have been identified:

Control authority of differential drag: To increase the control authority of differential drag, the goal is to minimize the residual drag force in the minimal drag configuration and, vice versa, to maximize the residual drag force in the maximum drag configuration. The former can be achieved via the 2D profile optimization tool and for the latter the following two options were identified:

- **Option #1a**: As the drag coefficient is maximal for surfaces perpendicular to the flow, the goal is to maximize the share of surface elements which fulfill this condition.
- **Option #1b**: A targeted insertion of sections in which multi reflections are promoted poses a means to increase the energy and momentum exchange per particle.

Control authority of differential lift: To increase the control authority of differential lift, the following two options were identified:

- **Option #2a:** Since the magnitude and direction of the lift vector of a surface element depends significantly on its orientation to the flow, the goal is to align the largest proportion of surface so that the overall lift force is maximum and points in the desired direction.
- **Option #2b:** Reducing the areas which generate lift in the opposite direction represents an effective means to increase the overall lift force.

Optimization strategy: The first step in optimizing the satellite designs is to optimize the nominal flight configuration with respect to aerodynamic drag via the extended 2D profile optimization tool. Subsequently, the influence of the individual options are assessed and a best possible overall design derived.

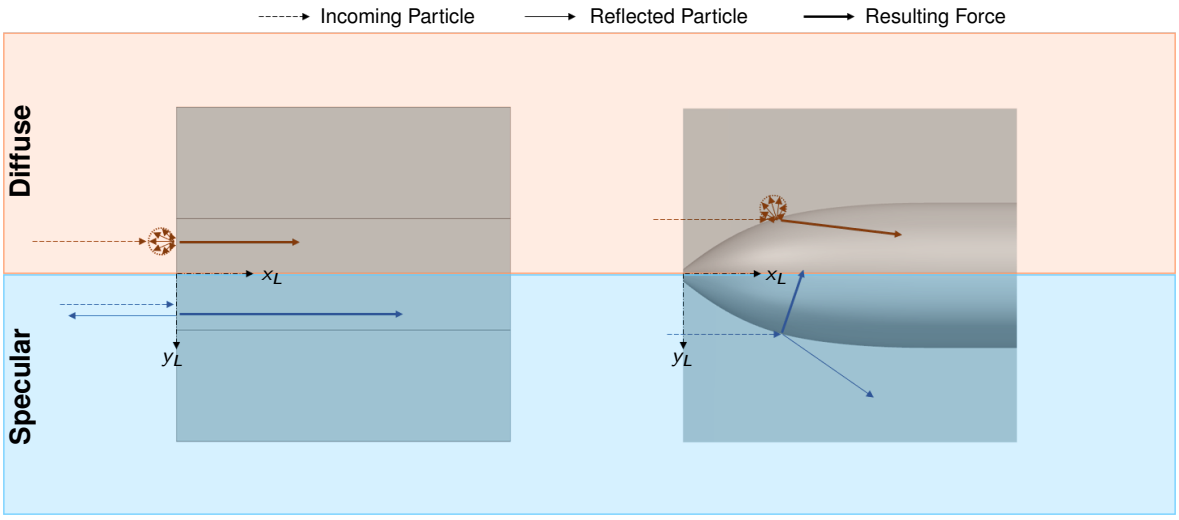

(a)

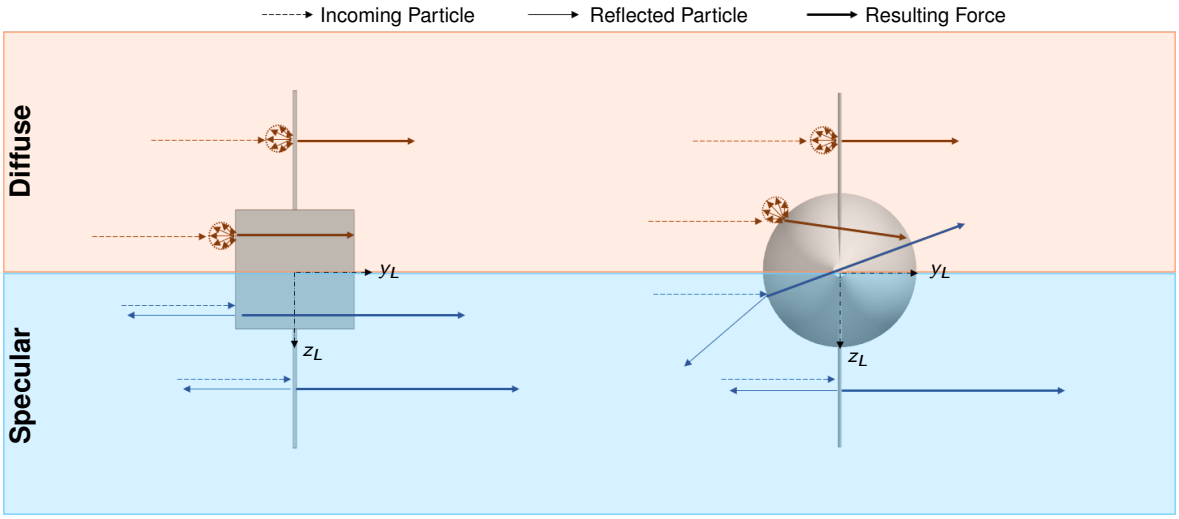

(b)

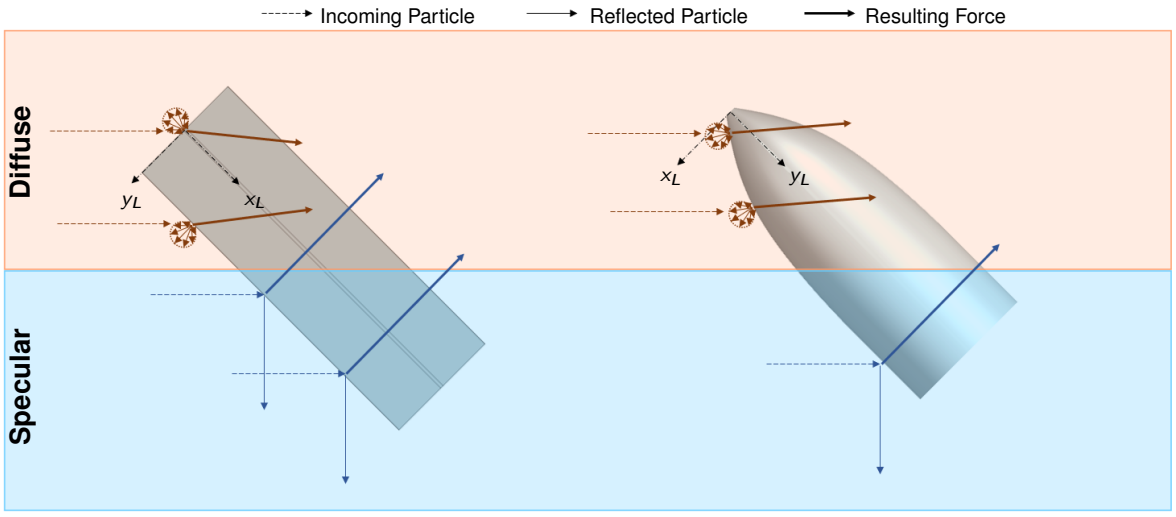

(c)

Figure 9.8: Exemplary graphical representation of satellite aerodynamics in nominal flight configuration (a), in the maximum drag configuration (b) and the maximum lift configuration (c).

Table 9.4: Overview over the surface properties assessed.

	$\boldsymbol{\alpha}_{T,1}$	$\boldsymbol{\alpha}_{T,2}$	$\boldsymbol{\alpha}_{T,3}$
Specular reflection ($f_M = 0.00$)	0.00	0.09	0.30
Diffuse re-emission ($f_M = 1.00$)	1.00	0.91	0.70

Table 9.5: Derived CLL input parameters for the specular case ($f_M = 1.00$).

	$\boldsymbol{\alpha}_{T,1} = 0.00$	$\boldsymbol{\alpha}_{T,2} = 0.09$	$\boldsymbol{\alpha}_{T,3} = 0.30$
α_n	0.00	0.0900	0.3000
σ_t	0.00	0.0459	0.1627

9.2.2 Methods and tools

Calculation tools for satellite aerodynamics

As for this type of study the aerodynamic properties of a large number of different designs need to be determined, it is not practicable to employ the computationally intensive DSMC method during the preliminary design stage. Consequently, the ADBSat tool [153], an open source software that allows for a fast approximation of the aerodynamics of satellites in the low-Earth orbit altitude range developed at the University of Manchester, is used. The tool's benefits are the availability of various gas-surface interaction models to represent the physics of free-molecular flow under different conditions and its shading algorithm, which allows for a fast determination of elemental flow exposure. The major disadvantage, however, is that the method is not applicable for concave surfaces since multiple reflections cannot be considered. Therefore, promising designs and any geometries for which multiple reflections are expected, are instead assessed via PICLas [41].

For an application of ADBSat, the surface mesh of the satellite, the atmospheric conditions, the GSI model as well as its respective input parameters need to be specified by the user. As optimal satellite designs for the extreme cases of specular refection and diffuse re-emission are to be developed, an additional GSI model to represent specular reflections is required. In this case, the Cercignani-Lampis-Lord (CLL) GSI model is employed [27, 95, 96]. For the assessment, variations in α_T are considered. In line with the analysis of Traub, Herdrich, and Fasoulas [169], the values for the diffuse case were set so that the first value represents the extreme case of full accommodation $\alpha_T = 1.00$, the second value corresponds to traditional surface materials[29] $\alpha_T = 0.91$ and the third value indicates what might be possible with improved materials $\alpha_T = 0.70$. To ensure comparability, the same increments were also applied for the specular case (see Tab. 9.4). As the closed-form solutions presented by Walker, Mehta, and Koller [184] are expressed as functions of σ_t and σ_n, the conversions presented in Subsection 4.3.1 are applied to ensure consistent application of all models. The resulting values for the surface properties under investigation are listed in Tab. 9.5.

[29] The value was originally obtained by applying the SESAM model [124] in [169].

Table 9.6: Results for the reference design for diffuse re-emission ($\alpha_T = 1.00$) and specular reflection ($\alpha_T = 0.00$).

Parameter	Unit	Diffuse	Specular	Variation
t_L	d	157.09	142.40	-9.35 %
$f_{D,min}$	$\mathrm{m\,s^{-2}}$	2.157×10^{-6}	2.380×10^{-6}	+10.34 %
$f_{D,max}$	$\mathrm{m\,s^{-2}}$	1.046×10^{-5}	1.960×10^{-5}	+87.38 %
$f_{L,max}$	$\mathrm{m\,s^{-2}}$	3.110×10^{-7}	6.900×10^{-6}	+2118.65 %
$f_{D,@L_{max}}$	$\mathrm{m\,s^{-2}}$	7.721×10^{-6}	1.157×10^{-5}	+49.85 %
$C_L/C_{D\max}$	-	0.040	0.596	+1380.57 %
δf_D	$\mathrm{m\,s^{-2}}$	8.303×10^{-6}	1.722×10^{-5}	+107.39 %
δf_L	$\mathrm{m\,s^{-2}}$	6.221×10^{-7}	1.380×10^{-5}	+2118.29 %
$\beta_{D,min}$	$\mathrm{kg\,m^{-2}}$	25.91	13.83	-46.62 %
$\beta_{D,@L_{max}}$	$\mathrm{kg\,m^{-2}}$	35.10	23.42	-33.28 %
$\beta_{D,max}$	$\mathrm{kg\,m^{-2}}$	125.64	113.89	-9.35 %

Reference satellite

The impacts of geometry modifications are specified with respect to a reference satellite, a 3U CubeSat augmented with two additional solar panels (see Fig. 9.7 (left)). The main body (subscript b) has a length of $l_b = 0.3\,\mathrm{m}$, a width of $w_b = 0.1\,\mathrm{m}$ and a height of $h_b = 0.1\,\mathrm{m}$, which results in a main body volume of $V_b = 0.003\,\mathrm{m}^3$. The panels (subscript p) have a length of $l_p = 0.3\,\mathrm{m}$, a width of $w_p = 0.003\,\mathrm{m}$ and a height of $h_p = 0.1\,\mathrm{m}$. The total satellite mass is $m = 5\,\mathrm{kg}$. In analogy to Section 9.1, comparability of the results is assured by a constant volume of the main body $V_b = \mathrm{const}$. Additionally, a maximum total height $h_{t,max} = 0.3\,\mathrm{m}$ and length $l_{t,max} = 0.3\,\mathrm{m}$ are defined. The relevant parameters of the reference satellite for the diffuse and specular case are listed in Tab. 9.6. Here, t_L and $f_{D,min}$ represent the lifetime and the specific drag force in the minimal drag configuration. $f_{D,max}$ is the specific drag force in the maximum drag configuration, $f_{L,max}$ the specific lift force in the maximum lift configuration, $f_{D,@L_{max}}$ the specific drag force in the maximum lift configuration, $C_L/C_{D\max}$ the lift to drag ratio in the maximum lift configuration. $\beta_{D,min}$ is the minimum ballistic (drag) coefficient, $\beta_{D,max}$ the maximum ballistic (drag) coefficient and $\beta_{D,@L_{max}}$ the ballistic (drag) coefficient in the maximum lift configuration. Finally, δf_D and δf_L are the maximum achievable differential drag and lift forces.

Necessary extensions to the 2D optimization tool

Before the 2D profile is optimized, the type of volume derivation needs to be defined to be compliant with the given volume restriction. Originally, three different volume derivation options are available (see Fig. 9.9 (left)). To expand the possibilities according to the objectives of this study, the following additional parameters are included for geometry option B:

- **Extrusion height** h_b: The height of the main body can be altered.
- **Nose width** w_n: The width of the frontal edge can be altered.

An overview of the available 3D body design options is given in Fig. 9.9.

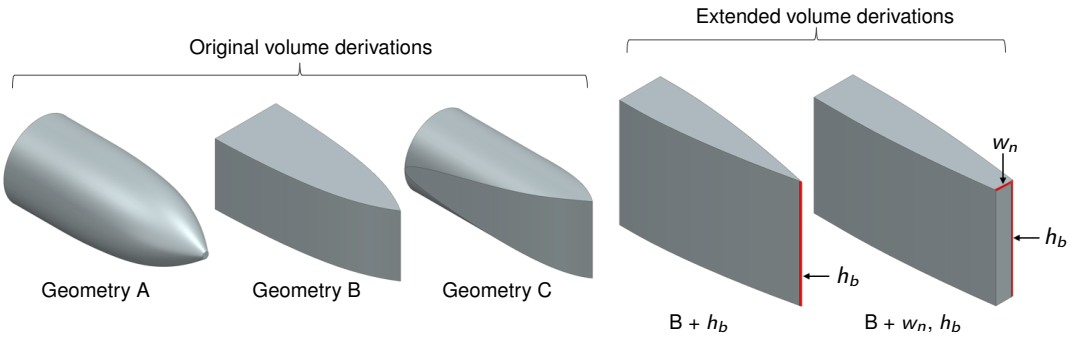

Figure 9.9: Available 3D volume derivations for the 2D profile optimization.

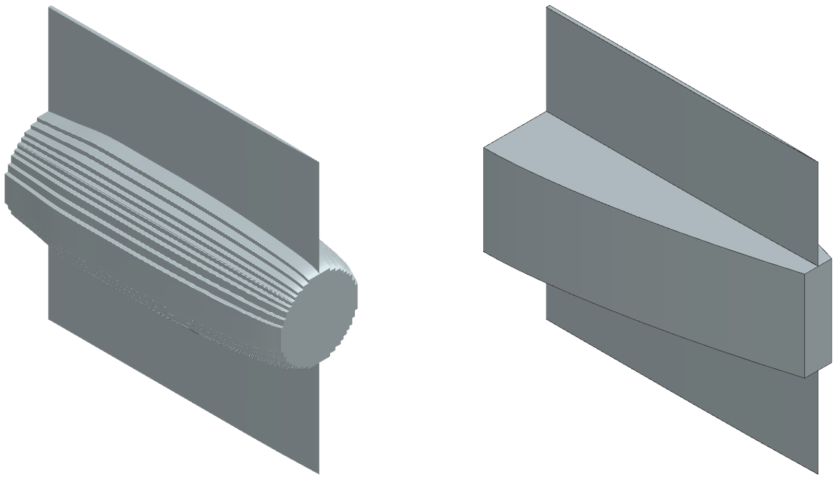

(a) Diffuse re-emission. **(b)** Specular reflection.

Figure 9.10: Recommended designs for a differential lift and drag application assuming diffuse re-emission and complete thermal accommodation (a) and specular reflection with vanishing energy accommodation (b).

9.2.3 Optimal satellite designs for differential lift and drag

The recommended design for differential lift and drag application assuming diffuse re-emission and complete thermal accommodation (a) and specular reflection with vanishing energy accommodation (b) are depicted in Fig. 9.10.

Diffuse re-emission

In case of diffuse re-emission, the optimal designs for a pure differential drag and pure differential lift application do not share many geometric characteristics. Thus, the challenge is to find an optimum trade-off with respect to the optimization priorities stated. Based on the results of a parameter study during which different design variations and their respective influence on the experienced specific lift and drag forces were examined (see Fig. 9.17 for detailed results), an optimal design was identified (see Fig. 9.10 (a)). The following steps were applied: (1) rotate the lifetime-optimized 2D profile for the main body, (2) extrude the lifetime-optimized 2D profile for the panel and (3) add a rasterized cross section along the main body to increase the share of surface elements perpendicular to the flow in the maximum drag configuration. This simultaneously augments the overall lift forces in the maximum lift configuration as the lift vectors of

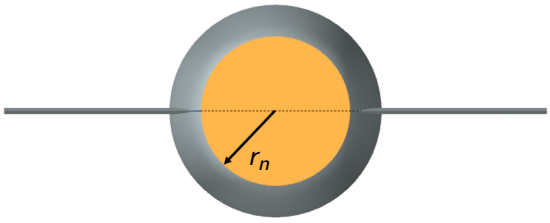

Figure 9.11: Graphical visualization of the nose radius r_n.

Table 9.7: Results for the recommended design for diffuse re-emission at $\alpha_T = 1.00$. Variations are indicated with respect to the reference satellite.

Parameter	Unit	Value	Variation
t_L	d	176.35	+12.26 %
$f_{D,min}$	$\mathrm{m\,s^{-2}}$	1.922×10^{-6}	-10.89 %
$f_{D,max}$	$\mathrm{m\,s^{-2}}$	1.043×10^{-5}	-0.29 %
$f_{L,max}$	$\mathrm{m\,s^{-2}}$	3.208×10^{-7}	+3.15 %
$f_{D,@L_{max}}$	$\mathrm{m\,s^{-2}}$	7.362×10^{-6}	-4.65 %
$C_L/C_{D\max}$	-	0.044	+8.18 %
δf_D	$\mathrm{m\,s^{-2}}$	8.508×10^{-6}	+2.47 %
δf_L	$\mathrm{m\,s^{-2}}$	6.416×10^{-7}	+3.13 %
$\beta_{D,min}$	$\mathrm{kg\,m^{-2}}$	25.99	+0.31 %
$\beta_{D,@L_{max}}$	$\mathrm{kg\,m^{-2}}$	36.82	+4.90 %
$\beta_{D,max}$	$\mathrm{kg\,m^{-2}}$	141.04	+12.26 %

the respective surface elements are at a maximum and all point in the desired direction. The rasterization is performed via the *midpoint circle algorithm* [126], an algorithm used to determine the points needed for rasterizing a circle. As an input, the algorithm requires the nose radius r_n of the base satellite design derived with geometry option A and a step size x_r, which is depended on the nose radius via $x_r = r_n/n$. The parameter n can be set by the user. A graphical definition of the nose radius is depicted in Fig. 9.11. A sensibility analysis revealed that large values of n are beneficial. In the depicted case, $n = 14.3$ to maintain $V_b = \text{const}$. The resulting design is shown in Fig. 9.10 (a) for the case of complete energy accommodation $\alpha_T = 1.00$ and all relevant data listed in Tab. 9.7. The force distribution of the frontal half of the conventional optimal design (upper) and the rasterized design (lower) in the maximum drag configuration is depicted in Fig. 9.12. Here, it can clearly be seen how the rasterized cross sections augment the drag force in the maximum drag configuration as the curved shape of the conventional optimized body results in reduced drag forces. Nevertheless, the outer shell of the body still follows the profile derived via the 2D profile optimization tool and the residual lift force in the minimal drag configuration is reduced accordingly. In the following, the resulting flow field for the reference satellite (left) and the optimized satellited (right) shall be assessed in closer detail. In Fig. 9.13, the top row indicates the flow field in the nominal configuration for the reference (a) and the optimized (b)

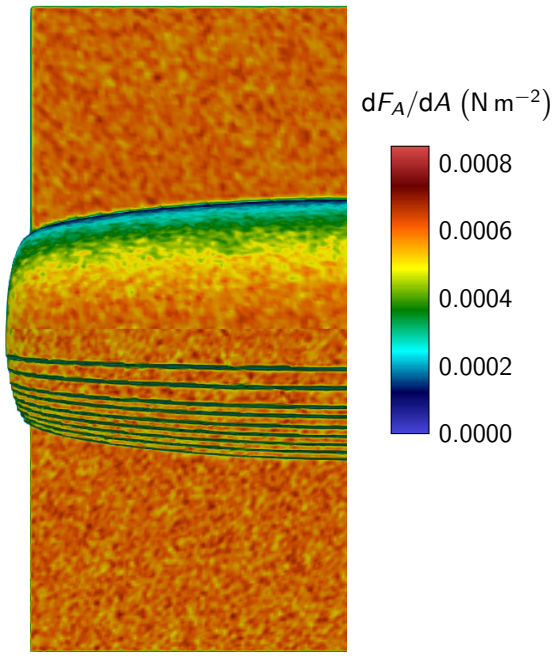

Figure 9.12: View of the aerodynamic force distribution of the frontal half of the conventional optimal design (top) and the rasterized design (bottom) in the maximum drag configuration.

satellite. The middle row shows the flow field in the maximum drag configuration for the reference (c) and the optimized (d) satellite. Finally, the bottom row indicates the flow field in the maximum lift configuration for the reference (e) and the optimized (f) satellite. Assessing Fig. 9.13 (a) and (b) in closer detail, it can be observed that due to the optimized 2D profile the preceding shock is reduced (less particles are reflected anti-parallel to the velocity) and a smoother transition to the increased values parallel to the satellite results. This condition directly relates to reduced drag forces due to momentum conservation. With respect to the flow fields for the maximum drag configuration ((c) and (d)), the qualitative behavior of the two cases is rather similar. This was a major goal during the optimization as this is necessary to realize increased available differential drag forces. Finally, the bottom row ((e) and (f)) indicates the reduction of opposed lift forces induced by the frontal area, where the shock preceding the frontal area in the optimized case is less distinct with respect to the reference satellite.

Specular reflection

The optimal designs for pure differential drag (Fig. 9.14, (a)) and lift (Fig. 9.14, (b)) in the case of specular reflections do share most of their geometric features. In both cases, a largest possible main body height ($h_b = h_{max}$) is optimal so that, as a consequence, the optimal design does not comprise panels at all. The main difference between the two designs is a slightly curved side profile in the differential drag case, whereas a purely wedge shaped profile is applied for

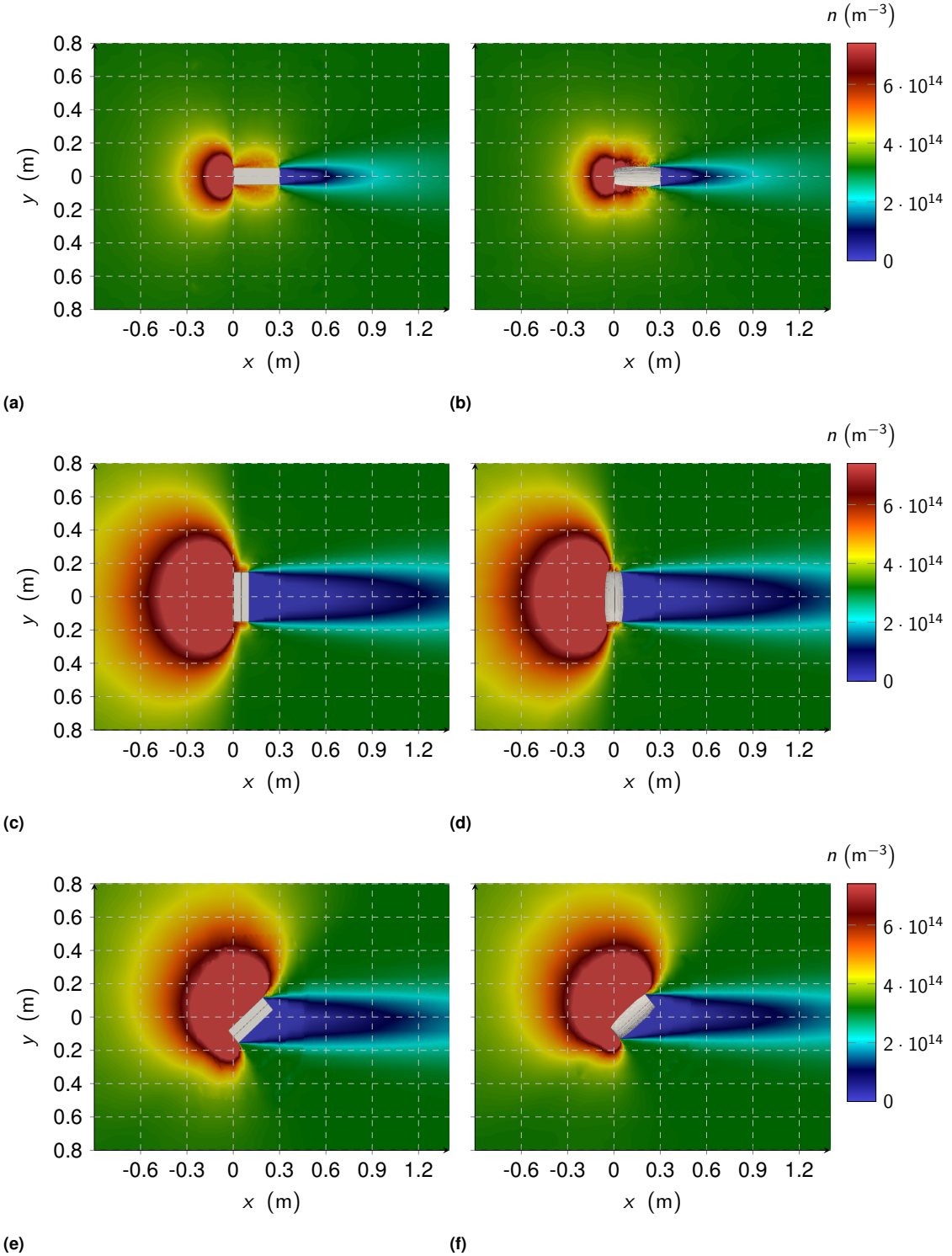

Figure 9.13: Particle density n in the flow field around the reference satellite (left) and the optimized design (right) for fully diffuse re-emission and $\alpha_T = 1.00$.

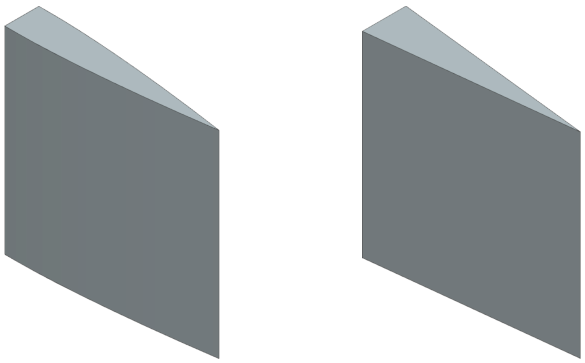

(a) (b)

Figure 9.14: Theoretically optimal design for a differential drag (a) and lift (b) application assuming specular reflection with vanishing energy accommodation.

Table 9.8: Results for the recommended design for specular reflection at $\alpha_T = 0.00$.

Parameter	Unit	Value	Variation w.r.t diffuse	Variation w.r.t specular
t_L	d	427.14	+171.91 %	+199.96 %
$f_{D,min}$	$\mathrm{m\,s^{-2}}$	7.934×10^{-7}	-63.11 %	-66.66 %
$f_{D,max}$	$\mathrm{m\,s^{-2}}$	1.871×10^{-5}	+78.87 %	-4.54 %
$f_{L,max}$	$\mathrm{m\,s^{-2}}$	6.945×10^{-6}	+2133.12 %	+0.65 %
$f_{D,@L_{max}}$	$\mathrm{m\,s^{-2}}$	1.064×10^{-5}	+37.81 %	-8.04 %
$C_L/C_{D\max}$	-	0.653	+1520.48 %	+9.45 %
δf_D	$\mathrm{m\,s^{-2}}$	1.792×10^{-5}	+115.83 %	+4.07 %
δf_L	$\mathrm{m\,s^{-2}}$	1.389×10^{-5}	+2132.76 %	+0.65 %
$\beta_{D,min}$	$\mathrm{kg\,m^{-2}}$	14.49	-44.08 %	+4.77 %
$\beta_{D,@L_{max}}$	$\mathrm{kg\,m^{-2}}$	25.49	-27.38 %	+8.84 %
$\beta_{D,max}$	$\mathrm{kg\,m^{-2}}$	341.61	+171.90 %	+199.95 %

differential lift. While this represents the theoretical optimal designs, their practicability is questionable as they are narrow and pointed, therefore offering little usable space for corresponding payloads. Moreover, they are virtually impossible to manufacture. A more practicable solution can be obtained by enforcing a user defined nose width w_n, which in the following is defined as $w_n = 0.03\,\mathrm{m}$. As can be seen in Fig. 9.10 (b), this additional constraint has far-reaching effects on the optimal satellite design. The relevant data is listed in Tab. 9.8. As soon as a frontal area is enforced, it is not optimal to maximize the total height of the main body, as this would consequently also maximize the frontal area and, therefore, the associated drag in the minimum drag configuration. As a result, a more compact and less slender design results, which again includes dedicated panels. The resulting flow fields are shown in Fig. 9.15. In accordance with Fig. 9.13, the top row indicates the flow field in the nominal configuration for the reference satellite (a) and the optimized design (b). The middle row shows the flow field in the maximum drag configuration for the reference (c) and the optimized (d) satellite. The bottom row indicates the flow field in the maximum lift configuration for the reference (e) and the optimized (f) satellite. When assessing

Fig. 9.15 (a) and (b) in closer detail, it becomes apparent that, due to the optimized 2D profile, the particles are more laterally redirected than reflected oppositely. This significantly reduces the residual drag force in the minimal drag configuration. With respect to the flow fields for the maximum drag configuration ((c) and (d)), it is observable that due to the curved side surface, the angular range of the reflected particles has been somewhat widened, which has a negative effect on the resulting maximum drag force. Nevertheless, higher specific differential drag forces can be achieved overall, since the advantages obtained in the minimum drag configuration compensate these disadvantages by far. Finally, the reduction of opposed lift forces generated by the frontal area is visible in the bottom row ((e) and (f)), where the shock preceding the frontal area for the optimized design is significantly reduced. In this case, too, the angular range of the reflected particles is somewhat more broadly open, which again is slightly disadvantageous. As in the case of differential drag, however, the advantages outweigh the disadvantages so that higher specific differential lift forces can be realized overall.

9.2.4 Discussion, remarks and potential

Discussion

In the following, the results obtained for a variety of different designs are discussed in closer detail. More sophisticated optimization strategies, such as a targeted introduction of areas that promote multiple reflections or a variation of the panel position, could not effectively contribute to an improvement. To provide additional insights, Fig. 9.16 shows the results for the different satellite designs depicted in Fig. 9.17 gathered with ADBSat and PICLas. In all cases, except for design 2a and 2b, the results are in excellent agreement. The deviations for designs 2a and 2b are caused by multiple reflections, which are (intentionally) promoted by the designs. This effect, however, is not taken into account within ADBSat. Finally, the analysis reveals that, although geometry variations can lead to an optimization of the aerodynamic properties, the benefits of design variations are outperformed by the effects of the reflection properties of the surfaces. To support this statement, Fig. 9.18 shows the resulting increases in the available lift forces over main body heights h_b with respect to the reference satellite for geometry B. This assumes diffuse re-emission for varying nose widths w_n and levels of α_T. Clearly, the achievable lift force for the reference satellite with $\alpha_T = 0.91$ and $\alpha_T = 0.70$ is significantly larger than for any of the optimized geometries with $\alpha_T = 1.00$. Consequently, not only is changing the extreme case of the reflection mechanism an effective means of achieving greater atmospheric lift than targeted design optimizations, but already reducing the level of α_T for diffuse re-emitting materials. Thus, achieving improvements in the material characteristics represents a more powerful means than optimizing the geometry.

Remarks

Within Section 9.2, optimal designs for simultaneous differential lift and drag control were developed for both extreme cases of scattering mechanisms. While it was aimed at an increase in the achievable differential forces, a reduction of the residual drag in the minimum drag configuration

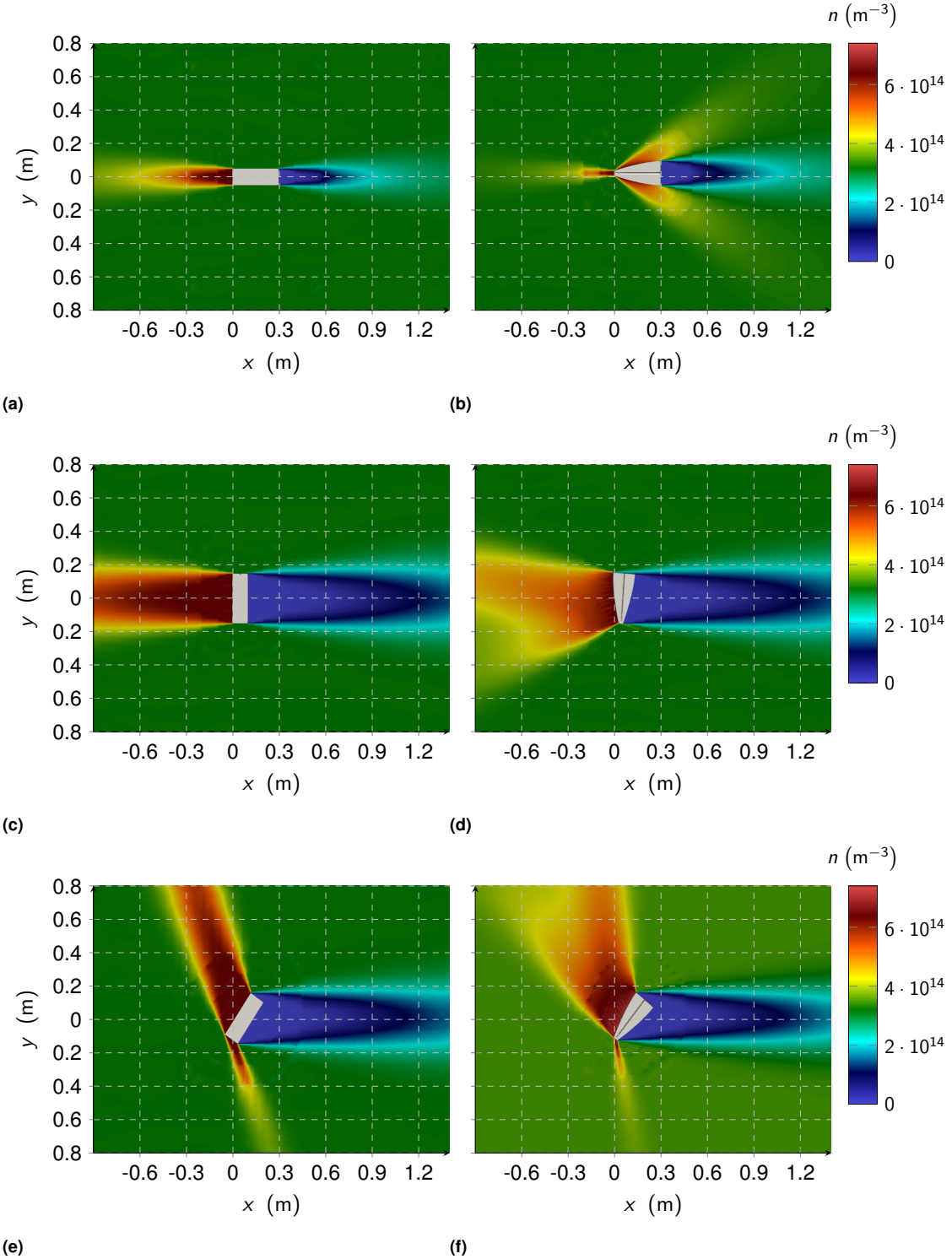

Figure 9.15: Particle density n in the flow field around the reference satellite (left) and the optimized design (right) for fully specular reflection and $\alpha_T = 0.00$.

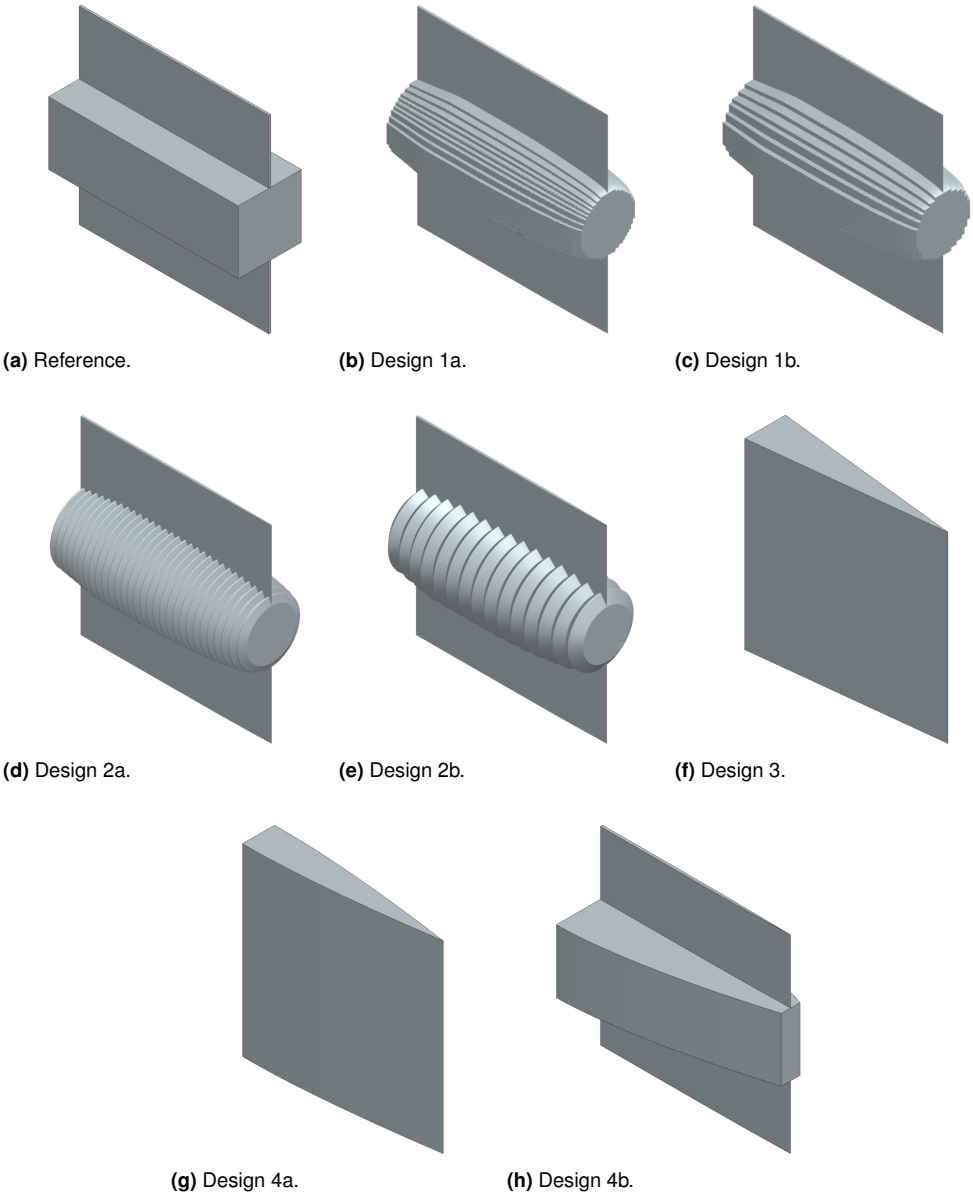

(a) Reference. **(b)** Design 1a. **(c)** Design 1b.

(d) Design 2a. **(e)** Design 2b. **(f)** Design 3.

(g) Design 4a. **(h)** Design 4b.

Figure 9.16: Overview of different design options evaluated with PICLas and ADBSat.

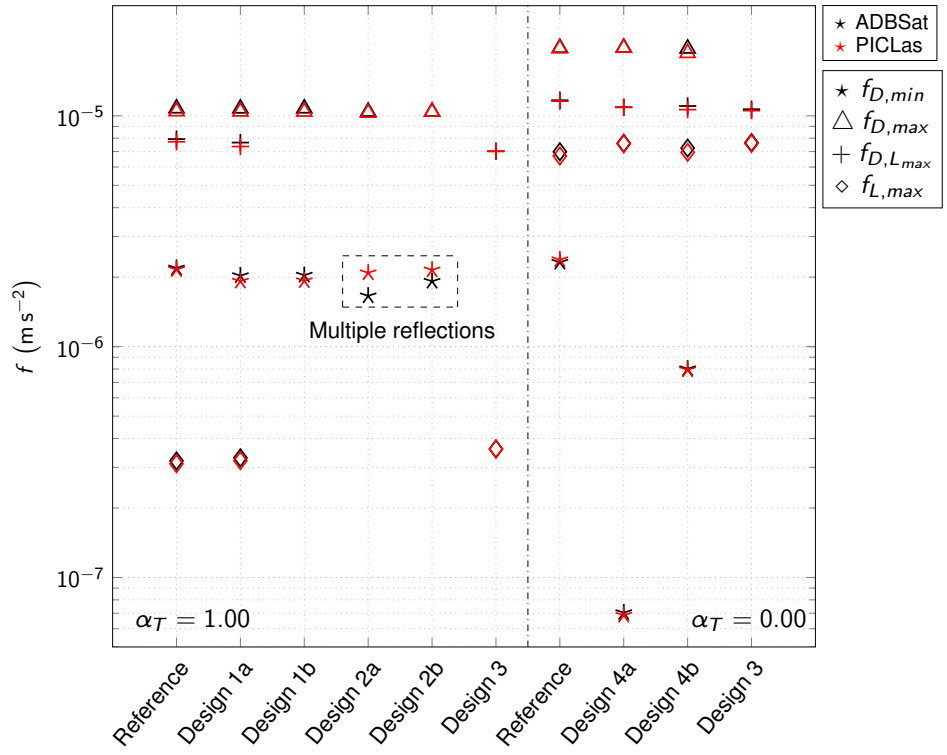

Figure 9.17: Comparison of the results gathered with ADBSat and PICLas for the different design options presented in Fig. 9.16.

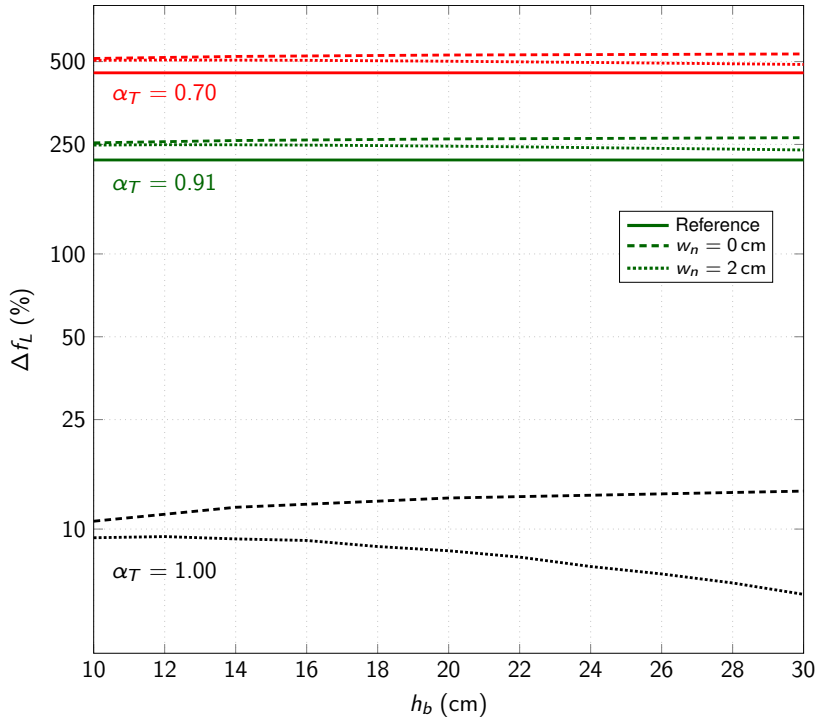

Figure 9.18: Influence of the main body height and the surface properties on the increase in aerodynamic lift with respect to the reference satellite with $\alpha_T = 1.00$.

remained the top priority to meet the overall optimization goal of this work. For both cases, geometries could be developed which show improvements in all relevant parameters. The two most critical parameters for a future improvement of the sustainability of the methodology are (a) the achievable lift to drag ratio C_L/C_D, as this ultimately determines the level of induced decay, and (b) the residual drag in the minimal drag configuration $f_{D,min}$, which governs the level of natural decay. In case of diffuse re-emission and complete energy accommodation, the achievable ratio was increased by 8.18 % and the residual drag in the minimum drag configuration reduced by 10.89 % with respect to the reference satellite. In case of specular reflection and vanishing energy accommodation, the achievable ratio was increased by 1520.48 % and the residual drag in the minimum drag configuration reduced by 63.11 %. However, in the diffuse case, very far-reaching changes to the design are required to achieve this gain so that the effort justifies the benefit only to a limited extent. Therefore, an actual application of the developed strategies in a real mission is rather unrealistic. Accordingly, it is important that advanced surface materials are identified and characterized in the near future.

Potential

Within the scope of this dissertation, design optimizations with respect to geometry variations and surface material characteristics have been performed. Whereas significant progress has been achieved, more sophisticated and technologically demanding interventions offer far-reaching potential. The following options have been identified:

- **Option #1:** An insertion of diffusers and the consideration of so-called 'ring structures' [58].
- **Option #2:** A targeted modification of the reflection properties of individual surface areas.
- **Option #3:** A targeted exploitation of the partial thermal accommodation coefficient $\alpha_{T,p}(\psi_i, \psi_r)$, which depends on the respective angle of incident ψ_i and reflection ψ_r.
- **Option #4:** A targeted manipulation of the particle flow via surface charging.

All of the options hold potential for innovative design optimizations in the future.

Chapter 10

Concluding remarks

10.1 Answers to the sub-research questions

Based on the findings of this dissertation, the following answers to the sub-research questions can be formulated:

1. *What are the relevant boundary conditions for an application of differential lift and drag of satellites in the VLEO regime?*

The most decisive boundary conditions for the methodology are the density ρ of the thermosphere and its molecular composition, which is dominated by atomic oxygen. The atmospheric density, arguably the most relevant environmental condition, decreases exponentially with altitude and varies dynamically on different time scales due to a number of external drivers, commonly referred to as 'space weather'. These drivers represent the largest sources of uncertainty in the prediction of thermospheric conditions. The abundance and reactivity of the main atmospheric constituent, atomic oxygen, renders it the most important constituent for space applications and satellite aerodynamics. It causes degradation to basically all exposed materials and heavily adsorbs on traditional satellite surfaces. As a result, the lift to drag ratios C_L/C_D experienced in orbit are low and the possibilities for spacecraft design optimization efforts are limited.

2. *How does the nature of the in- and out-of-plane relative motion differ and which implications does it have on the simultaneous control via differential lift and drag?*

As the nature of the in- and out-of-plane relative motion fundamentally differs, so does its control. The unstable nature of the in-plane motion can be exploited for efficient maneuvers via passive drifting periods during which no control input is required. The out-of-plane motion, in contrast, is generally bounded and its sinusoidal nature necessitates both satellites to constantly and actively oscillate contrariwise to produce differential lift in the desired direction. In case of simultaneous control, the challenge is to harmoniously combine both conflicting requirements, for which applying yaw angle differences $\delta\psi$ has been identified as the most appropriate means.

3. *How do differential lift and drag compare?*

According to the basic definition of atmospheric drag, its direction is anti-parallel to the relative

velocity vector and acts largely within the orbital plane. Therefore, aerodynamic lift, defined as any aerodynamic force that is perpendicular to drag, represents the only suitable means to exert aerodynamic forces in the direction perpendicular to the orbital plane. In terms of control, two key differences are worth highlighting. (a) For pure differential drag, the maximum control force is obtained when only one satellite deviates from the nominal configuration, which is in line with the requirements for efficient maneuvers. For pure differential lift, both satellites have to rotate contrariwise and, therefore, constantly deviate from the nominal configuration. (b) Due to the diffuse re-emission of the incident particles observed for traditional surface materials to date, the achievable control forces for differential lift are significantly lower than for differential drag. In orbital mechanics, it is well known that tangential forces represent an effective means to adjust the orbit size and shape (i.e., adjustments in a and e), a fact that augments the control authority of differential drag, whereas adjustments to the orbital plane (i.e., adjustments in Ω and i) require large control inputs. In combination with the low control forces to date, this limits the possibilities for out-of-plane adjustments via differential lift.

4. *Which mathematical tools and models are suitable for planning desired maneuver sequences precisely and efficiently?*

Regarding the mathematical tools and models employed, two different approaches were pursued in parallel. The first approach, the planning simplified maneuver sequences via analytic algorithms based on the Schweighart-Sedwick equations [147], permits fast and efficient preliminary assessments and Monte Carlo-like applications of the algorithms. From these, general, top-level insights into the methodology can be gained with little computational effort. The second approach, i.e., the sophisticated scheduling of optimal, three-dimensional maneuver trajectories via the GVP and LPE in terms of mean nearly non-singular relative orbital elements $\bar{\boldsymbol{\varepsilon}}_{ns}$ and by means of direct transcription, is computationally expensive but allows to gain critical insights which could hardly be obtained by simple means.

5. *Can critical parameters be identified to further develop the methodology?*

In the VLEO regime, aerodynamic considerations are the dominant driver of the satellite design and are all the more important for the methodology under study, which seeks to exploit aerodynamic forces in a targeted manner. In terms of differential drag, increasing the maximum ballistic coefficient $\beta_{D,max}$ represents the most effective means to further improve the methodology. Thereby, the orbital decay during the maneuver can be decreased (decreased levels of natural decay) while equally the available control authority increases. With regard to differential lift, the critical parameter is the achievable lift to drag ratio C_L/C_D, which determines the level of induced decay. Any improvements would directly render an application of differential lift more efficiently.

6. *What are the main limitations, drawbacks and challenges of the methodology and how can they be mitigated?*

The main limitations of the methodology identified are that (a) the available control authority is limited and highly depends on the current environmental conditions and that (b) the possibili-

ties for out-of-plane adjustments via differential lift are very limited to date. As a direct result of limitation (a), the resulting maneuver durations are long. The major drawback is arguably the large level of orbital decay, which is irreversible and inevitably reduces the overall mission duration. Throughout this dissertation, efforts have been made to mitigate this effect. With respect to the challenges, these are clearly the high uncertainty associated with all parameters affecting the aerodynamic forces as well as their dynamic nature. Therefore, a practical implementation of the methodology requires sophisticated and robust control strategies able to cope with these challenging conditions, which represents the most urgent next stage in development.

7. *Can maneuvers be identified that are particularly suitable for the methodology?*

The results have shown that the methodology is far more suited for the in- than for the out-of-plane control, for which the available control authority is limited and which is associated to large values of orbital decay. Nevertheless, the application of yaw angle deviations $\delta\psi$ allows for an efficient simultaneous control of both motions, which can be realized whenever the control tasks are balanced so that the decay induced for the out-of-plane control can effectively be exploited for the in-plane control. Generally, this is the case for relaxed maneuver requirements. Once specular reflecting surface features become practically available, a re-evaluation of this statement is required. In any case, yaw angle deviations $\delta\psi$ are predestined for a simultaneous drag and lift application, as thereby both control forces can be exerted in the optimal directions.

10.2 Conclusion

This dissertation aims at contributing to the emerging research field of the Very-Low Earth Orbit regime by addressing the guiding research question *"How can optimal simultaneous three-dimensional relative motion control of satellite formations in the Very-Low Earth Orbit regime be realized via differential lift and drag?"*. The aim of the work is to create a comprehensive and holistic overall system view of the methodology. Particular emphasis is placed on advancing the methodology of differential lift, which has received little attention in the literature so far, but is a key enabler of three-dimensional formation flight control via aerodynamic forces. The common thread that runs through this dissertation is the consideration of orbital decay, as this represents the greatest challenge for a sustainable operation in these regimes. Whenever possible, efforts are made to minimize it. Specifically for this purpose optimal satellite geometries are developed. Combined with the optimal trajectory planning tool, these allow for a holistic view of the problem that has not yet been considered in literature.

Following a comprehensive literature review, the methodology's state-of-the-art is highlighted and necessary research gaps identified. Consequently, two different approaches to address the problem under investigation from a mathematical point of view have been developed in parallel. The rationale for the parallel development is that both approaches have different strengths, limitations and, consequently, target applications. Notably, both tools allow for a complementary application. The first approach, the planning of maneuvering sequences via analytic algorithms based on the Schweighart-Sedwick equations, permits preliminary assessments and Monte Carlo-like

applications from which general, top-level insights into the methodology can be gained in short time and with only little computational effort. The second approach, the sophisticated planning of optimal three-dimensional maneuver trajectories via Gauss' form of the variational equations in terms of mean nearly non-singular orbital elements and by means of direct transcription, allows to flexibly schedule optimal and high fidelity maneuver sequences taking possible constraints and relevant boundary conditions into account. For the latter, the in- and out-of-plane relative motion is simultaneously controlled by applying deviations in the yaw angles $\delta\psi$ of the respective satellites and the trajectory optimal in the sense that the overall decay during the maneuver is minimized. This tool incorporates the main perturbation effects in VLEO, namely atmospheric forces and the J_2 effect, in the planning process. Moreover, more detailed effects such as the dynamically varying atmospheric densities as well as atmospheric co-rotation with the Earth are included. This unprecedented level of fidelity allows to gain insights which could hardly be obtained by other means. The developed tools and methods have been applied to explore and outline the design space of possible maneuver variants, through which profound insights into the methodology could be gained.

Although differential lift is indispensable for the three-dimensional control of satellite formations, its possibilities are currently limited due to a variety of reasons, among which the low lift to drag ratios experienced for diffusely re-emitting surfaces is the most prominent. Consequently, any adjustment is associated with severe levels of orbital decay. Therefore, it can be anticipated that this method will find only limited application in the immediate future. However, should specular or near-specular reflecting materials become available in the future, some of the identified reasons will no longer be relevant and a re-evaluation of the statement will turn out differently. Indeed, it must be understood that in case of the in-plane motion, a certain level of decay cannot be prevented as this represents the actual means of control. Thus, the only effective means to improve the methodology in terms of the resulting decay is to reduce the level of natural decay via satellite shape optimization and to accept longer maneuver times. In case of differential lift, on the other hand, which per se is not responsible for any loss of energy as this can again be attributed to the associated drag, the practicability of the methodology will directly profit from any increase in the available lift to drag ratios. Therefore, there is far-reaching potential for improvement through design and surface material optimization. This is especially true if it is considered that there exist relevant maneuvers which can be realized solely via differential lift.

In summary, within this dissertation an in-depth investigation into the simultaneous in- and out-of-plane relative motion control via differential lift and drag is presented. The novel feature is the focus on minimizing orbital decay, which is a common theme throughout the work and is new to the literature. Accordingly, the governing research question is answered satisfactorily. Future efforts should aim to bring the methodology closer to real-world orbital applications as well as to extend its area of application. In any case, the present work serves as a valuable foundation.

10.3 Prospects

10.3.1 Critical steps towards a practical control option

In the following, critical future steps to bring the methodology closer to a real-world application are elaborated.

Uncertainty assessment

The fast and efficient nature of the planning tool presented and discussed in Chapter 6 allows to perform Monte Carlo-like assessments which enable to derive general, top-level statements and conclusions. In a next step, the functionality of the tool can be extended to include uncertainties in the initial relative states $\{\boldsymbol{\rho}_0, \dot{\boldsymbol{\rho}}_0\}$, the environmental bulk properties q and the ballistic coefficients β_D and β_L. Doing so, their impacts can be quantified and the most critical parameters identified.

On-line compensation

The presence of unmodeled dynamics, uncertainties, and disturbances inevitably causes the observed trajectory to deviate from the scheduled path (see Fig. 7.19). To ensure the success of the maneuver, measures, and strategies able to compensate for these deviations are critical. For differential drag, progress has already been made by Dell'Elce [37] and Dell'Elce and Kerschen [38] in form of a model predictive control algorithm. With respect to own efforts, a robust bang-bang type control approach originally developed for the in-plane control via differential drag by Pérez and Bevilacqua [120, 121] was applied in a second phase to regulate the residual out-of-plane relative motion via differential lift [169]. Both advances can serve as starting points for further developments.

Towards a real mission application

Future efforts should be dedicated towards an extension of the optimal planning tool presented in Chapter 7 towards an incorporation of the following aspects:

- **Sensor errors:** To date, the effects of sensor errors on differential drag and lift based maneuvers have not been assessed. Since the navigation accuracy for Cube- and NanoSats is limited, an evaluation of the performance subjected to sensor errors is required.
- **Upcoming maneuver planning:** For satellite missions, upcoming maneuvers are planned well in advance. To ensure successful execution of the maneuvers, the relevant parameters (e.g. the initial state vectors or the solar and geomagnetic proxies) must be accurately predicted for the duration of the planned mission to ensure a successful maneuver.
- **Adequate power supply:** So far, no requirements on the orientation of the solar panels with respect to the Sun have been set. Thus, in a next step energy and power supply considerations have to be included.
- **Operational aspects:** To maintain contact times and to realize data up- and downlinks, operational aspects have to be taken into consideration in future planning efforts.

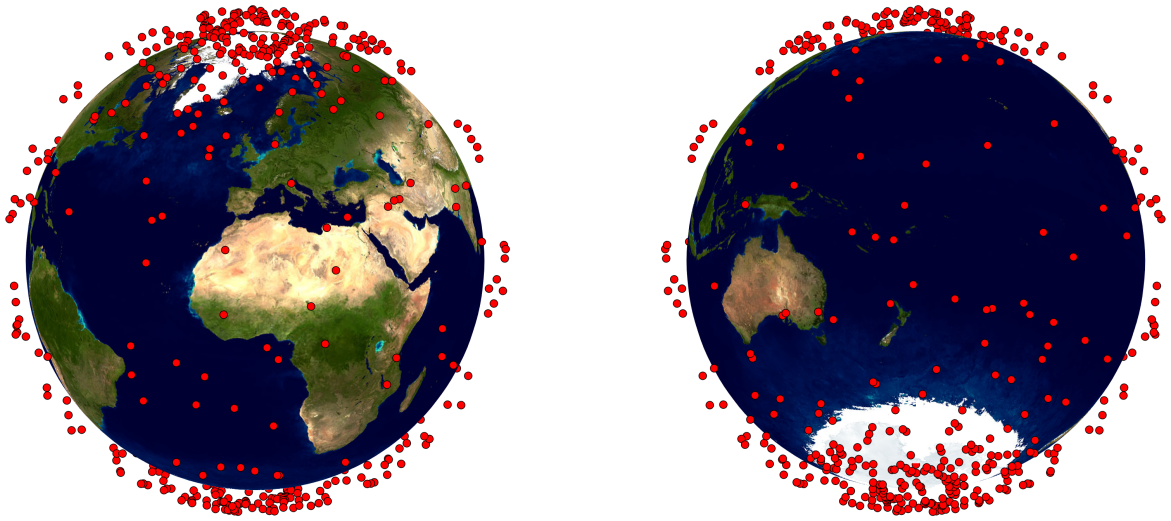

Figure 10.1: Locations at which proximity warnings (pass of tracked debris item within 1000 m predicted distance) have been triggered through the Combined Space Operations Center for the University of Stuttgart's small satellite Flying Laptop from its launch in July 2017 until June 2023 ($h_0 \approx 600$ km, $i \approx 98°$).

10.3.2 Potential alternative areas of application

Collision avoidance via differential lift and drag

The drastic projected increase in the number of satellites in LEO in the coming years (see Fig. 1.3, [4]), as well as the continuous increase in space debris resulting from rocket launches, collisions and/or anti-satellite tests will inevitably result in more frequent close encounters between objects in space, which not only poses a threat to functioning satellites, but in the worst case could render the regime unusable for decades by triggering an avalanche-like process known as the Kessler syndrome. Such a scenario would have drastic consequences for our modern information society and there is an urgent need for alternative strategies. In this respect, only active collision avoidance maneuvers represent a suitable means to reduce the collision risk once a critical approach to another object has been predicted. Traditionally, such maneuvers are initiated by electric or chemical thrusters. Accordingly, satellites without dedicated propulsion system are at the mercy of this danger, which poses a great danger to the satellites themselves and, for the reasons mentioned for the entire altitude range. In the low LEO regime, aerodynamic forces represent a promising means of adjusting the trajectory to significantly reduce the risk of collision. This is of particular interest for satellites of the widespread and emerging CubeSat class, which are often not equipped with a propulsion system due to their constructional limitations. Another prominent example is the institute's own satellite 'Flying Laptop' (FLP), which was launched on 14 July 2017 into a quasi circular orbit at an altitude of 600 km, and which regularly receives collision warnings to which it is unable to respond because it is not equipped with a dedicated propulsion system. Locations at which proximity warnings (pass of tracked debris item within 1000 m predicted distance) for the FLP have been triggered through the Combined Space Operations Center are displayed in Fig. 10.1.

However, a successful and target-oriented application of the methodology involves far-reaching challenges, which largely result from the uncertainties underlying the methodology.

While collision warnings comprise large levels of uncertainties anyway, these reinforce each other with uncertainties associated to orbit adjustments via aerodynamic forces. To make an effective contribution, maneuvers must result in a guaranteed reduction in collision probabilities. If this can be accomplished, however, this represents an effective contribution to the preservation of a regime that is indispensable for the modern information society. Initial progress in terms of collision avoidance via aerodynamic drag have been made by Omar and Bevilacqua [115] and more recently in own efforts (see Refs. [174, 175, 176]). Collision avoidance via aerodynamic lift, however, has not yet been considered in the literature.

Ionospheric aerodynamics

Throughout this dissertation, differences in the neutral aerodynamic forces have been envisaged as a promising means to control formation flying. A different possible means of aerodynamic control, however, are *ionospheric* aerodynamic forces which are caused by the interaction of an electrically charged platform and the ionosphere [23, 24, 155, 156, 157]. As the mass density of the thermosphere above 600 km decays at a faster rate than the mass density of the ionosphere, the methodology is particularly promising for altitudes where the control authority of neutral aerodynamics become too low for a practical use [154]. According to the results from Capon [23], ionospheric aerodynamic drag represents 0.05 - 18.35 % of the total aerodynamic drag force experienced by three representative objects at an altitude of 500 km for surface potentials between –0.75 V and –30 V, increasing to 0.89 - 78.68 % of the total aerodynamic drag force at 1500 km altitude. So far, however, ionospheric lift hast not been incorporated in the assessments even though, as stated by Smith [154],

> *"*[...] *it is possible to produce a lift component of ionospheric aerodynamics on an asymmetrical object, such as a flat plate at an angle of attack, and/or an object with an asymmetrical charge distribution, such as a sphere with only a single hemisphere charged. In both cases, the electrical field deflects the ionospheric flow asymmetrically such that a net lift component of acceleration is achieved."* [154]

Since in the case of neutral aerodynamics and diffuse re-emission of particles lift is significantly inferior to drag, augmenting the residual neutral lift force with an equidirectional ionospheric component might be an additional means of improving the practicability. This, however, has not been considered in literature so far.

Exploiting natural highways for enhanced end of life solutions

As shown by Alessi et al. [3], resonances related to high-degree geopotential harmonics, lunisolar perturbations and solar radiation pressure can be exploited to ensure a timely deorbit when being amplified by atmospheric drag [3, 143, 144]. Again, possible advantages of a simultaneous application of atmospheric lift and drag remained unexplored so far. The advances made within this dissertation can serve as starting points for future investigations.

10.3.3 Complementary application with other innovative concepts

The methodology discussed in this framework represents one of several promising enabling technologies in the field of VLEO. To enable enhanced mission concepts the working principles of the most promising systems must be harmoniously combined.

Atmosphere-breathing electric propulsion

Atmosphere-breathing electric propulsion (ABEP) is a potential enabling technology for satellites orbiting in VLEO. An ABEP system draws in the residual atmosphere through an intake and uses it as propellant for an electric thruster to compensate for the aerodynamic drag [131, 177]. Due to strict requirements on the alignment of the intake and the thruster, combining both enabling technologies in a target-oriented way represents a challenging task [11].

Thermal radiation

Possible concepts for drag reduction in VLEO include the development of technologies to harness solar energy and thermal energy decay for drag reduction and attitude control, as the active emission of 1 W of electromagnetic power is associated with a generated force of 3.3 nN [42]. This simple principle can be exploited, e.g. for attitude control of spacecraft using previously unused heat losses. Accordingly, thermal radiation could be a potential means of augmenting atmospheric lift to increase the control capability perpendicular to the orbital plane.

Bibliography

[1] U. Ahsun. “Dynamics and control of electromagnetic satellite formations”. Dept. of Aeronautics and Astronautics. Dissertation. Boston, Massachusetts, USA: Massachusetts Institute of Technology, 2007.

[2] U. Ahsun. “Dynamics and control of electromagnetic satellite formations in low Earth orbits”. In: *AIAA Guidance, Navigation, and Control Conference and Exhibit*. Keystone, Colorado, USA, 2006. ISBN: 978-1-62410-046-8. DOI: 10.2514/6.2006-6590.

[3] E. M. Alessi et al. “Natural highways for end-of-life solutions in the LEO region”. In: *Celestial Mechanics and Dynamical Astronomy* 130.5 (2018). PII: 9822. ISSN: 0923-2958. DOI: 10.1007/s10569-018-9822-z.

[4] S. Alfano, D. L. Oltrogge, and R. Shepperd. “LEO constellation encounter and collision rate estimation: an update”. In: *2nd IAA Conference on Space Situation Awareness (ICSSA)*. Washington D.C., USA, 2020.

[5] B. Andrievsky, A. L. Fradkov, and E. V. Kudryashova. “Control of two satellites relative motion over the packet erasure communication channel with limited transmission rate based on adaptive coder”. In: *Electronics* 9.12 (2020). PII: electronics9122032, p. 2032. DOI: 10.3390/electronics9122032.

[6] R. H. Battin. *Introduction to the mathematics and methods of astrodynamics*. Reston: American Institute of Aeronautics and Astronautics, 2000. ISBN: 9781563473425. DOI: 10.2514/4.861543.

[7] T. Beauchamp. *What A Flock Of Starlings Taught Me About Life*. URL: https://themuttonclub.com/what-a-flock-of-starlings-taught-me-about-life/ (visited on 11/27/2022).

[8] J. Beck. “Development of a MATLAB based simulation tool for formation flight maneuver trajectories using differential lift and drag”. Bachelor thesis. Stuttgart, Germany: The University of Stuttgart, 2022.

[9] M. K. Ben-Larbi, T. Jusko, and E. Stoll. “Input-output linearized spacecraft formation control via differential drag using relative orbital elements”. In: *Advances in Space Research* 67.11 (2021). PII: S0273117720308425, pp. 3444–3461. ISSN: 02731177. DOI: 10.1016/j.asr.2020.12.005.

[10] O. Ben-Yaacov and P. Gurfil. “Stability and performance of orbital elements feedback for cluster keeping using differential drag”. In: *The Journal of the Astronautical Sciences* 61.2 (2014), pp. 198–226. DOI: 10.1007/s40295-014-0022-0.

[11] T. Bender. “Development and assessment of novel mission concepts using a combination of ABEP and Aerodynamic Forces”. Bachelor thesis. Stuttgart, Germany: The University of Stuttgart, 2022.

[12] D. Biber. *Raw art photography*. 2022. URL: https://www.danielbiber.com/ (visited on 09/14/2022).

[13] L. Blitzer. “Satellite orbit paradoxon. A general view”. In: *American Journal of Physics* 39 (1971), pp. 882–886.

[14] A. C. Boley and M. Byers. “Satellite mega-constellations create risks in low Earth orbit, the atmosphere and on Earth”. eng. In: *Scientific reports* 11.1 (2021). Journal Article, p. 10642. DOI: 10.1038/s41598-021-89909-7. eprint: 34017017.

[15] B. Bowman et al. “A new empirical thermospheric density model JB2008 using new solar and geomagnetic indices”. In: *AIAA/AAS Astrodynamics Specialist Conference and Exhibit*. AIAA/AAS Astrodynamics Specialist Conference and Exhibit. Honolulu, Hawaii, USA, 2008. DOI: 10.2514/6.2008-6438.

[16] M. Brown et al. “SSA experiments for the australian M2 formation flying cubesat mission”. In: *21st Advanced Maui Optical and Space Surveillance Technologies Conference*. Maui, Hawaii, USA, 2020.

[17] M. K. Brown et al. “Future decreases in thermospheric neutral density in low Earth orbit due to carbon dioxide emissions”. In: *Journal of Geophysical Research: Atmospheres* 126.8 (2021). ISSN: 2169-897X. DOI: 10.1029/2021JD034589.

[18] S. Bruinsma. “The DTM-2013 thermosphere model”. In: *Journal of Space Weather and Space Climate* 5.A1 (2015). ISSN: 2115-7251. DOI: 10.1051/swsc/2015001.

[19] S. Bruinsma et al. “Evaluation of the DTM-2009 thermosphere model for benchmarking purposes”. In: *Journal of Space Weather and Space Climate* 2.A04 (2012). ISSN: 2115-7251. DOI: 10.1051/swsc/2012005.

[20] S. Bühler. “Improvements of analytic algorithms to ensure the feasibility of rendezvous maneuver using aerodynamic forces”. Bachelor thesis. Stuttgart, Germany: The University of Stuttgart, 2020.

[21] S. Bühler et al. “Development and verification of enhanced algorithms to ensure the success of rendezvous maneuvers using aerodynamic forces”. In: *69th Deutscher Luft- und Raumfahrtkongress*. Aachen, Germany, 2020.

[22] S. Bühler et al. “Enhanced algorithms to ensure the success of rendezvous maneuvers using aerodynamic forces”. In: *CEAS Space Journal* 13 (2021). PII: 362, pp. 637–652. ISSN: 1868-2502. DOI: 10.1007/s12567-021-00362-8.

[23] C. Capon. “Ionospheric aerodynamics in low Earth orbit”. Dissertation. Canberra, Australia: University of New South Wales Canberra, 2017.

[24] C. J. Capon et al. “Effect of ionospheric drag on atmospheric density estimation and orbit prediction”. In: *Advances in Space Research* 63.8 (2019). PII: S0273117719300213, pp. 2495–2505. ISSN: 02731177. DOI: 10.1016/j.asr.2019.01.013.

[25] C. Cappelletti, S. Battistini, and B. Malphrus. *Cubesat handbook. From mission design to operations*. London: Academic Press, 2021. ISBN: 012817885X. DOI: 10.1016/C2018-0-02366-X.

[26] F. Casella and M. Lovera. “High accuracy simulation of orbit dynamics: an object oriented approach”. In: *EUROSIM*. Ljubljana, Slovenia, 2007.

[27] C. Cercignani and M. Lampis. “Kinetic models for gas-surface interactions”. In: *Transport Theory and Statistical Physics* 1.2 (1971), pp. 101–114. ISSN: 0041-1450. DOI: 10.1080/00411457108231440.

[28] B. K. Ching, D. R. Hickman, and J. M. Straus. “Effects of atmospheric winds and aerodynnamic lift on the inclination of the orbit of the S3-1 satellite”. In: *Journal of Geophysical Research* 82.10 (1977), pp. 1474–1480.

[29] A. Chulliat et al. *The US/UK world magnetic model for 2015-2020*. Ed. by National Geophysical Data Center, NOAA. Boulder, Colorado, USA: National Geophysical Data Center, NOAA, 2015. DOI: 10.7289/V5TB14V7.

[30] W. H. Clohessy and R. S. Wiltshire. “Terminal guidance system for satellite rendezvous”. In: *Journal of the Aerospace Sciences* 27.9 (1960), pp. 653–658. ISSN: 1936-9999. DOI: 10.2514/8.8704.

[31] G. E. Cook. “The aerodynamic drag of near Earth satellites”. In: *Nature* 190.4774 (1960), pp. 392–393. ISSN: 0028-0836. DOI: 10.1038/190392b0.

[32] G. E. Cook. “The effect of aerodynamic lift on satellite orbits”. In: *Planetary and Space Science* 12.11 (1964), pp. 1009–1020. ISSN: 00320633. DOI: 10.1016/0032-0633(64)90077-7.

[33] N. H. Crisp et al. “The benefits of very low earth orbit for earth observation missions”. In: *Progress in Aerospace Sciences* 117.2 (2020), p. 100619. ISSN: 03760421. DOI: 10.1016/j.paerosci.2020.100619.

[34] S. D’Amico. “Autonomous formation flying in low Earth orbit”. Dissertation. Milan, Italy: Politecnico di Milano, 2010.

[35] S. D’Amico and O. Montenbruck. “Proximity operations of formation-flying spacecraft using an eccentricity/inclination vector separation”. In: *Journal of Guidance, Control, and Dynamics* 29.3 (2006), pp. 554–563. ISSN: 0731-5090. DOI: 10.2514/1.15114.

[36] D. A. Danielson et al. *Semianalytic satellite theory*. Monterey, California, USA: Naval Postgraduate School, 1995. URL: https://apps.dtic.mil/sti/pdfs/ADA531136.pdf.

[37] L. Dell’Elce. “Satellite orbits in the atmosphere. Uncertainty quantification, propagation and optimal control”. Space Structures and Systems Laboratory. Dissertation. Liège, Belgum: Université de Liège, 2015.

[38] L. Dell’Elce and G. Kerschen. “Optimal propellantless rendez-vous using differential drag”. In: *Acta Astronautica* 109 (2015), pp. 112–123. ISSN: 00945765. DOI: 10.1016/j.actaastro.2015.01.011.

[39] E. Doornbos. *Thermospheric density and wind determination from satellite dynamics*. Berlin, Heidelberg: Springer Berlin Heidelberg, 2012. ISBN: 978-3-642-25128-3. DOI: 10.1007/978-3-642-25129-0.

[40] D. P. Drob et al. “An update to the Horizontal Wind Model (HWM). The quiet time thermosphere”. In: *Earth and Space Science* 2.7 (2015), pp. 301–319. ISSN: 23335084. DOI: 10.1002/2014EA000089.

[41] S. Fasoulas et al. “Combining particle-in-cell and direct simulation Monte Carlo for the simulation of reactive plasma flows”. In: *Physics of Fluids* 31.7 (2019), p. 072006. ISSN: 1070-6631. DOI: 10.1063/1.5097638.

[42] S. Fasoulas et al. “High precision attitude control system based on the emission of electromagnetic radiation”. In: *35th International Electric Propulsion Conference*. Atlanta, Georgia, USA, 2017.

[43] Astro- und Feinwerktechnik Adershof GmbH. *Reaction Wheel RW1 for Small Satellites*. URL: https://www.astrofein.com/en/reaction-wheels/reaction-wheel-rw1/ (visited on 11/27/2022).

[44] J. M. Forbes. “Ionosphere-thermosphere basics - I Neutral atmosphere vertical structure”. In: *Advanced School on Space Weather*. International Centre for Theoretical Physics. Trieste, Italy, 2006.

[45] C. Foster et al. “Constellation phasing with differential drag on planet labs satellites”. In: *Journal of Spacecraft and Rockets* 20.5 (2017), pp. 1–11. ISSN: 0022-4650. DOI: 10.2514/1.A33927.

[46] J. Foust. *Dozens of starlink satellites from latest launch to reenter after geomagnetic storm*. 2022. URL: https://spacenews.com/dozens-of-starlink-satellites-from-latest-launch-to-reenter-after-geomagnetic-storm/ (visited on 09/14/2022).

[47] J. Foust. *Majority of tracked Russian ASAT debris has deorbited*. spacen. 2022. URL: https://spacenews.com/majority-of-tracked-russian-asat-debris-has-deorbited/ (visited on 11/22/2022).

[48] D. Friedrich. “Development of analytic algorithms for formation establishment maneuvers of satellite formations via aerodynamic forces”. Bachelor thesis. Stuttgart, Germany: The University of Stuttgart, 2021.

[49] G. Gaias and S. D’Amico. “Impulsive maneuvers for formation reconfiguration using relative orbital elements”. In: *Journal of Guidance, Control, and Dynamics* 38.6 (2015), pp. 1036–1049. ISSN: 0731-5090. DOI: 10.2514/1.G000189.

[50] J. W. Gangestad, B. S. Hardy, and D. A. Hinkley. “Operations, orbit determination, and formation control of the AeroCube-4 cubesats”. In: *27th Annual AIAA/USU Conference on Small Satellites*. Logan, Utah, USA, 2013.

[51] E. Gill. *Together in space. Potentials and challenges of distributed space systems*. Delft, The Netherlands: Delft University of Technology, 2008.

[52] E. Gill and H. Runge. “Tight formation flying for an along-track SAR interferometer”. In: *Acta Astronautica* 55.3-9 (2004). PII: S0094576504001870, pp. 473–485. ISSN: 00945765. DOI: 10.1016/j.actaastro.2004.05.044.

[53] S.-P. Gong, J.-F. Li, and H.-X. Baoyin. “Solar radiation pressure used for formation flying control around the Sun-Earth libration point”. In: *Applied Mathematics and Mechanics* 30.8 (2009). PII: 807, pp. 1009–1016. ISSN: 0253-4827. DOI: 10.1007/s10483-009-0807-z.

[54] A. Goodenough et al. “Birds of a feather flock together: Insights into starling murmuration behaviour revealed using citizen science”. In: *PLoS One* 12(6) (2017). DOI: 10.1371/journal.pone.0179277.

[55] D. Hastings and H. Garrett. *Spacecraft-environment interactions*. eng. Cambridge Atmospheric and Space Science. Cambridge, UK: Cambridge University Press, 2009. 319 pp. ISBN: 9780511525032. DOI: 10.1017/CBO9780511525032.

[56] C. Heather and J. Ashley. *Orbital debris. Quaterly news*. Ed. by National Aeronautics and Space Administration. National Aeronautics and Space Administration, 2020. URL: https://orbitaldebris.jsc.nasa.gov/quarterly-news/pdfs/odqnv27i1.pdf.

[57] F. Hild. “Adaptation and application of PICLas for the design of VLEO satellite geometries”. Master thesis. Stuttgart, Germany: The University of Stuttgart, 2021.

[58] F. Hild et al. “Optimisation of satellite geometries in very low Earth orbits for drag minimisation and lifetime extension”. In: *Acta Astronautica* 201 (2022). PII: S0094576522004970, pp. 340–352. ISSN: 00945765. DOI: 10.1016/j.actaastro.2022.09.032.

[59] F. Hild et al. “Results of a VLEO Satellite Design Optimisation for Drag Minimisation”. In: *2nd International Conference on Flight Vehicles, Aerothermodynamics and Re-entry Missions and Engineering (FAR)*. Heilbronn, Germany, 2022.

[60] G. W. Hill. “Researches in the lunar theory”. In: *American Journal of Mathematics* 1.1 (1878), p. 5. ISSN: 00029327. DOI: 10.2307/2369430.

[61] C. Homm. “Implementation of simultaneous in- and out-of-plane control of a rendezvous manoeuvre of two spacecraft using aerodynamic forces”. Bachelor thesis. Stuttgart, Germany: The University of Stuttgart, 2020.

[62] M. Horsley. “An investigation into using differential drag for controlling a formation of cubesats”. In: *Advanced Maui Optical and Space Surveillance Technologies Conference*. Maui, Hawaii, USA, 2011.

[63] M. Horsley, S. Nikolaev, and A. Pertica. “Small satellite rendezvous using differential lift and drag”. In: *Journal of Guidance, Control, and Dynamics* 36.2 (2013), pp. 445–453. ISSN: 0731-5090. DOI: 10.2514/1.57327.

[64] Y. Hu et al. “Differential aerodynamic force-based formation control of nanosatellites using yaw angle deviation”. In: *Journal of Guidance, Control, and Dynamics* 44.12 (2021), pp. 1–15. ISSN: 0731-5090. DOI: 10.2514/1.G006141.

[65] J. Huang et al. “Coulomb control of a triangular three-body satellite formation using nonlinear model predictive method”. In: *33rd Chinese Control Conference*. Nanjing, China, 2014. ISBN: 978-9-8815-6387-3. DOI: 10.1109/ChiCC.2014.6896281.

[66] X. Huang, Y. Yan, and Y. Zhou. “Optimal Lorentz-augmented spacecraft formation flying in elliptic orbits”. In: *Acta Astronautica* 111 (2015). PII: S009457651500065X, pp. 37–47. ISSN: 00945765. DOI: 10.1016/j.actaastro.2015.02.012.

[67] M. Hunter and S. D’Amico. “Closed-form optimal solutions for propulsive-differential drag control of spacecraft swarms”. In: *AAS/AIAA Astrodynamics Specialist Conference*. Charlotte. North Carolina, USA, 2022.

[68] ISO 14222. *ISO 14222 space environment (natural and artificial). Earth upper atmosphere*. URL: https://www.iso.org/standard/54507.html.

[69] D. Ivanov, M. Kushniruk, and M. Ovchinnikov. “Study of satellite formation flying control using differential lift and drag”. In: *Acta Astronautica* 152 (2018), pp. 88–100. ISSN: 00945765. DOI: 10.1016/j.actaastro.2018.07.047.

[70] D. Ivanov, U. Monakhova, and M. Ovchinnikov. “Nanosatellites swarm deployment using decentralized differential drag-based control with communicational constraints”. In: *Acta Astronautica* 159 (2019). PII: S0094576518317090, pp. 646–657. ISSN: 00945765. DOI: 10.1016/j.actaastro.2019.02.006.

[71] D. Ivanov, M. Ovchinnikov, and S. Tkachev. “Nanosatellites formation flying control approaches overview”. In: *IOP Conference Series: Materials Science and Engineering* 984.1 (2020), p. 012023. ISSN: 1757-8981. DOI: 10.1088/1757-899X/984/1/012023.

[72] D. Ivanov et al. “Decentralized control of nanosatellite tetrahedral formation flying using aerodynamic forces”. In: *Aerospace* 8.8 (2021). PII: aerospace8080199, p. 199. DOI: 10.3390/aerospace8080199.

[73] D. Ivanov et al. “Decentralized differential drag based control of nanosatellites swarm spatial distribution using magnetorquers”. In: *Advances in Space Research* 67.11 (2021). PII: S0273117720303471, pp. 3489–3503. ISSN: 02731177. DOI: 10.1016/j.asr.2020.05.024.

[74] D. Ivanov et al. “Deployment and maintenance of nanosatellite tetrahedral formation flying using aerodynamic forces”. In: *69th International Astronautical Congress*. International Astronautical Federation. Bremen, Germany, 2018.

[75] D. Ivanov et al. “Writing with sunlight: cubesat formation control using aerodynamic forces”. In: *70th International Astronautical Congress (IAC)*. Washington D.C., USA, 2019.

[76] A. C. Jimenez. “On the coupling of orbit and attitude determination of satellite formations from atmospheric drag. Observability and Estimation Performance”. Dissertation. Delft: Delft University of Technology, 2020.

[77] R. Kaneda et al. “The relative position control in formation flying satellites using super-conducting magnets”. In: *Journal of the Japan Society for Aeronautical and Space Sciences* 56.652 (2008), pp. 203–210. ISSN: 1344-6460. DOI: 10.2322/jjsass.56.203.

[78] T. S. Kelso. *CelesTrak. EOP and space weather data*. 2022. URL: https://celestrak.org/SpaceData/ (visited on 09/14/2022).

[79] D. J. Kessler and B. G. Cour-Palais. “Collision frequency of artificial satellites: The creation of a debris belt”. In: *Journal of Geophysical Research* 83.A6 (1978), p. 2637. ISSN: 01480227. DOI: 10.1029/JA083iA06p02637.

[80] L. King et al. *Spacecraft formation-flying using inter-vehicle coulomb forces*. Michigan Technological University, 2002. URL: http://www.niac.usra.edu/files/studies/final_report/601King.pdf.

[81] E. M. C. Kong et al. “Electromagnetic formation flight for multisatellite arrays”. In: *Journal of Spacecraft and Rockets* 41.4 (2004), pp. 659–666. ISSN: 0022-4650. DOI: 10.2514/1.2172.

[82] G. Koppenwallner. “Comment on special section. New perspectives on the satellite drag environments of Earth, Mars, and Venus”. In: *Journal of Spacecraft and Rockets* 45.6 (2008), pp. 1324–1327. ISSN: 0022-4650. DOI: 10.2514/1.37539.

[83] G. Koppenwallner. *Energy accommodation coefficient and momentum transfer modeling*. HTG Hyperschall Technologie Göttingen, 2009.

[84] R. Kristiansen and P. J. Nicklasson. “Spacecraft formation flying. A review and new results on state feedback control”. In: *Acta Astronautica* 65.11-12 (2009), pp. 1537–1552. ISSN: 00945765. DOI: 10.1016/j.actaastro.2009.04.014.

[85] K. D. Kumar et al. “Maintenance of satellite formations using environmental forces”. In: *Acta Astronautica* 102 (2014), pp. 341–354. ISSN: 00945765. DOI: 10.1016/j.actaastro.2014.05.001.

[86] M. F. Larsen and J. W. Meriwether. “Vertical winds in the thermosphere”. In: *Journal of Geophysical Research* 117 (2012). DOI: 10.1029/2012JA017843.

[87] D. F. Lawden. *Optimal trajectories for space navigation*. Butterworths, 1963.

[88] D.-H. Lee, H.-J. Lee, and H.-C. Bang. “Formation flying of small satellites using coulomb force”. In: *International Journal of Aeronautical and Space Sciences* 7.1 (2006), pp. 84–90. ISSN: 2093-274X. DOI: 10.5139/IJASS.2006.7.1.084.

[89] F. G. Lemoine et al. *The development of the joint NASA GSFC and NIMA geopotential model EGM96*. NASA/TP-1998-206861. Ed. by NASA Goddard Space Flight Center. Greenbelt, Maryland, USA: NASA Goddard Space Flight Center, 1998.

[90] C. L. Leonard. “Formationkeeping of spacecraft via differential drag”. Master’s thesis. Massachusetts Institute of Techology, 1986. 161 pp.

[91] C. L. Leonard, W. Hollister, and E. Bergmann. “Orbital formationkeeping with differential drag”. In: *Journal of Guidance, Control, and Dynamics* 12.1 (1987), pp. 108–113. ISSN: 0731-5090. DOI: 10.2514/3.20374.

[92] A. W. Lewin. “Low-cost operation of the ORBCOMM satellite constellation”. In: *Journal of Reducing Space Mission Cost* 1.1 (1998), pp. 105–117. ISSN: 13857479. DOI: 10.1023/A:1009987231306.

[93] S. Livadiotti. “Application of orbital aerodynamics to satellite attitude control”. Dissertation. Manchester, UK: The University of Manchester, 2021.

[94] S. Livadiotti et al. “A review of gas-surface interaction models for orbital aerodynamics applications”. In: *Progress in Aerospace Sciences* 119.1 (2020), p. 100675. ISSN: 03760421. DOI: 10.1016/j.paerosci.2020.100675.

[95] R. G. Lord. “Some extensions to the Cercignani–Lampis gas–surface scattering kernel”. In: *Physics of Fluids A: Fluid Dynamics* 3.4 (1991), pp. 706–710. ISSN: 0899-8213. DOI: 10.1063/1.858076.

[96] R. G. Lord. “Some further extensions of the Cercignani–Lampis gas–surface interaction model”. In: *Physics of Fluids* 7.5 (1995), pp. 1159–1161. ISSN: 1070-6631. DOI: 10.1063/1.868557.

[97] G. March. “Communication analysis of QB50 cubesat network”. Master’s thesis. Pisa, Italy: University of Pisa, 2014.

[98] C. Marianowski. “Satellite design considerations and analysis for differential lift and drag control methods”. Master thesis. Stuttgart, Germany: The University of Stuttgart, 2022.

[99] F. L. Markley and J. L. Crassidis. *Fundamentals of spacecraft attitude determination and control*. eng. Vol. 33. Space Technology Library. New York, NY: Springer, 2014. 486 pp. ISBN: 9781493908028.

[100] MathWorks. *Aerospace toolbox*. URL: https://de.mathworks.com/help/aerotbx/index.html (visited on 11/27/2022).

[101] MathWorks. *atan2 function*. URL: https://de.mathworks.com/help/matlab/ref/atan2.html (visited on 11/27/2022).

[102] MathWorks. *fminsearch function*. URL: https://de.mathworks.com/help/matlab/ref/fminsearch.html (visited on 11/27/2022).

[103] MathWorks. *ode113 integrator*. URL: https://de.mathworks.com/help/matlab/ref/ode113.html (visited on 11/27/2022).

[104] MathWorks. *reshape function*. URL: https://de.mathworks.com/help/matlab/ref/reshape.html (visited on 11/27/2022).

[105] A. Maute. *Thermospheric winds*. High atitude observatory, National Center for Atmospheric Science. 2016. URL: https://cedarscience.org/sites/default/files/2016/2016CEDAR_Sunday_Maute.pdf (visited on 09/14/2022).

[106] J. C. Maxwell. “VII. On stresses in rarified gases arising from inequalities of temperature”. In: *Philosophical Transactions of the Royal Society of London* 170 (1879), pp. 231–256. ISSN: 0261-0523. DOI: 10.1098/rstl.1879.0067.

[107] J. C. McDowell. *General catalog of artificial space objects*. 2022. URL: https://planet4589.org/space/gcat (visited on 09/14/2022).

[108] K. Moe and M. M. Moe. “Gas–surface interactions and satellite drag coefficients”. In: *Planetary and Space Science* 53.8 (2005), pp. 793–801. ISSN: 00320633. DOI: 10.1016/j.pss.2005.03.005.

[109] K. Moe, M. M. Moe, and C. J. Rice. “Simultaneous analysis of multi-instrument satellite measurements of atmospheric density”. In: *Journal of Spacecraft and Rockets* 41.5 (2004), pp. 849–853. ISSN: 0022-4650. DOI: 10.2514/1.2090.

[110] U. V. Monakhova and D. S. Ivanov. “Joining a formation flying of small satellites up using a magnetic orientation system for control using aerodynamic forces”. In: *XLIII Academic Space Conference* (Moscow, Russia). 2019, p. 060013. DOI: 10.1063/1.5133211.

[111] O. Montenbruck and E. Gill. *Satellite orbits. Models, methods and applications*. eng. Berlin and Heidelberg: Springer, 2000. 369 pp. ISBN: 9783642635472. DOI: 10.1007/978-3-642-58351-3.

[112] P. Moore. "The effect of aerodynamic lift on near-circular satellite orbits". In: *Planetary and Space Science* 33.5 (1985), pp. 479–491. ISSN: 00320633. DOI: 10.1016/0032-0633(85)90093-5.

[113] D. Mostaza Prieto. "Characterisation and Applications of Aerodynamic Torques on Satellites". Dissertation. Manchester, UK: The University of Manchester, 2017.

[114] D. Mostaza Prieto, B. P. Graziano, and P. C.E. Roberts. "Spacecraft drag modelling". In: *Progress in Aerospace Sciences* 64 (2014), pp. 56–65. ISSN: 03760421. DOI: 10.1016/j.paerosci.2013.09.001.

[115] S. R. Omar and R. Bevilacqua. "Spacecraft collision avoidance using aerodynamic drag". In: *Journal of Guidance, Control, and Dynamics* 43.3 (2020), pp. 567–573. ISSN: 0731-5090. DOI: 10.2514/1.G004518.

[116] J. H. Park et al. "Aerodynamic shape optimization of space vehicle in very-low-earth-orbit". In: *29th International Symposium on Rarefied Gas Dynamics*. Xi'an, China, 2014, pp. 1331–1336. DOI: 10.1063/1.4902745.

[117] M. A. Patterson and A. V. Rao. "GPOPS-II: A MATLAB software for solving multiple-phase optimal control problems using hp-adaptive gaussian quadrature collocation methods and sparse nonlinear programming". In: *ACM Transactions on Mathematical Software* 41.1 (2014), pp. 1–37. ISSN: 00983500. DOI: 10.1145/2558904.

[118] M. A. Peck et al. "Spacecraft formation flying using lorentz forces". en. In: *Journal of the British Interplanetary Society* 60 (2007), pp. 263–267.

[119] J. N. Pelton and S. Madry, eds. *Handbook of small satellites. Technology, design, manufacture, applications, economics and regulation*. Springer International Publishing, 2020. ISBN: 9783030207076.

[120] D. Pérez and R. Bevilacqua. "Differential drag spacecraft rendezvous using an adaptive Lyapunov control strategy". In: *Acta Astronautica* 83 (2013), pp. 196–207. ISSN: 00945765. DOI: 10.1016/j.actaastro.2012.09.005.

[121] D. Pérez and R. Bevilacqua. "Lyapunov-based spacecraft rendezvous maneuvers using differential drag". In: *AIAA Guidance, Navigation, and Control Conference*. Portland, Oregon, USA, 2011.

[122] J. M. Picone et al. "NRLMSISE-00 empirical model of the atmosphere. Statistical comparisons and scientific issues". In: *Journal of Geophysical Research: Space Physics* 107.A12 (2002), SIA 15-1-SIA 15–16. ISSN: 01480227. DOI: 10.1029/2002JA009430.

[123] M. D. Pilinski. "Dynamic gas-surface interaction modeling for satellite aerodynamic csomputations". Dissertation. Boulder, Colorado, USA: University of Colorado, 2011.

[124] M. D. Pilinski, B. M. Argrow, and S. E. Palo. "Semiempirical model for satellite energy-accommodation coefficients". In: *Journal of Spacecraft and Rockets* 47.6 (2010), pp. 951–956. ISSN: 0022-4650. DOI: 10.2514/1.49330.

[125] V. L. Pisacane. *The space environment and its effects on space systems*. Washington, DC: American Institute of Aeronautics and Astronautics, Inc, 2016. ISBN: 978-1-62410-353-7. DOI: 10.2514/4.103537.

[126] M. L. V. Pitteway. "Algorithm for drawing ellipses or hyperbolae with a digital plotter". In: *The Computer Journal* 10.3 (1967), pp. 282–289. ISSN: 0010-4620. DOI: 10.1093/comjnl/10.3.282.

[127] G. E. Pollock, J. W. Gangestad, and J. M. Longuski. "Analytical solutions for the relative motion of spacecraft subject to Lorentz-force perturbations". In: *Acta Astronautica* 68.1-2 (2011). PII: S0094576510002638, pp. 204–217. ISSN: 00945765. DOI: 10.1016/j.actaastro.2010.07.007.

[128] G. W. Prölss. *Physics of the Earth's space environment. An introduction*. Springer Berlin Heidelberg, 2004. ISBN: 978-3-642-05979-7. DOI: 10.1007/978-3-642-97123-5.

[129] V. Ray et al. *Improved drag coefficient modeling with spatial and temporal Fourier coefficient expansions Theory and applications*. en. 2019. DOI: 10.13140/RG.2.2.35940.53124.

[130] P. C. E. Roberts et al. "DISCOVERER - Radical redesign of Earth observation satellites for suistained operation at significantly lower altitudes". In: *68th International Astronautical Congress (IAC)*. Adelaide, Australia, 2017.

[131] F. Romano. "RF helicon plasma thruster for an atmosphere-breathing electric propulsion system (ABEP)". Dissertation. Stuttgart, Germany: The University of Stuttgart, 2021. ISBN: 978-3-8439-4953-8.

[132] C. W. T. Roscoe et al. "Formation establishment and reconfiguration using differential elements in J2-perturbed orbits". In: *Journal of Guidance, Control, and Dynamics* 38.9 (2015), pp. 1725–1740. ISSN: 0731-5090. DOI: 10.2514/1.G000999.

[133] C. M. Saaj et al. *Electrostatic forces for satellite swarm navigation and reconfiguration*. European Space Agency, 2006. URL: https://www.esa.int/gsp/ACT/doc/ARI/ARI%20Study%20Report/ACT-RPT-MAD-ARI-05-4107b-Electrostatic-Surrey.pdf.

[134] C. Sabol, R. Burns, and C. A. McLaughlin. “Satellite formation flying design and evolution”. In: *Journal of Spacecraft and Rockets* 38.2 (2001), pp. 270–278. ISSN: 0022-4650. DOI: 10.2514/2.3681.

[135] T. E. Sarris et al. “Daedalus: a low-flying spacecraft for in situ exploration of the lower thermosphere–ionosphere”. In: *Geoscientific Instrumentation, Methods and Data Systems* 9.1 (2020), pp. 153–191. DOI: 10.5194/gi-9-153-2020.

[136] S. A. Schaaf and P. L. Chambre. *Flow of rarefied gases*. Princeton University Press, 1958.

[137] R. Schamberg. *A new analytic representation of surface interction for hyperthermal free molecular flow*. Santa Monica, California, 1959.

[138] D. P. Scharf, F. Y. Hadaegh, and S. R. Ploen. “A survey of spacecraft formation flying guidance and control (part I): Guidance. Guidance”. In: *American Control Conference*. Denver, Colorado, USA: IEEE, 2003, pp. 1733–1739. ISBN: 0-7803-7896-2. DOI: 10.1109/ACC.2003.1239845.

[139] H. Schaub and K. T. Alfriend. “Impulsive feedback control to establish specific mean orbit elements of spacecraft formations”. In: *Journal of Guidance, Control, and Dynamics* 24.4 (2001), pp. 739–745. ISSN: 0731-5090. DOI: 10.2514/2.4774.

[140] H. Schaub and J. L. Junkins. *Analytical mechanics of space systems*. Washington, DC: American Institute of Aeronautics and Astronautics, Inc, 2018. ISBN: 978-1-62410-521-0. DOI: 10.2514/4.105210.

[141] H. Schaub, G. G. Parker, and L. B. King. “Challenges and prospects of coulomb spacecraft formations”. In: *Advances in the Astronautical Sciences 115(1)* (2003).

[142] H. Schaub et al. “Spacecraft formation flying control using mean orbit elements”. In: *Journal of the Astronautical Sciences* Jan.-March. 2000.Vol. 48, No.1 (2000).

[143] G. Schettino et al. “A frequency portrait of low Earth orbits”. In: *Celestial Mechanics and Dynamical Astronomy* 131.8 (2019). PII: 9912. ISSN: 0923-2958. DOI: 10.1007/s10569-019-9912-6.

[144] G. Schettino et al. “Exploiting dynamical perturbations for the end-of-life disposal of spacecraft in LEO”. In: *Astronomy and Computing* 27 (2019). PII: S2213133718300945, pp. 1–10. ISSN: 22131337. DOI: 10.1016/j.ascom.2019.02.001.

[145] S. A. Schweighart. “Development and analysis of a high fidelity linearized J2 model for satellite formation flying”. Master’s thesis. Boston: Massachusetts Institute of Techology, 2001. 100 pp. URL: 10.2514/6.2001-4744.

[146] S. A. Schweighart. “Electromagnetic formation flight dipole solution planning”. Dept. of Aeronautics and Astronautics. Dissertation. Boston, Massachusetts, USA: Massachusetts Institute of Technology, 2005.

[147] S. A. Schweighart and R. J. Sedwick. “High-fidelity linearized J2 model for satellite formation flight”. In: *Journal of Guidance, Control, and Dynamics* 25.6 (2002), pp. 1073–1080. ISSN: 0731-5090. DOI: 10.2514/2.4986.

[148] P. Sengupta and S. R. Vadali. “Relative motion and the geometry of formations in keplerian elliptic orbits with arbitrary eccentricity”. In: *Journal of Guidance, Control, and Dynamics* 30.4 (2007), pp. 953–964. ISSN: 0731-5090. DOI: 10.2514/1.25941.

[149] L. H. Sentman. “Free molecule flow theory and its application to the determination of aerodynamic forces”. In: *Technical Report, Lockheed Aircraft Corporation* (1961).

[150] SES. *O3b MEO*. URL: https://www.ses.com/our-coverage/o3b-meo (visited on 11/27/2022).

[151] X. Shao et al. “Satellite formation keeping using differential lift and drag under J2 perturbation”. In: *Aircraft Engineering and Aerospace Technology* 89.1 (2017), pp. 11–19. ISSN: 0002-2667. DOI: 10.1108/AEAT-06-2015-0168.

[152] X. Shao et al. “Satellite rendezvous using differential aerodynamic forces under J2 perturbation”. In: *Aircraft Engineering and Aerospace Technology* 87.5 (2015), pp. 427–436. ISSN: 0002-2667. DOI: 10.1108/AEAT-09-2013-0168.

[153] L. A. Sinpetru et al. “ADBSat: Methodology of a novel panel method tool for aerodynamic analysis of satellites”. In: *Computer Physics Communications* 275 (2022). PII: S0010465522000443, p. 108326. ISSN: 00104655. DOI: 10.1016/j.cpc.2022.108326.

[154] B. Smith. “A comprehensive examination of low Earth orbit aerodynamic accelerations for satellite formation control”. Dissertation. Canberra, Australia: University of New South Wales Canberra, 2019.

[155] B. Smith, C. Capon, and M. Brown. “Ionospheric drag for satellite formation control”. In: *Journal of Guidance, Control, and Dynamics* 42.12 (2019), pp. 2590–2599. ISSN: 0731-5090. DOI: 10.2514/1.G004404.

[156] B. Smith et al. “Investigation into the practicability of differential lift-based spacecraft rendezvous”. In: *Journal of Guidance, Control, and Dynamics* 40.10 (2017), pp. 2682–2689. ISSN: 0731-5090. DOI: 10.2514/1.G002537.

[157] B.G.A. Smith et al. “Ionospheric drag for accelerated deorbit from upper low earth orbit”. In: *Acta Astronautica* 176 (2020). PII: S0094576520304252, pp. 520–530. ISSN: 00945765. DOI: 10.1016/j.actaastro.2020.07.007.

[158] R. Sun et al. “Neural network-based sliding mode control for atmospheric-actuated spacecraft formation using switching strategy”. In: *Advances in Space Research* 61.3 (2017), pp. 914–926. ISSN: 02731177. DOI: 10.1016/j.asr.2017.11.011.

[159] R. Sun et al. “Neural-network-based sliding-mode adaptive control for spacecraft formation using aerodynamic forces”. In: *Journal of Guidance, Control, and Dynamics* 41.3 (2017), pp. 757–763. ISSN: 0731-5090. DOI: 10.2514/1.G003063.

[160] R. Sun et al. “Roto-translational spacecraft formation control using aerodynamic forces”. In: *Journal of Guidance, Control, and Dynamics* 40.10 (2017), pp. 2556–2568. ISSN: 0731-5090. DOI: 10.2514/1.G003130.

[161] R. Sun et al. “Spacecraft formation control using aerodynamic and Lorentz force”. In: *Aircraft Engineering and Aerospace Technology* 92.4 (2020), pp. 587–597. ISSN: 0002-2667. DOI: 10.1108/AEAT-10-2019-0207.

[162] E. K. Sutton. “Normalized force coefficients for satellites with elongated shapes”. In: *Journal of Spacecraft and Rockets* 46.1 (2009), pp. 112–116. ISSN: 0022-4650. DOI: 10.2514/1.40940.

[163] S. K. Tealib et al. “Analysis of the effects of electromagnetic forces on the relative motion of a charged spacecraft formation flying”. In: *Artificial Satellites* 55.3 (2020), pp. 87–99. DOI: 10.2478/arsa-2020-0007.

[164] S. K. Tealib et al. “Satellite formation flying control using an innovative technique subject to electromagnetic acceleration”. In: *International Journal of Space Science and Engineering* 6.2 (2020), p. 147. ISSN: 2048-8459. DOI: 10.1504/IJSPACESE.2020.110360.

[165] J. Thoemel and T. van Dam. “Autonomous formation flight using solar radiation pressure”. In: *CEAS Space Journal* 13.4 (2021). PII: 344, pp. 555–566. ISSN: 1868-2502. DOI: 10.1007/s12567-020-00344-2.

[166] C. Traub, S. Fasoulas, and G. Herdrich. “Progress in satellite formation flight control using differential aerodynamic forces made at the Institute of Space Systems (IRS)”. In: *AAS/AIAA Astrodynamics Specialist Conference*. South Lake Tahoe, California, USA, 2020.

[167] C. Traub, S. Fasoulas, and G. H. Herdrich. “A planning tool for optimal three-dimensional formation flight maneuvers of satellites in VLEO using aerodynamic lift and drag via yaw angle deviations”. In: *Acta Astronautica* 198 (2022). PII: S0094576522001606, pp. 135–151. ISSN: 00945765. DOI: 10.1016/j.actaastro.2022.04.010.

[168] C. Traub, S. Fasoulas, and G. H. Herdrich. “Assessment of the dependencies of realistic differential drag controlled in-plane reconfiguration maneuvers on relevant parameters”. In: *AAS/AIAA Astrodynamics Specialist Conference*. South Lake Tahoe, California, USA, 2020.

[169] C. Traub, G. H. Herdrich, and S. Fasoulas. “Influence of energy accommodation on a robust spacecraft rendezvous maneuver using differential aerodynamic forces”. In: *CEAS Space Journal* 12.1 (2020), pp. 43–63. ISSN: 1868-2502. DOI: 10.1007/s12567-019-00258-8.

[170] C. Traub et al. “A review and gap analysis of exploiting aerodynamic forces as a means to control satellite formation flight”. In: *67th Deutscher Luft- und Raumfahrtkongress*. Friedrichshafen, Germany, 2018.

[171] C. Traub et al. “On the exploitation of differential aerodynamic lift and drag as a means to control satellite formation flight”. In: *CEAS Space Journal* 12.1 (2020), pp. 15–32. ISSN: 1868-2502. DOI: 10.1007/s12567-019-00254-y.

[172] J. Tschauner and P. Hempel. “Rendezvous zu einem in elliptischer bahn umlaufenden ziel”. In: *Astronautica Acta* 11 (1965), pp. 312–321.

[173] S. Tsujii, M. Bando, and H. Yamakawa. “Spacecraft formation flying dynamics and control using the geomagnetic Lorentz force”. In: *Journal of Guidance, Control, and Dynamics* 36.1 (2013), pp. 136–148. ISSN: 0731-5090. DOI: 10.2514/1.57060.

[174] F. Turco. “Design and implementation of a tool to simulate collision avoidance using aerodynamic drag for the Flying Laptop”. Master thesis. Stuttgart, Germany: The University of Stuttgart, 2022.

[175] F. Turco et al. “An analysis tool for collision avoidance manoeuvres using aerodynamic drag”. In: *Acta Astronautica* 211 (2023), pp. 116–129. ISSN: 00945765. DOI: 10.1016/j.actaastro.2023.05.038.

[176] F. Turco et al. “Analysis of collision avoidance manoeuvres using aerodynamic drag for the Flying Laptop satellite”. In: *19th PEGASUS Student Conference*. Rome, Italy, 2023.

[177] S. Vaidya et al. “Development and analysis of novel mission scenarios based on Atmosphere-Breathing Electric Propulsion (ABEP)”. In: *CEAS Space Journal* 14.4 (2022). PII: 436, pp. 689–706. ISSN: 1868-2502. DOI: 10.1007/s12567-022-00436-1.

[178] D. A. Vallado and D. Finkleman. “A critical assessment of satellite drag and atmospheric density modeling”. In: *Acta Astronautica* 95 (2014), pp. 141–165. ISSN: 00945765. DOI: 10.1016/j.actaastro.2013.10.005.

[179] D. A. Vallado and W. D. McClain. *Fundamentals of astrodynamics and applications*. 4th ed. Space Technology Library. Hawthorne, CA: Published by Microcosm Press, op. 2013. XXII, 1106, [1] s. ISBN: 1881883205.

[180] S. Varma. “Control of satellites using environmental forces : aerodynamic drag / solar radiation pressure”. Dissertation. Toronto, Ontario, Canada: Ryerson University, 2011. URL: http://digital.library.ryerson.ca/islandora/object/RULA:944.

[181] S. Varma and K. D. Kumar. “Satellite formation flying using solar radiation pressure and/or aerodynamic drag”. In: *Proceedings of the 12th International Space Conference of Pacific-basin Societies (ISCOPS)*. Montreal, Quebec, Canada, 2010.

[182] J. Virgili Llop. “Spacecraft flight in the atmosphere”. School of Engineering. Dissertation. Cranfield University, 2014. 218 pp.

[183] A. Wächter and L. T. Biegler. “On the implementation of an interior-point filter line-search algorithm for large-scale nonlinear programming”. In: *Mathematical Programming* 106.1 (2006), pp. 25–57. ISSN: 0025-5610. DOI: 10.1007/s10107-004-0559-y.

[184] A. Walker, P. Mehta, and J. Koller. “Drag coefficient model using the Cercignani–Lampis–Lord gas–surface interaction model”. In: *Journal of Spacecraft and Rockets* 51.5 (2014), pp. 1544–1563. ISSN: 0022-4650. DOI: 10.2514/1.A32677.

[185] J. Walsh and L. Berthoud. “Reducing spacecraft drag in very low Earth orbit through shape optimisation”. In: *7th European Conference for Aeronautics and Space Sciences (EUCASS)* (Milan). 2017.

[186] J. Walsh, L. Berthoud, and C. Allen. “Drag reduction through shape optimisation for satellites in Very Low Earth Orbit”. In: *Acta Astronautica* 179 (2021). PII: S0094576520305579, pp. 105–121. ISSN: 00945765. DOI: 10.1016/j.actaastro.2020.09.018.

[187] U. Walter. *Astronautics*. Cham: Springer International Publishing, 2018. ISBN: 978-3-319-74372-1. DOI: 10.1007/978-3-319-74373-8.

[188] M. Walther. “Analysis of the feasibility range of rendezvous maneuvers using aerodynamic forces”. Bachelor thesis. Stuttgart, Germany: The University of Stuttgart, 2019.

[189] M. Walther et al. “Improved success rates of rendezvous maneuvers using aerodynamic forces”. In: *CEAS Space Journal* 12.1 (2020), p. 15. ISSN: 1868-2502. DOI: 10.1007/s12567-020-00314-8.

[190] M. Walther et al. “Improvements to the feasibility range of rendezvous maneuvers using aerodynamic forces”. In: *68th Deutscher Luft-und Raumfahrtkongress*. Darmstadt, Germany, 2019.

[191] B. Wie. *Space vehicle dynamics and control*. eng. AIAA education series. Reston, Virginia: American Inst. of Aeronautics and Astronautics, 2008. 950 pp. ISBN: 9781563479533.

[192] T. Williams and Z.-S. Wang. “Uses of solar radiation pressure for satellite formation flight”. In: *International Journal of Robust and Nonlinear Control* 12.2-3 (2002), pp. 163–183. ISSN: 1049-8923. DOI: 10.1002/rnc.681.

[193] H.-H. Yeh and A. Sparks. “Geometry and control of satellite formations”. In: *Proceedings of the 2000 American Control Conference.* Chicago, IL, USA, 2000, pp. 384–388. ISBN: 0-7803-5519-9. DOI: 10.1109/ACC.2000.878926.

[194] Z. Yoon et al. “Orbit deployment and drag control strategy for formation flight while minimizing collision probability and drift”. In: *CEAS Space Journal* 12.3 (2020), pp. 397–410. ISSN: 1868-2502. DOI: 10.1007/s12567-020-00308-6.

[195] S.-T. Yu and C.-Z. Fan. “Aerodynamic analysis and drag-reduction design for ultra-low-orbit satellite”. In: *IOP Conference Series: Materials Science and Engineering* 887.1 (2020), p. 012013. ISSN: 1757-8981. DOI: 10.1088/1757-899X/887/1/012013.

Publications by the author

The contents of this dissertation were published in the following publications, in which the author was corresponding author or substantially involved as co-author:

[21] S. Bühler, **C. Traub** et al. "Development and verification of enhanced algorithms to ensure the success of rendezvous maneuvers using aerodynamic forces". In: *69th Deutscher Luft- und Raumfahrtkongress*. Aachen, Germany, 2020.

[22] S. Bühler, **C. Traub** et al. "Enhanced algorithms to ensure the success of rendezvous maneuvers using aerodynamic forces". In: *CEAS Space Journal* 13 (2021), pp. 637–652.

[58] F. Hild, **C. Traub** et al. "Optimisation of satellite geometries in Very Low Earth Orbits for drag minimisation and lifetime extension". In: *Acta Astronautica* 201 (2022), pp. 340–352.

[59] F. Hild, M. Pfeiffer, **C. Traub** et al. “Results of a VLEO Satellite Design Optimisation for Drag Minimisation”. In: *2nd International Conference on Flight Vehicles, Aerothermodynamics and Re-entry Missions Engineering (FAR)*. Heilbronn, Germany, 2022

[166] **C. Traub**, S. Fasoulas, and G. H. Herdrich. "Progress in satellite formation flight control using differential aerodynamic forces made at the Institute of Space Systems (IRS)". In: *AAS/AIAA Astrodynamics Specialist Conference*. South Lake Tahoe, California, USA, 2020.

[167] **C. Traub**, S. Fasoulas, and G. H. Herdrich. "A planning tool for optimal three-dimensional formation flight maneuvers of satellites in VLEO using aerodynamic lift and drag via yaw angle deviations". In: *Acta Astronautica* 198 (2022), pp. 135–151.

[168] **C. Traub**, S. Fasoulas, and G. H. Herdrich. "Assessment of the dependencies of realistic differential drag controlled in-plane reconfiguration maneuvers on relevant parameters". In: *AAS/AIAA Astrodynamics Specialist Conference*. South Lake Tahoe, California, USA, 2020.

[169] **C. Traub**, G. H. Herdrich, and S. Fasoulas. "Influence of energy accommodation on a robust spacecraft rendezvous maneuver using differential aerodynamic forces". In: *CEAS Space Journal* 12.1 (2020), pp. 43–63.

[170] **C. Traub** et al. "A review and gap analysis of exploiting aerodynamic forces as a means to control satellite formation flight". In: *67th Deutscher Luft- und Raumfahrtkongress*. Friedrichshafen, Germany, 2018.

[171] **C. Traub** et al. "On the exploitation of differential aerodynamic lift and drag as a means to control satellite formation flight". In: *CEAS Space Journal* 12.1 (2020), pp. 15–32.

[175] F. Turco, **C. Traub** et al. “An analysis tool for collision avoidance manoeuvres using aerodynamic drag”. In: *Acta Astronautica* 211 (2023), pp. 116-119.

[176] F. Turco, **C. Traub** et al. “Analysis of collision avoidance manoeuvres using aerodynamic drag for the Flying Laptop satellite”. In: *19th PEGASUS Student Conference*. Rome, Italy, 2023.

[177] S. Vaidya, **C. Traub** et al. "Development and analysis of novel mission scenarios based on Atmosphere- Breathing Electric Propulsion (ABEP)". In: *CEAS Space Journal* 14.4 (2022), pp. 689–706.

[189] M. Walther, **C. Traub** et al. "Improved success rates of rendezvous maneuvers using aerodynamic forces". In: *CEAS Space Journal* 12.1 (2020), p. 15-32.

[190] M. Walther, **C. Traub** et al. "Improvements to the feasibility range of rendezvous maneuvers using aerodynamic forces". In: *68th Deutscher Luft-und Raumfahrtkongress*. Darmstadt, Germany, 2019.

Supervised student theses

The results of the following student theses, which have been supervised by the author, have been incorporated into this dissertation:

[8] J. Beck. "Development of a MATLAB based simulation tool for formation flight maneuver trajectories using differential lift and drag". Bachelor thesis. Stuttgart, Germany: The University of Stuttgart, 2022.

[11] T. Bender. "Development and assessment of novel mission concepts using a combination of ABEP and Aerodynamic Forces". Bachelor thesis. Stuttgart, Germany: The University of Stuttgart, 2022.

[20] S. Bühler. "Improvements of analytic algorithms to ensure the feasibility of rendezvous maneuver using aerodynamic forces". Bachelor thesis. Stuttgart, Germany: The University of Stuttgart, 2020.

[48] D. Friedrich. "Development of analytic algorithms for formation establishment maneuvers of satellite formations via aerodynamic forces". Bachelor thesis. Stuttgart, Germany: The University of Stuttgart, 2021.

[57] F. Hild. "Adaptation and application of PICLas for the design of VLEO satellite geometries". Master thesis. Stuttgart, Germany: The University of Stuttgart, 2021.

[61] C. Homm. "Implementation of simultaneous in- and out-of-plane control of a rendezvous manoeuvre of two spacecraft using aerodynamic forces". Bachelor thesis. Stuttgart, Germany: The University of Stuttgart, 2020.

[98] C. Marianowski. "Satellite design considerations and analysis for differential lift and drag control methods". Master thesis. Stuttgart, Germany: The University of Stuttgart, 2022.

[174] F. Turco. "Design and implementation of a tool to simulate collision avoidance using aerodynamic drag for the Flying Laptop". Master thesis. Stuttgart, Germany: The University of Stuttgart, 2022.

[188] M. Walther. "Analysis of the feasibility range of rendezvous maneuvers using aerodynamic forces". Bachelor thesis. Stuttgart, Germany: The University of Stuttgart, 2019.

Appendix A

Emerging trends in spaceflight

Three trends have been and currently are revolutionizing the way humans conduct spaceflight, namely an exploitation of the Very-Low Earth Orbit regime, the miniaturization of satellites and the distribution of payload tasks among multiple coordinated units. A synergetic exploitation of these trends promises breakthroughs in various fields of application.

A.1 Exploitation of VLEO

The term Very Low Earth Orbits refers to a subset of Low Earth Orbits in which the aerodynamic drag created by the interaction between the spacecraft's surface and the remaining atmospheric particles ensures a natural orbital decay that results in uncontrolled re-entry within a time frame generally considered too short for sustained satellite operations. Due to density variations in the thermosphere caused by natural effects, often referred to as "space weather", this time frame is highly variable and is also significantly affected by the initial orbital parameters and design characteristics of a particular spacecraft. The approximate altitude range for VLEO is below 450 km [33], although no definitive standards have yet been established. In this range, typical timescales to re-entry after orbital decay for objects not supported by drag mitigation measures are often given as weeks, months, or at most a few years. Despite the challenges involved, operating spacecraft in lower orbits promises a variety of potential benefits for future scientific and commercial space missions [33]. The recent interest in the VLEO regime can be divided into commercial interests, scientific interests, and the desire for a safe long-term operating environment.

Commercial interests: The global market for satellite-based Earth observation data is ever expanding. In terms of Earth observation, the operation of satellites at lower altitudes can be associated with a number of benefits, which are excellently illustrated in the publication of Crisp et al. [33]. The second emerging market, referred to as *global connectivity*, aims to provide broadband internet to the missing 50 % of the world's population via satellite constellations (for example, the company *O3b* [150] ("the other 3 billion")). Global connectivity is a prerequisite for successful application of the Internet of Things and for (semi-)autonomous systems, which explains the proposed development and launch of mega-satellite constellations by SpaceX and Amazon. Regardless of the business case of interest, the VLEO system is advantageous in terms of launch costs, as the payload performance of an orbital launch vehicle generally increases as altitude decreases. As a result, a larger number of satellites can be delivered to orbit per launch at no additional cost, or conversely, the cost per satellite of a given mass decreases [33].

Scientific interests: The Earth's atmosphere is a complex dynamical system that responds to forces from above and below and which is not well quantified yet [135]. The least known region of the atmosphere is the lower thermosphere, because it is too high to be observed with ground-based instruments but too low for sustained in situ measurements[30]. Due to its importance for space applications, a need for future investigation exists.

Safe operational environment: As the amount of space debris continues to increase, there is a very real risk of congestion in the middle and upper LEO region. This problem could reach a point at which satellite deployment in this highly critical region is no longer practical due to the extreme risk of hypervelocity collisions, with extant debris having multiplied as a consequence of a collisional cascade, a scenario known as the *Kessler syndrome* [79]. Boley and Byers [14] argue that to date, there is little appreciation the capacity of the Earth's orbit is finite. A recent example of an irresponsible act is the Russian direct-ascent anti-satellite test (ASAT) conducted on Nov. 15, 2021, in which a Russian missile destroyed Cosmos 1408, a defunct Soviet satellite, and a field of at least 1,700 traceable pieces of debris in low orbit was created [47]. As a direct consequence, ESA's Sentinal-1A satellite, which is orbiting 200 km above the Russian satellite, had to alter its orbit by 140 m in May 2022 to prevent collision with one of the debris fragments. Findings by Brown et al. [17] indicate that this predicament could even worsen as the increase in CO_2 concentration causes a cooling of the upper atmosphere and a decrease in atmospheric density. Their analysis predicts the decrease to reach a maximum of –30 % even if the Paris Agreement target to limit global warming to 1.5 °C is met. This would result in increased orbital lifetimes of debris particles of 30 % compared to the year 2000. [17]

For VLEO, the very environmental features that render a sustainable access challenging guarantee that orbits of interest will remain almost free of space debris in perpetuity. Both, an involuntary failure and a deliberate deactivation of a VLEO satellite's drag-mitigating subsystem incur its rapid disposal through orbit deterioration by atmospheric drag. Any orbital debris stemming from destroyed VLEO satellites, as well as defunct auxiliary hardware or upper rocket stages, is rapidly removed through orbit deterioration by atmospheric drag, thus hardly contributing to the threat of collisions within a growing population of enduring space debris in LEO. This holds true even if one or more of the announced mega constellations were to be deployed.

A.2 Miniaturization of satellite systems

As figuratively described by Pelton and Madry [119], the very first satellites launched into orbit in the late 1950s and early 1960s all belonged to the "small" class of satellites, even though that categorization did not yet exist. However, this changed quite rapidly in the years that followed as individual satellites increased in mass and technical sophistication [119]. Today, the advent of powerful but inexpensive electronics and innovative manufacturing techniques enables the miniaturization of satellites with increased functionality per unit mass. These standardized satellites using "Commercial-off-the-Shelf" parts can be developed faster and cheaper, allowing new entities to participate. This represents an important enabler of so-called "NewSpace" or "Space 2.0" ventures [119]. Small satellites are classified into *nanosatellites*, with a mass between 1 kg - 10 kg, *picosatellites*, with a mass between 0.1 kg - 1 kg and *femtosatellites*, which weigh less than 100 g. *CubeSats* are a class of standardized nanosatellites which range in sizes from 1U (10 cm × 10 cm × 10 cm) to 6U (30 cm × 20 cm × 10 cm) and weigh between 1 kg - 8 kg [119].

[30] This is why scientists often informally refer to this region as the "ignorosphere."

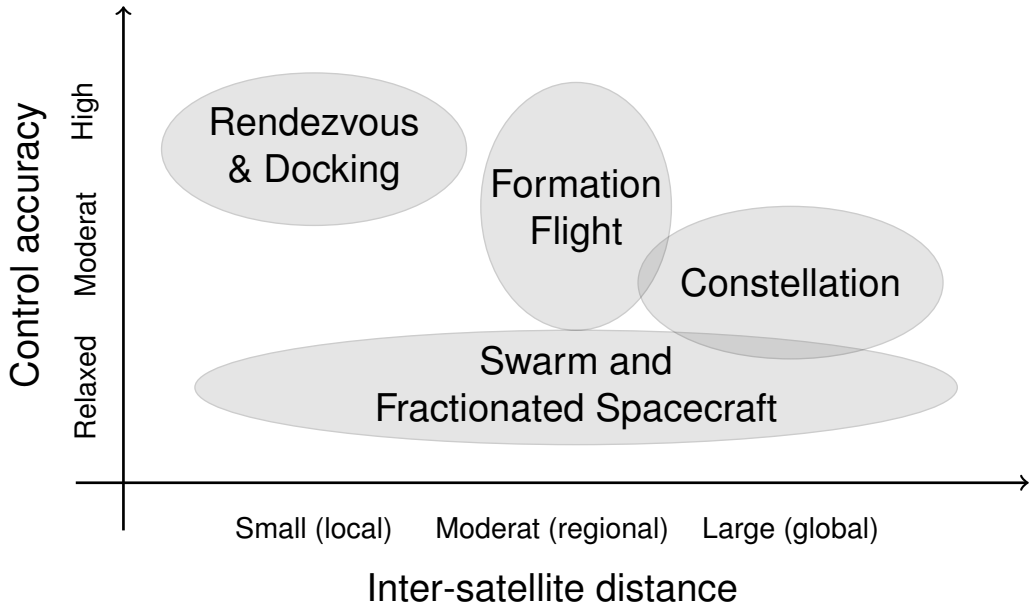

Figure A.1: Categorization of distributed space systems with respect to their inter-satellite distance and their requirements on control accuracy as proposed by Gill [51] (reproduced from Gill [51]).

A.3 Distributed space systems

The terminology *distributed space systems* describes the merging of multiple satellites to solve a common problem in a collaborative manner . This approach promises benefits in performance, flexibility, scalability and cost. In addition, it enables new types of mission concepts which would not be feasible without a payload distribution. [25] Distributed space systems may be classified by different metrics. Among others, the degree of autonomy, the nature of communication, the inter-satellite distance, the type of control and its accuracy, the number of satellites or the types of relative trajectories are consulted [76]. In his inaugural speech at TU Delft, Gill [51] proposed a classification based on the inter-satellite distance and the control requirements. With respect to the inter-satellite distance, Gill [51] distinguishes between local systems, with separations of a few meters, regional systems, with separations of a few meters to several hundred kilometers, to global systems with separation of more than a thousand kilometers. In terms of control accuracy, Gill [51] proposes to distinguish between relaxed, moderate and high demands. Based on this differentiation, Gill [51] identifies four different classes of DSS, illustrated in Fig. A.1.

This dissertation limits itself to a discussion of satellite formations which, according to Scharf, Hadaegh, and Ploen [138], are defined as: *"A set of more than one spacecraft whose dynamic states are coupled through a common control law."* Furthermore, the authors extend that at least one member of the set has to track a desired state relative to another member and that the tracking control law must depend upon this relative state. The second point is described as the critical differentiation from a constellation, where the orbit corrections are solely based on an individual satellite's position and velocity. [138] Cappelletti, Battistini, and Malphrus [25] associate formations with small relative inter-satellite distances, on-board closed-loop control and inter-spacecraft communication.

Constantin Traub

Curriculum vitae

+49 (0)711 685 60820
ctraub@irs.uni-stuttgart.de

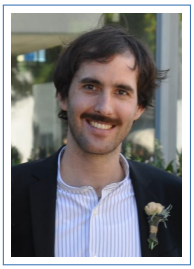

Current position

Since July 2023 — **Postdoctoral Researcher**
Institute of Space Systems (IRS), University of Stuttgart, Stuttgart, Germany

Education

2018-2023 — **Doctor of Engineering Sciences (Dr.-Ing.)**
Institute of Space Systems (IRS), University of Stuttgart, Stuttgart, Germany

2015–2017 — **Master of Science**
Technical University of Munich (TUM), Munich, Germany

2011–2015 — **Bachelor of Science**
Technical University of Munich (TUM), Munich, Germany

Theses

Dissertation — *"Differential aerodynamic forces as a means to control satellite formation flight"*
Supervisors — Prof. Dr.-Ing. Stefanos Fasoulas, Prof. Dr.-Ing. Enrico Stoll, Dr. Jan Thoemel
Grade — Summa cum laude (mit Auszeichnung)

Master's thesis: — *"Assessments of the Impacts of Plant Growth on the Air-Revitalization Systems of Different Sized Space Habitats using the Virtual Habitat"*
Supervisors — Prof. Dr. Ulrich Walter (TUM), Michael K. Ewert (NASA)
Grade — 1.0

Experience

Vocational

03/2017-09/2017 — **Visiting scientist**
NASA's Johnson Space Center, Houston, Texas, United States

Teaching

Since 2021 — **Lecturer and Tutor**
'Orbital mechanics in LEO', 'Space Systems' and 'Energy Systems for Space Applications'

Others

Since 2021 — **Reviewer**
'CEAS Space Journal', 'Journal of Spacecraft and Rockets' and 'Journal of Guidance Control and Dynamics'